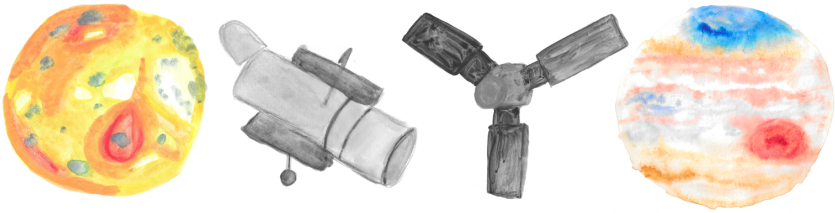

University of Liège

Thesis submitted in partial fulfilment of the requirements for the degree of Doctor of Science

Variability of Jupiter's aurora, moons, and magnetosphere investigated using advanced data analysis

Linus Head
supervised by
Prof. Denis Grodent and Dr. Bertrand Bonfond

LIÈGE université

To my parents.
À Chloé.

Summary

After more than 70 years of study, Jupiter's aurorae, moons, and magnetosphere have become fertile ground for investigation by large-scale, automated data- and image-analysis methods. This thesis comprises four related investigations of Jupiter's aurora, magnetosphere, and its moon Io, in which advanced image-analysis techniques are applied to large datasets to draw novel conclusions about their origins and properties.

The first study explores the neutral sodium cloud(s) around Io and their interaction with the plasma torus and Jupiter's wider space environment. Despite the presence of an unprecedentedly bright jet in late 2014, the brightness of the Io plasma torus and Jupiter's extended sodium nebula were unaffected. Conversely, a period of simultaneous enhancement of the plasma torus and sodium nebula in 2015 was not accompanied by a conjugate enhancement in the jet. This indicates that the jet does not contribute toward populating these two structures, at least not in a straight-forward way.

The second study concerns the variability of the size and brightness of the jovian UV main auroral emission. This analysis shows that the main emission is both brighter and more contracted from its average position at dusk than at dawn.

Additionally, the main emission is shown to have undergone a global contraction and brightening when the magnetosphere was compressed. The fact that the main emission is brighter at dusk than at dawn, and that it globally brightens during magnetospheric compression, contrasts with the predictions and observations of field-aligned currents in the magnetosphere, indicating that the generation of the main emission may predominantly occur via other mechanisms.

The third study investigates the "bridge" features sometimes seen in the dusk-side UV polar aurora. Juno crossings of these bridges reveal that existing theories on the generation of the polar aurora involving large-amplitude electrostatic waves are consistent with the measured properties of bridges. They are also characterised by the presence of majority-upward-travelling electrons, which indicates that they may be instances of the Zone-II main emission that have become separated from the rest of the Zone-I aurora. This interpretation is strengthened by the presence of bridge-like signatures (electrostatic waves, significant upward electron flux) for the main emission when bridges are not visually present in the aurora, and the lack of these features in the main emission when separate bridges are present.

The fourth and final study deals with signatures of plasma injection in the UV outer emission. The electron distributions during Juno crossings of injection signatures, as well as the inverse proportionality identified between surface magnetic-field strength and auroral brightness, indicate that pitch-angle scattering in the equatorial plasma sheet is likely the dominant mechanism to produce injection signatures. Evidence is provided that there exist two classes of injection signature, dawn-storm and non-dawn-storm signatures; this latter class

had been previously presented in the literature in only a limited and tentative fashion. Finally, injection-signature brightness is correlated with both the dissipative Alfvénic flux and field-aligned current density measured by Juno. Since both Alfvénic and current-based generation mechanisms are not supported by other properties of injection signatures, it is suggested that Alfvénic flux and field-aligned currents are secondary products of the plasma injection and do not meaningfully contribute towards auroral injection signatures.

In all, this thesis highlights the usefulness of advanced and automated image-analysis techniques in the study of Jupiter's aurora, its moons, and its magnetosphere. The results of this thesis also contribute to the growing body of evidence that precipitating electrons contributing to the UV main auroral emission are dominated by stochastic, broadband acceleration by Alfvén waves, rather than (or perhaps alongside) acceleration from quasi-static field-aligned potentials.

Résumé

Après plus de 70 ans d'études, les aurores, les lunes, et la magnétosphère de Jupiter demeurent un terrain fertile pour l'étude par des méthodes d'analyse automatisées à grande échelle de données et d'images. Cette thèse présente quatre études distinctes des aurores, de la magnétosphère, et de la lune Io de Jupiter, dans lesquelles des techniques avancées d'analyse d'images sont appliquées à de vastes ensembles de données afin de tirer des conclusions inédites sur leurs origines et leurs propriétés.

La première étude explore les nuages de sodium neutre entourant Io et leur interaction avec le tore de plasma et l'environnement spatial de Jupiter. Malgré la présence d'un jet d'une luminosité exceptionnelle fin 2014, la luminosité du tore de plasma d'Io et de la nébuleuse de sodium étendue de Jupiter est restée inchangée. Inversement, une période d'augmentation simultanée de la luminosité du tore de plasma et de la nébuleuse de sodium en 2015 ne s'est pas accompagnée d'une augmentation concomitante du jet. Ceci indique que le jet ne contribue pas à la formation de ces deux structures, au moins pas de manière directe.

La seconde étude porte sur la variabilité de la taille et de

la luminosité de l'émission aurorale principale UV de Jupiter. Cette analyse montre que l'émission principale est à la fois plus brillante et plus contractée par rapport à sa position moyenne au crépuscule qu'à l'aube. De plus, il est démontré que l'émission principale subit une contraction et une augmentation de luminosité globales lorsque la magnétosphère est comprimée. Le fait que l'émission principale soit plus brillante au crépuscule qu'à l'aube, et qu'elle s'intensifie globalement lors de la compression magnétosphérique, contraste avec les prédictions et les observations des courants alignés sur le champ magnétique dans la magnétosphère, indiquant que la génération de l'émission principale pourrait se produire principalement via d'autres mécanismes.

La troisième étude examine les structures en forme de « bridges » parfois observées dans l'aurore polaire UV du côté crépusculaire. Les observations de ces bridges par Juno révèlent que les théories existantes sur la génération de l'aurore polaire, impliquant des ondes électrostatiques de grande amplitude, sont cohérentes avec les propriétés mesurées des bridges. Ils sont également caractérisés par la présence d'électrons qui en majorité s'éloignent de la planète, ce qui suggère qu'il pourrait s'agir de cas d'émission principale de la Zone II qui se sont séparées du reste de l'aurore de la Zone I. Cette interprétation est renforcée par la présence de signatures des bridges (ondes électrostatiques, flux d'électrons ascendant significatif) pour l'émission principale lorsque les bridges ne sont pas visibles dans l'aurore, et par l'absence de ces caractéristiques dans l'émission principale lorsque des bridges séparés sont présents.

La quatrième et dernière étude porte sur les signatures d'injection de plasma dans l'émission externe UV. La distribution

des électrons lors des passages de Juno au-dessus des signatures d'injection, ainsi que la proportionnalité inverse observée entre l'intensité du champ magnétique de surface et la luminosité aurorale, indiquent que la diffusion angulaire dans le disque de plasma équatorial est probablement le mécanisme dominant à l'origine des signatures d'injection. J'ai démontré qu'il existe deux types de signatures d'injection : les signatures liées aux « dawn storms » et celles qui n'y sont pas liées ; cette dernière catégorie n'avait été présentée dans la littérature jusqu'ici que de manière limitée et préliminaire. Enfin, la luminosité des signatures d'injection est corrélée à la fois au flux Alfvénique dissipatif et à la densité de courant aligné avec le champ magnétique, mesurés par Juno. Puisque les mécanismes de génération par effet Alfvénique et par courant ne sont corroborés par aucune autre propriété des signatures d'injection, il est suggéré que le flux Alfvénique et les courants alignés sur le champ magnétique sont des produits secondaires du processus de diffusion angulaire et ne contribuent pas de manière significative aux signatures d'injection aurorales.

En résumé, cette thèse met en lumière l'utilité des techniques d'analyse d'images avancées et automatisées pour l'étude des aurores de Jupiter, de ses lunes, et de sa magnétosphère. Les résultats de cette thèse contribuent également à l'ensemble croissant de preuves indiquant que les électrons précipités à l'origine de l'émission principale aurorale UV, sont principalement accélérés d'une façon stochastique et avec une large distribution en énergie par des ondes d'Alfvén, plutôt que par (ou en parallèle avec) des potentiels quasi-statiques alignés avec le champ magnétique.

Acknowledgements

Before we get into the thesis proper, I should like to convey a few words of thanks to those people who have made this thesis possible.

First and foremost, I am required to tell you that this thesis benefits from the support of the French Community of Belgium in the context of the FRIA Doctoral Grant awarded to L. A. Head (me).

I would first like to thank my colleagues at the LPAP and wider AGO department, who welcomed me warmly into the team and who have guided and advised me during the course of this thesis. A particular thanks goes to Guillaume Sicorello, with whom I have shared an office for the last four years. I have greatly appreciated bouncing ideas off of you; I will miss you almost as much as you will miss me.

J'aimerais également remercier les membres de mon comité de thèse - Prof. Denis Grodent, Dr. Bertrand Bonfond, Prof. Jean-Claude Gérard, et Prof. Marc van Droogenbroeck - pour leur aide avec mes études et leurs commentaires sur ce manuscrit. En particulier, je suis profondément redevable au Prof. Denis Grodent et Dr. Bertrand Bonfond, mes deux promoteurs, pour leur inébranlable soutien et conseil pendant mon docto-

rat. Ça mérite à peine qu'on le mentionne que sans vous cette thèse n'aurait jamais vu la lumière du jour. Merci de m'avoir donné l'opportunité de faire mon stage de recherche au LPAP, de m'avoir aidé à trouver un financement, et puis pour les quatre dernières années d'encouragement et discussion, même avec mon français parfois lacunaire. J'apprécie énormement le fait que vous avez toujours trouvé du temps pour m'aider à poursuivre mes recherches dans le bon sens, même quand moi-même je ne voyais pas le chemin. Vous avez été tous les deux des promoteurs d'exception et j'en suis sûr que vous continuerez de l'être pour vos futurs étudiants. J'espère que cette thèse reflète fidèlement la qualité de votre supervision.

I also want to thank my parents for their support and faith in me over the last 28 years. To my father: thank you for making up those stories about the Martian bucketheads and mounticores, for looking through the telescope with me, and for fostering an interest and curiosity about space that has led me to where I am today. To my mother: thank you for the long hours spent reading to me, helping me with homework after school, and instilling the discipline and resilience without which I would have surely not completed this thesis; your encouragement has meant more than I can express. I hope I have made you both proud.

Et enfin j'aimerais remercier ma merveilleuse épouse, Chloé. Tu as été une présence constante pendant ces quatre années et m'as accompagné à travers les hauts et les bas de mon doctorat. Merci d'avoir assisté avec patience aux répétitions de mes différentes présentations, d'avoir toujours été là à la fin de la journée pour m'écouter parler de ce que j'ai fait, et de m'avoir permis de garder mes pieds sur Terre même si ma tête était souvent ailleurs. Cette thèse est dédiée à toi.

Contents

Chapter 1

Motivation

You've been working on that thing for years.

Unnamed Tatooine child, *Star Wars Episode I: The Phantom Menace*

Indeed I have, unnamed Tatooine child. Indeed I have.

Welcome to my thesis. This work has kept me happily occupied for the last four years; I hope that it can do the same for you, dear reader, at least for the next few hours. With any luck, the contents of this thesis might be useful or instructive, potentially somewhat interesting and, if you're lucky, occasionally even entertaining. In any case, I should very much like to briefly present the "Why?" of my work, before we get into any great detail about the "How?", or indeed the "So what?".

The ultraviolet (UV) aurorae of Jupiter are some of the most captivating and intriguing phenomena in the solar system. First detected during the Voyager 1 flyby in 1979 (Broadfoot et al., 1979), these stunning spectacles are 100 times more

powerful than the aurorae of the Earth, and ten times as powerful as the second-place solar-system aurorae, those of Saturn (Grodent, 2015). They have remained the subject of consistent scientific interest since their discovery, and especially since the advent of the first images from the Hubble Space Telescope (HST) (Dols et al., 1992). More recently, the Juno spacecraft, currently in orbit around Jupiter, has provided a wealth of both auroral image data and in-situ measurements of Jupiter's magnetosphere, which has led to a far superior understanding of the processes at work in the combined magnetospheric-ionospheric-auroral system at Jupiter. However, despite the advancements made in the collective understanding of Jupiter's aurorae in the last 40 years, many questions surrounding their behaviour and origins remain unanswered. While the moon footprints (Bonfond et al., 2017c) and signatures of magnetospheric plasma injections (Dumont et al., 2018) have been robustly identified as the consequences of certain magnetospheric processes, the origins of many other auroral features remain elusive. This mystery is not limited to dimmer, transient features in the aurora; even the origin of the main emission, which consistently accounts for a large portion of the auroral power output in the UV (Grodent, 2015), has not yet been indisputably determined (Bonfond et al., 2020), with several theories (Cowley and Bunce, 2001; Saur et al., 2018) proposed to explain various aspects of the main emission.

The aurorae of Jupiter, besides being the most powerful auroral display in the solar system, also show a great deal of variability; no two images of the aurora are exactly alike. This variability presents itself in many forms, both globally over the entire aurora and locally in the various auroral components. The aurora may vary as a whole in terms of global brightness,

size, position, and so forth. Likewise, the various individual components that make up the aurora at any given time can themselves vary in their characteristics. The presence or absence of auroral components come together to produce a wide range of global auroral configurations (Grodent et al., 2018). Despite the all-encompassing nature of auroral variability, very few studies have attempted its characterisation directly. Of those, many focus on the global view of the aurora (e.g. Grodent et al., 2018; Nichols et al., 2019), leaving the short-term ($<$ 1 hour) and small-scale variability comparatively understudied (Palmaerts et al., 2024). In particular, despite the ever-increasing number of them identified, the variability of specific classes of auroral feature remains fundamentally uncharacterised, especially in a systematic fashion. This may be due to the large quantity of image data from both HST and Juno that would have to be processed to give a long-term, systematic understanding of - as well as the relatively sophisticated techniques required to perform this processing in such a way as to detect, characterise, and classify - the full range of auroral features.

Given the large datasets that are now available, automated analysis techniques are becoming ever more important within the field. Automated and sophisticated image-analysis techniques have previously been applied to detect and track bright features in Jupiter's dawn-side aurora (Rutala et al., 2022) or to identify recurring auroral morphologies using principal-component analysis (Nichols et al., 2019). Nevertheless, one of the principle motivations for this thesis is the relative lack of automated analysis in the literature and hence the scientific usefulness of performing automated analysis of many aspects of the jovian aurora, especially with the potential to combine the

automated analysis of remote-sensing measurements with data from Juno's in-situ instruments. This is especially true when considering the variability of the jovian aurora, since an investigation of the variability necessarily necessitates more than a case study of a single auroral image; indeed, frequently, it is "the more, the merrier" when it comes to drawing statistical conclusions about auroral variability from image datasets. Of course, Jupiter's aurora is not the only variable aspect of the Jupiter-moon-magnetosphere system. Io and its famous volcanism also show a great deal of variability, and the neutral-sodium structures present around Io (which, like the aurorae, are expected to arise from its volcanism; Morgenthaler et al. 2024) are also prime candidates for investigation using automated methods. As such, this thesis does not limit itself to the study of Jupiter's aurora (though this represents a large part of the thesis) and also investigates Io and its neutral-sodium emission to give a wider picture of the variability present in many different aspects of the Jupiter-moon-magnetosphere system. The goals of the present work are thus:

- to identify, characterise, and classify a wide range of features present in the aurorae of Jupiter and neutral-sodium clouds of Io;
- to perform this analysis in a systematic and automated fashion;
- to apply these techniques to the bulk of the data from TRAPPIST, HST and Juno-UVS; and
- to extract from this analysis, in combination with in-situ measurements, conclusions regarding the origins of

various features and to use these conclusions to tackle unanswered questions surrounding Jupiter's aurorae, its magnetosphere, and the connection between the two.

This thesis is largely based on my previously published and peer-reviewed first-author articles. Its structure is therefore as follows:

- Chapter 2, introduction: an overview of the relevant theory behind Jupiter, its magnetosphere, its moons, its aurorae, and the interplay between these components.
- Chapter 3, instrumentation: an overview of the instruments used to collect the data used in this work.
- Chapter 4, variability of Io's sodium jet: the (lack of) interaction between the sodium jet of Io and the wider magnetosphere (De Becker, Head, et al., 2023).
- Chapter 5, variability of the size of the main emission: how the size of the main emission affects and is affected by other parameters, such as main-emission brightness and compression of the magnetosphere (Head et al., 2024).
- Chapter 6, characterisation and investigation of the UV auroral bridge(s): how compression of the magnetosphere varies the morphology of and plasma properties associated with Jupiter's "bridge" polar aurora (Head et al., 2025).
- Chapter 7, investigation of the variability of injection signatures: evidence from Juno observations that injection signatures can be split into two classes (Head et al., 2026).

- Chapter 8, conclusions and perspectives: the overall conclusions of the thesis and my suggestions for future work.

The contents of chapters 4 to 7 are thus essentially identical to the relevant published articles; the theory and background presented in these works has been removed from the relevant chapter and instead collated into a dedicated introduction in chapter 2 to avoid needless repetition. Supplementary material, where present in the published works, has been moved to the relevant section in the main body of the text.

Chapter 2

Introduction

The Queen wishes it. She's curious about the planet.

Capt. Panaka, *Star Wars Episode I: The Phantom Menace*

2.1 Overview of Jupiter

Jupiter is the largest and most massive planet in the Solar System. It possesses, at time of writing, 97 confirmed moons, of which the four Galilean moons (Io, Europa, Ganymede, and Callisto) are some of the largest moons in the Solar System. Io interacts directly (and indirectly, as the predominant source of plasma) with Jupiter's vast magnetosphere to create the aurorae of Jupiter, which are the most powerful aurorae in the Solar System and present a number of key differences compared to the terrestrial aurorae. Jupiter, its magnetosphere, its moons, its aurorae, and the interaction between these dif-

Table 2.1: Physical properties of Jupiter and the Galilean moons.

Body	Mass (kg)	R (km)	SMA (R_J)	P (hr)
Jupiter	1.90×10^{27}	71 488±0.4[1]	10 887.2859*	9.92492†
Io	8.93×10^{22}	1 821.49±0.01	5.897	42.305568
Europa	4.80×10^{22}	1 560.8±0.3	9.384	84.611112
Ganymede	1.48×10^{23}	2 631.2±1.7	14.97	171.734112
Callisto	1.08×10^{23}	2 410.3±1.5	26.34	400.570560

"R" refers to the equatorial radius of the body. "SMA" refers to the semi-major axis of the body. "P" refers to the sidereal orbital period of the body around Jupiter. Values taken from Archinal et al. (2018) and Jacobsen (2021) unless otherwise stated.
* This refers to Jupiter's semi-major axis with respect to the solar-system barycentre.
† This refers to Jupiter's sidereal System-III rotational period; from Seidelmann and Divine (1977).
[1] From Galanti et al. (2026).

ferent elements are the focus of this thesis. A number of key properties of Jupiter and the Galilean moons are summarised in Table 2.1.

Jupiter's most emblematic element is arguably its distinctive striped or banded atmosphere, in combination with its many storms, most notably the Great Red Spot. Despite this, Jupiter's atmosphere is only treated in a broad and indirect sense in this thesis and will therefore not be discussed in any great detail in this section. The interested reader is invited to consult one of the many excellent reviews of Jupiter's atmosphere for further details (Taylor et al., 2004; Ingersoll et al., 2004; Xinyi et al., 2025). For this work, it is necessary to know that Jupiter's atmosphere has an approximately (though not exactly) solar-like elemental abundance profile and is dom-

inated by H_2 (86.0% by number) and He (13.6%), with the remaining 0.4% consisting primarily of CH_4, NH_3, H_2O, and H_2S (Taylor et al., 2004). In the polar auroral regions, the interaction between CH_4 and precipitating energetic particles produces "higher hydrocarbons" such as C_2H_6 and C_2H_2. This means that Jupiter's (UV) aurorae have spectra that are dominated by H_2 (and H) emission lines with weaker hydrocarbon emissions superimposed (see Clarke et al. 2004a and section 2.5). Since Jupiter does not possess a solid surface, altitude is determined in reference to the "1-bar level", the level at which Jupiter's atmospheric pressure matches that of the Earth at sea level, which is used to define an altitude of 0 km. This choice is motivated by the presence of the ammonia-ice cloud deck at approximately this altitude, from which sunlight is reflected, giving rise to the visible planetary limb (Ingersoll et al., 2004).

Jupiter's atmosphere is embedded within its vast magnetosphere. A transitory region, called the thermosphere, starts at an altitude of approximately 250 km (Vasavada et al., 1999). This layer undergoes partial ionisation through the absorption of solar extreme-UV radiation and interaction with precipitating high-energy particles (Yelle and Miller, 2004); the ion and free-electron portions of the thermosphere are called the "ionosphere". In this region, there is sufficient free-electron and ion (mainly H^+ and H_3^+) density (10^4-10^5 cm^{-3}) to meaningfully affect the propagation of electromagnetic waves. The ionosphere is a key component of the Jupiter-magnetosphere coupling system, where it is the source of momentum that is transferred to the plasma of the magnetosphere to enforce corotation, and has itself been the subject of a great many published works (e.g. Hinson et al., 1997, 1998; Wang et al., 2023b; Melin et al., 2024; Sicorello et al., 2025, and many, many more

besides). However, the ionosphere is itself not studied as part of the work included in this thesis. Indeed, to understand the results of this thesis, one need only consider the ionosphere as "the layer of the atmosphere where the aurorae occur".

Above the ionosphere lies Jupiter's vast magnetosphere. The magnetosphere is an enormous region of space around Jupiter that is filled with plasma, mostly sourced from Io's volcanism, and is discussed in more detail below in section 2.3. As a consequence of the processes occurring in its magnetosphere, Jupiter is also home to the largest and most powerful aurorae in the solar system. Superficially, they broadly resemble the aurorae of the Earth, but their behaviour and origins are vastly different. The UV aurorae, which can be said to be the main subject of this thesis, are discussed in far more detail below in sections 2.5 to 2.9.

2.2 Io

Io is the innermost of Jupiter's Galilean moons. It is the most volcanically active body in the Solar System, with some 400 active volcanoes identified thus far (Williams et al., 2023). This intense volcanism is fundamentally powered by a 1:2:4 orbital resonance between Io, Europa, and Ganymede. Periodic gravitational interaction with Europa and Ganymede forces Io's orbit to be slightly eccentric. Since the tidally locked Io's orbital speed thus varies over the course of an orbit (but its rate of rotation does not), periodic tidal stresses are applied to Io, heating its interior and providing an energy source to power its volcanism (Peale et al., 1979; Lainey et al., 2009), which, owing to the lack of plate tectonics on Io, differs greatly in its character

from terrestrial volcanism (Khurana et al., 2011). Io's volcanism can take the form of lava lakes, plumes (Geissler and Goldstein, 2007; Williams and Howell, 2007), large volcanic depressions ("Paterae"; Radebaugh et al. 2001), or even "stealth volcanism", in which large amounts of SO_2 are ejected in a plume without an accompanying dust or condensate element, rendering the plume invisible in reflected sunlight (de Pater et al., 2020, 2021). Eruptions on Io can manifest as flow-dominated or explosion-dominated eruptions. Flow-dominated eruptions, also known as Promethean volcanism after the eponymous Prometheus Patera, are slower, longer eruptions comparable to shield volcanism found on Earth (Keszthelyi et al., 2001) or (at least formerly) on Venus (Head et al., 1992). Explosion-dominated eruptions, also known as Pillanian volcanism after the dramatic 1997 explosive eruption of Pillan Patera, are shorter-lived, more-violent eruptions (Marchis et al., 2002). The plumes resulting from this volcanism can extend hundreds of kilometres away from Io's surface; it was one of these plumes emanating from Pele Patera imaged by Voyager 1 that first lead to the discovery of active volcanism on Io (Morabito et al., 1979).

Io possesses a thin atmosphere of mainly SO_2 (de Pater et al., 2023). The presence of this atmosphere was first suggested by Binder and Cruikshank (1964) who observed that Io reflected 10% more sunlight immediately after exiting from Jupiter's shadow than it had before. This was suggested to be the consequence of a thin N_2 or CH_4 atmosphere that would condense into a layer of frost on the moon's surface in the absence of sunlight in Jupiter's shadow and form a reflective surface in time for Io to exit from eclipse. Later observations using the Hubble Space Telescope did not see the same post-eclipse

brightening (Secosky and Potter, 1994), and so the extent to which this effect be genuine is contested. Nevertheless, Io's thin atmosphere has been established to largely undergo condensation in the absence of sunlight (Fanale et al., 1979), though it is now known to overwhelmingly consist of SO_2 rather than N_2 or CH_4 (Fanale et al., 1981). The first direct observation of Io's atmosphere came via the detection of its comparatively dense ionosphere by Pioneer 10 (Kliore et al., 1974). Atomic sodium was also detected around Io and originally taken to be a majority component of its atmosphere (Brown and Chaffee, 1974; McElroy et al., 1974), though this sodium was later shown to form a large "sodium neutral cloud" around Io (Trafton et al., 1974; Macy and Trafton, 1975), which is discussed further below. This cloud is hypothesised to come from particles escaping from Io's atmosphere (Wilson et al., 2002); further evidence for atmospheric escape is provided by the presence of a similar potassium neutral cloud (Trafton, 1975) and the detection of sulphur and oxygen ions in Jupiter's magnetosphere (Kupo et al., 1976; Broadfoot et al., 1979; Bridge et al., 1979), which are sourced mainly from electron-impact ionisation of Io's SO_2 atmosphere (Bolton et al., 2015).

It is expected that Io's volcanism represents a key source of material for its (tenuous and patchy) atmosphere, either directly or indirectly. The first evidence for this came from three discoveries made in 1979: that Io has active surface volcanism (Morabito et al., 1979); the identification of solid SO_2 in Io's spectrum (Fanale et al., 1979; Smythe et al., 1979), and; the observation of gaseous SO_2 above the volcanic centre Loki Patera (Pearl et al., 1979). These three elements indicate that Io's atmosphere is fundamentally volcanic in origin, though it is not necessarily directly sourced from volcanic outgassing. Io's

global atmosphere has since been directly observed (Lellouch et al., 1990), where it was found that only 3-15% of Io's surface is covered with an atmosphere at any one time, which may be indicative of a locally (volcanically) sourced atmosphere (Lellouch et al., 1992). Feaga et al. (2009) showed that the density of the atmosphere correlates well with the locations of known volcanic plumes/hot spots on Io. Sublimation of surface SO_2 frost by solar heating may also contribute to the production of Io's atmosphere. Indeed, work suggests that sublimation is the dominant atmosphere-production mechanism at Io (Lellouch, 2005), with direct volcanic outgassing potentially contributing as little as 3% of atmospheric supply (Retherford et al., 2007). SO_2 density has been observed to peak at the subsolar point on Io (as expected for a sublimation-driven atmosphere; Jessup et al. 2004) and the atmosphere has been observed to (partially) collapse during or after eclipse in Jupiter's shadow (Roth et al., 2011; Trafton et al., 2012; Tsang et al., 2016). Indeed, Io's atmosphere has been shown to be asymmetric at both day/night and upstream/downstream of its orbit around Jupiter (Dols et al., 2012; Blöcker et al., 2018). This asymmetrical atmosphere may help to resolve the apparent incompatibility between the results described above. The Jupiter-facing atmosphere is expected to be dominated by direct volcanic outgassing (Spencer et al., 2012) whereas the anti-jovian atmosphere would be dominated instead by sublimation (Tsang et al., 2012, 2013). Nevertheless, at time of writing, the scientific consensus is that Io's atmosphere is a fundamentally sublimation-driven atmosphere, particularly in the equatorial dayside hemisphere, whereas volcanic outgassing may be more important in the nightside hemisphere and in the polar regions (see Bagenal and Dols 2020 and references therein).

Io's low mass (and hence weak gravitational field) and its location within the densest portion of Jupiter's magnetosphere mean that particles within Io's atmosphere have a tendency to escape. These escaping particles represent the primary source of mass for Jupiter's magnetosphere (Hill et al., 1983); Io injects some 600-2600 kg s^{-1} of neutral material into the magnetosphere (Bagenal and Dols, 2020), of which approximately 1000 kg s^{-1} is subsequently ionised (Bagenal and Delamere, 2011), predominantly via collision with thermal electrons present in the Io plasma torus (Bagenal and Dols 2020; discussed below). Photoionisation, in which neutral molecules are ionised by high-energy solar photons, only accounts for some 10-15% of these iogenic ions (Saur et al., 1998, 1999). However, collisional ionisation is not the only mechanism to provoke atmospheric escape. Direct expulsion of material from volcanic eruptions was suggested as another possibility, but modelling indicates that volcanic explosions would not be able to sufficiently accelerate material to Io's escape velocity (Strom et al., 1981). Jeans (thermal) escape, in which a portion of the particles with a given thermal distribution attain sufficient kinetic energy via collision with other atmospheric particles, is expected to account for the majority of escaping particles below 1 eV (Sieveka and Johnson, 1984). When a neutral particle is ionised in Io's upper atmosphere, it gains a net electric charge and therefore suddenly experiences an interaction with Jupiter's magnetic field. Since, at the orbit of Io, the plasma flow is essentially in full corotation with Jupiter (as it is frozen in place relative to Jupiter's rotating magnetic field), the newly ionised particles are very quickly accelerated from Io's orbital velocity ($\sim$18 km s^{-1}) to corotation velocity ($\sim$60 km s^{-1}; Bagenal and Dols 2020). In addition to this sudden increase in bulk velocity, the

ion is also forced to gyrate in the plane parallel to the local magnetic field. This process is known as ion pickup, which introduces mainly high-energy ions to the surrounding plasma (Bagenal and Dols, 2020). After these ions have been picked up by the surrounding plasma flow, some portion are reneutralised via charge exchange, collision, disassociation, and recombination with the surrounding material (e.g. Summers et al., 1989; Schneider et al., 1991; Smyth, 1992; Dols et al., 2008). However, despite being reneutralised, these particles have still undergone acceleration by Jupiter's magnetic field. Reneutralisation thus releases these particles from the influence of the magnetic field whilst maintaining their velocity, which allows them to rapidly travel through the magnetosphere and form large clouds of neutral material. These neutral clouds are discussed further below in section 2.4.

2.3 Magnetosphere and magnetic field

Defining a "magnetosphere" is a somewhat complicated affair. The magnetosphere can be understood to be the region where the planetary magnetic field "dominates" over the solar magnetic field and typically takes the form of a "bubble" of plasma surrounding a planet, though exactly what "dominates" means in this context is debated, and the word "bubble" is typically avoided in serious scientific discourse. Khurana et al. (2004) suggest that a magnetosphere is "a sphere of influence around a planet in which the forces associated with the magnetic field of the planet prevail over all other forces", though again the extent to which magnetic forces "prevail over all other forces" is debatable. Kivelson and Bagenal (2006) include a discus-

sion of the difficulties of accurately defining "magnetosphere". They suggest that the magnetosphere is the "volume of space from which the solar wind is excluded by a planet's magnetic field" but also note that the solar wind is typically not entirely excluded by a magnetosphere and that even planets with no intrinsic magnetic field form cavities in the solar wind that may be considered to be (pseudo-)magnetospheres. The magnetosphere can also be, somewhat tautologically, considered to be the region of space contained within the magnetopause, which itself is the boundary layer separating the magnetosphere from the solar wind. In practice, it is relatively straightforward to identify when a spacecraft has passed the magnetopause, since there is an obvious and striking discontinuity in the magnetic field. This work is not a detailed study of the magnetosphere itself, but instead uses the magnetosphere and its properties to contextualise observations of related systems, such as the aurora, and so the "definition" of the magnetosphere as the region of space around a planet dominated by its magnetic field is largely sufficient.

While the governing processes are broadly similar, Jupiter's magnetosphere is starkly different from that of the Earth in terms of size, composition, and interaction with the solar wind. Jupiter's magnetosphere (as often seems to be the case for Jupiter) is the largest in the solar system. It reaches out to approximately 75 Jupiter radii (R_J; Khurana et al. 2004) on its sunward side (making it not just larger than Earth's magnetosphere, but also larger relative to the size of the planet, since the equivalent distance for the Earth is only 10 Earth radii; Fairfield 1971) and extends away from Jupiter in a long "magnetotail". This magnetotail is long enough to almost reach the orbit of Saturn ($\sim$7000 R_J; Scarf 1979; Kurth et al. 1982;

Sittler Jr. et al. 1987). Jupiter's magnetosphere is so large due to a combination of three major factors. Firstly, Jupiter's magnetic field is far stronger than Earth's magnetic field (dipole moment 2.8×10^{20} T m^3 vs 1.3×10^{16} T m^3) which naturally leads to a higher magnetic pressure to balance the dynamic (ram) pressure exerted by the incoming solar wind and hence a larger magnetosphere. Secondly, Jupiter is further from the Sun than the Earth, and the density of the solar wind falls with increasing distance from the Sun as r^{-2} (Persinger and Vares, 2014), meaning that it exerts less dynamic pressure on the jovian magnetosphere. Thirdly, unlike Earth's magnetosphere, which is typically dominated by lighter elements drawn from the solar wind, Jupiter's magnetosphere consists of heavier ions (such as S^{n+} or O^+) from its volcanic moon, Io. The thermal pressure and centrifugal force of this rotating heavy plasma inflates Jupiter's vast magnetosphere yet further, taking it from approximately 42 R_J for a theoretical magnetic-field-only magnetosphere to its measured extent of 75 R_J (Khurana et al., 2004). This extent is only a "typical" or "steady-state" value, and the size of the jovian magnetosphere can vary in response to both internal and external variation (between approximately 45 and 100 R_J; Joy et al. 2002), as is discussed in far more detail in chapter 5.

Jupiter's magnetosphere is typically divided into three regions: the inner (<10 R_J), middle (10-40 R_J), and outer (>40 R_J) magnetosphere, motivated by differences in plasma density and dominant processes. Io's plasma torus, which contains ions sourced from Io and provides material to the rest of the magnetosphere, is found between approximately 5.2 and 10 R_J (Khurana et al., 2004), which motivates the choice of boundary between the inner and middle magnetospheres. In the middle

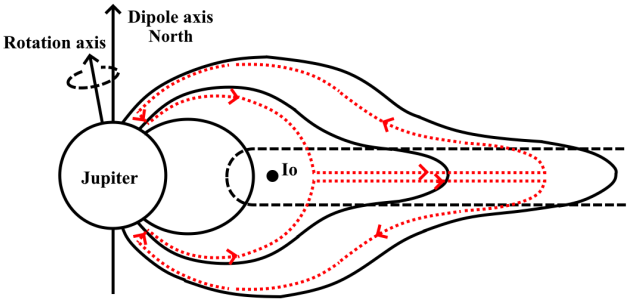

Figure 2.1: Schematic of the approximate morphology (not to scale) of three example magnetic field lines crossing the magnetic equator at different distances in Jupiter's magnetosphere. Jupiter's axis of rotation is offset from its dipole axis by approximately 9.6°. Solid black lines indicate the morphology of the magnetic field. Dashed lines indicate the approximate extent of the equatorial plasma sheet. Dotted red lines indicate the expected behaviour of field-aligned electrical currents in the Cowley and Bunce (2001) current-loop model. Reproduced with modification from Cowley and Bunce (2001).

magnetosphere, the plasma, which is held in corotation with Jupiter by its magnetic field at shorter distances, gradually breaks down with increasing distance, until it is considered to have "fully" broken down (i.e. the plasma lags corotation by at least a factor of two; Khurana et al. 2004) at approximately 40 R_J, motivating the choice of boundary between the middle and outer magnetosphere. Through these three regions, there is also a thin, dense sheet of outflowing plasma from the Io torus that is confined to the magnetic equator, called the "equatorial plasma sheet", which carries a strong (>160 MA) azimuthal

current (Khurana et al., 2004) and is hence also sometimes referred to as the "equatorial current sheet" or "magnetodisc". In the inner magnetosphere, Jupiter's internal magnetic field dominates, and the total magnetic field can be approximated as a tilted dipole (Thomas et al., 2004). However, further from Jupiter, the magnetic field produced by the equatorial current sheet has a greater impact, which works to "pull" the total magnetic field outward in the middle and outer magnetosphere; a schematic is given in Figure 2.1. Note that this schematic has been simplified for ease of understanding. In reality, the "stretching" of the magnetic field would become more aligned with the centrifugal (and not magnetic) equator at distances beyond $\sim$50 R_J (Khurana and Schwarzl, 2005). The radius of Jupiter and distance of Io are also not to scale, though the magnetic field lines do indeed become significantly stretched only beyond Io's orbit. Note also that Jupiter's magnetic north is found in its northern hemisphere, unlike the Earth.

The jovian magnetosphere is populated by four separate sources of plasma; they are, in order of decreasing importance, the Io plasma torus, the solar wind, Jupiter's ionosphere, and Jupiter's icy moons. Outflow from the Io plasma torus is, by far, the greatest source of plasma, injecting some 1000 kg s^{-1} into the wider magnetosphere (Smyth and Combi, 1988). The solar wind is expected to provide less than 100 kg s^{-1}, and the ionosphere and icy moons even less, at around 20 kg s^{-1} (Hill et al., 1983; Cooper et al., 2001). This means that, by mass, the magnetosphere consists mainly of sulphur and oxygen and their compounds (Thomas et al., 2004), rather than the solar-wind-sourced hydrogen magnetosphere of the Earth (Kivelson and Bagenal, 2006).

Ionised material ejected from Io (either as ions or neut-

rals that are subsequently ionised) is forced into corotation by Jupiter's magnetic field and thus forms a dense "torus" of ions between approximately 5.2 and 10 R_J, held in place latitudinally by centrifugal confinement and radially by the rate of outward diffusion. This torus is inclined relative to Io's orbital plane by 6.4°, approximately two-thirds of Jupiter's dipole tilt (Moncuquet et al., 2002), and also orbits Jupiter faster than Io, causing it to "wash over" Io at a relative speed of approximately 54 km s^{-1}. Interaction between Io and the impacting torus is itself likely a significant source of material for the torus. Plasma in the torus slowly (0.05 km s^{-1}; Thomas et al. 2004) diffuses outward, forming the equatorial plasma sheet and populating the rest of the magnetosphere. Since the torus is essentially a steady structure, this mass loss must be balanced by the addition of new ionised material from Io. This plasma also interacts with the other Galilean satellites and there is some evidence that a similar (though much weaker) plasma torus exists for Europa (Intriligator and Miller, 1982; Schreier et al., 1993) and Callisto (Eviatar and Paranicas, 2005).

Being able to accurately model the jovian magnetic field is incredibly important to the study of Jupiter's magnetosphere and aurorae. While it is important for a number of reasons, this work (which is predominantly a study of Jupiter's aurorae) uses models of the magnetic field to "map" regions of Jupiter's aurora out into the magnetosphere, or vice versa; accurate modelling of the magnetic field, especially in higher latitude regions, is therefore essential to retrieve reliable ionosphere-magnetosphere mappings. Earlier missions to Jupiter were largely confined to the equatorial plane, which precluded measurement of the high-latitude magnetic field and meant that early magnetic field models, such as the O4 (Acuña and Ness,

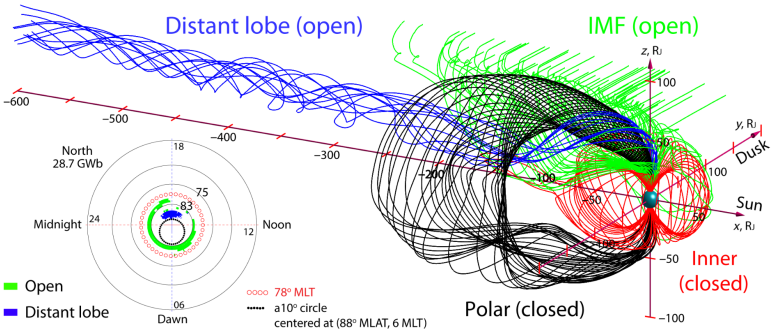

Figure 2.2: Results of a simulation of Jupiter's magnetic field, taken from Zhang et al. (2021). Illustrative field lines threading four different regions of the aurora are annotated.

1976) or O6 (Connerney, 1992; Dougherty et al., 1996) models, were of limited use for mapping, given that they were not considered to be reliable beyond the third spherical harmonic (Connerney, 1992). The later VIP4 model (Connerney et al., 1998) also used observations of the location of the Io auroral footprint in addition to in-situ magnetic-field measurements to produce a more reliable model. However, the Juno spacecraft, which does not orbit Jupiter in the equatorial plane but rather in a highly elliptic polar orbit that allows it to sample the high-latitude magnetic field as well as many different sectors within the magnetosphere, has led to great improvements in our models of the magnetic field. Data from the Juno mission were used to produce the JRM09 (Connerney et al., 2018) and later the JRM33 (Connerney et al., 2022) models which include the first 10 and 18 spherical-harmonic terms, respectively. A separate model, the Con2020 model (Connerney et al., 2020),

was also produced for the contribution to the total field by the equatorial current sheet. A combination of the JRM33 and Con2020 models provides a far more accurate mapping between the ionosphere and magnetosphere than earlier models, especially for the inner and middle magnetospheres (or equivalently the outer and main auroral emissions), including the moon footprints (Hue et al., 2023). The mapping is considered to be less reliable for the polar aurora/more distant regions of the magnetosphere, in which the contribution from open field lines (i.e. connected directly to the solar wind) is both important and poorly understood, with key questions about which parts of the polar aurora (if any) represent regions of open magnetic flux (Vogt et al. 2011, Zhang et al. 2021, Jenkins et al. 2024, and Figure 2.2). In this region, local-time effects not taken into account by the JRM33 and Con2020 models also become significant, but these models can still be used to draw qualitative conclusions.

Unlike the Earth, whose solid surface makes it straightforward to define a latitude and longitude (though the latter has historically posed a problem; Bennett 1985) and hence to position oneself relative to the planet's rotation, Jupiter lacks a solid surface. Its various fluid layers are not at all guaranteed to rotate at the same rate, which may make it challenging to define a surface longitude in the terrestrial sense. Additionally, Jupiter is not a perfect sphere but instead a flattened (oblate) spheroid which gives us the choice between planetocentric and planetographic latitude when defining position on the surface. The differences between these two latitudes are illustrated in Figure 2.3. In this work, all latitudes are planetocentric. To define longitude, this work employs the commonly used left-handed System-III system of coordinates (Seidelmann and Di-

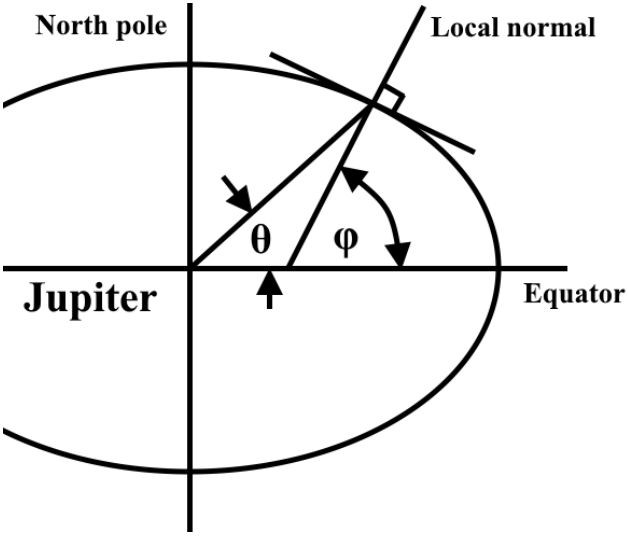

Figure 2.3: Illustration of the difference between jovicentric latitude θ and jovigraphic latitude φ.

vine, 1977). As implied by the name, the System-III longitude follows from earlier System I and II longitudes, with the three longitude systems assuming different jovian rotation periods. System I and System II were used by early observers to track cloud patterns at the equator and at higher latitudes, respectively, and these cloud layers rotate at slightly different rates (9 hr 50 mins 30.003 s against 9 hr 55 mins 40.632 s; Raymond Hide 2001). In contrast, the System-III rotation rate is not determined from the behaviour of cloud layers but instead from the period of the jovian decametric radio emission, 9 hr 55 min 29.711 s (Seidelmann and Divine, 1977). This radio emission is modulated by the rotation rate of Jupiter's

magnetic field and consequently also of Jupiter's liquid-metal interior. It is therefore commonly considered to be the "true" rotation rate. Note that accurate determination of the rotation period is extremely important, even small errors in the rotation period may accumulate and cause us to "lose" our reference point, making it impossible to compare data gathered over long time periods. Importantly, since System-III longitude is defined relative to the rotation of the magnetic field, this means that structures whose morphologies are controlled by the magnetic field (such as the aurora, the main subject of this thesis) are "fixed" in System-III longitude. All longitudes given in this work are thus System-III longitudes. A further longitude, the illusive System IV, has also been defined with a rotation period 3% longer than that of System III, which better fits certain periodicities seen in the Io plasma torus (Roesler et al., 1982; Sandel and Dessler, 1988; Thomas et al., 2004).

An related concept of equal importance is that of local time and magnetic local time. Local time is the slightly more intuitive concept. Midday is defined as the System-III longitude on Jupiter that points toward the Sun (the sub-solar longitude), with the remaining hours of the (24-hour) clock being defined relative to this point. More precisely, for a left-handed System-III longitude ϕ between 0° and 360°, and sub-solar longitude ϕ_{SS}, the local time t is defined as

$$t = (\phi_{SS} - \phi) \cdot \frac{24}{360} + 12. \tag{2.1}$$

This means that local time increases in the opposite sense to left-handed System-III longitude on the globe of Jupiter. Magnetic local time instead maps each point on the surface of Jupiter to a longitude in the equatorial magnetosphere using a

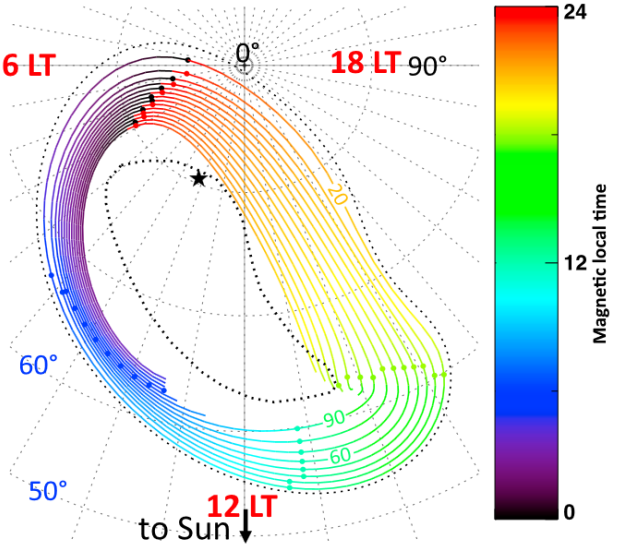

Figure 2.4: The Vogt et al. (2011) flux-equivalence magnetic mapping from the northern auroral region to the equatorial magnetosphere. Each contour represents a radial distance into the magnetosphere, from 20 R_J to 150 R_J spaced by 10 R_J. Magnetic local time is encoded in colour along each contour. Local times (on the globe of Jupiter) are given in red. Modified from Vogt et al. (2011).

model of Jupiter's magnetic field before performing the same calculation. In the southern aurora, the differences between these two local times are minimal. In the northern aurora, however, the difference can be meaningful; an example is given in Figure 2.4 which shows that, while the entire northern aurora is essentially located at a local time of 12:00, the contour

of the aurora does still contain the entire 00:00-23:59 range in magnetic local time. Unless otherwise specified, references in this work to "local time" (and related concepts like the day, night, dawn, and dusk aurorae) are to the magnetic local time, which is considered to be more useful for interpreting the aurora.

Thanks to the Juno spacecraft, we currently have access to in-situ measurements of the particles and waves present in Jupiter's magnetosphere. The concepts and elements relevant to this work are as follows:

- Monodirectional, bidirectional, field-aligned, isotropic: These refer to the directionality of electrons/waves compared to the local magnetic field vector. Monodirectional = up or down along the magnetic field. Bidirectional = up **and** down along the magnetic field. Field-aligned = aligned with the local magnetic-field vector. Isotropic = in all directions.

- Monoenergetic/"inverted V": An electron distribution in which the electrons all have the same energy. It typically presents as a discrete "inverted V" in electron energy spectra (e.g. Mauk et al., 2018).

- Broadband/stochastic: An electron distribution/acceleration process in which the electrons have a range of energies, since each electron is accelerated stochastically (randomly) rather than by a fixed potential drop.

- Beams (or beam distribution): An electron distribution in which the vast majority of electrons have pitch angles that are very closely aligned with the local magnetic-field vector, resulting in collimated "beams" of electrons

along magnetic field lines. Electron beams have been frequently observed above Jupiter's aurora and are discussed in depth in the literature (e.g. Mauk et al., 2017c; Salveter et al., 2025), though it is often left to the reader to make the "pew-pew" sound effects.

- Pancake distribution: An electron pitch-angle distribution with an essentially flat perpendicular profile but where the loss cones have been emptied and is typically considered to be the result of isotropic scattering of electrons (Horne and Thorne, 2000; Salveter et al., 2022). It could be said (by more-imaginative members of the community) to resemble a stack of pancakes on a plate when electron flux is plotted against pitch angle.

- Butterfly distribution: Similar to the pancake distribution but with a marked decrease in electron flux at 90°, resulting in a pitch-angle distribution that (broadly) resembles the wing of a butterfly. Also referred to as a "cigar" distribution (Mauk and Saur, 2007), which does make me wonder whether anyone in the field has ever actually seen a butterfly or a cigar.

- Electrostatic waves: A type of longitudinal plasma wave in which oscillation only occurs in the electric field parallel to the direction of wave travel $\mathbf{k}$ (Swanson, 2003); $\delta\mathbf{E} \times \mathbf{k} = 0$ and hence, per Faraday's Law, $\delta\mathbf{B} = 0$, whence the term "electrostatic".

- Alfvén waves: Alfvén waves are plasma waves that travel in a magnetised plasma. Classical Alfvén waves are transverse and can carry an electrical current. However, since

the variation in the electrical and magnetic fields occurs perpendicularly to the local magnetic-field vectors, classical Alfvén waves cannot provoke auroral electron acceleration. They may become partially compressional (i.e. the magnetic field undergoes compression in the direction of travel of the wave) in certain plasma regimes, however (Hasegawa, 1976; Lysak and Lotko, 1996), such as the case of kinetic or inertial Alfvén waves. These latter inertial Alfvén waves occur when the wavelength becomes comparable to the electron inertial length and can hence provoke meaningful auroral electron acceleration.

How these concepts relate to the (different parts of the) aurora is discussed further in sections 2.5 to 2.9.

The last of these elements, Alfvén waves, are of such key importance to this work and to the field in general that they merit their own separate discussion. Alfvén waves travel at the Alfvén speed

$$v_A = \frac{B}{\sqrt{\mu_0 \rho}}, \tag{2.2}$$

where B is the local magnetic-field strength, μ_0 the permeability of free space, and ρ the local plasma density. As mentioned above, under ideal magnetohydrodynamical conditions, Alfvén waves are purely transverse and thus cannot provoke auroral acceleration. If these ideal conditions are not met, however, such as for finite electron pressure and ion gyroradius (Hasegawa, 1976; Goertz and Boswell, 1979; Lysak and Lotko, 1996), the Alfvén wave may become partially longitudinal (provoking a parallel electric field) and thus able to induce meaningful electron acceleration along field lines (Lysak, 2023). The dispersion relation for a fully transverse (shear)

Alfvén wave is given by

$$\omega^2 = k_\parallel^2 v_A^2, \tag{2.3}$$

where ω is the angular frequency and $k_\parallel$ the field-parallel wave number (Lysak and Lotko, 1996). In the inertial regime (such as in the cold plasma just above the ionosphere where electron-inertial-length effects must be taken into account), this dispersion relation is modified as

$$\omega^2 = k_\parallel^2 v_A^2 \frac{1 + k_\perp^2 \rho_i^2}{1 + k_\perp^2 \lambda_e^2}, \tag{2.4}$$

where $k_\perp$ is the field-perpendicular wave number, ρ_i the ion gyroradius, and λ_e the electron inertial length (Lysak, 2023). It can be seen that this dispersion relation now includes a perpendicular component $k_\perp$ which indicates that inertial Alfvén waves are partially longitudinal and therefore able to provoke (auroral) electron acceleration along field lines. The Poynting flux S (that is, the energy flux transmitted by the wave) of an inertial Alfvén wave is given by

$$S = \frac{\delta B^2 c}{\mu_0}, \tag{2.5}$$

where δB is the magnitude of the perturbation of the magnetic field and c the speed of light (Saur et al., 2003). Alfvén waves, like other waves, are reflected at density gradients (of which there are several in the jovian magnetosphere; Jacobsen et al. 2007; Lysak et al. 2021) which means that there are likely to be Alfvén waves propagating in both directions along a given field line. These counter-propagating Alfvén waves interact non-linearly and provoke a cascade toward shorter wavelengths able to provoke meaningful auroral electron acceleration; this is discussed in more detail in section 2.6.

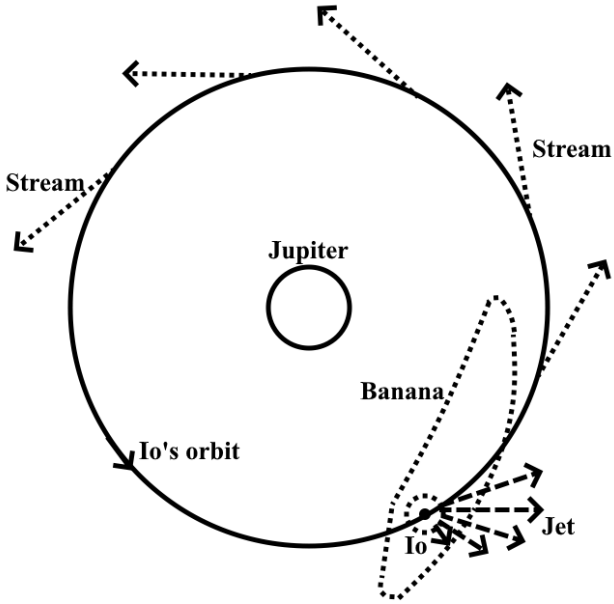

Figure 2.5: Schematic of the various neutral-cloud morphologies present around Jupiter/Io, reproduced from Wilson et al. (2002).

2.4 Neutral clouds

Io is surrounded by a number of clouds formed of neutral particles, each with different morphologies owing to their different source mechanisms. These include the "banana", the jets, the streams, and the extended nebula, as shown in Figure 2.5. These clouds are largely composed of sulphur and oxygen atoms from Io (Bagenal and Dols, 2020). However, importantly, they also contain a trace amount of neutral sodium,

which, despite making up only a few percent of the material in the neutral clouds, is by far their brightest constituent, owing to the sodium D-line doublet (589 nm) and its large scattering cross-section for the bright sunlight in this wavelength range (Bergstralh et al., 1975). This sodium comes from photodissociation (or electron-impact dissociation; Schneider et al. 1991) of sodium-bearing molecules, likely NaCl, which are directly outgassed from magma and plumes on Io (Moullet et al., 2010). The ease of detection of the sodium emission (and, to a lesser extent, the potassium emission; Trafton 1975) has led to its use as a tracer for the properties and behaviour of the neutral clouds as a whole (Thomas et al., 2004). However, more recent observations of the neutral clouds have cast doubts on the ability of sodium to accurately reflect the behaviour of more abundant species. For example, the sodium "stream" (discussed below) is not expected to have an oxygen counterpart, since oxygen has a far longer lifetime against ionisation in the torus (Schneider and Bagenal, 2007). This potential unsuitability of sodium as a tracer for mass outflow in the stream may also limit our ability to draw conclusions on the link between processes close to Io (streams, jets, ...) and their effect on the extended (sodium) nebula, also discussed below.

These clouds are separated in a number of distinct components. The main component is known as the "banana" cloud, owing to its curved banana-like shape centred on Io (see Figure 2.5). The particles that form the banana cloud arise from atmospheric sputtering of sodium atoms by the ions in the plasma torus and remain neutral throughout their lifetimes (Smyth and Combi, 1988). The banana shape of this cloud arises because sputtered particles have greater speeds in the forward (east) direction, along with thickening of the cloud

due to radiation pressure. Since these neutral particles do not interact (directly) with Jupiter's magnetic field, they form a partial torus in Io's orbital plane. The relatively low lifetime of atomic sodium in Jupiter's magnetosphere before being photoionised, and hence no longer contributing to the neutral sodium emission, of 2-5 hours (Smyth and Combi, 1988; Smyth, 1992) means that sodium, and other similarly short-lived species like potassium and sulphur, cannot form a full torus around Io. Atomic oxygen, with a much longer photoionisation lifetime of at least 20 hours (Thomas, 1992), does appear to survive long enough to form a full neutral cloud along Io's entire orbit (Bagenal and Dols, 2020).

In addition to the main "banana" cloud, jets are often (though not always) observed in the sodium emission that extends away from Io. Unlike the slow escape of neutral particles from Io's atmosphere that feeds the banana, the particles that form the jet start as pickup ions (see section 2.2) that are accelerated to corotation velocity and therefore stripped away from Io's atmosphere. These pickup ions are reneutralised within seconds via charge exchange with neutral sodium in Io's atmosphere (Wilson and Schneider, 1999). However, these reneutralised sodium atoms maintain their pickup velocity but no longer feel the influence of Jupiter's magnetic field. They are therefore ejected from Io's atmosphere at $\sim$60 km s^{-1}, far greater than Io's escape velocity of 2.6 km s^{-2} (Schneider and Bagenal, 2007). This rapid reneutralisation of pickup ions preferentially takes place in the anti-jovian region of Io's ionosphere. This is due to the presence of a persistent anti-jovian electric field at Io (Neubauer, 1980), likely related to the well-documented radial current system in Jupiter's magnetosphere that links Io to Jupiter's ionosphere (e.g. Belcher, 1987). In practice,

this means that the jet is always pointed away from Jupiter and, since the reneutralised sodium gains a gyromotion during its short-lived pickup-ion phase, located in the plane perpendicular to the local magnetic field at Io, rather than in Io's orbital plane like the banana. Though called a "jet", the 3D morphology of these structures is expected to more closely resemble a fan rather than a collimated jet (Wilson et al., 2002). A similar structure is occasionally seen that is directed toward Jupiter. This is expected to arise from a similar mechanism as the jet, but instead using negatively charged dust grains (rather than positively charged sodium ions that are reneutralised) that contain sodium-bearing molecules (Grava et al., 2021a). Like the jet, the persistent radial electric field at Io would push these dust grains toward Jupiter before the sodium-bearing molecules release sodium atoms via sputtering processes, giving rise to a sub-jovian neutral-sodium cloud that resembles the jet.

There exist also "streams" of sodium within the neutral clouds (e.g. Schneider et al., 1991). These streams are similar in behaviour and morphology to the jets. However, unlike the jets, which arise from rapid reneutralisation of pickup ions within Io's atmosphere, the streams are expected to arise from reneutralisation and disassociation of sodium-bearing ions that have escaped the atmosphere and find themselves in the plasma torus ahead of Io in its orbit (Wilson et al., 2002). These ions must survive for 3-10 hours before undergoing reneutralisation (and hence escape into the stream), unlike the jet progenitor ions that survive for only a few seconds. The similarity in source process, and corresponding similarity in morphology, can make it difficult to distinguish between the jet and stream neutral clouds. Like the cloud, the stream is located in the

magnetic equatorial plane (Wilson and Schneider, 1999).

In addition to the above neutral clouds, which are observed relatively close to Io, there exists also the extended (sodium) nebula (Mendillo et al., 1990), or "Mendillosphere" (Bagenal and Dols, 2020). This extended nebula is centred on Jupiter and extends for at least 500 R_J, which gives it a larger angular diameter from Earth than the Moon and makes it a candidate for the largest object in the Solar System. It is anticipated that this extended sodium nebula is fed by escape from the other neutral clouds, especially from the jet, whose particles have sufficient velocity to escape from Io entirely (Wilson et al., 2002; Mendillo et al., 2007; Bagenal and Dols, 2020). However, some observations, including those by De Becker, Head, et al. (2023) and presented in chapter 4 of this thesis, are not compatible with this interpretation.

Although the connection between Io's volcanism, its atmosphere, and its space environment has been relatively well established, there are a number of aspects that remain challenging to interpret with our current understanding. Key among these is the apparent disconnect between the behaviour of Io's atmosphere and the neutral clouds. Io's atmosphere is known to be remarkably stable, showing no or little change during periods when other (supposedly connected) elements of the Io-Jupiter-magnetosphere system underwent dramatic changes. Roth et al. (2020) observed that Io's atmosphere was essentially unaffected by notable increases in volcanic activity in 2016-2017. Previous work had found that increased volcanic activity at Io was contemporaneous with increased plasma-torus brightness (Yoshioka et al., 2018), and, more recently, atmospheric escape (which feeds both the plasma torus and neutral clouds) was identified to be predominantly volcanic in origin, owing

to the lack of correlation between neutral-cloud enhancements and any obvious insolation signatures (Morgenthaler et al., 2024). Enhancements in the brightness of the extended sodium nebula and the plasma torus are often observed to be coincident (Yoshikawa et al., 2017; Yoneda et al., 2015), though enhancement of the torus brightness often lags behind that of the sodium nebula by 20-80 days (Bagenal and Delamere, 2011; Brown and Bouchez, 1997; Tsuchiya et al., 2018), indicative of the plasma transport time (Morgenthaler et al., 2024). Mendillo et al. (2004) had previously suggested that the observed brightness variability of the extended sodium nebula be linked to changes in the activity of Loki Patera. However, Roth et al. (2020) found instead a decrease in the brightness of the sodium nebula during a period where Loki Patera was increasing its activity. This is incompatible with the notion that volcanic activity drives an increase in the concentration of atmospheric NaCl, whose disassociation provides the neutral Na atoms for the extended sodium nebula; the concentration of NaCl in Io's atmosphere was, in any case, observed by Roth et al. (2020) to remain constant during this period.

These results present a challenge for our understanding of the connection between Io's volcanism, its atmosphere, and its wider space environment. It has been determined that volcanic eruptions on Io do not produce ejecta with sufficient velocity to escape Io directly (Strom et al., 1981); therefore, any volcanic material that eventually escapes Io must necessarily pass through the atmosphere. If, then, variations in torus/neutral-cloud brightness are related to variations in the volcanic output from Io, why are these changes not reflected in the behaviour of Io's atmosphere? This remains an open question, though several scenarios have been invoked to explain this apparent

discrepancy. Volcanic activity on Io is typically measured via the brightness of its volcanic hotspots, with the (reasonable) assumption that the level of volcanic outgassing be correlated with the brightness of the emission. However, the existence of "stealth" plumes, volcanic plumes without a detectable visual signature (de Pater et al., 2020), may allow the level of mass loading of the atmosphere from volcanic outgassing to vary independently of the observed hotspot activity. Additionally, the ability of volcanic plumes to feed the atmosphere/space environment may vary with the location of the volcano on Io. Plumes near Io's poles, where its atmosphere is thinner, may be more able to interact with Io's space environment and drive atmospheric escape, which may make global hotspot activity a poor proxy for the loading of the torus/sodium nebula if this activity predominantly occurs near Io's equator (Morgenthaler et al., 2024). Volcanic activity, while unable to drive mass loss from Io ballistically (typical thermal velocity $\sim$ 1 km s^{-1} compared to the escape velocity of 2.6 km s^{-1}; Schneider and Bagenal 2007), produces plumes that may "float" material (including sodium/sodium-bearing molecules) to sufficient altitudes to allow for interaction with Io's space environment and hence enhanced mass loss, without needing to contribute toward a change in Io's atmosphere. Morgenthaler et al. (2024) found convincing evidence that enhancements in the escape of sodium- and sulphur-bearing molecules occur simultaneously and are driven by increased activity from a single location on Io (though not the same location each time). Indeed, dimmer hotspots (which typically decay after enhancements over a period of 1-3 months) were found to be more correlated with the enhancement timescales of the plasma torus/sodium nebula than brighter, faster-decaying hotspots. This provides more evid-

ence that the global hotspot activity on Io is perhaps a poor proxy for atmospheric escape.

2.5 Overview of the ultraviolet aurora

An aurora is defined as the emission of light due to the interaction between a planetary atmosphere and an external source of energetic particles (Chamberlain and Hunten, 1987). It is important to note this definition states that the energetic particles come from outside the atmosphere (so that, for example, lightning is not considered an aurora) and that no mention is made of the presence of a planetary magnetic field. While magnetic fields are commonly associated with (terrestrial) aurorae, there exist forms of aurora, such as the venusian dayglow, that do not require a planetary magnetic field. Aurorae have been observed (with references to their first published detection) on Mercury (at X-ray wavelengths; Starr et al. 2012), Venus (Fox and Stewart, 1991), Earth (Issāršumuēreš, ca. 679 BCE), Mars (Bertaux et al., 2005), Jupiter (Broadfoot et al., 1979) and its moons (Hall et al., 1998; Roesler et al., 1999), Saturn (Sandel and Broadfoot, 1981), Uranus (Broadfoot et al., 1986), and Neptune (Broadfoot et al., 1989).

Jupiter's aurorae are the most powerful aurorae in the Solar System, emitting some 100 times more power than the aurorae of the Earth (Clarke et al., 2004a). The upper atmosphere of Jupiter is essentially driven by the energy deposited by the aurora (O'Donoghue et al., 2021), which outpowers the solar UV flux by a factor of 20-50. The first indication that Jupiter might have UV aurorae was not a direct detection of the aurorae themselves, but instead the detection of intense non-thermal

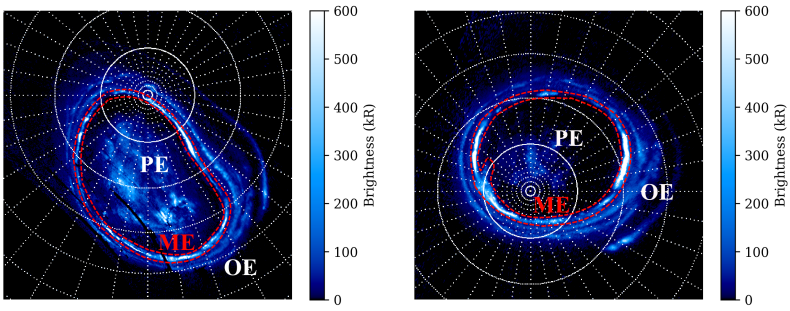

(a) Northern aurora.

(b) Southern aurora.

Figure 2.6: A polar-projected Juno-UVS maps of the UV aurora from Juno's 11$^{\text{th}}$ orbit in both hemispheres showing the position of the main emission (ME; red dashed lines) and the outer (OE) and polar (PE) emission. Gridlines are spaced by 10°. Details of the production of these maps are given in chapter 3.

radio emission attributed to electron cyclotron emission (Burke and Franklin, 1955). This indicated that Jupiter might possess a very strong magnetic field (20 000 times stronger than that of the Earth). Jupiter was known to possess an atmosphere and so it was predicted that interaction between the atmosphere and these gyro-rotating electrons might produce an aurora. Modulation of decametric radio emission by the position of Io also indicated that there may be an electromagnetic interaction between Jupiter and its moons (Bigg, 1964). It would not be until the Voyager 1 flyby of Jupiter in March 1979 that the ultraviolet aurora would be directly detected (Broadfoot et al., 1979) though not spatially resolved beyond being loc-

alised to Jupiter's poles due to the limited spatial resolution of the ultraviolet spectrograph on board Voyager 1. The UV emission seen by Voyager 1 was typical of the excitation of H_2, itself dominated by the Lyman and Werner bands, as well as the Ly-α line of atomic hydrogen (Clarke et al., 2004a). Subsequent observations by the International Ultraviolet Explorer (IUE) from Earth orbit also indicated that the jovian aurorae were essentially fixed with regard to Jupiter's rotation (Clarke et al., 1980), unlike the terrestrial aurorae which remain largely (though not always, such as the Stable Auroral Red (SAR) arcs; Hoch 1973) fixed with regard to the Sun. Clarke et al. (1980) also noted considerable differences in the observed UV auroral power versus central-meridian longitude of Jupiter for the northern and southern hemispheres, which was an indication that the auroral geometry is notably different between hemispheres. It was also observed that Jupiter's aurorae are "always on", unlike the terrestrial aurorae (though there does exist a dayside-cusp aurora due to constant direct precipitation from the solar wind; Frey et al. 2002).

The launch of the Hubble Space Telescope in 1990 provided the ability to take high-resolution UV images of Jupiter's aurorae, since UV wavelengths are blocked from ground-based telescopes by the upper atmosphere. The first observations of the UV aurora were reported by Dols et al. (1992), though these observations were made using the Faint Object Camera (FOC) on board HST which allowed for only a limited identification of the main auroral emission due to its low sensitivity. Gérard et al. (1994) later first identified the now-established dawn-dusk asymmetry in the brightness of the main emission using FOC images. The auroral footprint of Io, the first auroral confirmation of the electromagnetic link between Io and

Jupiter mentioned above, was also detected in FOC images (Prangé et al., 1996), though the low sensitivity prevented consistent identification of this otherwise persistent auroral feature. The Io footprint takes the form of a discrete auroral emission that follows Io in its orbit around Jupiter, discussed further below. Only once the Wide Field and Planetary Camera 2 (WFPC2), also used to take the now-famous Hubble Deep Field image (Williams et al., 1996), was installed on HST could the Io footprint be consistently detected in both hemispheres (Clarke et al., 1998). These observations also allowed for the clear separation of the UV aurora into its traditional three regions (Grodent et al., 2003a,b) though the contemporary O4 magnetic-field model (Acuña and Ness, 1976) was not accurate enough to associate these auroral regions with particular regions of the magnetosphere.

The UV aurorae of Jupiter are typically divided into three distinct regions (Clarke et al., 2004a); an example of these regions in the northern and southern aurora is given in Figure 2.6. The most obvious region is the main emission, also sometimes called the "main oval" in literature in reference to the Earth's own auroral oval. This thesis avoids the term "main oval" for three reasons. Firstly, as identified by Grodent et al. (2008), the jovian main emission cannot easily be considered a single continuous oval but instead frequently shows morphological discontinuities. Secondly, Jupiter's main emission does not take the form of an oval, especially in the northern hemisphere, where the main emission could best be described as bean-shaped. Thirdly, the use of the term "main oval" implies some similarity in origin to the terrestrial auroral oval, when, in reality, the two aurorae originate from entirely different source processes. Nevertheless, like the Earth's own aurorae,

the jovian main emission takes the form of a semi-continuous auroral band around Jupiter's magnetic poles (Grodent, 2015). Inside (or poleward) of the main emission, we find the "polar region" or "polar emission". The equivalent region in Earth's aurorae is called the "polar cap"; this terminology is typically avoided in relation to Jupiter's polar aurorae since the terrestrial "polar cap" describes the area poleward of the auroral oval where limited auroral emission is present (e.g. Zhang et al., 2007), whereas Jupiter's polar region is perhaps the most dynamic part of the jovian aurorae. The aurora outside (or equatorward) of the main emission is known as the "outer emission" and typically presents itself as a diffuse background emission interspersed with brighter, more distinct injection signatures (Dumont et al., 2018). This region also contains the moon footprints, which are a series of discrete auroral patches that are magnetically connected to Jupiter's Galilean moons. Motion of the moons through Jupiter's magnetospheric plasma generates plasma (Alfvén) waves that accelerate electrons in Jupiter's ionosphere along field lines that cross the moon, producing these discrete emissions (in both hemispheres, though with different morphologies) that follow the moon in its orbit around Jupiter (Kivelson et al., 1996; Saur, 2004; Bonfond and Sulaiman, 2024). Thus far, moon footprints connected to all four of Jupiter's Galilean moons have been observed, though that of Callisto was only recently detected unequivocally in Juno image data (Rabia et al., 2025); previous attempts to confirm the presence the Callisto footprint in HST data (Bhattacharyya et al., 2018) were based only on an observed bright feature in approximately the expected location without other characteristics that would be expected of a footprint. Indeed, a similar process and footprint has been observed for Saturn's

moon Enceladus (Pryor et al., 2011), indicating that the moon-footprint phenomenon is universal. These three auroral regions each account for approximately one third of the total auroral emitted power (Grodent et al., 2018), though this is just a typical value and the comparative contributions of the different regions can vary dramatically depending on conditions in the magnetosphere (e.g. Palmaerts et al., 2024). These auroral regions are discussed in much greater detail in sections 2.6 to 2.9. WPFC2 also imaged Jupiter during the impact of the comet Schoemaker-Levy 9 in 1994 (Clarke et al., 1995), where auroral emission was observed both at the impact site as well as at the opposite conjugate point and understood as the result of shock waves that had travelled all the way around the planet to provoke electron acceleration and auroral emission (Bauske et al., 1999).

Some of the most-sensitive and highest-resolution (at least, before the arrival of Juno) observations of the jovian aurora were (and still are; e.g. Nichols et al. 2023) made using the Space Telescope Imaging Spectrograph (STIS), installed on HST in 2002. Observations made using STIS and its superior time resolution have allowed the identification of transient features in the jovian UV aurora, such as auroral flares (Waite et al., 2001). The improved sensitivity compared to FOC and WPFC2 also allowed observation of the dimmer emissions both poleward and equatorward of the main emission, such as the long tail of emission behind the Io footprint (Clarke et al., 2002; Bonfond et al., 2009). Similar footprints for Europa and Ganymede were also identified using STIS observations (Clarke et al., 2002). A robust detection of the Callisto footprint would not occur until relatively late into the Juno mission (Rabia et al., 2025). HST-STIS continues to be an essential tool in

the study of Jupiter's aurora, with recent work comparing UV images from HST-STIS with infrared images from the JIRAM instrument on board Juno (Gérard et al., 2018) and the James Webb Space Telescope (Nichols et al., 2025) to show that, while the morphology of the aurora in the two wavebands is similar, there are sometimes certain features present in the infrared with no UV counterpart.

Unlike previous missions, the latest spacecraft to visit Jupiter, Juno, benefits from having both an UltraViolet Spectrograph (UVS) and a highly elliptical polar orbit, which makes it perfectly placed to image the aurora in both hemispheres, though not simultaneously. Juno was launched in 2011 and arrived at Jupiter in July 2016. Its contribution to our understanding of Jupiter and its magnetosphere started even before it arrived at the planet, during the approach, where its in-situ measurement of solar-wind conditions combined with HST-STIS imaging of the UV aurora suggested that the latter become brighter during periods of compression of the magnetosphere by the solar wind (Nichols et al., 2017). Since entering orbit around Jupiter, Juno, with its combination of in-situ and remote-sensing observations, has greatly advanced our knowledge of the aurora. In no particular order, a few highlights include:

- Connerney et al. (2018): The creation of a new magnetic-field model for Jupiter (JRM09) based on magnetic-field data collected by Juno during its first nine orbits, including the identification of small-scale magnetic anomalies missed by prior models. This magnetic-field model would be further refined after Juno's first 33 orbits (JRM33; Connerney et al. 2022) and an additional model of the contribution of Jupiter's magnetospheric current sheet to

the total magnetic field in the magnetosphere would also be created (Connerney et al., 2020).

- Mauk et al. (2017b) and Allegrini et al. (2017): Before Juno's arrival at Jupiter, it was supposed that the electron precipitation that contributes to Jupiter's bright main auroral emission be dominated by discrete acceleration processes, such as electrical currents induced by quasi-permanent electric fields. Juno found limited evidence of these electric fields, instead revealing a main emission dominated by bidirectional, stochastic acceleration, such as that provoked by Alfvén waves (Salveter et al., 2022).

- Mauk et al. (2020): It was observed that Jupiter's main emission does not present as a single uniform region of aurora, but instead as two adjacent (and distinct) auroral regions. The Zone-I main emission is dominated by downward-travelling electrons, and the Zone-II main emission instead by upward-travelling electrons (though a significant portion of downward-travelling electrons also exists here to provoke auroral emission). This is curious, since the region of Earth's aurora equivalent to the Zone-II main emission, the "black aurora", does not show any significant auroral emission (Marklund et al., 2001).

- Mura et al. (2018): The tail of the Io footprint, instead of being a continuous, straight structure, instead presents a series of spots with a swirling, two-pronged pattern, which indicates that the interaction between Io and Jupiter's ionosphere is more complex than previously assumed.

- Sulaiman et al. (2022) and Lorch et al. (2022): There is some direct evidence that the main emission, like the moon footprints, is powered by Alfvénic fluctuations rather than current-based electron acceleration.

- Bonfond et al. (2021): Jupiter's bright dawn storms were found to be analogous to Earth's auroral substorms, providing evidence that common processes between the two (fundamentally different) magnetospheres do exist.

These are, of course, accompanied by many more works published by a large number of collaborators and institutions around the world. While the bulk of these published works comes from American institutions (as Juno is an American mission), Belgian institutions punch far above their weight. A search for "juno AND jupiter AND aurora" in the `www.lens.org` scholarly-work database, filtered for works published since Juno's arrival in 2016, yields (at time of writing; 17$^{\text{th}}$ January 2026) a total of 532 works. 227 of these works have at least one American author, most notably from the Southwest Research Institute (122) and John Hopkins University (101). However, 113 of these works have at least one Belgian author, almost exclusively from the University of Liège (108) with the remaining works attributed to the Royal Observatory of Belgium and the Katholieke Universiteit Leuven.

The basic mechanism to produce an aurora is relatively easy to understand and requires only a source of high-energy particles that impact a planetary atmosphere. At Jupiter, these high-energy particles are both sourced from and energised within the magnetosphere, via a wide variety of mechanisms. This stands in contrast to the terrestrial aurorae, where the relevant magnetospheric particles are typically energised

via interaction with the solar wind (Dungey, 1961). In both magnetospheres, processes (a wide variety of them depending on the auroral morphology or structure being considered) occur and induce particles/waves to travel along magnetic field lines and provoke auroral emission in the ionosphere at the corresponding point. At Jupiter, this is mostly the consequence of collisional excitation of H and H_2 with precipitating electrons; the (visible) aurorae of Jupiter are therefore likely a purplish-red, due to the Balmer-α atomic-hydrogen line at 656.3 nm (Ingersoll et al., 1998), in contrast to the green-and-red atomic-oxygen aurorae of the Earth (558 nm and 630 nm, respectively; Ishii et al. 2004). The relevant UV H_2 emissions are the Lyman and Werner bands (80-190 nm; the wavelength range is given together since there is considerable overlap; Gustin et al. 2013) which contain a number of rovibrational transitions. Unlike atomic hydrogen, which emits Lyman-α emission at 120.6 nm (Clarke et al., 1980) when excited electrons (n = 2) return to the ground state (n = 1), the Lyman and Werner bands arise from spontaneous vibrational de-excitation of H_2 (excited by electron impact; Stone and Zipf 1972) which produces a forest of emission lines due to quantisation of molecular vibrational energy. In essence, the aurorae of Jupiter function like an old-fashioned[1] cathode-ray television set, in which the aurora is merely the "screen" showing the behaviour of the magnetically linked regions of the magnetosphere. Our analysis of the aurora therefore allows us to indirectly probe the physics occurring in the magnetosphere (and atmosphere), though our ability to draw conclusions from this analysis is limited by the

[1] A metaphor that my younger readers will doubtless not understand and my older readers doubtless resent being described as "old fashioned".

accuracy of our magnetic-mapping models.

2.6 Main emission

It should first be noted that the jovian UV "main emission" is fundamentally an empirical definition. It does not describe a region of the aurora which has been determined, by in-situ measurement or otherwise, to originate from a common source process. Instead, the main emission is defined as the bright, semi-continuous band of aurora that is consistently visible in both hemispheres. The brightness and continuity of the main emission may vary, but most images of the aurora display an identifiable main emission. The empiricism of the definition of the main emission does therefore not presuppose a single common process that gives rise to the entirety of the emission; instead, different regions of the main emission may have different source processes, or may instead share a number of superimposed origins. This is in contrast to, for example, the moon footprints which are defined using their connection to Jupiter's moons.

Nevertheless, many contemporary theories for the generation of the main emission do attempt to present a unified origin for the entire main emission. Historically, the most commonly accepted origin for the main emission was the breakdown of plasma corotation in Jupiter's middle magnetosphere and the thence-ensuing field-aligned currents that would accelerate electrons onto Jupiter's atmosphere and hence produce an aurora (Hill, 1979; Cowley and Bunce, 2001). Under this Corotation Enforcement Current (CEC) theory, a current loop exists that passes from Jupiter's ionosphere, into the

magnetosphere, radially outward through the central plasma sheet, before returning to the ionosphere along distant field lines. This current loop works to accelerate the plasma of the magnetosphere into corotation with Jupiter by way of a $\mathbf{J} \times \mathbf{B}$ force. This force acts a transfer of (angular) momentum from Jupiter's ionosphere to the magnetosphere, coupling the two (Hill, 1979). In a steady-state magnetosphere, once corotation was achieved, no further transfer of angular momentum from the ionosphere would occur. However, Jupiter's magnetosphere contains a source of plasma, Io and its plasma torus. Plasma from the plasma torus constantly flows outward under the influence of interchange instability, since otherwise plasma generated from Io would infinitely accumulate in the inner magnetosphere (Ioannidis and Brice, 1971; Khurana et al., 2004). To maintain corotation, angular momentum must constantly be transferred to the outward-flowing plasma. This presents an interesting balance; the angular-momentum transfer required to enforce corotation in the outward-flowing plasma increases with distance from Jupiter, but the rate at which the ionosphere can transfer angular momentum to the magnetosphere is itself limited by the friction between the ionosphere and lower layers of Jupiter's atmosphere, which keeps the ionosphere itself in corotation with the rest of the planet (Clarke et al., 2004a). At a certain distance, determined by the mass flow rate from the Io torus and the conductivity of the ionosphere (Hill, 1979), the corotation can no longer be enforced and is said to "break down". Since the plasma is no longer rotating around Jupiter at the same rate as the magnetic field, a system of field-aligned electrical currents is produced (Ray et al., 2009); a schematic is shown in Figure 2.1. Under CEC theory, these electrical currents accelerate electrons in Jupiter's

ionosphere and produce the main emission.

Observations support a number of aspects of the CEC theory. Jupiter's magnetosphere is indeed held in corotation close to Jupiter before this corotation breaks down at 20-30 R_J (Belcher et al., 1980; Bagenal et al., 2016). CEC models also predict a main emission that is broadly consistent with observations in terms of position, thickness, and brightness (Cowley and Bunce, 2001; Ray et al., 2010). Transfer of momentum from the ionosphere to the magnetosphere via corotation enforcement has been observationally established (Wang et al., 2021; Al Saati et al., 2022). Field-aligned currents have been detected by Juno with intensities sufficient to power the main emission (Nichols and Cowley, 2022; Kamran et al., 2022); these currents have also been observed to undergo enhancement at the same time as the brightness of the main emission (Nichols et al., 2020). CEC theory also predicts a relationship between main-emission brightness and characteristic electron energy (Knight, 1973) that is consistent with observation (Gustin et al., 2004; Gérard et al., 2016).

More recently, however, certain aspects of the jovian main UV emission have proven to be difficult to understand under CEC theory. The field-aligned currents observed by Juno to have sufficient intensities to power the main emission are themselves highly fragmented, patchy (Connerney et al., 2017a), and north-south asymmetric within the magnetosphere (Kotsiaros et al., 2019), in contrast to the continuous and relatively steady main emission. The high-latitude field-aligned potentials that would precipitate electrons (unidirectionally and monoenergetically) onto Jupiter's atmosphere have only been rarely detected by Juno (e.g. Connerney et al., 2017a; Mauk et al., 2017c), and, even when they are detected, the elec-

tron distributions observed above the main emission remain decidedly broadband and bidirectional (Mauk et al., 2018; Sulaiman et al., 2022), dominated by stochastic acceleration (Salveter et al., 2022). The behaviour and variability of the main emission is also not entirely well predicted by CEC theory. Models of the field-aligned currents in the magnetosphere suggest the presence of a considerable day-night asymmetry: the night-side currents are expected to be significantly more intense than the day-side currents (Khurana, 2001; Chané et al., 2017). These models also predict a lesser dawn-dusk asymmetry, where the dawn-side aurora is approximately an order of magnitude brighter than the dusk-side aurora, due to the enhanced bendback of the magnetic field in the dawn-side middle magnetosphere and the enhanced radial and field-aligned currents that this would entail (Khurana, 2001; Ray et al., 2014). Indeed, these asymmetries in the intensity of the field-aligned currents have been observationally confirmed by Juno (Lorch et al., 2020). If these field-aligned currents give rise to the main emission, we would therefore expect the brightness of the main emission to show similar asymmetries. However, these asymmetries are not reflected in the main emission, indicating that field-aligned currents might not contribute to the brightness of the main emission in a straightforward way. Instead, the dawn-dusk asymmetry is the predominant asymmetry in the brightness of the main emission; in contrast with models and observations of field-aligned currents, it is instead the dusk-side main emission that emits, on average, more power than the dawn-side main emission by a factor of $\sim$4 (Bonfond et al., 2015a; Groulard et al., 2024). The modelled response of the main emission to compression of the magnetosphere by the solar wind is also broadly inconsistent with observation.

Early models indicated that the brightness of the main emission should decrease during solar-wind compressions (Southwood and Kivelson, 2001). The more-recent current models of both Chané et al. (2017) and Sarkango et al. (2019) would indicate that the day-night asymmetry become yet more pronounced during periods of solar-wind compression, with the model of Sarkango et al. (2019) even predicting a drop in the intensity of field-aligned currents on the day side. Observationally, however, the main emission appears to increase its day-side brightness during magnetospheric compression (Nichols et al., 2017; Kita et al., 2016; Yao et al., 2022), consistent with some current models (Cowley et al., 2007) and MHD simulations (Feng et al., 2022); in Head et al. (2024) and chapter 5 of this thesis, it is shown that this brightening is global in the main emission.

An alternative main-emission generation mechanism based on Alfvén waves has also been proposed (Saur et al., 2003). In this Alfvénic scenario, it is instead turbulence in the central plasma sheet in the middle magnetosphere (itself provoked by the outflow of plasma from the Io torus; Saur et al. 2018) that gives rise to the main emission. This turbulence produces small-scale Alfvénic perturbations that propagate along magnetic field lines toward Jupiter. However, in their original state, these Alfvén waves would not have wavelengths comparable to the kinetic scale of electrons in the ionosphere and would thus be unable to produce any meaningful auroral precipitation. Alfvén waves, like other types of wave, undergo reflection at the boundary between two different media. When these Alfvén waves encounter the sharp jump in density at the ionosphere, they are reflected and directed back towards the central plasma sheet. The density jump at the central plasma

sheet also represents a reflection boundary, and so field lines connected to turbulent regions in the magnetosphere will contain Alfvén waves travelling in both directions. These Alfvén waves interact non-linearly and provoke a "cascade" toward shorter and shorter wavelengths. Eventually, Alfvén waves will be produced with wavelengths that approach the inertial scale of ionospheric electrons, allowing them to resonantly (and non-resonantly, which may, in fact, dominate; Hess et al. 2010; Mottez and Génot 2011) accelerate these electrons and hence provoke auroral emission (Saur et al., 2018).

Unlike in the CEC scenario, the acceleration provoked by Alfvén waves is both broadband and bidirectional (Saur et al., 2018). This is more in line with Juno observations of electron distributions seen above the main emission (Mauk et al., 2017c; Salveter et al., 2022). Modelling of this scenario also returns Alfvénic Poynting fluxes in the direction of the ionosphere sufficient to power the main emission (Saur et al., 2018). The observed relationship between main-emission brightness and characteristic electron energy, while accountable via CEC theory, is also predicted in this alternative Alfvénic scenario (Clark et al., 2018). Alfvénic flux above the main emission has been observationally confirmed to have sufficient Poynting flux to generate the main emission (Lorch et al., 2022), though only at altitudes greater than $\sim$10 R_J; it is expected that this Alfvénic flux is so efficiently converted into electron acceleration at lower altitudes that it is no longer detectable by Juno (Sulaiman et al., 2022). Like under CEC theory, the predicted location of the main emission matches observations (Saur et al., 2003). Unlike CEC theory, however, in which field-aligned currents are predicted and observed to be more intense in the dawn- and night-side sectors, turbulence in the

middle magnetosphere is observed to be more intense at dusk (Tao et al., 2015). This would produce a brighter main emission at dusk, which is consistent with observation (Groulard et al., 2024). Despite these successes, there still remain issues with the Alfvénic model, particularly in the realm of simulation; as yet, MHD simulations including Alfvénic processes are yet to fully reproduce the observed properties of the main emission (Feng et al., 2022). In any case, further refinement of the Alfvénic model is required before a paradigm shift from the CEC theory to the Alfvénic theory for the generation of the main emission can be considered. Indeed, the two mechanisms may both contribute, with momentum being transferred to keep the magnetosphere in corotation by the field-aligned current loop and Alfvénic processes on those same field lines accounting for the largest part of the main auroral emission.

While the main emission is frequently touted as a steady and consistent auroral structure, especially compared to the Earth's own auroral oval, it is hoped that the above discussion hints that the properties of the main emission are anything but. Indeed, the main emission shows a great deal of variability, both in its brightness and morphology. These properties are known to vary in magnetic local time (Grodent et al., 2003a) and in response to magnetospheric (Bonfond et al., 2012; Tao et al., 2018) or interplanetary conditions (Nichols et al., 2017; Yao et al., 2022). The main emission is also typically not a single continuous auroral arc; instead, it often shows a "pre-noon discontinuity" (Radioti et al., 2008) which is often followed by the "Palmaerts spot", a localised enhancement of the main-emission brightness at noon (Palmaerts et al., 2024). This is attributed to the presence of a persistent thermal-pressure minimum and reduced plasma-

velocity gradient in this section of the magnetosphere, itself caused by interaction of the rotating magnetospheric plasma with the magnetopause (Khurana, 2001; Chané et al., 2013, 2018; Palmaerts et al., 2014). This discontinuity thus marks the boundary between the dawn-side and dusk-side main emission, which themselves differ noticeably in their morphology, with the dusk-side typically presenting as far more disrupted and discontinuous (Nichols et al., 2009b; Palmaerts et al., 2024) than the dawn-side aurora. The main emission is also home to a number of identifiable discrete features, such as the auroral bridges (Pardo-Cantos 2019; Palmaerts et al. 2024; discussed further below) and dawn storms, which are bright, amorphous features on the dawn-side main emission that slowly transform into injection signatures in the outer emission (Bonfond et al. 2021; also discussed further below). Besides discrete features, the main emission has also been noted to undergo modulation of its shape with magnetic local time. Compared to its average position which remains fixed in System-III longitude (Ballester et al., 1996) - where this average has been calculated by looking at the position of the aurora for many different subsolar longitudes, thus removing this local time effect - the dawn-side main emission is typically "expanded" and the dusk-side main emission typically "contracted" (Grodent et al., 2003a). Though the work of Grodent et al. (2003a) used Earth-based HST observations (which, due to the shape of the aurora in the north, preferentially observed the aurora with subsolar longitudes of around 180° in System-III longitude), their conclusion about the magnetic-local-time dependence of main-emission size is supported by later work (Head et al. 2024; included as chapter 5 of this thesis). The fact that the morphology of the main emission can vary with magnetic local time reveals something

rather profound about Jupiter's aurora. Unlike Earth's aurorae, which derive their energy from the solar wind, Jupiter's aurorae are fundamentally powered by the internal interaction between its magnetic field and the iogenic plasma of the magnetosphere. They are therefore generated independently of the solar wind. However, the magnetic-local-time dependence of the main emission implies that the solar wind can exert some influence all the way into Jupiter's middle magnetosphere (Khurana, 2001; Murakami et al., 2016). As mentioned above, the brightness of the (day-side) main emission was found to be correlated with the pressure of solar wind (Kita et al., 2016; Nichols et al., 2017) or the compression of the magnetosphere (Yao et al., 2022), supporting the notion that the solar wind exerts some measure of influence on the main emission.

However, the solar wind is not the only source of variability for the brightness or morphology of the main emission. Variability in the mass outflow rate of plasma from Io (which may be related to a variable volcanic activity on Io; see discussion in section 2.4) may also affect the main emission. A period of increased mass loading of the Io torus was found to coincide with a brighter northern aurora in 2015 (Tao et al., 2018). At the time, this was suggested to be the consequence of the more intense field-aligned currents that a greater degree of torus mass outflow would imply (Nichols, 2011). Since this mass outflow would increase the density of the central plasma sheet in the magnetosphere, it would also increase the contribution of the plasma sheet to the global magnetic field within Jupiter's magnetosphere compared to the internal field (Hill, 2001; Bonfond et al., 2012). This would "pull" the magnetic field lines outward in the magnetosphere, which, for a static main-emission source region, would cause the main emission to expand equat-

orward. This interpretation is compatible with the appearance of greater numbers of plasma-injection signatures in the jovian aurorae while the main emission was observed to be expanded, which is consistent with increased mass outflow from Io (Bonfond et al., 2012). It is currently not fully understood to what extent external and internal processes work to modulate the size of the main emission.

Regardless of how exactly the size of the main emission is controlled by external (compression of the magnetosphere by the solar wind) or internal (expansion of the magnetosphere by mass outflow from the Io torus) processes, there remains the question of how exactly information on the state of compression/expansion of the magnetosphere is translated into a variable size of the main emission. Vogt et al. (2022b) suggest two scenarios, which are illustrated in Figure 2.7:

1. Figure 2.7a: A change in the topology of the magnetic field in the magnetosphere causes a fixed main-emission source region to connect to the ionosphere along a farther (closer) field line, which would result in a contraction (expansion) of the main emission.

2. Figure 2.7b: The magnetic field topology does not change significantly during a compression/expansion of the magnetosphere, but these instead cause the source region of the main emission to move radially in the magnetosphere. As above, this would cause the main-emission source to connect along different field lines and hence change the size of the main emission in the ionosphere.

Both of these scenarios would be indistinguishable based on observations of the size of the main emission alone. To break

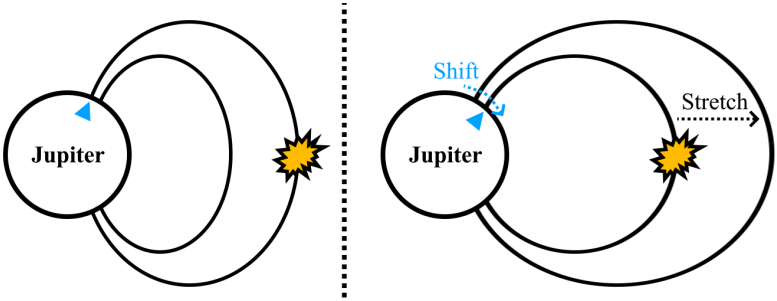

(a) Change in magnetic field.

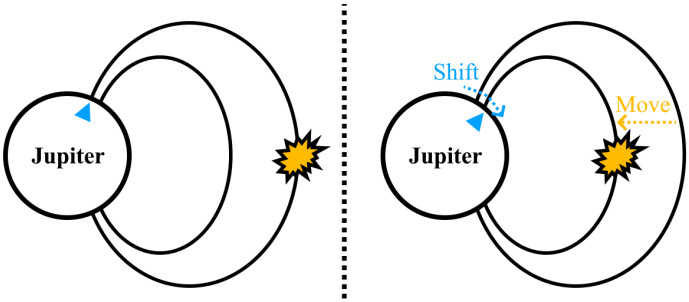

(b) Movement of source region.

Figure 2.7: Illustration of the two scenarios described in the text to explain the variable size of the main emission. The (idealised dipolar) magnetic field topology is illustrated by the solid black lines. The magnetospheric source region of the main emission is denoted in orange, and the latitudinal position of the main emission on Jupiter in blue.

this degeneracy, we require an auroral feature whose magnetospheric source is known to remain at a fixed radial distance. Luckily, Jupiter's magnetosphere provides us with three (or

four; Rabia et al. 2025) of these features: the Galilean moons and their corresponding footprints. In the first scenario, since the magnetic field is being stretched, the main-emission source region and the moons would all find themselves connecting to the ionosphere along different field lines, and thus the moon footprints would display a latitudinal shift from their nominal positions proportional to the expansion or contraction of the main emission. In the second scenario, since the magnetic field is comparatively unaffected and it is instead the main-emission source region that is moving radially in the magnetosphere, the moon footprints would not be expected to move latitudinally with the varying size of the main emission. These two effects may themselves be related (Bonfond et al., 2012), but we may attempt to see whether one typically dominates over the other. Vogt et al. (2022b) themselves attempted to disentangle these two effects using HST images of the aurora, finding that the Ganymede footprint only sometimes moves with the main emission, but this investigation was hampered by large uncertainties with the planetary-limb fitting procedure and hence the position of the main emission. Bonfond et al. (2012) also provided limited evidence for the second scenario. In a single HST image series, the footprint of Ganymede was observed inside the main emission, indicating that the main-emission source region had moved inside the orbit of Ganymede. However, this conclusion is mired by the fact that the viewing geometry was very poor (the footprint of Ganymede was located right on the planetary limb) and the main emission was very faint in this sector, making it difficult to identify its exact position. This auroral geometry has also not been observed since.

Dawn storms, mentioned above, are bright, amorphous features that are superimposed on the dawn-side main emission

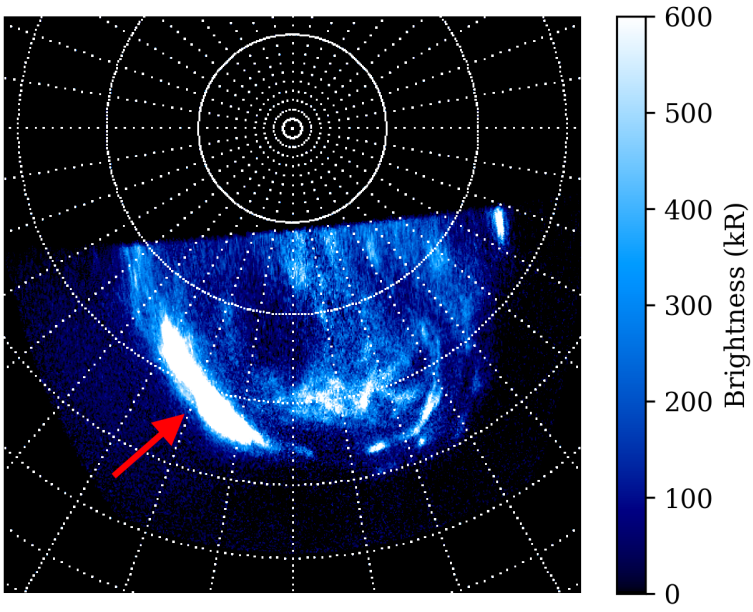

Figure 2.8: A polar-projected HST-STIS image of the northern UV aurora taken on 2019-05-29 with a dawn storm highlighted with a red arrow. Gridlines are spaced by 10°.

(Bonfond et al., 2021). Being such distinctive and bright features, they were identified early in the history of observation of Jupiter's UV aurora (Gérard et al., 1994). An example of a dawn storm is visible in Figure 2.8. Both HST (Ballester et al., 1996) and Juno (Bonfond et al., 2021) have indicated that dawn storms have lifetimes on the order of hours but no single, consistent morphology throughout their lives. Instead, they follow a reasonably consistent evolutionary track (though

steps can sometimes be missed or occur out of order; Bonfond et al. 2021) in which they start their lives as bright spots poleward of the night-side main emission, associated with large-scale reconnection in the distant magnetotail. They then move onto the main emission in the early morning, taking the form of a series of blob-like "beads" attributed to plasma instabilities in the near magnetotail (at least on Earth; Yao et al. 2017). These beads evolve into the "traditional" dawn storm (the "expansion phase", since the dawn storm widens in both latitude and longitude) as the source process undergoes dipolarisation in the middle magnetosphere. Finally, the evolutionary track ends in plasma injection, giving rise to bright injection signatures in the post-noon outer emission (discussed further in section 2.8). Due to the limited (∼40-minute) exposure time of HST (and the limited range of "good" viewing geometries for the aurora in both hemispheres), the full evolution of a dawn storm is yet to be observed; nevertheless, the transition from dawn storm to injection signature has been directly observed in a single case (Gray et al., 2016). One interpretation of the typical-but-not-universal evolutionary sequence of dawn storms is that a perturbation (from some accumulation of mass and/or energy in the magnetotail) propagates inward and facilitates various plasma instabilities with variable efficiency, rather than each type of plasma instability directly provoking the next in the sequence (Bonfond et al., 2021).

Particle measurements made by Juno indicate that the main emission may be split into two distinct zones, which are naturally called the Zone-I and Zone-II aurora (Mauk et al., 2020); a schematic description of these two zones is given in Figure 2.9. The Zone-I aurora is associated with predominantly downward-travelling electrons, which makes this the

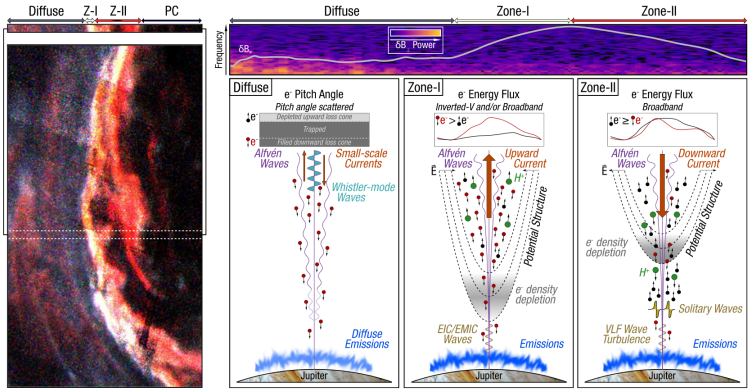

Figure 2.9: Left: a view of the UV aurora from Juno's 6$^{\text{th}}$ orbit. Right: a schematic view of the low-altitude diffuse, Zone-I, and Zone-II aurorae, with the expected electron energy distribution and processes occurring on the field line annotated. The Alfvénic-flux spectrum and calculated δB_ϕ is given above. Taken from Sulaiman et al. (2022).

more "typical" zone to find strong auroral emission. The Zone-II aurora, conversely, is dominated by upward-travelling electrons. However, this region is still home to considerable auroral emission, indicating that a significant population of downward-travelling electrons must still be present. These two regions are typically located right next to one another, with the Zone-II aurora usually, but not always (Al Saati et al., 2022), being slightly poleward of the Zone-I aurora. The emission of the Zone-II aurora has been suggested to be the result of broadband, bidirectional electron acceleration, initially caused by upward electron beams (Elliott et al., 2018, 2020) observed above the polar aurora by Juno (Mauk et al., 2017c), which

subsequently give rise to large-amplitude electrostatic waves (Sulaiman et al., 2022). It is interesting to note that similar processes on Earth and Saturn do not give rise to appreciable auroral emission (Sulaiman et al., 2022); indeed, the Zone-II equivalent in the terrestrial aurorae is known as the "black aurora" precisely because it does not show any appreciable emission (Marklund et al., 2001)

2.7 Polar emission

The polar emission is considered to be the auroral emission poleward of the main emission. It contains at least three morphologically distinct subregions: the active region, the dark region, and the swirl region (Grodent et al., 2003b; Grodent, 2015). These regions are roughly denoted for a typical HST-STIS view of the northern aurora in Figure 2.10. The active region is the brightest and most dynamic part of the polar region. It frequently contains features that rapidly vary their brightness, such as flashes and flares, hence the term "active region". It maps to a magnetospheric local time of approximately noon and is located just poleward of, or even continuous with, the main emission. There exists also an duskward extension of the active region (called the "dusk active region" to differentiate from the above-discussed "noon active region") which also shows similar properties (Nichols et al., 2017), though the typical HST viewing geometry makes it difficult to ascertain to what extent these two regions are continuous or comparable.

In the dawn-side polar region, there exists the "dark region", which, as the name suggests, is notable for its complete absence of any meaningful UV emission (Grodent, 2015). It has

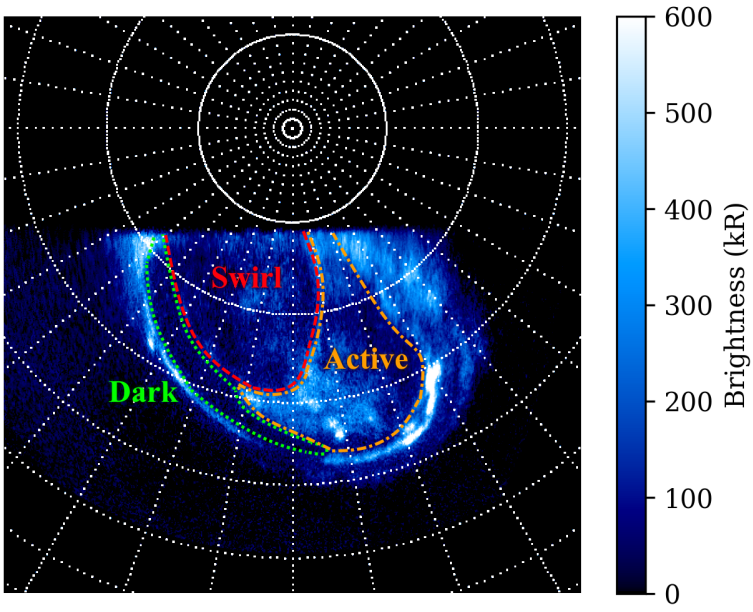

Figure 2.10: A polar-projected HST-STIS image of the northern UV aurora tkaen on 2019-03-09 with the approximate locations of the swirl, dark, and active regions highlighted by red dashed, green dotted, and orange dot-dashed lines, respectively. Gridlines are spaced by 10°.

been associated (Grodent et al., 2003b) with a similar region of the ionosphere, the rotating Dark Polar Region (Stallard et al., 2003) in which the ionosphere is subcorotating. The dark region is expected to be dark because it corresponds to the return flow of flux tubes in the Vasyliūnas cycle, which are depleted by pinched reconnection in the night side and hence not expec-

ted to provoke auroral emission (Cowley et al., 2003; Kivelson and Southwood, 2005; Swithenbank-Harris et al., 2019).

Finally, the central portion of the polar region is denoted as the "swirl region" owing to the chaotic or turbulent pattern of (relatively dim) auroral emission that it typically contains (Grodent, 2015). It is historically considered to map to open field lines, though more recent simulations do not support this interpretation (Zhang et al., 2021), which is based on contemporary and historical magnetic-field-mapping models that are known to behave poorly in this region (Grodent, 2015). Vogt et al. (2011), using a flux-equivalence mapping that is considered to be more reliable in the polar region than field-line-tracing methods, suggest that the swirl region instead maps to Jupiter's magnetospheric cusp. This region also occasionally contains polar auroral filaments (Nichols et al., 2009a), which are discussed further below.

In addition to these broad polar subregions, the polar emission also contains a number of distinct auroral features, perhaps more than any other region. Of these, perhaps the most spectacular are the polar flares; an example is given in Figure 2.11. A polar flare was first detected in HST-STIS images by Waite et al. (2001) who observed a 30-fold increase in its brightness within 70s. The power emitted by these flares is often above 1 TW, which is comparable to the power of the entire UV aurora (Palmaerts et al., 2024). They have been suggested to be the consequence of sudden increases in the solar-wind dynamic pressure (Waite et al., 2001) or day-side reconnection in the magnetopause (Grodent et al., 2003b). These intense flares are also typically observed when the dawn-side main emission is abnormally bright (Palmaerts et al., 2024), indicative of compression of the magnetosphere (Yao et al., 2022), supporting

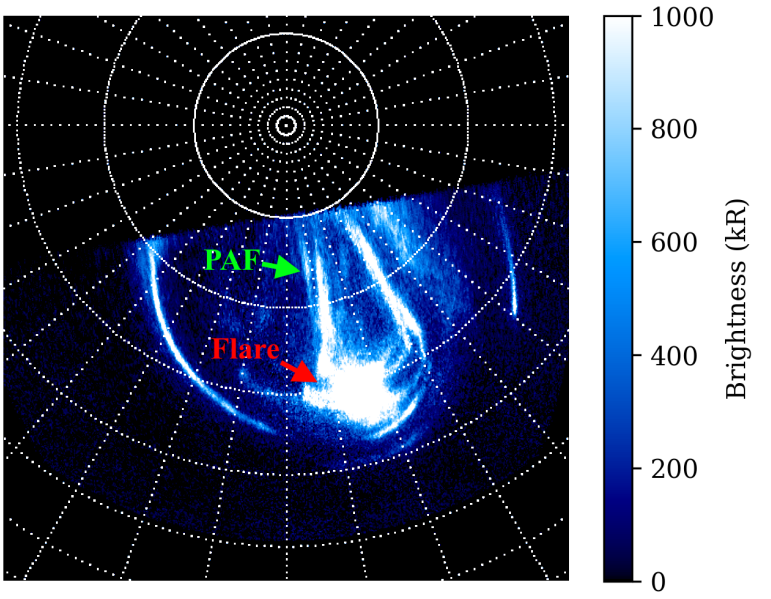

Figure 2.11: A polar-projected HST-STIS image of the northern UV aurora taken on 2019-07-21 showing a polar flare (red) and a polar auroral filament (PAF; green). Gridlines are spaced by 10°.

the idea that the appearance of these flares is fundamentally controlled by the solar wind.

"Flashes" are active-region brightenings that last less than 30 seconds but often show minute-scale (quasi-)periodicities (Palmaerts et al., 2024); in practice, they appear as "up-and-down" brightenings of the active region. Unlike the flares, which appear as a totally new blob-like structure in the au-

rora, these flashes appear to increase and decrease the brightness of existing active-region structures such as the bridges. Confusingly, flashes are also known as quasi-periodic flares (Bonfond et al., 2011), despite flashes and flares being visually (Palmaerts et al., 2024) and phenomenologically (Grodent et al., 2003b; Bonfond et al., 2016) distinct. They are suggested to be internally driven as they occur consistently even during periods of solar-wind quiescence (Kimura et al., 2015; Bonfond et al., 2016), unlike flares which are expected to be related to increased solar-wind activity (Waite et al., 2001). Additionally, these flashes can occasionally cover essentially the entire active region while remaining in sync across their entire surface (Bonfond et al., 2016), which is implied to map to widely different locations within Jupiter's vast magnetosphere. Since the speed required to transmit information between these distant regions of the magnetosphere (to maintain the synchronicity) would be prohibitorily high, it is instead suggested that the brightness of these flashes is modulated by a process occurring at a very low altitude (Bonfond et al., 2016).

In addition to the flares and flashes, there exist also the transient "bright polar spots" (Haewsantati et al., 2021), which are typically dimmer but longer lasting than flares. They are located on the border with the swirl region and can be seen at any local time (Palmaerts et al., 2024). They also sometimes exhibit a reoccurrence periodicity between 3 and 47 minutes, which is a periodicity often seen elsewhere in Jupiter's magnetosphere, such as in radio emissions (e.g. MacDowall et al., 1993; Hospodarsky et al., 2004) or X-ray emission (e.g. Dunn et al., 2016), which has been linked to the presence of standing Ultra-Low Frequency (ULF) waves in Jupiter's magnetosphere (Khurana and Kivelson, 1989; Manners and Masters,

2020; Nichols et al., 2017).

Polar auroral filaments are auroral features intermittently found in the swirl region (or, in my own experience, along the boundary between the swirl region and dusk-side active region) that are roughly aligned toward the Sun (Nichols et al., 2009a); an example is visible in Figure 2.11. Despite being Sun-aligned, they are apparently unrelated to the conditions of the impinging solar wind. Polar auroral filaments have been suggested to be related to the slow propagation of plasmoids in Jupiter's extended magnetotail (Grodent, 2015), though they remain under-observed and under-studied.

Jupiter's UV auroral bridges, as shown in Figure 2.12, are an auroral feature that has long been known to the scientific community (e.g. Nichols et al., 2009b) but which have long avoided detailed study that might shed some light on their properties and origins. Bridges pose a particular problem to me right now, as I am unsure whether to put them in the section on the main emission or the polar emission. In the end, as you are already doubtless aware, I have decided to discuss them as part of the polar emission, since, at least from a superficial morphological perspective, they are indisputably found interior to the main emission. However, as we shall see in chapter 6, there is some evidence to suggest that they have a closer phenomenological link to the main emission. Since I included dawn storms in the section on the main emission, despite being phenomenologically closer to injection signatures in the outer emission, I suppose that I am categorising my auroral features by location rather than by origin, which, in any case, is poorly understood for many features in the UV aurora. "Bridges" (Pardo-Cantos, 2019) refer to arcs of the type shown in Figure 2.12 which stretch from the main emission, through the polar

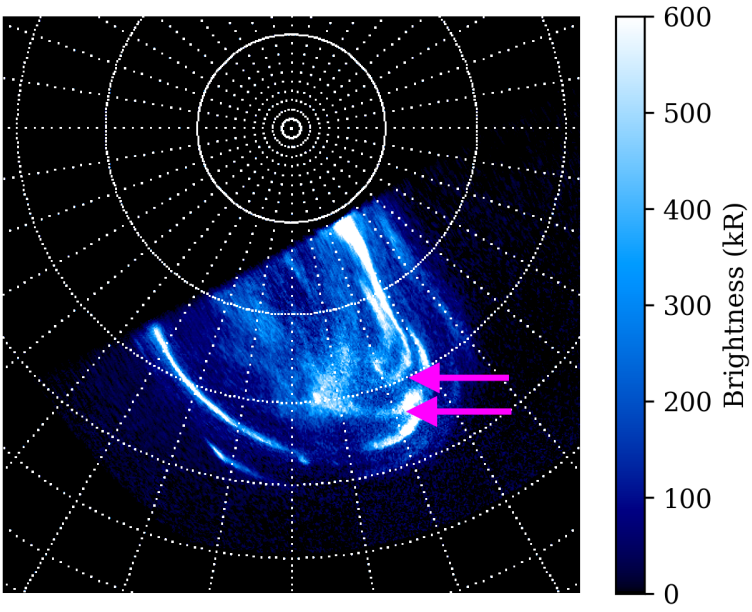

Figure 2.12: A polar-projected HST-STIS image of the northern UV aurora taken on 2019-02-09 with bridges highlighted by magenta arrows. Gridlines are spaced by 10°.

collar (Greathouse et al., 2021), to the day-side active region (Nichols et al., 2017), though they may not fully span this gap. Bridges may appear alone or in a group, or not at all, and exclusively in the dusk-side polar collar (Pardo-Cantos, 2019).

The term "bridge" is a relatively recent invention that aims to highlight its bridge-like nature between the main emission and the active region. Previous terms, such as "arcs parallel to

the main oval" (Nichols et al., 2017) or "arc-like feature of the polar active region" (Grodent, 2015), risk confusion with similar auroral arcs, such as polar auroral filaments (Nichols et al., 2009a), which are superficially similar but not necessarily related to bridges. Bridges have, until now, been the subject of only limited direct study. Pardo-Cantos (2019) analysed a set of three bridges identified in HST-STIS data, which were found to map to the dusk-side magnetosphere between local times of 10 and 22 hr beyond 60 R_J. Initially, these bridges, based on their position in the magnetosphere, were suggested to be the consequence of vorticity in the dusk-side plasma flow caused by Kelvin-Helmholtz instabilities (Fukazawa et al., 2006). However, Kelvin-Helmholtz instability, or indeed dusk-side reconnection (e.g. Grodent et al., 2003a; Cowley et al., 2003), is not individually sufficient to explain the properties of bridges (Nichols et al., 2017).

Beyond the HST-STIS images used by Pardo-Cantos (2019), bridges have also been observed in Juno-UVS images of the UV aurora (Greathouse et al., 2021). This work identified bridges in both hemispheres and in the full range of possible System-III longitudes, but only in the dusk-side aurora. The fact that these bridges can occur at any System-III longitude indicates that they have a fundamentally magnetospheric origin, rather than being modulated by effects in the ionosphere. The appearance of bridges in the aurora has also been (tentatively) associated with compression of the magnetosphere by the solar wind (Nichols et al., 2007, 2009b, 2017). Work has also suggested that the bridge is stable over at least 3 (Nichols et al., 2009b) and later 5 hours (Palmaerts et al., 2024), compatible with the timescales for solar-wind compression events. If correct, this would imply that bridges can have lifetimes of

several days (Chané et al., 2017). The exact manner in which bridges connect to the main emission also shows some variability. They sometimes disrupt the continuous nature of the dusk-side main emission (e.g. Groulard et al., 2024) and sometimes appear alongside a completely unperturbed main emission (e.g. Nichols et al., 2009b). This may indicate that the source of the bridges may, on occasion, interact with the main-emission source process.

2.8 Outer emission

Jupiter's UV outer emission, which is defined as the auroral emission equatorward of the main emission, can be split into three separate categories: discrete emissions, the diffuse emission, and the moon footprints; an example of these three classifications is given in Figure 2.13. The moon footprints, being phenomenologically distinct from the rest of the aurora, are commonly considered to form a fourth "region" of the UV aurora, and are hence discussed here in their own separate section 2.9. The discrete outer emission typically takes the form of amorphous patchy aurora or long auroral arcs parallel to the main emission. The outer patches have been robustly shown to be linked to plasma injection in Jupiter's magnetosphere (Dumont et al., 2014; Nichols et al., 2023). These plasma injections were first measured in-situ by the Galileo spacecraft (Mauk et al., 1997). They are expected to arise from interchange instability, a process by which the constant radial outflow of plasma from the Io torus is compensated by the inward flow ("injection") of hot plasma from the distant magnetosphere (Paranicas et al., 1991). This injected plasma typically, but not

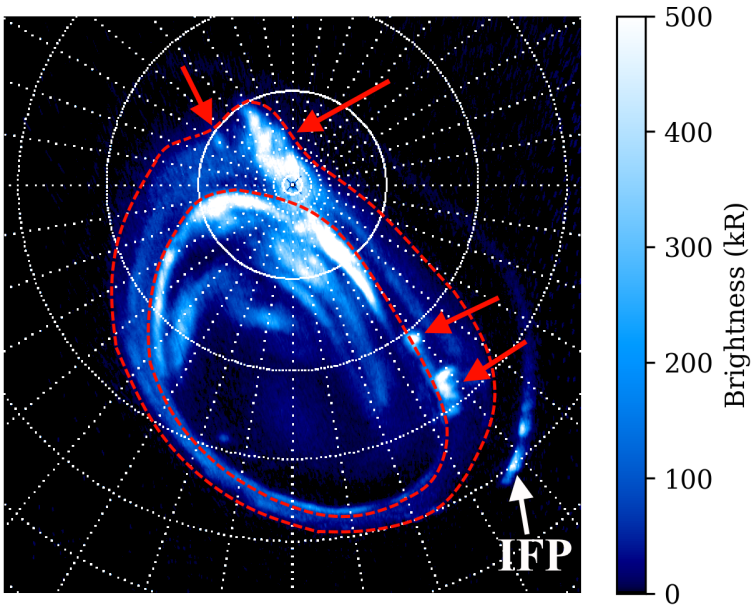

Figure 2.13: A polar-projected Juno-UVS image of the northern UV aurora during Juno's 7th with discrete outer-emission features highlighted by red arrows. A white arrow indicates the location of the Io footprint. Red dashed lines denote the approximate bounds of the diffuse emission. Gridlines are spaced by 10°.

always (Haggerty et al., 2019), gives rise to patches of aurora in the outer emission that are denoted as "injection signatures". It should be noted that plasma injections have been identified in Earth's magnetosphere but instead give rise to pulsating diffuse auroral patches (Momberg et al., 2024). Despite being

transient and limited in spatial extent, these injection signatures can occasionally emit more power than the main emission (Palmaerts et al., 2024). They are found at all System-III longitudes between the main emission and the statistical Io footpath (e.g. Bonfond et al., 2017c) and map to radial distances in the central plasma sheet between 7 and 40 R_J. This, combined with their observed lifetimes greater than 45 minutes (Dumont et al., 2014), were compatible with Galileo observations of plasma injections and first led to the association of injections with patchy outer emissions. Later, an increase in the brightness of injection signatures was observed alongside an expanded main emission, a potential signature of increased mass outflow from the Io torus (section 2.6) and thus enhanced hot plasma injections to balance the outflow of magnetic flux that this would engender (Bonfond et al., 2012), which strengthened the link between injections and patchy aurora. Large injection signatures were also observed during a period of solar-wind quiescence (Kimura et al., 2016), indicating that the appearance of these structures is likely internally driven. Subsequent Juno traversals of plasma injections with simultaneous HST observation of the UV aurorae have since essentially confirmed that patchy outer emissions are related to magnetospheric plasma injections (Nichols et al., 2023). Alongside these patchy injection signatures, the outer emission is also home to distinct arc-like structures that run parallel to the main emission. These arcs show isotropic electron distributions (Radioti et al., 2009) and were observed to enhance in brightness following a detected plasma injection (Gray et al., 2017), though they remain, thus far, distinct from injection signatures in the literature.

The prevailing understanding of the origins of injection signatures suggests that pitch-angle-anisotropic electron dis-

tributions (with enhanced perpendicular-pitch-angle electron flux; Li et al. 2008) induced by injections lead to the production of plasma waves in the central plasma sheet (Daly et al., 2023). These plasma waves counteract the anisotropy and impose isotropic pitch-angle scattering on the local magnetospheric electrons (Li et al., 2008), filling the loss cone (the electrons with velocity vectors close enough to the local direction of the magnetic field to travel all the way to the ionosphere before they would be magnetically mirrored by the convergence of the field lines), which then leads to auroral precipitation (Mauk et al., 2002). This process has been directly observed in a plasma injection by Juno (Menietti et al., 2021). However, this is not the only proposed explanation; some observations of plasma injections and their signatures may be better explained by acceleration of electrons by Alfvén waves at high latitude. In this second scenario, changes in the magnetic-field topology induced by an injection may launch Alfvén waves toward the ionosphere (Gray et al., 2017), where they would accelerate electrons in much the same way as discussed in section 2.6. Dumont (2023) suggests that the preferred appearance of injection signatures in the northern hemisphere may be a consequence of the higher maximum surface field strength in the north which would be more consistent with low-altitude Alfvénic acceleration rather than pitch-angle scattering in the equatorial plane. This Alfvénic mechanism is suggested to be able to provide sufficient energy flux to power the equatorward aurora (Gershman et al., 2019). It is not yet entirely clear to what extent these two mechanisms (pitch-angle scattering and high-latitude Alfvénic acceleration) contribute toward producing injection signatures. A third scenario has also been suggested, in which field-aligned electrical currents are formed on

the flanks of the plasma injection which then give rise to a corresponding auroral signature (Radioti et al., 2010), which is the predominant mechanism present in the analogous process on Earth (Chen and Wolf, 1993). However, electron acceleration from field-aligned currents is typically unidirectional and monoenergetic, which results in characteristic "inverted-V" electron energy distributions, which are only rarely reported in the jovian middle magnetosphere where these injections occur (Salveter et al., 2022) making this third scenario less likely than the prior two. In the first (pitch-angle scattering) scenario, the electron acceleration imparted from the plasma injection is expected to be isotropic (Li et al., 2017); therefore, an increase in the electron energy flux in the downward direction should lead to corresponding increases in the upward and perpendicular flux. Additionally, in the scattering scenario, the precipitating electron flux would be controlled by the loss-cone angle in the ionosphere, which is itself controlled by the strength of the surface magnetic field. Since a stronger magnetic field (through conservation of the first adiabatic invariant) works to close the loss cone (Gérard et al., 2013), we would expect higher average electron fluxes (and hence higher auroral brightness) in regions of weaker surface field. In the second (high-latitude Alfvénic acceleration) scenario, the electron acceleration is expected to be largely field-aligned (though bidirectional and broadband; Saur et al. 2018) and hence enhancements in the downward electron energy flux should only be accompanied by a similar enhancement in the upward direction, not perpendicularly. Alfvénic acceleration is also expected to be more efficient at higher surface field strength (Hess et al., 2013) and thus the aurora should be brighter in regions of stronger surface magnetic field, contrary to the scattering

scenario. These characteristics provide metrics to assess the extent to which these two mechanisms contribute toward the production of auroral injection signatures, which remains elusive. Gérard et al. (2013) could detect neither a proportional (high-latitude Alfvénic) nor inversely proportional (pitch-angle scattering) relation between injection-signature brightness and surface field strength, though this analysis was based on a single injection signature seen in both hemispheres.

Injection signatures have previously been associated with dawn storms in the UV aurora (Bonfond et al., 2021), where they are suggested to be the final step in the proposed four-step evolution of a dawn storm, with the bright "true" dawn storm occurring on the main emission just beforehand. This transition from dawn storm to injection signature has been previously seen in HST data (Gray et al., 2016). However, not all injection signatures are necessarily preceded by a dawn storm; in one instance, an injection signature was observed to arise in Juno-UVS images with no prior dawn storm (Bonfond et al., 2017a). Though the limited number of confirmed cases makes drawing concrete conclusions challenging, this observation suggests that not all injection signatures arise as the consequence of dawn storms. Even in the absence of large-scale magnetotail reconfiguration (the proposed root cause of dawn storms), quasi-constant small-scale-plasmoid or drizzle-like outflow have both been suggested as mechanisms for outward mass transfer in the magnetosphere, and hence plasma injections (Bagenal, 2007; Bagenal and Delamere, 2011; Yao et al., 2025).

As these injection signatures develop and move equatorward, they undergo ageing (Mauk et al., 1999; Dumont, 2023). Due to magnetic-curvature drift (in which gyrating particles encounter variations in the local magnetic-field vector during a

gyration; Burchill 2026), the electrons within the plasma injection undergo energy-dependent longitudinal drift (Mauk et al., 1999): electrons with higher energies advance in System-III longitude compared to those electrons with lower energy. Observationally, this means that the longitude peak in colour ratio (see section 3.1.1) within an injection signature (which arises from higher-energy electrons that can penetrate deeper into Jupiter's atmosphere) is found ahead of the brightness peak (which is approximately aligned with the centre of electron density in the injection) in aged injection signatures. It should be noted that very old injections are expected to have exhausted their very-high-energy electrons, bringing the colour-ratio peak back in line with the brightness peak, but, in general, a significant longitudinal difference between these two peaks can be taken as an indicator of injection ageing.

Besides injection signatures and the moon footprints, the outer emission is home to the diffuse aurora. The diffuse aurora is always present, to some extent, just equatorward of the main emission, which, somewhat confusingly, has lead to the entire outer emission being described as the "diffuse aurora" (e.g. Li et al., 2017; Mauk et al., 2020). This is a particular problem when interpreting Juno data and attributing these interpretations to the diffuse aurora. During the investigation that constitutes chapter 7 and Head et al. (2026), I noted that Juno very rarely passes over a "pristine" diffuse aurora with no superimposed injection signatures, at least at low altitude; during the first 40 perijoves (78 auroral passes with data acquisition), Juno crossed a discrete feature in 63 cases, leaving only 15 cases (19% of the dataset) where only the diffuse aurora was crossed. Since they are typically brighter than the diffuse aurora, we might expect the instrument signatures

(waves, particles, ...) of these discrete features to dominate over the properties of the weaker diffuse aurora. Of course, injection signatures and the diffuse aurora may (and indeed are expected to; Dumont et al. 2018; Li et al. 2021) originate from very similar source processes, so this might not be such a great issue. However, I would still caution against the assumption that everything equatorward of the main emission be the "diffuse aurora" without taking into account the various auroral elements that the outer emission can contain. The diffuse aurora is expected to arise from pitch-angle scattering in the central plasma sheet by whistler-mode waves in the middle magnetosphere (Bhattacharya et al., 2001).

2.9 Moon footprints

Embedded within the outer emission are the moon footprints. They are discussed here in their own section due to their separate origin from the rest of the outer emission, as well as being the subject of a considerable amount of study in the literature; see the recent review by Bonfond and Sulaiman (2024). It is understandable that the moon footprints are of such particular scientific interest; while the jovian main emission and many polar-emission structures have superficial terrestrial equivalents (though typically with completely different source processes), Earth's aurora does not contain an equivalent footprint for our own Moon. Since the detection of an electrically conductive ionosphere on Io (Kliore et al., 1975), which is in motion relative to Jupiter's rotating magnetic field, it was hypothesised that there would be an electrical current linking Io to Jupiter's ionosphere (Piddington and Drake,

1968), which was detected by Voyager 1 during its flyby of Io (Acuña et al., 1981). This current would cause electrons to precipitate into Jupiter's ionosphere at the "footprint" of the magnetic field lines that thread Io. It was initially proposed that this interaction occur via a DC current carried by Alfvén waves (Piddington and Drake, 1968; Goldreich and Lynden-Bell, 1969). To close the DC current loop via Alfvén waves, the Alfvén travel time from Io to Jupiter and back needs to be less than the time it takes Io to fully cross a given magnetic field line. Since Jupiter's magnetosphere was initially presumed to be composed of tenuous, low-density plasma (Thomas et al., 2004), it would have an Alfvén speed essentially equal to the speed of light, which would allow this DC current loop to close. However, this model ran into difficulties upon the discovery of the dense Io plasma torus (Bagenal and Sullivan, 1981). This structure, the higher density of which slows down the propagation of Alfvén waves, increases the two-way Alfvén travel time between Io and Jupiter to such an extent that Alfvén waves no longer have the time to bounce back to Io from Jupiter before Io has left their field line. This makes it impossible to close a DC circuit. In light of this, an alternative (and more promising) theory was developed, that of the "Alfvén wing" (Drell et al., 1965; Neubauer, 1980), which is discussed further below.

The first direct observation of this auroral footprint was made in the infrared aurora (Connerney et al., 1993) and later followed by the UV aurora (Prangé et al., 1996; Clarke et al., 1996). The installation of the STIS instrument on board HST allowed for the imaging of fainter auroral structures, which permitted the first images of the footprints of Europa and Ganymede (Clarke et al., 2002). Detection of the Callisto footprint is made more difficult by the comparative weakness of its

interaction with the surrounding plasma (Hess and Delamere, 2012) as well as the overlap between its expected location and the far-brighter main emission (Clarke et al., 2004a). Nevertheless, attempts were made to identify the Callisto footprint in HST-STIS images of the aurora (Bhattacharyya et al., 2018). This work provided a two cases in which an auroral feature with a position broadly consistent with the expected Callisto footprint was identified, without necessarily observing the expected dynamic behaviour of a footprint. A far more convincing detection of the Callisto footprint was made during Juno's 22$^{\text{nd}}$ orbit (Rabia et al., 2025), in which a series of auroral spots were identified that were located in the expected location (by comparison with the precise locations of the other three observed moon footprints; Hue et al. 2023) and, importantly, showed subcorotation rates consistent with that of Callisto. In-situ measurements by Juno during the crossing of the Callisto flux tube showed electron properties comparable with those of the other moon footprints, hinting toward the universality of the moon-footprint source process.

As mentioned above, the prevailing model for the production of the Io footprint is that of the Alfvén wing (Neubauer, 1980, 1998). Unlike the DC current model, in which a current loop is maintained by Alfvén waves propagating along a field line between Io and Jupiter, the Alfvén wings consist of the combination of many Alfvén waves (an Alfvén wave packet; Hess et al. 2013) propagating along many field lines (as illustrated in Figure 2.14), induced since Io acts as an obstacle to the incoming plasma flow of the corotating magnetosphere. These Alfvén waves then propagate away from Io at the Alfvén speed. When these Alfvén waves approach Jupiter, they are forced towards kinetic (electron-inertial-length) wavelengths,

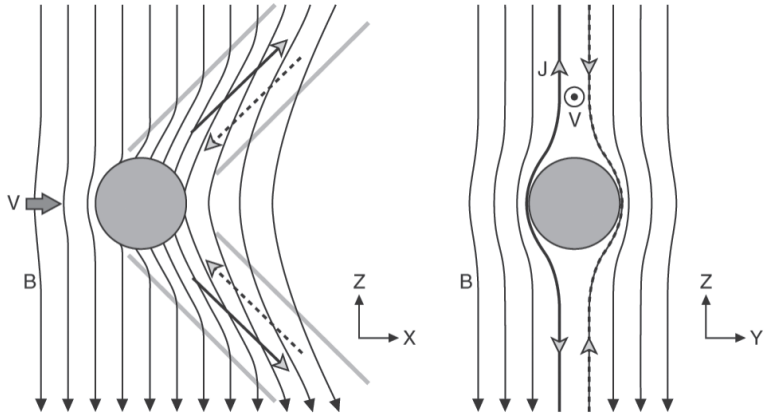

Figure 2.14: A schematic view of the Alfvén wing produced by the interaction between Io and the plasma of the magnetosphere. "V" denotes the velocity of the plasma flow and "J" the induced current density. The perturbed magnetic-field geometry is indicated by the solid black lines. The propagation of Alfvén waves across multiple field lines is denoted by solid and dashed grey-capped arrows. Taken from Kivelson et al. (2004).

which induces a parallel electric field to accelerate electrons onto Jupiter's ionosphere and hence create the auroral footprint (Lysak and Song, 2003; Swift, 2007). This Alfvén-wing interaction between Io and Jupiter has been observed by Juno during its flybys of the moon (e.g. Sulaiman et al., 2023, 2024). Similar Alfvén wings have been observed for Europa (e.g. Huybrighs et al., 2023; Allegrini et al., 2020) and Ganymede (e.g. Hue et al., 2022; Szalay et al., 2020).

By itself, a monodirectional Alfvén-wing model would imply a relatively simple structure for the moon footprints: a

single patch of auroral emission at the point that the Alfvén wing intersects Jupiter's ionosphere. However, the presence of reflection at the boundaries of the plasma torus and Jupiter's ionosphere lead to a more complex multi-dot structure for the moon footprints (Bonfond et al., 2008), the brightness of which is modulated by the System-III longitude of Io within the torus (Moirano et al., 2023). The brightest spot is that associated with the unreflected Alfvén wing and is thus called the Main-Alfvén-Wing (MAW) spot. If the moon footprints were governed entirely by the reflection of the Alfvén wing, the MAW spot would also be the first spot in the sequence. However, depending on the System-III longitude of the moon, the MAW spot may be preceding by a dimmer spot. This spot is caused by beams of electrons that are generated at the MAW spot in one hemisphere and travel along a magnetic field line to the other hemisphere and give rise to a secondary footprint spot, the so-called Transhemispheric Electron Beam (TEB) spot (Bonfond et al., 2008). Since Io does not orbit in the same plane as the plasma torus, these electron beams and Alfvén wings traverse different total columns of the plasma torus, with minima around System-III longitudes of 20° or 200°(Connerney et al., 1998). When the moon is located at these minima, we would expect the TEB spot to precede the MAW spot which has been observed robustly for Io (e.g. Bonfond et al., 2008, 2009), convincingly for Ganymede (Bonfond et al., 2013a; Hue et al., 2022), and tentatively for Europa (Allegrini et al., 2020; Rabia et al., 2023). The fact that all three (robustly confirmed) UV moon footprints display this behaviour (alongside other properties such as positive correlation between surface field strength and footprint brightness; Bonfond et al. 2017b) indicates that the Alfvén-wing mechanism is universal across

the interactions between Jupiter and its moons. The moon footprints are also unique in the sense that they have a precisely known origin in the magnetosphere. If the position of the moon is known at the time that a particular auroral image was taken, then it is possible to combine the position of the moon with a magnetic-field model (and potentially knowledge of the expected footprint lead angle; Bonfond et al. 2009; Hue et al. 2023) to compare the expected and true position of the moon footprint in the aurora; the difference between these two positions may sometimes contain useful scientific information. This technique has previously been used to attempt to disentangle the effects of variable magnetic topology and variable plasma distributions in the magnetosphere on the observed size of the main emission (Vogt et al., 2022b; Moirano et al., 2024) and is used to similar ends in chapter 5.

Chapter 3

Instrumentation and methods

I'll try spinning. That's a good trick.

Anakin Skywalker, *Star Wars Episode I: The Phantom Menace*

This work made use of image and in-situ data from the Juno spacecraft, Hubble Space Telescope, and the ground-based TRAPPIST telescopes located in Chile and Morocco. This section gives an overview of their technical details and how they are used in this thesis, as well as a general description of the data-analysis methods employed in this work.

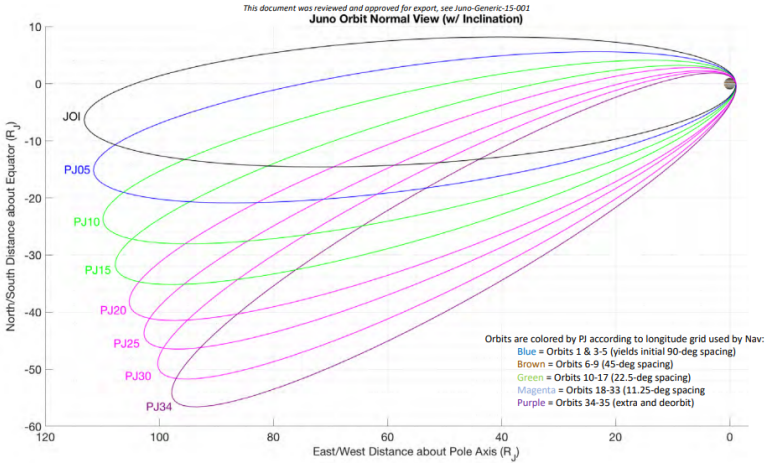

Figure 3.1: The evolution of Juno's orbit from the Jupiter Orbital Insertion (JOI) to PJ34, viewed from the side, showing the latitude precession. Jovian north is up. Taken from `https://lasp.colorado.edu/mop/files/2018/06/Orbit_Geometry_Graphics_MJB_180302.pdf` with credit to M. Brennan and S. Stephens.

3.1 Instrumentation

3.1.1 Juno

The Juno spacecraft is a spin-stabilised spacecraft currently in orbit around Jupiter, launched from Cape Canaveral in 2011 and which arrived at Jupiter in July 2016. It is, at time of writing, still operational and completed its 80^{th} orbit on the 23^{rd} January 2026. Juno is in a highly elliptical polar orbit around Jupiter. During an orbit, Juno passes over the northern aurora

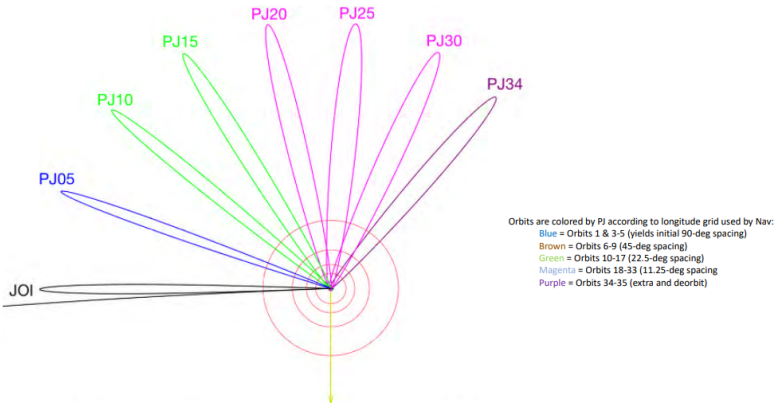

Figure 3.2: The evolution of Juno's orbit from the Jupiter Orbital Insertion (JOI) to PJ34, viewed from above Jupiter's north pole, showing the local-time precession. The direction to the Sun is given by a yellow arrow. Taken from `https://lasp.colorado.edu/mop/files/2018/06/Orbit_Geometry_Graphics_MJB_180302.pdf` with credit to M. Brennan and S. Stephens.

to perform its closest approach to the planet (a "perijove" or PJ; approximate altitude 3500 km; Cowley et al. 2017), before passing over the southern aurora and back out to apojove ($\sim$110 R_J; Cowley et al. 2017). Passes over the aurora occur at an altitude of $\sim$1 R_J. Strictly speaking, the term "perijove" (analogous to the similar terms "perigee" for the Earth and "perihelion" for the Sun) refers to the point of closest approach to Jupiter during and orbit. However, in this thesis and generally in the literature, each of Juno's passes from the northern to the southern aurora is referred to as a "perijove", compris-

ing approximately four hours before and after the true perijove time. This polar orbit allows Juno to sample many different regions of Jupiter and its space environment. It passes over Jupiter's polar auroral regions, through its equatorial plasma sheet, and out through the magnetopause. Juno has also performed a limited number of flybys of Io (e.g. Paranicas et al., 2024), Europa (e.g. Kurth et al., 2023), and Ganymede (e.g. Hansen et al., 2022). Juno's orbit has evolved throughout its mission such that its perijove, originally located essentially in Jupiter's equatorial plane, has migrated toward the northern and dawn-side hemisphere, as shown in Figures 3.1 and 3.2; Juno's orbit has continued to evolve in a similar fashion beyond PJ34, including several reductions in orbital period as a result of its flybys of Io, Europa, and Ganymede. This means that, toward later stages of its mission, Juno passes over the northern hemisphere at lower altitude and greater velocity, and over the southern hemisphere at higher altitude and lower velocity. As a consequence, observations of Jupiter's northern aurora become of higher resolution but "patchier" (since Juno has less time to collect data) toward later perijoves, and the southern aurora is observed with decreasing spatial resolution. The perijove has also migrated from the dusk-side magnetosphere through night toward the dawn, which has allowed to us to sample different local-time regions of the magnetosphere. Juno is a spin-stabilised spacecraft that completes a rotation every 30 seconds. Power is provided by three solar panels, the largest in operation on any space probe. It is equipped with a number of instruments, including for both in-situ (waves, particles, fields) and remote-sensing (infrared, UV, visible) data collection. A list of these instruments is given in Table 3.1. Of the Juno instruments listed in Table 3.1, this work makes use of the Ultra-

Violet Spectrograph (UVS), FluxGate Magnetometer (FGM or MAG; "MAG" refers to full magnetometer setup including the Advanced Stellar Compass), the Jovian Energetic particle Detector Instrument (JEDI; the "p" in "particle" is mysteriously not capitalised, which I can only assume to be an unintended oversight), and the Radio and Plasma Wave Sensor (Waves, or occasionally WAVES, despite not being an acronym).

Table 3.1: Instruments on board Juno.

Instr.	PI	Description
MWR	M. Janssen	Microwave radiometer; used to measure the abundance of water and ammonia in Jupiter's deep atmosphere.
JIRAM	A. Adriani	Infrared spectrometer; used to map the distribution of H_3^+ in Jupiter's auroral regions.
MAG	J. Connerney	Magnetometer; used to map Jupiter's magnetic field.
GS	J. Anderson	Gravity measurement via radio waves; used to map the distribution of mass inside Jupiter.
JADE	D. McComas	Particle detector; measures the energy and direction of low-energy electrons and ions.

continued...

Table 3.1: Instruments on board Juno.

Instr.	PI	Description
JEDI	B. Mauk	Particle detector; measures the energy and direction of high-energy electrons and ions.
JCM	M. Malin	Visible-wavelength camera; used for outreach and to study the dynamics of Jupiter's clouds.
Waves	W. Kurth	Radio- and plasma-wave detector; used to investigate fields and particles in Jupiter's magnetosphere.
UVS	G. R. Gladstone	Ultraviolet spectrograph; used to image Jupiter's ultraviolet aurora.

"Instr." gives the commonly used instrument acronym. "PI" gives the Principal Investigator of the instrument. "Description" gives a (non-exhaustive) description of the functionality and purpose of the instrument.

UltraViolet Spectrograph (UVS)

Juno possesses an imaging spectrograph, the UltraViolet Spectrograph (UVS), which operates in the 68-210 nm range (Gladstone et al., 2017); a schematic of the instrument is given in Figure 3.3. The slit of the instrument is typically pointed per-

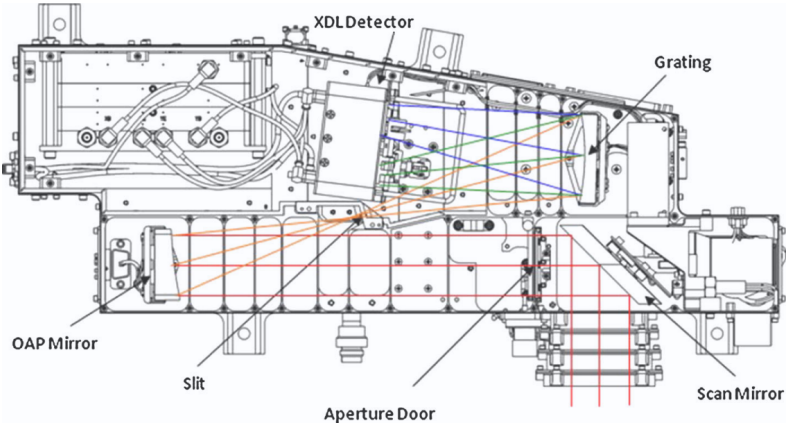

Figure 3.3: A schematic of the UVS instrument, with the path of light rays from the entrance to the detector denoted in colour. Taken from Gladstone et al. (2017).

pendicularly from the axis of rotation of the spacecraft, which allows UVS to "sweep" the aurora every 30 seconds. The exact orientation of this slit can be varied by ±30° by way of the scan mirror installed at the entrance of the instrument. The "slit" is also not simply a single slit; instead, it has a "dog-bone" shape, in which a thin (0.025°) slit is bookended by two perpendicularly orientated wider slits (0.2°). The detector encodes photon-detection events in both the X (spectral) and Y (spatial) direction, which, when the spin of the spacecraft is included, allows 3D (2 spatial dimensions + 1 spectral dimension) auroral data to be obtained. Further technical details are contained within Gladstone et al. (2017). One spin (UVS scan), especially at low altitude during a perijove, typically only corresponds to a very limited area of the aurora; to create

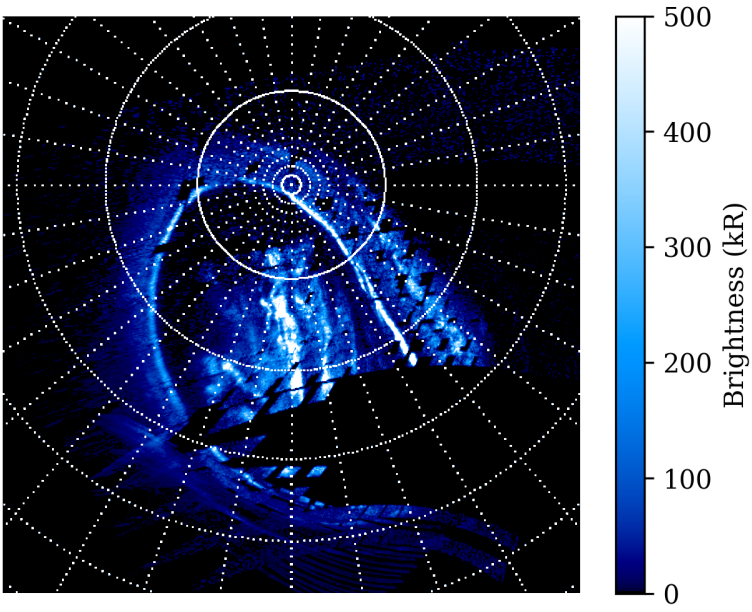

Figure 3.4: An example Juno-UVS image of the northern UV jovian aurorae from PJ23. Gridlines are spaced by 10°.

representative maps of the aurora, data from several spins can be collaged, as per e.g. Bonfond et al. (2017a). Including data from more spins allows a more global view of the aurora to be built up, though, since these data are not collected at the same time, this process can introduce non-synchronicity artefacts (e.g. Greathouse et al., 2021); this has been noted where relevant in this work. An example composite image from Juno-UVS is given in Figure 3.4, where a case with incomplete coverage has been selected to highlighted the contribution of individual

Juno spins to the full image. In this work, only the photons in the non-absorbed band (145-165 nm; e.g. Groulard et al. 2024) are considered, rather than the more-typical 155-162 nm band, due to its wider spectral range and correspondingly better signal-to-noise ratio, since a lot of the work contained in this thesis focuses on auroral morphology rather than absolute brightness values. Additionally, radiation noise from impacting relativistic electrons is subtracted as per Bonfond et al. (2021), made possible since electrons are not diffracted by the UVS grating and hence produce a quasi-uniform "illumination" of the detector which makes their influence easy to differentiate from that of UV photons. Photon count rates can be converted to brightness in kilo-Rayleigh (kR; 1 Rayleigh = $1/4\pi$ 10^{10} photons s^{-1} m^{-2} sr^{-1}) within the non-absorbed band as per Hue et al. (2019b) and further extrapolated to the brightness over the entire unabsorbed Lyman and Werner bands by multiplying by the empirical factor 4.4 (Groulard et al., 2024), calculated from a synthetic spectrum of H_2 (Gustin et al., 2013; Hue et al., 2019a), as simply taking the measured brightness in the full UV band would underestimate the total emitted brightness due to the absorption of a portion of the photons by hydrocarbons. The uncertainty in this brightness is mainly determined by the goodness of the in-flight calibration of the instrument effective area (Hue et al., 2019b); shot noise is considered to be negligible (Gérard et al., 2019). As for HST data (below), these UVS scans are projected onto the ellipsoid of Jupiter assuming an auroral altitude of 400 km above the one-bar level. Naturally, this is a necessary simplification, as auroral emission occurs over a range of altitudes and peaks at approximately 400 km (Benmahi et al., 2024b). However, since Juno's pointing is known to a far more reliable degree than

that of HST (due to Juno's more accurate star catalogue), no limb fitting is required, and the reported spacecraft orientation is sufficient to accurately map UVS pixels onto the globe of Jupiter.

Besides the auroral brightness, spectra from Juno-UVS can be leveraged to map the "colour ratio", which proxies the absorption of H_2 emissions by a particular hydrocarbon (such as CH_4) in Jupiter's atmosphere and can thus be used to investigate the electron penetration depth. This is done by taking the ratio of the emission intensity I in a weakly absorbed spectral band (such as 155-162 nm) and a strongly absorbed band (such as 123-130 nm, or 125-130 nm to avoid contamination from the instrument-broadened Lyman-α line; Gérard et al. 2019) and, as such, the CH_4 colour ratio CR_{CH_4} was historically defined as

$$CR_{CH_4} = \frac{I[155 - 162\ \text{nm}]}{I[125 - 130\ \text{nm}]}. \tag{3.1}$$

However, due to known calibration issues in Juno-UVS, this work instead takes the modified colour ratio from Vinesse et al. (2026),

$$CR_{CH_4} = \frac{I[155 - 162\ \text{nm}]}{I[135 - 140\ \text{nm}]}. \tag{3.2}$$

In any case, the colour ratio can be used as a proxy for electron penetration depth and hence the mean electron energy. CH_4 is essentially confined below the homopause (the altitude below which atmospheric constituents are considered to be well-mixed in the atmosphere) and hence can only be reached by high-energy electrons, since energy loss in precipitating electrons occurs gradually with each atmospheric collision and higher-energy electrons can thus sustain more collisions before

reaching energy equilibrium with their surroundings and becoming thermalised. Low-energy electrons produce H_2 auroral emission that is not attenuated by CH_4 absorption and therefore shows a low colour ratio. Higher-energy electrons instead have their emission largely absorbed by CH_4 in the 135-140-nm band, increasing the colour ratio. In this work, it is considered that a colour ratio above 20 represent total absorption of the aurora emission by CH_4. While it may be said qualitatively that a higher colour ratio represents auroral emission stemming from electrons with a higher characteristic energy, the exact conversion between colour ratio and characteristic electron energy is complicated and relies on electron-transport models such as TransPlanet (Lilensten et al., 1989; Benmahi et al., 2024a).

FluxGate Magnetometer (MAG)

Juno's magnetometer setup (MAG) consists of two separate instruments: the actual FluxGate Magnetometer (FGM) plus the Advanced Stellar Compass, which is used to determine the orientation of FGM's sensors (Connerney et al., 2017b). Two of these instrument sets are located on the 4-metre magnetometer boom attached to the end of one of Juno's three solar panels. These magnetometers allow for the measurement of the magnetic field in all three directions and can be configured to operate in a wide variety of dynamical ranges, up to 1.6 $\times 10^6$ nT and all the way down to 1600 nT, where the instrument resolution is 0.05 nT (for the sake of comparison, the magnetic field strength at the orbit of Ganymede is approximately 100 nT; Vogt et al. 2022a). The maximum (intrinsic) sampling rate of MAG is 64 Hz. Since Juno is known to spin

at 0.033 Hz (one spin every 30 seconds), it is possible to filter the spacecraft-induced magnetic field from the "true" environmental field. Further technical details are included in Connerney et al. (2017b). MAG data has been used to produce more-accurate magnetic-field models for Jupiter's intrinsic field (Connerney et al., 2018, 2022) and that of the magnetodisc (Connerney et al., 2020). Besides measuring Jupiter's magnetic field, MAG data can also be used to investigate the behaviour of Alfvén waves in Jupiter's magnetosphere by measuring the perturbations of the magnetic field that they produce (e.g. Gershman et al., 2019; Sulaiman et al., 2022).

Jupiter Energetic particle Detector Instrument (JEDI)

The Jupiter Energetic particle Detector Instrument (JEDI) is an instrument on board Juno that permits the detection of the energy and angle of incident energetic particles (Mauk et al., 2017a). In this work, JEDI is used exclusively to analyse electron fluxes, though it can also be used to investigate ions. JEDI allows the measurement of incident electrons in the 25-1000 keV range, which is a higher energy range than investigated by the similar JADE instrument. JEDI comprises three essentially identical detectors oriented at 90° from one another: the "90°" detector, the "180°" detector, and the "270°" detector, as shown in Figure 3.5. These detectors are composed of six solid-state detectors arranged in a 160° fan and allow for electron spectra in both energy and pitch angle to be produced. The measurements from these three detectors are combined to provide a representative view of the electron flux at Juno, though they do not provide a perfect angular coverage and the most field-aligned electrons are frequently unsampled in JEDI data (e.g.

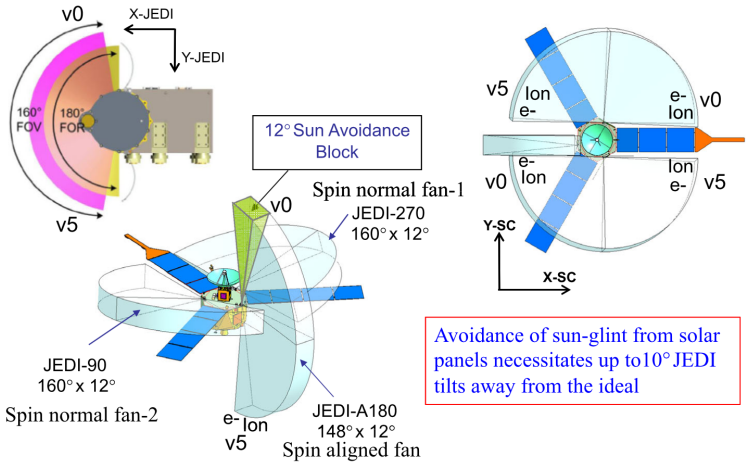

Figure 3.5: A schematic showing the relative orientations of the three JEDI detectors (JEDI-90, JEDI-A180, JEDI-270). Taken from Mauk et al. (2017a).

Mauk et al., 2017c). The intrinsic sampling rate of JEDI is 2 Hz. Technical details of the JEDI instrument are contained within Mauk et al. (2017a). JEDI measurements have been used in a number of studies of Jupiter and its aurora, including the important (and unexpected) discovery of substantial upward electron beams over Jupiter's polar region (Mauk et al., 2017c). Beyond this, JEDI measurements have also shown that the main emission is dominated by broadband electron acceleration (Salveter et al., 2022) and that Ganymede's small magnetosphere can be separated into a number of distinct regions (Clark et al., 2022).

Waves

Waves is a detector on board Juno that aims to investigate radio and plasma waves within Jupiter's magnetosphere (Kurth et al., 2017). It comprises five receivers, four that measure the electric field and one for the magnetic field. The four electric-field receivers each have different operating ranges, allowing Waves to sample the electromagnetic spectrum between 50 Hz and 41 MHz. The instrument itself consists of two antennas in a V-shape configuration (the electric antenna) plus a search-coil magnetic antenna (the magnetic antenna; Hospodarsky 2016), both with a sensitive axis parallel to the spacecraft spin axis to avoid contamination from the periodic effects of Juno's spin. This work exclusively uses data from the LFR-Lo electric receiver, since this receiver has an operating range of 50-20 000 Hz, sufficient to explore the range relevant for electrostatic waves (Sulaiman et al., 2022), which are important in the context of the work presented in chapter 6. Further technical details are contained within Kurth et al. (2017). The Waves investigation has improved our understanding of how plasma waves contribute towards broadband electron acceleration (Kurth et al., 2018) and how they are created by upward electron beams in the polar region (Tetrick et al., 2017).

3.1.2 Hubble Space Telescope

The Hubble Space Telescope (HST) is a 2.4m space-based telescope that was launched in 1990. While the images used in this work were been obtained, it occupied a circular low Earth orbit at an altitude of approximately 540 km with an orbital period of 95.4 minutes, though its altitude has dropped dramatically to 480 km since 2025; barring a reboosting mission

to return it to a safe altitude, HST will likely perform an uncontrolled reentry between 2029 and 2032 (Hubble Reentry Tracker, 2026). It is equipped, at any one time, with a maximum of five instruments, which have been replaced and upgraded several times in the intervening 36 years, allowing it to observe in the visible, near-infrared, and ultraviolet wavebands. HST has contributed to advancing our understanding of the universe in many areas, including, but by no means limited to, confirming the existence of supermassive black holes (Ferrarese et al., 1996), precisely measuring the rate of expansion of the universe (Freedman et al., 2001), and resolving the surface of a star for the first time (Gilliland and Dupree, 1996).

When HST was launched, it was equipped with five instruments: the Faint Object Camera (FOC), Faint Object Spectrograph (FOS), Goddard High-Resolution Spectrograph (GHRS), High-Speed Photometer (HSP), and Wide-Field and Planetary Camera (WFPC). None of these original instruments are still present on board HST. Instead, HST's current (and presumably final) loadout consists of the Cosmic-Origins Spectrograph (COS), Wide-Field Camera 3 (WFC3), Near-Infrared Camera and Multi-Object Spectrograph (NICMOS; hibernating), Advanced Camera for Surveys (ACS), and Space Telescope Imaging Spectrograph (STIS). Images of Jupiter's UV aurora have been taken using FOC (e.g. Gérard et al., 1994), WFPC2 (e.g. Clarke et al., 1998), WFC3 (e.g. Tsubota et al., 2025), ACS (e.g. Radioti et al., 2008), and STIS (e.g. Palmaerts et al., 2024), but only images taken using this latter instrument are considered in this work.

STIS was installed aboard HST in 1997 and operated continuously until a power fault in 2004 rendered it inoperable. This fault was fixed during the STS-125 Space-Shuttle mission

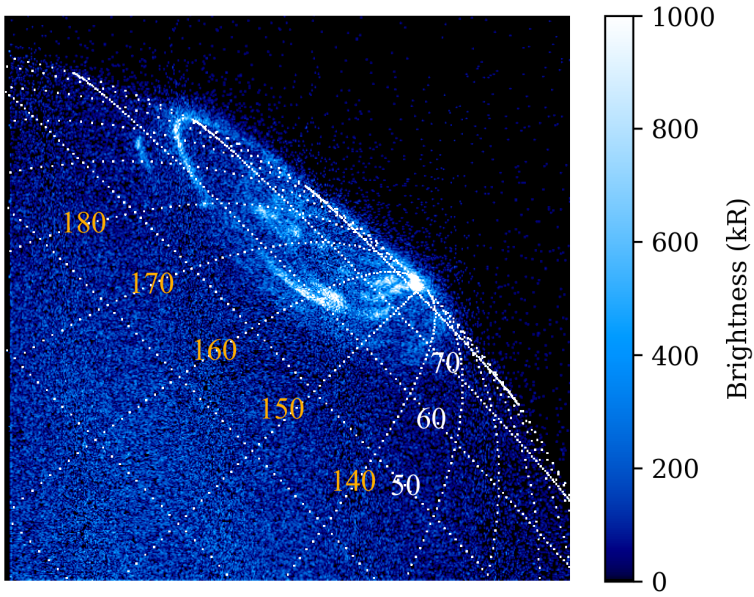

Figure 3.6: An example HST-STIS (30-second exposure) image of the northern UV jovian aurorae taken on 2019-02-09 18:05. Gridlines are spaced by 10°. The System-III longitudes (orange) and latitudes (white) of certain gridlines are noted.

in 2009, and STIS has since captured a large number of images of the jovian UV aurora split into a number of separate observing campaigns. These campaigns are typically denoted by the prefix "GO-" (General Observer) followed by a numeric identifier. A list of the campaigns considered in this work is given in Table 3.2 and the campaigns considered in each section of this thesis are given in the relevant chapters. Each observa-

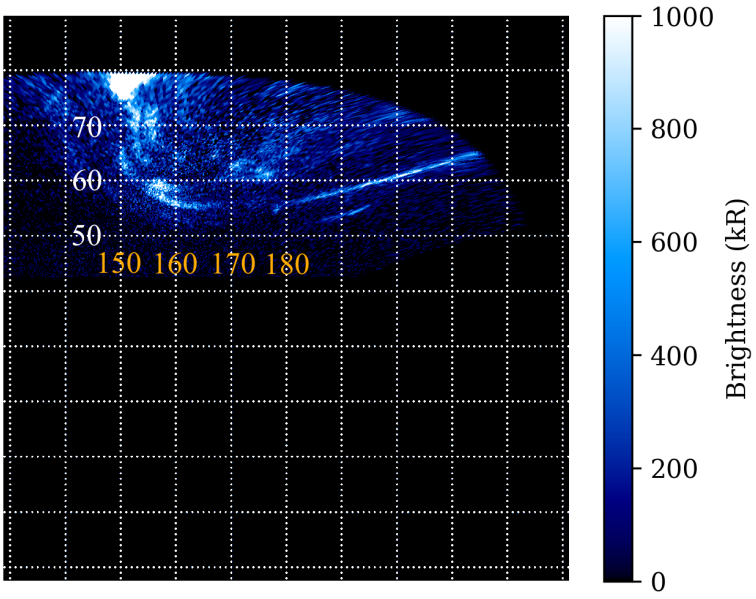

Figure 3.7: An example latitude-longitude map of the same HST-STIS image as in Figure 3.6. Latitude increases toward the northern jovigraphic pole at the top of the map. System-III longitude increases toward the right.

tion, at least in the case of HST-STIS observations of the UV aurora, lasts around 40 minutes, which is the so-called "dark time" that HST spends in Earth's shadow where contamination from geocoronal Lyman-α is minimised (Grodent et al., 2003a). In addition to a traditional CCD detector, in which pixels accumulate charge from impinging photons due to the photoelectric effect, the STIS instrument is equipped with two

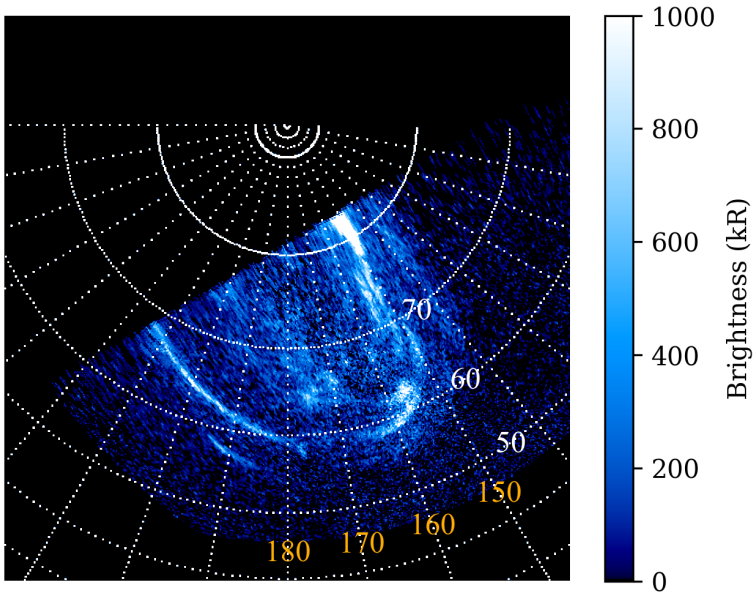

Figure 3.8: An example polar-projected image of the map shown in Figure 3.7.

1024×1024 Multi-Anode Microchannel Array (MAMA) photon counters with a field of view of 24.7"×24.7" and a pixel scale of 0.02437" (Rickman and Brown, 2025). In this detector, impinging photons produce a shower of $\sim 10^5$ electrons that allow individual events to be detected and counted (Timothy, 2016). One of these, the FUV-MAMA, operates in the 115-170 nm band and captures the H_2 Lyman and Werner bands, as well as the strong Lyman-α line of atomic hydrogen. STIS also possesses a Strontium-Fluoride (SrF_2) filter (130-182.5 nm) to

Table 3.2: HST campaigns considered in this work.

ID	PI	Start	End	# (N)	# (S)
11649	J-C. Gérard	2009-08-31	2009-09-11	0	3
12883	D. Grodent	2012-11-14	2014-01-24	9	12
13035	S. Badman	2014-01-01	2014-01-16	42	0
14105	J. Nichols	2016-05-16	2016-07-18	42	6
14634	D. Grodent	2016-11-30	2018-07-15	98	37
15638	D. Grodent	2019-02-09	2019-09-13	42	8
16193	B. Bonfond	2021-07-19	2021-08-17	5	0
16675	J. Nichols	2021-10-16	2023-07-30	10	5

"ID" denotes the HST programme number (GO-). "PI" gives the Principal Investigator of the programme. "Start" and "End" give the start and end dates of the campaign, respectively. "# (N)" gives the number of observations made of the northern aurora, and "# (S)" the number of the southern aurora.

exclude any remaining geocoronal contamination. The MAMA detector can also be operated in two modes: "ACCUM" (accumulative) in which images are produced like a traditional CCD detector; or "TIME-TAG" in which photon events are individually tracked. This latter mode allows images to be reconstructed later with any exposure time that the user desires. Auroral HST campaigns prior to GO-11649 used a mix of the "ACCUM" and "TIME-TAG" operating modes, which led to gaps in the data that complicated their analysis; only campaigns starting at GO-11649, which used exclusively the "TIME-TAG" mode, are considered in this work. Additionally, previous observations made using the ACS instrument are also not considered due to unresolved calibration issues that make them difficult to compare with STIS/Juno-UVS. Full technical

details of the STIS instrument and MAMA detectors are contained within Timothy (2016) and Rickman and Brown (2025). The CalSTIS pipeline (Katsanis and McGrath, 1998) provided by the Space Telescope Science Institute is used to apply the standard dark and flat-field corrections to STIS images, as well as correct for any geometric aberration present. It is also possible to remove planetary background emissions to isolate the UV aurora, as described by (Bonfond et al., 2011). The MAMA detector tracks photons counts (and hence count rates) which can be converted to a more-physical brightness in kR over the entire 70-180 nm band, which combines the H_2 Werner (88-165 nm) and Lyman (90-130 nm) bands (though this definition ignores the contribution from the atomic-hydrogen Lyman-α line.). This is performed using inferred conversion coefficients (Gustin et al., 2012), assuming a typical auroral colour ratio ([155-162 nm]/[123-130 nm]) of 2.5. Once these images are processed, they are also projected to the globe of Jupiter, which allows each pixel to be mapped to a particular latitude and longitude. This is performed using the limb-fitting procedure described by Bonfond et al. (2009), assuming an auroral altitude of 400 km, which provides a compromise between the altitude of the main emission at ∼200 km (Benmahi et al., 2024b) the Io footprint at ∼900 km (Bonfond et al., 2015b). This choice of projection altitude is naturally more impactful for HST observations than Juno-UVS observations, since HST always observes the aurora from the side. Once this fitting is performed, HST-STIS images (an example is given in Figure 3.6) can be transformed per the wishes of the user, such as into latitude-longitude maps (Figure 3.7) or polar-projected views of the aurora (as though observed from above the north pole; Figure 3.8). It is frequently these polar-projected im-

ages that form the base dataset for the work described in this thesis. This is to allow for easy comparison between images, since a given pixel in all images is located at the same latitude/longitude, without distorting auroral morphology like the latitude-longitude maps.

HST-STIS and Juno-UVS have different advantages and limitations that allow them to produce uniquely complementary datasets. As a low-Earth-orbit telescope, HST is limited to viewing the day-side aurora; this can be seen in Figure 3.8, in which the entire night-side half of the aurora is missing. This limitation means that HST images of the northern aurora are typically more complete than those of the southern aurora, since the magnetic-field topology in the north is such that the aurora is shifted from the jovigraphic pole toward $\sim$160° in System-III longitude (by about 10°latitude), which makes it possible to view most of the aurora from Earth if timed correctly, though the exact proportion of the aurora that is visible depends on the jovian season due to Jupiter's orbital obliquity of 3.13°. The primary advantages of HST-STIS over Juno-UVS are its simultaneous coverage of the (day-side) aurora and its ability to capture short-timescale ($\geq$10 s with reasonable signal-to-noise) variation. Unlike HST, Juno-UVS is not typically able to view the entire aurora at once; instead, images are built up from multiple spins worth of data. Since these spins necessarily do not occur at the same time, there is often a trade-off to consider when creating Juno-UVS images, as including enough spins to get full coverage of the aurora may introduce considerable time differences between parts of the image taken from different spins. HST, on the other hand, images the entire aurora at once, making it possible to compare the instantaneous behaviour of different parts of the

aurora without concern about time delays. Time-tag image data, in principle, may be collated into images with arbitrarily short "exposure" times (though the lower limit is typically set at 10 seconds to avoid unreasonably poor signal-to-noise ratios), making HST-STIS ideal for investigating minute-scale variability in the aurora (e.g. Bonfond et al., 2011). HST image series are necessarily limited to approximately 40 minutes, which is the portion of its 96-minute orbit during which the Sun is masked by the Earth. Juno-UVS gathers image data over multiple hours during each perijove, making it more suitable to the study of auroral variability over longer timescales (e.g. Bonfond et al., 2017a).

3.1.3 TRAnsiting Planets and PlanetesImals Small Telescope (TRAPPIST)

The TRAnsiting Planets and PlanetesImals Small Telescope(s), or TRAPPIST, are a pair of telescopes located at the La Silla observatory in Chile (TRAPPIST-South) and the Oukaïmeden observatory in Morocco (TRAPPIST-North), operated by the University of Liège. By complete coincidence, the acronym "TRAPPIST" (formed only from the most important and characteristic letters, such as the "i" in "planetesimals") is also the name of a class of artisanal Belgian beer, a coincidence that you, the reader, are doubtless as surprised to discover as the Belgians who came up with the name originally. Both TRAPPIST telescopes are 60-cm robotic Ritchey-Chrétien telescopes. TRAPPIST-North has a field of view of 20'×20' and a pixel scale of 0.60" px^{-1}, and TRAPPIST-South a field of view of 22'×22' and a pixel scale of 0.64" px^{-1} (Jehin et al., 2011). Both are equipped with a narrow-band Na-I filter (central

wavelength 589 nm, FWHM 3 nm) made by Custom Scientific Inc., which is of particular relevance to the work described in chapter 4. The existence of TRAPPIST telescopes in both the northern and southern hemispheres (and at different longitudes) allows a large portion of the sky to be observed. Full technical details of the TRAPPIST telescopes are contained within Jehin et al. (2011). The TRAPPIST telescopes have been applied to a wide variety of astrophysical fields. TRAPPIST discovered three (Gillon et al., 2016), and later seven (Gillon et al., 2017), planets around the ultra-cool red dwarf TRAPPIST-1, of which four were determined to be in the habitable zone where liquid water may exist (Wilson et al., 2021). TRAPPIST also observed the dwarf planet Eris during a stellar occultation, where its diameter was estimated to be slightly smaller than that of Pluto (Jehin et al., 2010). The first rings around a solar-system small body, 10199-Chariklo, were also discovered using TRAPPIST observations (Braga-Ribas et al., 2014). At time of writing, the work detailed in chapter 4 (De Becker, Head, et al., 2023), represents the only published instance of TRAPPIST being used to observe Io.

3.2 Automatic detection methods

Both HST and Juno have provided, and continue to provide us with, a large amount of image data. Over the last 36 years, HST alone has spent more than 200 hours observing the UV aurorae of Jupiter, and Juno-UVS has acquired (and continues to acquire) approximately 7 hours of image data during each of its closest approaches to Jupiter, though this duration is higher for earlier perijoves and lower for later ones. To

fully exploit this enormous corpus of image data, we require automated image-analysis techniques. While similar advanced image-analysis techniques have been applied to the jovian aurorae, such as for keogram feature analysis (Rutala et al., 2022) or principal-component analysis (Nichols et al., 2019), the work presented in this thesis represents the first application of these automated, advanced methods to a large amount (or, in some cases, essentially all) of the available image data of Jupiter's UV aurora. These methods include arc or feature detection and machine-learning-driven pixel-scale classification of auroral images.

In this work, the advanced image-analysis techniques described below are typically implemented in a bespoke fashion, rather than by applying off-the-shelf implementations. This was done in order to best fine-tune these techniques for their application to images of the jovian aurorae, as well as to better understand their exact workings and ensuring that no unnecessary/detrimental steps were included. While this frequently increased the time necessary to implement these techniques (as well as the time necessary to execute the code), it also made it easier to debug and to modify code to tackle related problems. Where existing code libraries have been used in this work, this has been noted in the text. The vast majority of the code produced over the course of this thesis was written in Python 3, with the occasional foray into IDL when strictly necessary. In some ways, and with no desire to pat (blow) one's own back (trumpet) beyond the strict minimum, this work represents the most advanced and wide-ranging automated analysis of HST/Juno-UVS images of the jovian aurora to date. It is hoped that the advances in our understanding of Jupiter, its magnetosphere, and its aurorae that this thesis has permitted

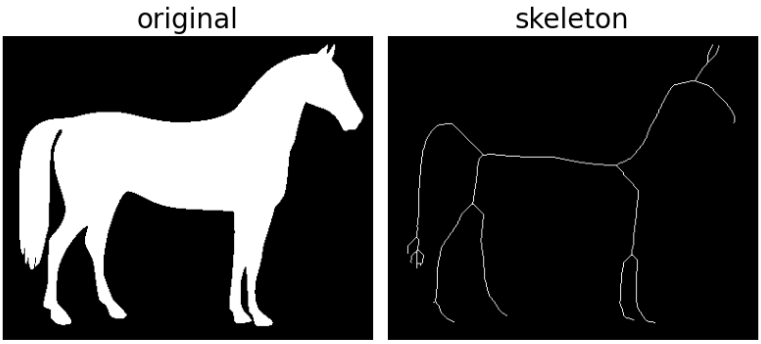

Figure 3.9: Left: an example pixel mask, presumably of a horse. Right: the skeletonised representation of the same pixel mask. Taken from `https://scikit-image.org/docs/0.25.x/auto_examples/edges/plot_skeleton.html`.

may inspire future application of even more advanced image-analysis techniques to an even more wide-ranging selection of data.

3.2.1 Arc detection

Arc detection, used in this thesis in chapters 5 and 6, has previously been widely applied to the terrestrial aurorae, to detect auroral arcs in all-sky images (e.g. Syrjäsuo and Pulkkinen, 1999) and to subsequently track their evolution (e.g. Syrjäsuo and Donovan, 2002), or to classify observed auroral arcs into a number of classes (Wang et al., 2023a). Auroral-arc detection in prior terrestrial work is frequently based on the technique of skeletonisation (Blum, 1967), in which a two-dimensional

region of an image (for example, an auroral arc) is reduced to a set of one-dimensional lines that best represent its structure. These reduced skeletonised representations are frequently less sensitive to noise and easier to analyse than the full two-dimensional arc images (Syrjäsuo and Pulkkinen, 1999). Naturally, many algorithms exist for performing skeletonisation. That used by the `skimage` Python library (and hence also chapter 5 of this thesis) iteratively removes pixels on the edge of a pixel mask under the condition that removing the pixel would not split the mask into two unconnected regions, and repeating this process until no further pixels can be removed. An example of `skimage` skeletonisation is given in Figure 3.9. An alternative method of detecting auroral arcs involves defining a bounding box in the image that contains the arc. However, in the case of auroral arcs on Jupiter, it is occasionally challenging to define a sensible bounding box for arc structures that have no clearly defined edge, whereas skeletonisation (though some thresholding must be performed to obtain a pixel mask) is not as sensitive to the boundaries of the region being considered. Skeletonisation, once applied to auroral images, also allows for the analysis of auroral arcs independently of the brightness, assuming that they are sufficiently bright to be detected in the first place. Dimmer arcs in the jovian aurora, such as polar auroral filaments found in the polar region (Nichols et al., 2009a), are practically invisible against the much-brighter main emission, but may be detected via a properly calibrated skeletonisation algorithm and thus analysed.

An alternative method for detecting auroral arcs is described and used in chapter 6. Unlike the previous technique, which was a custom application of a set of known techniques, this second technique was developed independently for the pur-

pose of detecting bridge arcs in the jovian aurora, starting from a set of reasonable assumptions based on the physics and properties of the bridges. The algorithm developed for the detection of these arcs, described in much more detail in chapter 6, might best be described as a "pathfinding" or "path of least resistance" algorithm. I am unaware of exactly which class of algorithm that of chapter 6 falls under, though doubtless it must fall under one of them. I do not consider this lack of theoretical algorithmic background to be disadvantage. Indeed, the algorithm was developed and designed to help answer a set of specific scientific questions, a quest in which it succeeded, insofar as it led to the publication of a peer-reviewed work (Head et al., 2025). There is a tendency, when novel techniques are developed in one field and applied to another, to put the method front-and-centre and only worry about the science goals of the work afterwards. This can lead to articles in which an exciting new method is applied, sometimes without a full understanding of the limitations and caveats, in which it might be forgotten that algorithms, even novel and sophisticated ones, exist in subservience to the science, and not the other way around. Even in the case of the application of a perfect algorithm to a pristine dataset, you will most likely wish to or be required to provide examples of the results that your algorithm produces. During the process of creating and applying your algorithms to your data, it is therefore a good idea to check individual cases to ensure that your algorithm is working as intended, before you are called upon to prove this in front of your peers. I would caution those interested in applying advanced image-analysis techniques to their own datasets to first carefully consider their science goals, and only then ask themselves where, or even if, novel techniques might

be applied. In chapter 6 and elsewhere, I often found that, while advanced techniques permitted the automatic analysis of often-large datasets, many of the scientific conclusions were drawn using simpler techniques, often involving manual analysis or case studies, themselves guided by the results of the automatic analysis.

3.2.2 Random-forest classification

In chapter 7, random-forest classification is used to refine manual designations of the locations of injection signatures in the UV aurora. Since this study "only" concerned itself with one image per perijove for the first forty perijoves (78 images), approximate locations of injection signatures were designated manually. Here, it was considered more important that the bounding polygon associated with each injection signature contain the entire feature rather than ensuring that its edges follow exactly the borders of the injection signature. To refine these (occasionally very approximate) bounding polygons, a random-forest classifier was trained on the manual designations and used to predict which pixels in the images are associated with injection signatures; this resulted in bounding polygons that much more closely followed the exact bounds of the injection signatures. More detail regarding this specific implementation of random-forest classification is given in chapter 7. Random-forest classification, at least compared to many other machine-learning methods, is relatively intuitive. It is an "ensemble" method, insofar as it combines the predictions of many models (in this case, of many decision trees, hence the "forest") to improve its predictive performance (Rokach, 2010). Each decision tree is created using a subset of the data and its manual

labels. In chapter 7, each pixel of the 1024×1024 images of the aurora (with its brightness, colour ratio, mapped location in the magnetosphere, ...) is a data point and the manual label is simply whether this pixel falls within a manually designated injection-signature bounding polygon. A much-simplified example is given in Figure 3.10 to illustrate how a decision tree

Pixel 0 Brightness: 250 kR Colour ratio: 14 R: 23 RJ Label: Yes	Pixel 1 Brightness: 180 kR Colour ratio: 6 R: 16 RJ Label: Yes	Pixel 2 Brightness: 578 kR Colour ratio: 9 R: 28 RJ Label: Yes
Pixel 3 Brightness: 685 kR Colour ratio: 13 R: 31 RJ Label: Yes	Pixel 4 Brightness: 477 kR Colour ratio: 19 R: 21 RJ Label: No	Pixel 5 Brightness: 404 kR Colour ratio: 9 R: 27 RJ Label: No
Pixel 6 Brightness: 606 kR Colour ratio: 17 R: 28 RJ Label: Yes	Pixel 7 Brightness: 61 kR Colour ratio: 18 R: 10 RJ Label: No	Pixel 8 Brightness: 22 kR Colour ratio: 12 R: 18 RJ Label: No

(a) Example image.

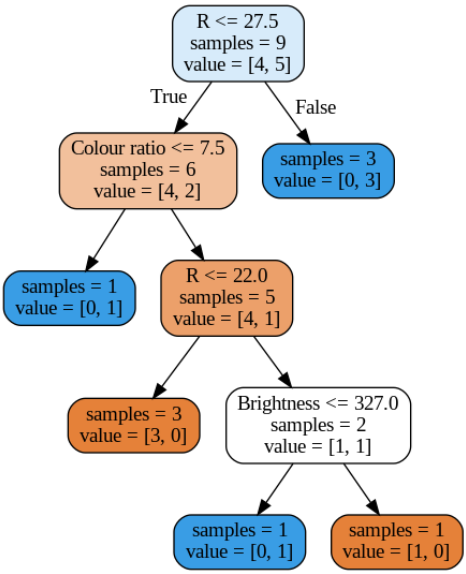

(b) Decision tree.

Figure 3.10: (a) An example "image" of the aurora, with the brightness, colour ratio, and mapped distance in the equatorial plane R labelled. "Label: Yes" (green pixels) are those that have been manually labelled as belonging to injection signatures, and "Label: No" (orange pixels) are those that do not belong to injection signatures. (b) The decision tree that reproduces the manual labels for each pixel. Boxes contain first the condition being tested, the number of data points being tested, and the current number of [No, Yes] manual labels.

of fewer than $N - 1$ splits (which represents the theoretical upper limit) can be used to reproduce a manual labelling of

N data points; the reader is invited to select a pixel of their choosing and follow the decision tree to confirm that it returns the correct labelling. Of course, the dataset used in chapter 7 has many more data points. While it is, in principle, possible to construct a single enormous decision tree that perfectly reproduces the manual labelling, it is often more useful to create a forest of many much-shorter decision trees trained on random subsets of the data that each make a prediction; the final prediction for each data point is simply the majority vote of the decision trees in the random forest (Kamath and Cantú-Paz, 2001). The lengths and number of these trees will depend on how accurately one wishes to reproduce the input labels. It is often disadvantageous to use decision trees of arbitrarily long length to perfectly reproduce the input labels, as this ("overfitting") limits the ability of the forest to make useful predictions for unseen data. It will often be necessary to tinker with the tree depth and count to produce suitable labellings, where the definition of "suitable" will depend on your data and goals. Whereas other machine-learning methods frequently create "black-box" models that are difficult to understand qualitatively, random-forest classification can report the relative importances of each quantity (brightness, colour ratio, ...) to the final classification. This makes random-forest classification especially useful to analyse physical systems, where the relative contribution of each variable may provide some physical insight (though not a full explanation, since the decision trees have an element of randomness). In practice, the `sklearn` package in Python 3 provides easy-to-use implementations of random-forest classification (and many other methods) that make it simple to use machine-learning methods on a wide range of potential datasets.

Chapter 4

Variability of the Io sodium jet

What's that? It's blowing up from the inside.

Unnamed Naboo pilot, *Star Wars Episode I: The Phantom Menace*

Io is the most volcanically active body in the Solar System. This volcanic activity results in the ejection of material into Io's atmosphere, which may then escape from the atmosphere to form various structures in the jovian magnetosphere, including the plasma torus and clouds of neutral particles. The physical processes involved in the escape of particles - for example, how the volcanoes of Io provide material to the plasma torus - are not yet fully understood. In particular, it is not clear to what extent the sodium jet, one of the sodium neutral clouds related to Io, is a proxy of processes that populate the various reservoirs of plasma in Jupiter's magnetosphere. In this study,

I report observations of the neutral sodium clouds carried out by the TRAPPIST telescopes, with particular attention paid to the neutral sodium jets. The purpose of these observations is to characterise the variability of the jets by measuring their size and brightness, as well as understanding the variation in their geometry, in order to improve understanding of Jovian magnetospheric dynamics, particularly of the particle sources from the Io plasma torus. These observations were carried out over 17 nights in 2014-2015, 30 nights in 2021, and 23 nights in 2022-2023, in which particular attention was paid to the sodium jet and the quantification of its physical properties (length, brightness). It was found that these properties can vary greatly from one jet to another and independently of the position of Io in its orbit. No clear link was found between the presence of jets and global brightening of the plasma torus and extended sodium nebula, indicating that jets do not contribute straightforwardly to their population. This work also demonstrates the advantage of regular and long-term monitoring to understanding the variability of the sodium jet and presents a large corpus of jet detections against which work in related fields may compare.

This section on the variability of the Io neutral-sodium jet follows from the work of De Becker, Head, et al. (2023), published by Astronomy and Astrophysics on 2023-09-23, of which I was joint first author. In particular, I was responsible for the development of automated analysis techniques for TRAPPIST images of the Io sodium jet and the interpretation of the results, as well as the larger part of the writing of the manuscript. The most relevant sections of the introduction are sections 2.2 (Io), 2.3 (magnetosphere and magnetic field), and 2.4 (neutral clouds).

Table 4.1: Observations made in 2014-2015.

	Date	Detected	Telescope	Observation time	ϕ_S (°)	ϕ_E (°)	θ_{S3} (°)
1	2014-12-04	Yes	TS	08:17:20 - 08:23:53	-93	-102	143
2	2014-12-06	Yes	TS	06:25:29 - 08:34:44	-53	-62	271
3	2014-12-08	No	TS	06:05:19 - 06:35:13	-16	-25	49
4	2014-12-12	No	TS	07:41:27 - 08:25:15	92	83	212
5	2014-12-19	No	TS	06:51:07 - 07:05:15	66	58	253
6	2014-12-21	Yes	TS	08:11:39 - 08:30:36	125	117	321
7	2015-01-11	Yes	TS	07:40:34 - 08:00:03	72	68	5
8	2015-01-13	No	TS	05:57:56 - 07:25:27	109	106	142
9	2015-01-20	No	TS	07:43:08 - 08:00:41	103	100	121
10	2015-01-23	No	TS	07:46:51 - 08:09:28	-6	-8	278
11	2015-01-28	Yes	TS	07:22:02 - 07:45:40	-72	-72	194
12	2015-02-01	No	TS	05:55:08 - 06:30:16	10	10	83
13	2015-02-12	Yes	TS	02:00:10 - 02:19:50	53	55	57
14	2015-03-29	Yes	TS	03:49:33 - 04:10:26	-137	-128	232
15	2015-03-30	Yes	TS	03:36:23 - 04:10:04	65	74	287
16	2015-03-31	Yes	TS	03:55:21 - 04:10:16	-90	-80	336
17	2015-04-01	Yes	TS	00:02:22 - 00:30:21	81	91	132

The "Detected" column indicates whether the presence of a jet-like structure was identified on this date. "TS" refers to the telescope used for the observation, TRAPPIST-South (IAU code I40). The "Observation time" column gives the observation period in UTC. ϕ_S is the average orbital angle of Io in images taken on this date, with 0° placing Io behind Jupiter with respect to the Sun, with positive orbital angles moving Io in an anti-clockwise direction. ϕ_E is the average Earth-Jupiter-Io angle. θ_{S3} is the average magnetic longitude of Io in System-III.

4.1 Observations

Observations with TRAPPIST-South were made over seventeen nights between 2014-12-04 and 2015-04-01. These observations were intended as test observations and thus there was no specific restriction on the period of observation; as a consequence, in some of these observations, Io was not in an ideal configuration to detect jet-like structures in the neutral sodium cloud. These images have undergone preliminary analysis in previous work (de Spiegeleire, 2019) upon which this work has developed using new methods created for later observations of

Table 4.2: Observations made in 2021.

	Date	Detected	Telescope	Observation time	ϕ_S (°)	ϕ_E (°)	θ_{S3} (°)
1	2021-04-28	No	TS	09:31:03 - 09:42:34	87	76	20
2	2021-04-29	No	TS	10:01:57 - 10:09:48	-66	-77	59
3	2021-05-14	Yes	TS	10:10:55 - 10:20:09	107	96	128
4	2021-05-15	No	TS	10:08:02 - 10:17:16	-50	-62	182
5	2021-05-22	No	TS	10:16:22 - 10:26:04	-65	-77	188
6	2021-05-29	No	TS	10:17:49 - 10:32:40	-81	-92	198
7	2021-05-30	No	TS	10:16:56 - 10:30:28	123	112	252
8	2021-05-31	No	TS	10:16:50 - 10:30:11	-35	-46	303
9	2021-06-05	No	TS	10:17:47 - 10:28:14	-97	-108	208
10	2021-06-06	Yes	TS	10:14:17 - 10:30:01	107	96	261
11	2021-06-07	Yes	TS	10:06:06 - 10:15:09	-53	-63	319
12	2021-06-12	No	TS	10:21:27 - 10:33:36	-113	-123	216
13	2021-06-13	No	TS	10:24:19 - 10:34:46	91	81	268
14	2021-06-20	No	TS	10:31:20 - 10:39:59	76	66	276
15	2021-06-23	No	TN	04:05:47 - 04:11:27	-89	-98	253
16	2021-06-24	Yes	TN	04:03:32 - 04:07:49	115	105	308
17	2021-06-28	Yes	TS	10:11:22 - 10:24:24	-100	-109	347
18	2021-06-30	No	TS	10:08:01 - 10:17:29	-103	-111	255
19	2021-06-30	No	TN	04:23:36 - 04:28:06	-54	-63	95
20	2021-07-01	No	TN	04:23:24 - 04:30:15	101	93	309
21	2021-07-02	Yes	TN	04:33:27 - 04:42:43	-55	-63	356
22	2021-07-04	No	TS	10:16:12 - 10:25:24	41	33	303
23	2021-07-08	No	TS	09:02:04 - 09:12:09	125	117	190
24	2021-07-15	No	TS	10:11:26 - 10:20:57	118	112	168
25	2021-07-16	No	TN	04:02:13 - 04:23:28	-91	-97	29
26	2021-07-23	Yes	TS	10:01:25 - 10:11:18	-57	-61	235
27	2021-09-26	No	TS	23:32:13 - 23:42:05	-41	-32	62
28	2021-10-01	No	TS	23:46:43 - 23:56:42	-102	-93	320
29	2021-10-02	No	TS	23:36:32 - 23:42:48	100	110	19
30	2021-10-03	No	TS	23:36:30 - 23:45:28	-57	-47	71
31	2021-10-10	No	TS	00:00:11 - 00:19:47	89	99	16

Column titles are identical to those of Table 4.1. "TN" refers to the TRAPPIST-North telescope (IAU code Z53).

Io. New observations began in April 2021 with TRAPPIST-South and in June 2021 with TRAPPIST-North. For these

Table 4.3: Observations made in 2022-2023.

	Date	Detected	Telescope	Observation time	ϕ_S (°)	ϕ_E (°)	θ_{S3} (°)
1	2022-05-26	Yes	TS	09:13:37 - 09:52:37	102	92	312
2	2022-06-19	No	TS	09:43:36 - 10:10:06	-52	-64	130
3	2022-07-03	Yes	TS	10:02:30 - 10:37:21	-82	-94	141
4	2022-08-19	Yes	TS	10:02:01 - 10:19:27	117	110	111
5	2022-08-20	No	TS	08:27:26 - 08:38:49	-54	-60	207
6	2022-09-03	Yes	TS	09:21:35 - 09:44:56	-78	-82	201
7	2022-09-04	No	TS	05:02:55 - 09:20:00	124	120	263
8	2022-09-05	Yes	TS	04:47:51 - 05:14:55	-71	-74	77
9	2022-09-14	No	TN	02:20:08 - 02:30:52	-61	-63	262
10	2022-09-27	No	TS	02:01:57 - 02:20:55	62	63	238
11	2022-11-23	Yes	TN	18:32:20 - 18:45:06	-86	-75	280
12	2022-11-27	Yes	TS	02:16:25 - 02:35:33	-130	-119	222
13	2022-11-27	No	TN	23:33:10 - 23:45:12	51	62	353
14	2022-11-29	No	TN	20:11:30 - 20:23:30	70	81	193
15	2022-12-21	No	TN	21:03:02 - 21:14:29	-129	-118	254
16	2022-12-22	No	TN	18:47:04 - 18:59:19	56	67	11
17	2022-12-23	No	TN	18:47:11 - 18:59:26	-102	-90	63
18	2022-12-24	No	TN	19:02:15 - 19:14:19	104	116	110
19	2023-01-06	No	TS	00:56:58 - 01:19:57	76	87	219
20	2023-01-07	No	TN	18:52:27 - 19:04:25	71	82	137
21	2023-01-14	No	TN	19:05:44 - 19:17:37	56	67	142
22	2023-01-15	No	TN	19:01:52 - 19:14:06	-101	-91	196
23	2023-01-16	No	TN	18:52:15 - 19:04:39	101	111	254

Column titles are identical to those of Tables 4.1 and 4.2.

observations, the periods of observation were chosen to ensure that Io was far from Jupiter in the observation plane and thus minimally affected by the light reflected from the planet. These observations were performed over 30 nights. Typically, a sequence of five image exposures followed by five bias and five dark exposures (to remove artefacts on the CCD chip from the heavy image saturation) were made with exposure times of 5, 15, and 60 seconds. Flat-field exposures with the sodium filter were taken at the end of each night that an observation of Io

was made, in a series of seven dithered frames on the bright sky of the nautical twilight.

An overview of the observations from 2014-2015 is given in Table 4.1, and observations from the 2021 and 2022-2023 viewing campaigns are listed in Tables 4.2 and 4.3 respectively.

4.2 Image processing

To allow for physical comparison of the brightness of the structures detected in these images, it is necessary to convert the image units from Analogue-to-Digital Unit (ADU) to rayleigh, which can be performed with the aid of standard stars. For example, for the 2014-2015 viewing campaign, the standard star HD72526, with a magnitude of 7.92, was measured to have a mean flux per second of 17678.6 ADU s^{-1}, while using the same instrumental setting as for our observations of Io. It is known that a magnitude-0 star has a spectral flux of 2.75×10^{-9} erg s^{-1} cm^{-2} $Å^{-1}$, and hence, using the FWHM of the sodium filter (33 Å), a flux of 9.08×10^{-8} erg s^{-1} cm^{-2}. HD72526, a magnitude-8 star, has therefore a flux of 5.73×10^{-11} erg s^{-1} cm^{-2}. Hence, a single ADU is equivalent to 3.24×10^{-15} erg s^{-1} cm^{-2} above the atmosphere. To account for the scattering of target photons by the atmosphere of the Earth, it is necessary to modify the expression to include the airmass X, becoming 1 ADU $= 3.24\times10^{-15}$ erg s^{-1} $cm^{-2}\cdot10^{0.13X}$. By definition, one rayleigh R is equivalent to $\frac{10^6}{4\pi}$ photons s^{-1} cm^{-2} Sr^{-1}. For a photon wavelength of 5890 Å, this is equivalent to 6.31×10^{-18} erg s^{-1} cm^{-2} $arcsec^{-1}$. Combining these two results leads to the expression

$$1 \text{ ADU} = 5.12 \cdot 10^{2+0.13X} \text{ R}, \tag{4.1}$$

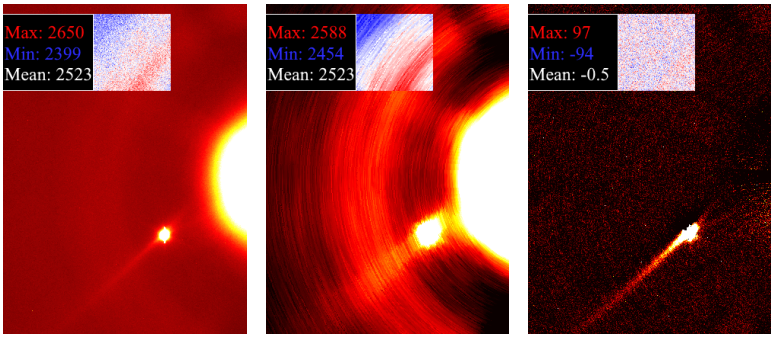

(a) Raw image.

(b) Extrapolated image background near Io.

(c) Image with background near Io removed.

Figure 4.1: The results of the background-removal process on a raw image of Io and Jupiter from 2014-12-04. Note that the apparent size of Io is augmented in the images by the overdensity of sodium near the moon. In all images, a square region absent of any bodies has been highlighted to show the effect of the background-removal process on the background pattern. The minimum, maximum, and mean pixel values for this square region have been annotated to one side.

which allows for the conversion of raw images in ADU to Rayleigh R.

The TRAPPIST telescopes were developed for the imaging of small solar-system bodies (such as asteroids or comets) and for exoplanet detection via the transit method. The use of these telescopes to instead detect the neutral sodium cloud around the relatively bright objects present in the jovian system therefore necessitates additional preprocessing. After im-

age reduction using the dark, bias, and flat frames, there remains a background pattern centred on Jupiter due to the telescope optics, predominantly an internal reflection of light from Jupiter which reveals the shadow of the telescope spider and secondary mirror (see Figure 4.1). Once this background has been removed, further preprocessing is required to facilitate the automatic detection of radial structures in the neutral sodium cloud.

To remove the azimuthal background pattern around Jupiter, a region of the image centred on Io is extracted. Since it is observed that the background pattern is approximately azimuthally symmetric about the centre of Jupiter, the image is then projected to an angle-radius projection centred on Jupiter. Gaps in the projected image are linearly interpolated along the azimuthal dimension. To remove it from the cropped image, it is noted that Io is spatially limited and azimuthally asymmetric about the centre of Jupiter, and hence a 10° median filter is applied to the image row at each pixel radius. It was noted a posteriori that the widths of the radial structures identified in this work were not comparable with the spatial extent of Io and the vertical saturation pattern, and so a median filtering with a window width chosen to remove Io from the image is unlikely to affect the strength of the signal from the radial structures. This filtered image is then re-projected into the original image space, with the presence of Io significantly diminished and the azimuthal background pattern still present. The results of this background-removal process are illustrated in Figure 4.1b and 4.1c.

To ensure that it operates as intended, the background-removal process was also applied to a region of an image taken on 2014-12-04 without any bright features, as shown in Figure

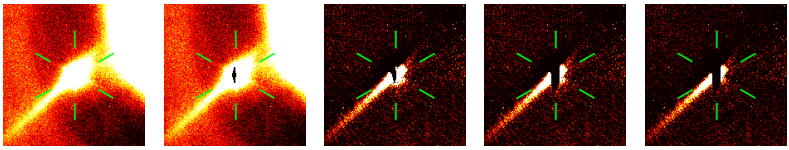

(a) (b) (c) (d) (e)

Figure 4.2: Preprocessing steps applied to an image taken on 2014-12-04, cropped around Io. The position of the six-pronged diffraction pattern is denoted by six green lines to aid the eye. It can be seen that the jet becomes more prominent with each step. Panel a: Raw image. Panel b: Comparison with the other moons. Panel c: Removal of the background. Panel d: Removal of the vertical saturation pattern. Panel e: Reduction of 60° rotational symmetry.

4.1. The azimuthal pattern present before the removal of the background was greatly diminished and the mean pixel value reduced to approximately zero ADU, which supports the use of this method to remove the azimuthally symmetric background pattern.

Once the image background close to Io has been removed, it is possible to compare the shape of the other moons present in the image with that of Io, to diminish other image artefacts originating from the telescope. This is performed by cropping the other moons from the image using the same pixel bound as before, normalising and inverting the cropped image, and then multiplying the cropped image of Io by the inverted images of the other moons. Pixels that are bright in the image of Io but dim in the images of the other moons (i.e. sodium-cloud structures) are left unchanged, whereas pixels that are bright

in both the image of Io and the images of the other moons (e.g. the diffraction pattern, image artefacts) are diminished. The results of this processing step (as well as the steps detailed below) are given in Figure 4.2.

The images taken on a particular night undergo the processing described above and are then stacked to increase the signal-to-noise ratio of any structures present. To aid the automated detection algorithm in finding true radial structures in the image data, it becomes necessary to remove or reduce the prominence of both the vertical saturation pattern (most visible in Figure 4.1a as a protrusion from the top and bottom of Io) and the six-pronged telescope diffraction pattern (the 'spiderweb'). Additionally, comparing the shape of the image of Io with the other Galilean moons will remove image artefacts that could be erroneously identified as jets. Indeed, no other features that could be interpreted as jets were seen near the other Galilean moons over the course of this work.

To remove the vertical saturation pattern from the image of Io, a suitable pixel bound was identified by taking half of the apparent pixel distance (or a quarter in the case of the far-brighter Jupiter) between Io and the other bodies present in the image, to avoid contamination. Io was then centred in the image and cropped out using this bound. To remove the vertical saturation pattern without diminishing the presence of radial structures in the neutral sodium cloud, it is necessary to remove features with 180° rotational symmetry and vertical reflectional symmetry. By summing the three images (original, 180°-rotated, vertically flipped) and taking the median, the saturation pattern can be isolated. Subtracting this saturation pattern from the image of Io then leaves true neutral sodium structures untouched whilst removing a source of

false detection from the algorithm.

It is possible to leverage its six-fold rotational symmetry to remove the spiderweb diffraction pattern from the images, which may otherwise prove a source of false detections. By rotating the cropped image of Io about its centre in 60° intervals and subtracting this from the original unrotated image, the effect of the spiderweb pattern is dramatically reduced. Whilst the pattern is nevertheless still present in images after this correction (due to an asymmetric diffraction pattern or the error in centring Io in the cropped image), it appears disrupted and hence far less 'jet-like' for the detection algorithm.

4.3 Methods

Using the preprocessing steps described in the previous section, an image of Io is obtained in which the saturation pattern and the diffraction pattern are diminished and radial structures highlighted. The most visible jets from the first two observation periods (2014-2015 and 2021) allowed for the verification of the radial and azimuthal profiles. As expected from preliminary analysis (de Spiegeleire, 2019) and as shown in Figure 4.3, the radial profile of the jet-like features may be fitted by a decreasing exponential function and the azimuthal profile by a Gaussian function. Therefore, automatic detection can be carried out by fitting an exponential function to the radial profile and a Gaussian function to the azimuthal profile at various intervals around Io.

Taking the central angle in 1° intervals for the full 360° around Io, a 10° region, centred on the central angle, is evaluated for the presence of a radial structure. This region is

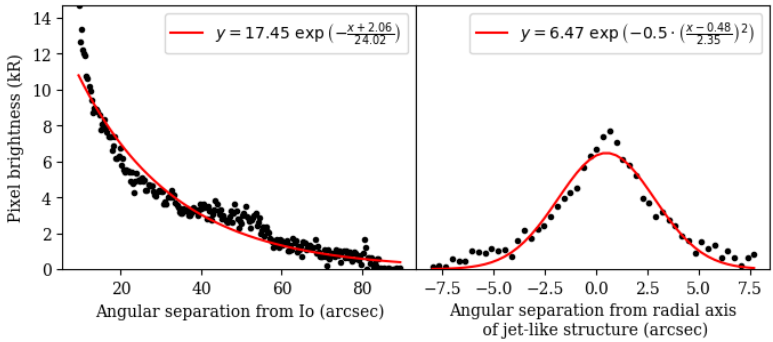

Figure 4.3: Example of fitted radial (left) and azimuthal (right) profiles for the jet-like structure observed on 2014-12-04. The fitted profile is given in red against the processed pixel brightnesses in black.

summed along the azimuthal axis, then normalised. A decreasing exponential function of the form $y = S_y e^{-x/S_x}$, where x is the radial distance from Io in arcseconds, y is the pixel brightness in kR, and S_x and S_y are constants to be found, is then fitted to the radial profile, and the R^2 goodness of fit evaluated for the fitting. Gaussian profiles of the form $y = a \exp\left(-\frac{x^2}{2\sigma^2}\right)$, where a and σ are again constants to be found, are fitted at ten evenly spaced radial points between a lower radial limit (15 pixels from the centre of Io; chosen to avoid contamination of the jet from sunlight reflected by Io) and the upper pixel bound identified previously, and the R^2 goodness of fit again evaluated for each of these Gaussian profiles. This method is preferred over a summation of the image over the radial dimension as it ensures that the azimuthal profile of the structure is indeed Gaussian at a range of distances from Io. The median

of the R^2 values is used as a measure of the goodness of fit of an azimuthal Gaussian profile to the structure. The product of the azimuthal and radial goodness-of-fit measures is taken as the indicator of the likelihood that a jet-like structure be present at this central angle (the "jet value"), which ranges from 0 (profile at this central angle poorly described by a jet) to 1 (profile at this central angle well-described by a jet).

It is worth noting that this method merely provides the angles around Io which best show a jet-like profile; it remains for the user to decide whether the angles returned show sufficiently jet-like appearances to be reasonably interpreted as jet-like structures in the neutral sodium cloud. To this end, the algorithm returns the cropped image of Io with suitable lower and upper brightness bounds such as to maximise the variation in brightness within the segment of image around the detected jet-like angle(s). If no structure is visible even with these ideal brightness bounds, it is reasonable to conclude that no structure is present for this date. If a structure appears to be present at the detected angle, the processed image of Io is compared with processed images of the other moons; if the same jet-like structure is observed around another moon, it is assumed to be a telescope artefact or related to the diffraction pattern, and the structure candidate discarded. While Europa also has a neutral sodium cloud (Burger and Johnson, 2004), the presence of jet-like features is yet to be reported in the literature and, even if present, a jet-like feature in the neutral sodium cloud of Europa would be unlikely to have the same observed instantaneous orientation as the feature in the cloud of Io.

In order to establish an objective threshold between true and false positive results from the auto-detection process, the

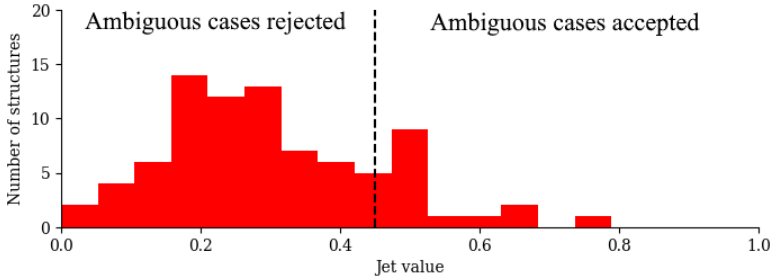

Figure 4.4: Histograms of the jet value of all jet-like-structure candidates, with a bin width of 0.05. A dashed line has been annotated to indicate the jet-value cutoff for ambiguous cases.

distribution of jet value over all auto-detected structures was investigated; see Figure 4.4. The jet values of the structures show a broadly bimodal distribution surrounding a jet value of 0.45. This limiting jet value was therefore taken as a stable cutoff to distinguish between true and false positives. However, this cutoff would lead to the discarding of several cases in which a clear radial structure is observed (due to noise or imperfect detection of the position of Io in the image); the results of this cutoff operation were therefore checked by a human operator and these misattributed cases nevertheless classed as positive detections of a radial structure in the neutral sodium cloud.

This work uses the JRM33 internal-magnetic-field model of Jupiter (Connerney et al., 2022) in conjunction with the Con2020 model of the external magnetic field due to the equatorial current sheet (Connerney et al., 2020) to model the magnetic field close to Io. These models are accessed via the JupiterMag Python wrapper made available as part of the

Magnetospheres of the Outer Planets Community Code project (Wilson et al., 2023; James et al., 2022).

4.4 Results

It is first necessary to identify the observational characteristics of the different structures in the Io neutral sodium cloud, primarily those of jets and of the banana, to allow for the interpretation of the images presented in this work.

- Jets are presumed to line approximately in the plane perpendicular to the local magnetic field at Io and to extend exclusively in the anti-jovian direction (Wilson et al., 2002). Therefore, structures displaying a jet-like morphology that extend in an anti-jovian direction when projected to the plane perpendicular to the local magnetic field at Io can be reliably interpreted as jets.

- The neutral sodium banana may appear observationally similar to jets in the sodium cloud. However, the banana is aligned with the orbital plane of Io, rather than the plane perpendicular to the local magnetic field, and is directed along, or slightly internal to, the orbit of Io (Wilson et al., 2002). Therefore, structures with a jet-like morphology that appear to extend inside the orbit of Io when projected to the plane perpendicular to the local magnetic field, and that are well aligned with the apparent direction of movement of Io, may be interpreted as observations of the banana rather than of a jet.

Images of Io processed according to section 4.2 for all observing runs discussed in this work are given in Figure 4.5.

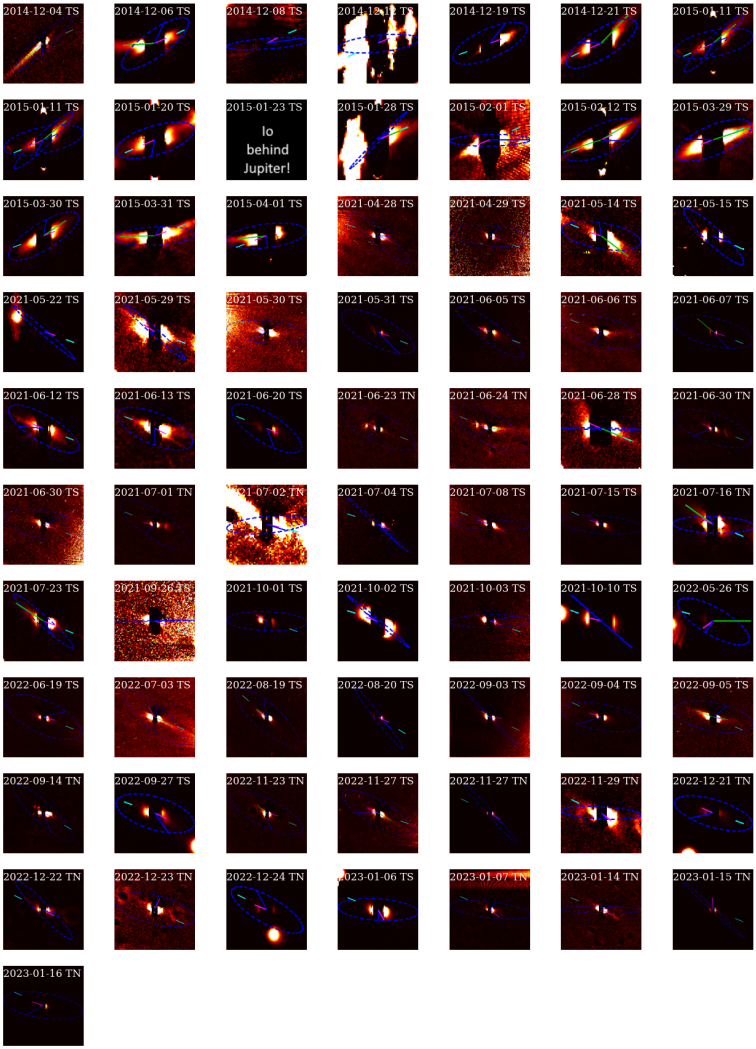
2014-12-04 TS
2014-12-06 TS
2014-12-08 TS
2014-12-12 TS
2014-12-19 TS
2014-12-21 TS
2015-01-11 TS
2015-01-11 TS
2015-01-20 TS
2015-01-23 TS
Io
behind
Jupiter!
2015-01-28 TS
2015-02-01 TS
2015-02-12 TS
2015-03-29 TS
2015-03-30 TS
2015-03-31 TS
2015-04-01 TS
2021-04-28 TS
2021-04-29 TS
2021-05-14 TS
2021-05-15 TS
2021-05-22 TS
2021-05-29 TS
2021-05-30 TS
2021-05-31 TS
2021-06-05 TS
2021-06-06 TS
2021-06-07 TS
2021-06-12 TS
2021-06-13 TS
2021-06-20 TS
2021-06-23 TN
2021-06-24 TN
2021-06-28 TS
2021-06-30 TN
2021-06-30 TS
2021-07-01 TN
2021-07-02 TN
2021-07-04 TS
2021-07-08 TS
2021-07-15 TS
2021-07-16 TN
2021-07-23 TS
2021-09-26 TS
2021-10-01 TS
2021-10-02 TS
2021-10-03 TS
2021-10-10 TS
2022-05-26 TS
2022-06-19 TS
2022-07-03 TS
2022-08-19 TS
2022-08-20 TS
2022-09-03 TS
2022-09-04 TS
2022-09-05 TS
2022-09-14 TN
2022-09-27 TS
2022-11-23 TN
2022-11-27 TS
2022-11-27 TN
2022-11-29 TN
2022-12-21 TN
2022-12-22 TN
2022-12-23 TN
2022-12-24 TN
2023-01-06 TS
2023-01-07 TN
2023-01-14 TN
2023-01-15 TN
2023-01-16 TN

Figure 4.5: Stacked images of all TRAPPIST viewing intervals presented in this work, cropped around Io and having undergone the processing described in section 4.2 of the main article. Images are orientated with north upward and west to the right. The direction toward the centre of Jupiter in the image is indicated by a short cyan line. The short magenta line centred at Io indicates the apparent direction of movement of Io in the image. The dashed blue ellipse represents the plane perpendicular to the local magnetic field at Io according to an observer on Earth, and the blue line between the centre of Io and the edge of this ellipse is the projection of the movement vector of Io in this plane. Green lines represent detected jet-like structures. On 2015-01-23, Io was eclipsed by Jupiter and hence not visible.

The imaging campaign of 2014-2015, despite being intended as a test of the ability of the TRAPPIST telescopes to observe the neutral sodium cloud, produced several clear images of jet-like structures. Of the 17 nights on which observations of Io took place, a jet-like structure was present for 10 of them. The structures detected vary in length and brightness, often changing their appearance greatly between consecutive nights.

In particular, the structure detected on 2014-12-04 (see Figure 4.6a) is notable for both its length and brightness compared to all other structures found in this work. This structure, if presumed to be in the plane perpendicular to the local magnetic field, extended in the anti-jovian direction (+78° from the projected direction of movement of Io) and is thus readily interpreted as a jet. Though the banana cloud is typically

the most prominent of the structures in the neutral sodium cloud (Grava et al., 2021b), this jet is far clearer than any other structure in this image. This jet is also remarkable for its apparent thinness, which may imply that sodium particles are ejected with single-value launch speeds or angles. This

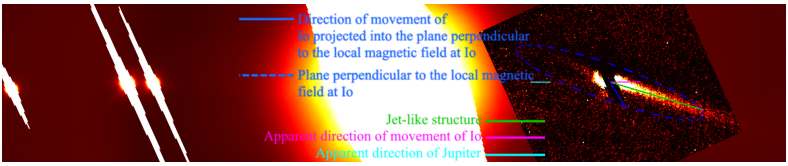

(a)

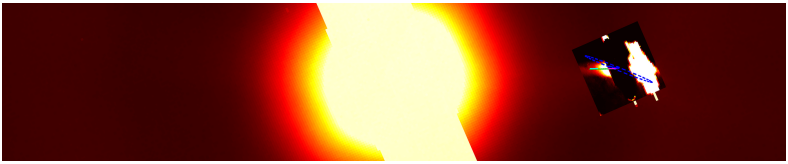

(b)

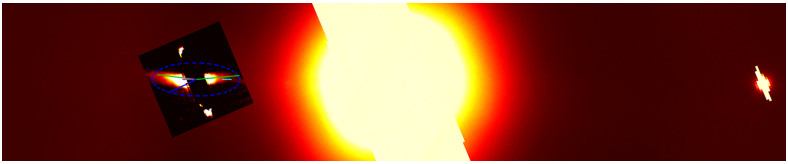

(c)

(d)

Figure 4.6: A sample of results of the automatic jet detection, overlaid on images of Io processed as per section 4.2. Images are orientated with north upward and west to the right, and Jupiter is located in the centre. The direction toward the centre of Jupiter in the image is indicated by a short cyan line. The short magenta line centred at Io indicates the apparent direction of movement of Io in the image. The dashed blue ellipse represents the plane perpendicular to the local magnetic field at Io according to an observer on Earth, and the blue line between the centre of Io and the edge of this ellipse is the projection of the movement vector of Io in this plane. Green lines represent detected jet-like structures. Panel a: 2014-12-04. Panel b: 2015-01-28. Panel c: 2015-02-12. Panel d: 2022-07-03.

is in disagreement with the "fan-like" structure presented in e.g. Wilson et al. (2002), which would result in a thicker jet, especially further from Io. A similarly clear (though visibly diminished) jet was also detected on 2014-12-06, which may be a continuation of the jet of 2014-12-04. The observation of 2014-12-08 is hampered by the proximity of Io to Jupiter, and the observation of 2014-12-12 by the proximity of Io to Europa, which have prevented the detection of the jet on the nights, if still present.

The jet detected on 2014-12-04 appears very similar to the observation of the "stream" neutral cloud from 1990-01-12 discussed by Schneider et al. (1991). Both structures show considerable lengths, are limited in width, and are directed away from Jupiter in the plane perpendicular to the magnetic field. However, the observation of the stream by Schneider et al.

(1991) showed a "hook" at its most distant point which is not present in the jet of 2014-12-04, despite the comparable lengths of the two structures. Nevertheless, the similarity between these two structures highlights the difficulty in visually distinguishing between the jet and a stream originated from the plasma torus close to Io, as the two are produced via very similar mechanisms and differ only in the duration between pickup and reneutralisation of the sodium (Wilson et al., 2002). In the viewing configuration of 1990-01-12, an anti-jovian jet that is emitted within the plane perpendicular to the local magnetic field would be masked by the stream, and hence it is not possible to say whether the stream and the jet are genuinely the same structure in this case, or whether the jet (if present) is simply not visible.

In 2021, while jet-like structures are again observed in the images from the TRAPPIST telescopes, they are noticeably less distinct than those structures observed in 2014. This variation cannot be uniquely due to the phase angle nor the System-III longitude of Io, since both parameters are well sampled in both the 2014-2015 and the 2021 campaigns, as shown in Figs. 4.7 and 4.8. Indeed, a case-by-case examination returns cases with very similar phase angles (e.g. 2014-12-21 and 2021-07-08; see Figure 4.9) or very similar System-III longitudes (e.g. 2014-12-06 and 2021-05-31; see Figure 4.10) in which a jet-like structure is visible in one set of images and not in the other. The 2021 campaign also demonstrated that the variation of the jet may be present over a timescale as short as a day. As shown in Table 4.2, no jet was detected on the night of 2021-06-23, whereas a jet appeared during the observation on the following night, 2021-06-24 (see Figure 4.11).

In the 2022-2023 imaging campaign, the jet-like structures,

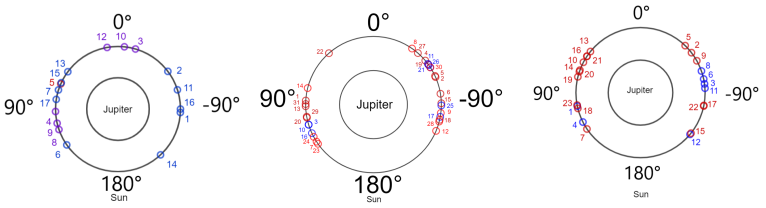

(a) (b) (c)

Figure 4.7: Io phase angle relative to the Sun for the observations detailed in this work. The position of Io is given as a small circle where the corresponding number refers to the case index given in tables 4.1, 4.2, and 4.3. Red circles indicate that no jet-like structure was observed on this date, whereas a blue circle indicates that at least one jet-like structure was observed. The cases in purple are those for which Io is behind Jupiter or close to another moon, so non-detection during these observations may be due to the configuration of the system as well as the absence or the faintness of the jet itself. Key phase angles, given in degrees, have been annotated around the diagram, as well as the position of the Sun in the diagram. Panel a: 2014-2015. Panel b: 2021. Panel c: 2022-2023.

of which several were observed, are again less distinct than in the 2014-2015 campaign. Compared to the very clear jet observed on 2014-12-04, cases without jet-like structures were encountered in the 2022-2023 campaign despite similar phase angle (e.g. 2022-12-23) or System-III longitude (e.g. 2023-01-14). Indeed, both of these parameters were very similar on 2022-12-22 ($\phi_E = 67°$, $\theta_{S3} = 11°$) and on 2015-01-11 ($\phi_E = 68°$, $\theta_{S3} = 5°$); however, as shown in Figure 4.12, while a clear

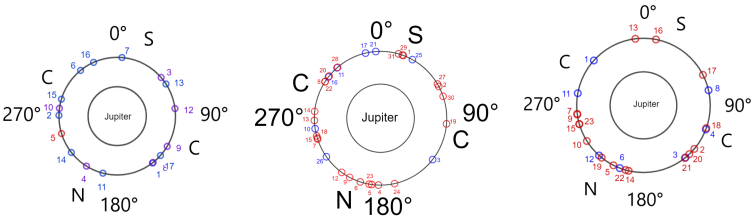

Figure 4.8: Position of Io in System-III longitude for the observations detailed in this work. The annotation of the positions of Io are as in Figure 4.7. The location of Io in the plasma torus is annotated, where 'N', 'S', and 'C' indicate that Io is located northward, southward, or in the centre of the plasma torus. Key System-III longitudes, given in degrees, have been annotated around the diagram. Panel a: 2014-2015. Panel b: 2021. Panel c: 2022-2023.

jet-like structure was observed on this latter date, the same orbital configuration did not produce any jet-like structures for the observation in 2022. These results imply that neither phase angle nor System-III longitude nor a combination of the two are uniquely responsible for the presence or absence of jet, and that this presence or absence must instead be largely controlled by some other parameter.

In several cases, a jet-like structure was observed which extended toward Jupiter, such as 2015-01-28 (see Figure 4.6b). In this case, the structure cannot be readily interpreted as a jet. However, due to the excellent alignment of this structure with both the apparent Io-Jupiter direction and the apparent direction of movement of Io, it may instead be interpreted as

(a)

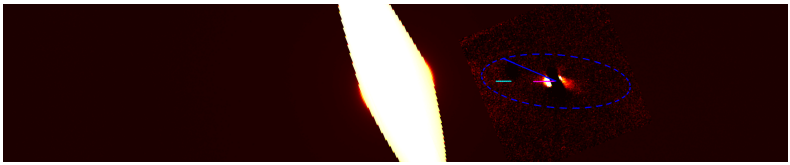

(b)

Figure 4.9: Comparison of Io in two cases with similar System-III longitudes. Orientation and annotation is as per Figure 4.6. a: 2014-12-06 ($\theta_{S3} = 271°$). b: 2021-05-31 ($\theta_{S3} = 303°$).

a detection of the banana neutral sodium cloud.

On several nights, such as 2015-02-12 (see Figure 4.6c), multiple jet-like structures were observed. In this case, one structure is well-aligned with the apparent direction of movement of Io and anti-aligned with the location of Jupiter on the image, which is the expected behaviour for the banana neutral sodium cloud in this configuration. The other structure, when projected to the plane perpendicular to the local magnetic field at Io, is directed toward Jupiter (-123° from the projected direction of movement of Io, though the small tilt of this plane makes exact determination of this angle difficult) but is anti-aligned with the apparent direction of movement of Io. Thus, it is not readily identifiable as either a jet or the banana. However, the banana does show a slight curvature inward of the

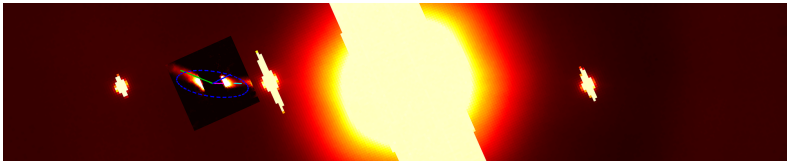

(a)

(b)

Figure 4.10: Comparison of Io in two cases with similar Earth-Jupiter-Io phase angles. Orientation and annotation is as per Figure 4.6. a: 2014-12-21 ($\phi_E = 117°$). b: 2021-07-08 ($\phi_E = 117°$).

orbit of Io in the jovian direction (Wilson et al., 2002), which, combined with the short observed length of the structure and the fact that Io was observed to be moving largely perpendicular to the viewing plane (phase angle 55°), implies that this case may be another detection of the banana neutral sodium cloud.

Jet-like structures that extended toward Jupiter but not in the apparent direction of movement of Io were also detected in several cases during this campaign; see Figure 4.6d for an example. It cannot be stated with certainty whether this structure represents a jet or the banana or indeed another structure in the neutral sodium cloud. It is possible that this is another

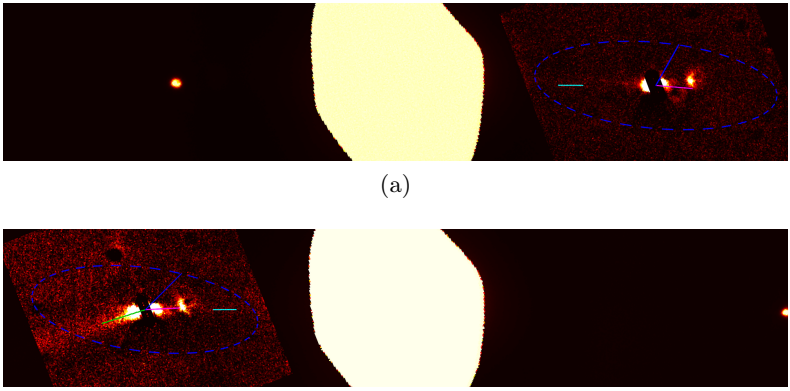

(a)

(b)

Figure 4.11: Comparison of Io over an interval of one day. Orientation and annotation is as per Figure 4.6. a: 2021-06-23. b: 2021-06-24.

detection of the inward-curving geometry of the banana, or is simply a result of the image artefacts that can be seen to the left and right of Io.

In this study, besides the cases explored above, a variety of structures were detected in the Io neutral sodium cloud with a variety of angular deviations from the movement vector of Io projected into the plane perpendicular to the local magnetic field, as shown in Figure 4.13. The majority of these structures extended in the anti-jovian direction, including many structures with high jet values (well described by jet-like profiles), and can therefore be readily interpreted as jets in the neutral sodium cloud. These structures are grouped around a projection angle of $+90°$ from the projected movement direction of Io

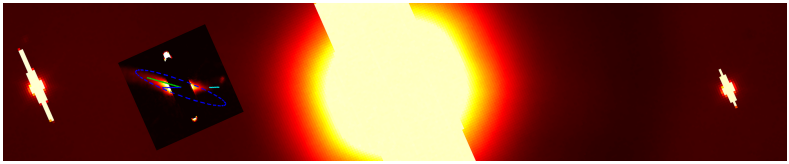

(a)

(b)

Figure 4.12: Comparison of Io in two cases with similar System-III longitudes and Earth-Jupiter-Io phase angles. Orientation and annotation is as per Figure 4.6. a: 2015-01-11 ($\theta_{S3} = 5°$, $\phi_E = 68°$). b: 2022-12-22 ($\theta_{S3} = 11°$, $\phi_E = 67°$).

in the plane perpendicular to the local magnetic field (i.e. almost exactly anti-jovian). This may be a selection effect rather than a physical preference; the vast majority of the observations discussed in this work were made when Io was moving toward or away from the observer, and so any structure aligned with the direction of movement of Io would be hidden by the emission from Io itself. Several structures that extended in the jovian direction also demonstrated the expected behaviour of the banana neutral sodium cloud. Of the remaining structures extending in the jovian direction detected in this work, many can be explained by one or more of the following restrictions:

- The non-uniform morphology of the banana and the de-

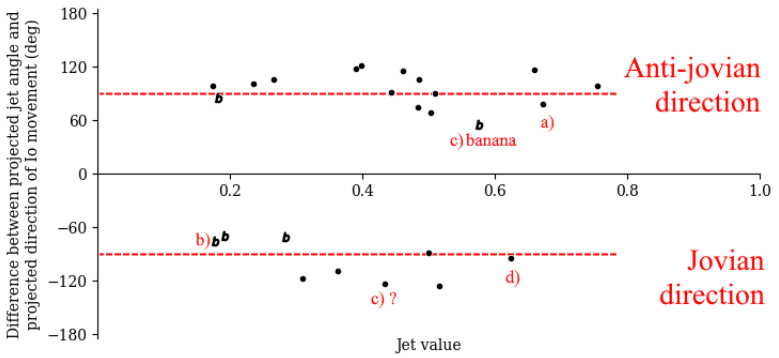

Figure 4.13: Jet value of detected structures against the angular deviation from the direction of movement of Io projected into the plane perpendicular to the local magnetic field at Io. Cases marked with a "b" are those for which the structure is well-aligned with the expected direction of the banana. Dashed lines indicate the expected orientation of an exactly anti-jovian (+90°) and jovian (-90°) structure. Annotation has been applied below those cases displayed in Figure 4.6.

gree of movement of Io perpendicular to the viewing plane may have led to a detection of the banana that was anti-aligned to the apparent direction of movement of Io;

- Io was observed close to Jupiter and the observed structure is well aligned with the apparent position of Jupiter in the image. Here, it is possible that the background-removal process and proximity to Jupiter is causing a jet-like artefact to appear in the images;

- The detected structure may be an artefact of the observation process, such as a limb of the saturation pattern not fully removed by preprocessing; here, the detected structure may be well aligned with the saturation pattern (though still not present in the processed images of the other moons, otherwise it would have been discarded after the auto-detection) or be significantly dimmer compared to other, clearer structures.

While this does not preclude the possibility that these cases be legitimate detections of a structure in the neutral sodium cloud that is neither a jet nor the banana, further observation is required to provide a detection that cannot be explained by the above restrictions. Nevertheless, there remain cases, such as that shown in Figure 4.6c, where a clear structure is observed to be directed toward Jupiter and away from the apparent direction of movement of Io. I propose that these cases may be detections of the sputtering of sodium from sodium-bearing molecules in dust grains within the orbit of Io (Grava et al., 2021b).

The apparent length of the jets identified in this work can be estimated by using the fitted radial exponential profiles. To ensure consistency between cases, the distance from Io at which the fitted profile descends below 10% of the average jet pixel value at the inner detection radius of 15 px was taken as a representative measure of structure length. Since it has been assumed that a jet will lie in the plane perpendicular to the local magnetic field at Io, it is possible to infer an intrinsic length from the apparent length and viewing geometry; derived intrinsic lengths for the jets identified in this work are given in Table 4.4. Using this consistent measure, it can be seen that

Table 4.4: Derived parameters for the jets identified in this work.

Date	Brightness (kR)	Length (km)	Length (R_{Io})	Length (R_J)
2014-12-04	8.42	184 000	101	2.6
2014-12-06	1.87	63 000	35	0.9
2014-12-21	0.76	66 000	36	0.9
2015-01-11	2.03	62 000	34	0.9
2015-02-12	3.10	67 000	37	0.9
2015-03-30	1.87	64 000	35	0.9
2015-03-31	1.14	82 000	45	1.1
2021-05-13	1.55	79 000	43	1.1
2021-06-06	1.07	101 000	55	1.4
2021-06-23	5.54	81 000	44	1.1
2021-07-15	2.72	54 000	30	0.8
2021-07-22	0.84	63 000	35	0.9
2022-05-26	1.08	83 000	46	1.2
2022-09-03	2.97	48 000	26	0.7
2022-09-05	2.42	65 000	36	0.9
2022-11-23	3.20	58 000	32	0.8

"Brightness" refers specifically to the brightness at a distance of 70 000 km from Io. "Length" refers to the extrapolated intrinsic length of the jet, assuming that it lies in the plane perpendicular to the local magnetic field at Io (1 R_{Io} = 1 Io radius; 1 R_J = 1 Jupiter radius).

jets are observed with a large range of intrinsic lengths, which can extend up to several hundred Io radii in the case of the clear jet of 2014-12-04.

Similarly, by removing the background from the reduced images and converting to rayleigh as per section 4.2, it is possible to compare the absolute brightness of the detected jets in a consistent manner. To allow for comparison between different cases, the average brightness in a 10° arc about the central axis

of the jet at an apparent distance of 70 000 km from the centre of Io was taken as a representative measure of jet brightness. This is distant enough from Io to be unaffected by reflected sunlight while remaining close enough that the jets present in this work are still detectable. The jet brightnesses obtained using this method are given in Table 4.4. The range of brightnesses observed falls within the expected 1-10 kR range for structures in the neutral sodium cloud of Io (Smyth, 1992). The clear jet of 2014-12-04 is almost twice as bright as any other detected structure.

The jets identified in this work do not show the expected "fan-like" or "hook" shape (Wilson et al., 2002) but instead present themselves as thin, collimated structures, especially in the case of the jet of 2014-12-04 (Figure 4.6a). While the length of the jet is related to the movement of reneutralised particles along their former magnetic gyrorotation axes, the jet width originates from the former movement of these particles parallel to the magnetic field at Io. Thus, a collimated jet implies a lack of a considerable component of velocity of pickup ions parallel to the magnetic field. This may have two explanations. Firstly, the neutral atoms that become ionised via pickup ionisation are very quickly reneutralised and ejected in a jet. This would not give the pickup ions sufficient time to attain thermal equilibrium parallel to the magnetic field, since they are generated from Io's relatively cold atmosphere (Lellouch et al., 2007) and hence does not start with a large parallel velocity component. Otherwise, it is possible that the pickup-ion plasma itself remains cold parallel to the magnetic field. In this case, the parallel temperature of the pickup ions can be estimated from the ratio of jet width to jet length, which gives a maximum launch angle from the central axis for particles in the jet. For

the jet of 2014-12-04, if particles are assumed to have a velocity along the jet axis of 100 km s^{-1} (Bagenal and Dols, 2020), the ratio between the length (126") and the width (20"), calculated from the distance from or along the central axis at which the pixel value descends below 10% of the peak pixel value, can be taken to arrive at a parallel temperature of sodium pickup ions of 7 eV. This would imply that the pickup-ion plasma remains relatively cold and consistent with the expected temperatures of neutralised pickup ions escaping from Io (Bagenal and Dols, 2020). A more in-depth analysis using modelling tools would further constrain this result.

As shown in Figure 4.14, the brightness of both the extended sodium nebula (Yoneda et al., 2015) and the plasma torus (Yoshikawa et al., 2017) increased towards the end of January 2015. In the period preceding this increase in brightness, multiple jets were observed with the TRAPPIST telescopes. Since the brightness of both the extended sodium nebula and the plasma torus is not observed to increase with the presence or absence of these jets, I conclude that a single instance of a jet does not considerably alter the brightness of these structures. This conclusion is reinforced by the lack of response even to the bright jet of 2014-04-12 (the first blue line in Figure 4.14).

It is possible that the jets observed in the 2014-2015 campaign are simply one long-lasting structure, albeit of varying length and brightness. While there were nights during this campaign on which no jet was observed, this may have been due to a variable intrinsic brightness or unfavourable viewing geometry that rendered the jet undetectable by the TRAPPIST telescopes. However, were this the case, it remains to be explained why the increase in brightness of the sodium nebula and plasma torus begins much later than the first observed jet,

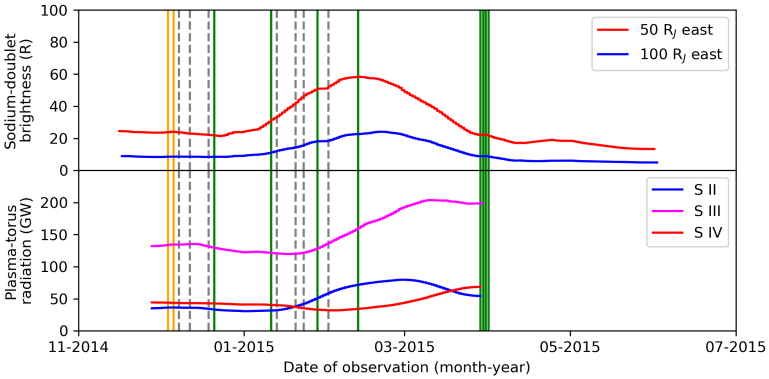

Figure 4.14: Comparison between the detections of jets during TRAPPIST observations with previous studies of the brightness of components of the jovian magnetosphere for the period surrounding the 2014-2015 viewing campaign. Jets identified in this work are given by solid green lines, and observations made of Io with no detected jets by a broken grey line. Orange lines denote the exceptional jets of 2014-12-04 and 2014-12-06. Top: the brightness of the extended sodium nebula in the sodium-doublet waveband, as taken from Figure 1 of Yoneda et al. (2015). The legend refers to the distance from Jupiter at which the measurements were obtained. Bottom: the brightness of the Io plasma torus in several sulphur-ion wavebands, as taken from Figure 3 of Yoshikawa et al. (2017). The legend refers to the ionisation levels of the sulphur ions.

which itself may have arisen before the start of the 2014-2015 viewing campaign. The speed of the neutral sodium ejected by a jet is such that a distance of 100 R_J could be achieved in 24 hours (Yoneda et al., 2015), and hence any response from the plasma torus or sodium nebula should be rapidly observable. If there is indeed a link between neutral sodium jets and the brightness of the plasma torus or sodium nebula, this result implies a more complex process than a simple input of matter.

4.5 Conclusion

The regular, long-term monitoring of the neutral sodium cloud of Io performed for the first time with the TRAPPIST telescopes led to a total of 25 detections of jet-like structures, with a particularly spectacular case on 2014-12-04, and the physical properties of these jet-like structures were established. Even if the number of detections does not allow for the determination of the precise time variation of those properties, by comparing observations made on different nights, it can be determined that the presence, length, and brightness of jet-like structures do not, or not only, depend on the orbital angle nor the System-III longitude of Io. Additionally, a jet can be clearly present during one night and entirely absent during the next, or the length and brightness of a jet observed over two or more consecutive nights can vary considerably within these observations. Future work should be considered to determine which physical processes most closely control the appearance of jets.

The geometry of a large proportion of the detected jet-like structures aligned well with the expected geometry of sodium jets. Additionally, five cases were observed in which a jet-like

structure could be clearly associated with the banana neutral sodium cloud. Many cases which did not fall into these two categories could be explained by the alignment inward of the orbit of Io of the principal axis of the banana. Of the remaining cases, which are observed to extend in an jovian direction but which cannot be explained by the banana, there is no unequivocal detection of a jet-like structure. While this does not preclude the presence of an unexplained jet-like structure in these cases, a clearer detection would be necessary to make firm conclusions.

A comparison between our data and the data from Yoshikawa et al. (2017) and Yoneda et al. (2015) shows that the relation between the presence of a jet and the brightness of larger structures, such as the extended sodium nebula or the plasma torus, is not straightforward. Even a bright jet, such as that of 2014-12-04, did not led to an immediate increase of brightness in the plasma torus and extended nebula, and the increase in brightness observed in these larger structures toward the end of January 2015 was not preceded by an especially large jet. This may imply that jets do not contribute directly to the population of these structures.

This work presents a database of jet detections spanning three periods between 2014 and 2023, with many observations made within each period. It is hoped that future work in neighbouring fields may make use of this database to probe the relationship between sodium jets and potentially related datasets, such as those pertaining to volcanism on Io, the other neutral sodium clouds, or the aurorae of Jupiter, in the same way as this work has compared this database to the brightness of the plasma torus and extended sodium nebula. The planned continued regular monitoring of the Io neutral sodium cloud with

the TRAPPIST telescopes will serve to enhance the value of this database.

This work also highlighted the need for modelling tools to explain the lack of fan-like structure in the jets identified in this work, as well as to more rigorously derive characteristics of the Io pickup-ion plasma from the observed jet geometries.

Chapter 5

Variability of the size of the main emission

You can't stop the change, any more than you can stop the suns from setting.

Shmi Skywalker, *Star Wars Episode I: The Phantom Menace*

Auroral emissions are a reflection of magnetospheric processes, and at Jupiter, it is not entirely certain how the morphology of the UV main emission (ME) varies with magnetospheric compression (by the solar wind or otherwise) or the strength of the central current sheet. This work leverages the observations from Juno-UVS to link ME variability with particular magnetospheric states. We employed novel arc-detection techniques to determine new reference ovals for the ME from perijoves 1 through 54, in both hemispheres, and analysed how the size and shape of the ME vary compared to this reference oval. While auroral-arc detection has previously been applied to the

terrestrial aurorae, this work represents the first application of auroral-arc detection to the aurorae of Jupiter. In this work, auroral-arc detection is applied to automatically characterise the global expansion and contraction of the ME and associate it with the conditions in Jupiter's magnetosphere, to further our understanding of the response of the morphology of the ME to conditions present in the magnetosphere. The morphology and brightness of the ME vary in local time: the dawn-side ME is typically expanded, while the dusk-side ME is contracted, compared to the reference oval, and the dusk-side ME is twice as bright as the dawn-side ME. Both the northern and southern ME and the day-side and night-side ME expand and contract from their reference ovals synchronously, which indicates that the variable size of the ME is caused by a process occurring throughout the Jovian magnetosphere. The poleward latitudinal shift of the auroral footprint of Ganymede correlates with the poleward motion of the ME, whereas a similar relation is not present for the footprint of Io. Additionally, the expansion of the ME correlates well with an increase in magnetodisc current. These two results suggest that a changing current-sheet magnetic field is partially responsible for the variable size of the ME. Finally, magnetospheric compression is linked to a global ME contraction and brightening, though this brightening occurs predominantly in the day-side ME. This observation, and the observation that the dusk-side ME is typically brighter than the dawn-side ME, stands in contrast to the modelled and observed behaviour of field-aligned currents and thus weakens the theoretical link between field-aligned currents and the generation of the auroral ME.

This section on the variability of the size of the main emission follows from Head et al. (2024), published by Astronomy

and Astrophysics on 2024-08-22, of which I was first author. The most relevant sections of the introduction are sections 2.6 (main emission) and 2.9 (moon footprints).

5.1 Methods

Images of the UV aurora were created as per section 3.1.1. For each perijove and each hemisphere, a 'exemplar' map was created, made of the 100 successive spins as close as possible to the perijove time and that cover at least 75% of the auroral region. Therefore, a total of 106 UVS images were used in this work, one in the northern and southern hemisphere for the first 54 perijoves, barring perijove 2, where the spacecraft entered safe mode and no image data were collected. *Hubble* Space Telescope (HST) images used in this work come from the GO-14105 and GO-14634 imaging campaigns, both using the Space Telescope Imaging Spectrograph (STIS) instrument with a strontium-fluoride filter to reduce the influence of geocoronal emissions. Images were processed into 10-second frames using the CALSTIS calibration tools from the Space Telescope Science Institute (Katsanis and McGrath, 1998), converted to brightness in kilo-rayleigh (kR) assuming a colour ratio of 2.5 (Gustin et al., 2012), and fitted to the ellipsoid of Jupiter as per Bonfond et al. (2009). HST-STIS and UVS cases used in this work are given in Tables 5.1 and 5.2 respectively. Expanded version of these tables are available in Head et al. (2024).

Table 5.1: HST-STIS cases used in this work.

ID	Date	Expansion (km)	MS comp.?
ocx837olq	2016-06-26 01:39:14	-800 ± 700	N
ocx838xzq	2016-06-26 22:19:19	-900 ± 900	N
ocx840t4q	2016-06-30 04:13:09	-3100 ± 900	Y
ocx844t7q	2016-07-14 16:23:27	-2000 ± 900	Y
ocx846gwq	2016-07-17 14:21:11	-1600 ± 700	Y
ocx842ewq	2016-07-18 18:58:22	-1400 ± 700	Y
ocx847eyq	2016-07-18 20:33:46	-2100 ± 700	Y
od8k25jlq	2017-01-22 15:31:08	0 ± 800	N
od8k29fiq	2017-01-23 20:07:50	-600 ± 800	N
od8k30i4q	2017-01-24 15:11:42	-2000 ± 800	Y
od8k31iaq	2017-01-24 16:47:04	-1000 ± 800	Y
od8k55tnq	2017-03-01 15:56:39	-600 ± 800	N
od8k56o2q	2017-03-05 18:29:08	-500 ± 800	N
od8k32anq	2017-03-17 08:39:23	-1200 ± 700	Y
od8k42fiq	2017-03-18 14:52:23	-500 ± 700	Y
od8k57itq	2017-03-19 09:57:00	-1600 ± 800	Y
od8k82ovq	2017-04-23 14:00:08	-1200 ± 800	N
od8k41ixq	2017-05-09 06:42:14	-300 ± 700	N

"ID" gives the unique identifier of the HST exposure. "Date" gives the average date and time of the HST exposure, in the format YYYY-MM-DD hh:mm:ss. "Expansion" refers to the day-side (visible by HST) expansion of the ME relative to the reference contour. ME expansions are given as positive where the detected ME is, on average, equatorward of the reference contour. Negative values indicate global contraction of the ME compared to the reference contour. "MS comp.?" denotes whether the magnetosphere was in a state of compression ("Y") or uncompressed ("N"), as determined by Yao et al. (2022).

Table 5.2: Juno-UVS cases used in this work.

Perijove	Date	Exp. (km)	Fig. 5.5	Fig. 5.6	Fig. 5.7	Fig. 5.9 IFP	Fig. 5.9 EFP	Fig. 5.9 GFP	Fig. 5.10 ME	Fig. 5.10 GFP
PJ1 N	2016-08-27 12:01:51	100±300	Yes	Yes	No	No	No	No	No	No
PJ1 S	2016-08-27 14:52:06	700±300	Yes	Yes	No	Yes	No	No	Yes	No
PJ3 N	2016-12-11 16:40:25	1300±300	Yes	Yes	No	No	No	No	No	No
PJ3 S	2016-12-11 19:11:02	300±300	Yes	Yes	Yes	Yes	No	Yes	Yes	Yes
PJ4 N	2017-02-02 12:42:45	-600±300	Yes	Yes	No	No	No	No	No	No
PJ4 S	2017-02-02 14:37:01	-100±300	Yes	Yes	Yes	Yes	No	Yes	Yes	Yes
PJ5 N	2017-03-27 08:45:48	-1700±300	Yes	Yes	No	No	No	No	No	No
PJ5 S	2017-03-27 11:38:04	-800±300	Yes	Yes	No	No	Yes	No	Yes	No
PJ6 N	2017-05-19 05:34:29	-400±300	Yes	Yes	No	No	No	No	No	No
PJ6 S	2017-05-19 07:40:01	-300±300	Yes	Yes	No	Yes	No	Yes	Yes	Yes
PJ7 N	2017-07-11 01:05:59	-400±300	Yes	Yes	No	No	No	No	No	No
PJ7 S	2017-07-11 03:51:29	0±200	Yes	Yes	Yes	Yes	Yes	No	Yes	No
PJ8 N	2017-09-01 21:20:23	600±300	Yes	Yes	No	No	No	No	No	No
PJ8 S	2017-09-01 23:28:24	400±300	Yes	Yes	Yes	Yes	Yes	Yes	Yes	Yes
PJ9 N	2017-10-24 17:23:42	-600±300	Yes	Yes	No	No	No	No	No	No
PJ9 S	2017-10-24 19:22:38	-300±300	Yes	Yes	No	Yes	No	Yes	Yes	Yes
PJ10 N	2017-12-16 17:55:38	-2100±300	Yes	Yes	No	No	No	No	No	No
PJ10 S	2017-12-16 19:36:38	-900±300	Yes	Yes	No	Yes	No	Yes	Yes	Yes
PJ11 N	2018-02-07 14:00:10	300±300	Yes	Yes	No	No	No	No	No	No
PJ11 S	2018-02-07 15:43:53	800±300	Yes	Yes	Yes	Yes	Yes	No	Yes	No
PJ12 N	2018-04-01 08:57:02	-1300±300	Yes	Yes	No	No	No	No	No	No
PJ12 S	2018-04-01 11:25:10	-1000±300	Yes	Yes	Yes	Yes	Yes	Yes	Yes	Yes
PJ13 N	2018-05-24 05:22:26	600±300	Yes	Yes	No	No	No	No	No	No
PJ13 S	2018-05-24 07:19:34	900±300	Yes	Yes	No	Yes	No	No	Yes	No
PJ14 N	2018-07-16 05:03:39	200±300	Yes	Yes	No	No	No	No	No	No
PJ14 S	2018-07-16 06:57:13	500±300	Yes	Yes	Yes	Yes	Yes	Yes	Yes	Yes
PJ15 N	2018-09-07 01:12:54	-1200±300	Yes	Yes	No	No	No	No	No	No
PJ15 S	2018-09-07 02:50:28	-500±300	Yes	Yes	No	Yes	Yes	No	Yes	No
PJ16 N	2018-10-29 21:09:47	400±300	Yes	Yes	No	No	No	No	No	No
PJ16 S	2018-10-29 22:45:00	400±300	Yes	Yes	No	Yes	Yes	Yes	Yes	Yes
PJ17 N	2018-12-21 17:02:10	-400±300	Yes	Yes	No	No	No	No	No	No
PJ17 S	2018-12-21 18:54:49	200±300	Yes	Yes	No	No	Yes	Yes	Yes	Yes
PJ18 N	2019-02-12 17:43:36	-	No	No	No	No	No	No	No	No
PJ18 S	2019-02-12 19:14:17	-700±300	No	Yes	No	Yes	No	Yes	Yes	Yes
PJ19 N	2019-04-06 11:55:26	200±300	Yes	Yes	No	No	No	No	No	No
PJ19 S	2019-04-06 13:54:35	700±200	Yes	Yes	No	No	No	Yes	Yes	Yes
PJ20 N	2019-05-29 08:07:26	-200±300	Yes	Yes	No	No	No	No	No	No
PJ20 S	2019-05-29 09:48:51	100±300	Yes	Yes	Yes	Yes	No	No	Yes	No
PJ21 N	2019-07-21 04:06:09	-700±300	Yes	Yes	No	No	No	No	No	No
PJ21 S	2019-07-21 05:59:19	-400±300	Yes	Yes	Yes	Yes	No	Yes	Yes	Yes
PJ22 N	2019-09-12 03:45:30	1800±300	Yes	Yes	No	No	No	No	No	No
PJ22 S	2019-09-12 05:20:05	1800±300	Yes	Yes	No	Yes	Yes	Yes	Yes	Yes
PJ23 N	2019-11-03 22:34:24	0±300	Yes	Yes	No	No	No	No	No	No
PJ23 S	2019-11-04 00:14:55	100±300	Yes	Yes	Yes	Yes	No	No	Yes	No
PJ24 N	2019-12-26 17:23:52	200±300	Yes	Yes	No	No	No	No	No	No
PJ24 S	2019-12-26 20:08:37	600±300	Yes	Yes	Yes	Yes	No	Yes	Yes	Yes
PJ25 N	2020-02-17 18:08:03	-	No	No	No	No	No	No	No	No
PJ25 S	2020-02-17 19:52:29	400±300	No	Yes	No	Yes	Yes	Yes	Yes	Yes
PJ26 N	2020-04-10 13:42:22	-1600±300	Yes	Yes	No	No	No	No	No	No
PJ26 S	2020-04-10 15:27:32	-700±300	Yes	Yes	No	Yes	Yes	No	Yes	No

continued...

Table 5.2: Juno-UVS cases used in this work.

Perijove	Date	Exp. (km)	Fig. 5.5	Fig. 5.6	Fig. 5.7	Fig. 5.9 IFP	Fig. 5.9 EFP	Fig. 5.9 GFP	Fig. 5.10 ME	Fig. 5.10 GFP
PJ27 N	2020-06-02 10:22:50	-900±300	Yes	Yes	No	No	No	No	No	No
PJ27 S	2020-06-02 12:21:20	-200±300	Yes	Yes	No	Yes	No	Yes	Yes	Yes
PJ28 N	2020-07-25 06:25:33	2300±300	Yes	No	No	No	No	No	No	No
PJ28 S	2020-07-25 07:54:55	2100±300	Yes	Yes	No	Yes	No	No	Yes	No
PJ29 N	2020-09-16 02:25:22	-1500±200	Yes	No	No	No	No	No	No	No
PJ29 S	2020-09-16 04:23:42	-300±300	Yes	Yes	Yes	Yes	No	No	Yes	No
PJ30 N	2020-11-08 01:57:01	3000±300	Yes	Yes	No	No	No	No	No	No
PJ30 S	2020-11-08 03:28:47	1000±300	Yes	Yes	No	Yes	No	Yes	Yes	Yes
PJ31 N	2020-12-30 21:59:18	-	No	No	No	No	No	No	No	No
PJ31 S	2020-12-30 23:43:37	100±300	No	Yes	Yes	No	No	No	Yes	No
PJ32 N	2021-02-21 17:36:05	-900±300	Yes	Yes	No	No	No	No	No	No
PJ32 S	2021-02-21 20:04:05	-1000±300	Yes	Yes	Yes	Yes	No	Yes	Yes	Yes
PJ33 N	2021-04-15 23:37:10	0±300	Yes	Yes	No	No	No	No	No	No
PJ33 S	2021-04-16 01:55:31	-500±300	Yes	Yes	No	Yes	No	No	Yes	No
PJ34 N	2021-06-08 07:53:29	800±300	Yes	Yes	No	No	No	No	No	No
PJ34 S	2021-06-08 09:45:58	300±300	Yes	Yes	Yes	Yes	No	No	Yes	No
PJ35 N	2021-07-21 08:14:03	600±300	Yes	Yes	No	No	No	No	No	No
PJ35 S	2021-07-21 10:15:36	100±300	Yes	Yes	No	Yes	No	Yes	Yes	Yes
PJ36 N	2021-09-02 22:40:39	300±300	Yes	Yes	No	No	No	No	No	No
PJ36 S	2021-09-03 00:43:55	900±300	Yes	Yes	Yes	Yes	No	Yes	Yes	Yes
PJ37 N	2021-10-16 17:12:14	-200±300	Yes	Yes	No	No	No	No	No	No
PJ37 S	2021-10-16 18:53:35	0±300	Yes	Yes	Yes	Yes	No	Yes	Yes	Yes
PJ38 N	2021-11-29 14:12:04	-200±300	Yes	Yes	No	No	No	No	No	No
PJ38 S	2021-11-29 16:13:59	300±300	Yes	Yes	Yes	Yes	Yes	Yes	Yes	Yes
PJ39 N	2022-01-12 10:33:08	-1100±300	Yes	No	No	No	No	No	No	No
PJ39 S	2022-01-12 12:55:09	500±300	Yes	Yes	No	No	No	Yes	Yes	Yes
PJ40 N	2022-02-25 02:01:00	-1500±300	Yes	Yes	No	No	No	No	No	No
PJ40 S	2022-02-25 03:55:23	-400±300	Yes	Yes	No	Yes	Yes	No	Yes	No
PJ41 N	2022-04-09 15:50:02	200±300	Yes	Yes	No	No	No	No	No	No
PJ41 S	2022-04-09 18:13:06	400±300	Yes	Yes	Yes	Yes	Yes	No	Yes	No
PJ42 N	2022-05-23 02:17:38	700±300	Yes	Yes	No	No	No	No	No	No
PJ42 S	2022-05-23 04:15:13	-300±300	Yes	Yes	No	Yes	No	Yes	Yes	Yes
PJ43 N	2022-07-05 08:57:25	-	No	No	No	No	No	No	No	No
PJ43 S	2022-07-05 13:45:48	-1600±300	No	No	No	No	No	No	Yes	No
PJ44 N	2022-08-17 15:08:57	-	No	No	No	No	No	No	No	No
PJ44 S	2022-08-17 17:19:53	100±300	No	Yes	Yes	Yes	No	No	Yes	No
PJ45 N	2022-09-29 17:35:46	-	No	No	No	No	No	No	No	No
PJ45 S	2022-09-29 19:33:52	300±300	No	Yes	Yes	Yes	No	No	Yes	No
PJ46 N	2022-11-06 21:21:19	1300±300	Yes	No	No	No	No	No	No	No
PJ46 S	2022-11-06 23:38:56	1000±300	Yes	Yes	No	Yes	No	Yes	Yes	Yes
PJ47 N	2022-12-15 03:40:45	800±300	Yes	No	No	No	No	No	No	No
PJ47 S	2022-12-15 05:12:33	1000±300	Yes	Yes	Yes	No	No	Yes	Yes	Yes
PJ48 N	2023-01-22 05:54:42	-	No	No	No	No	No	No	No	No
PJ48 S	2023-01-22 08:08:03	-600±300	No	Yes	Yes	Yes	Yes	No	Yes	No
PJ49 N	2023-03-01 06:09:16	-	No	No	No	No	No	No	No	No
PJ49 S	2023-03-01 08:32:36	200±300	No	Yes	No	No	No	Yes	Yes	Yes
PJ50 N	2023-04-08 08:36:41	-	No	No	No	No	No	No	No	No
PJ50 S	2023-04-08 10:35:05	-200±300	No	Yes	Yes	Yes	No	Yes	Yes	Yes
PJ51 N	2023-05-16 07:38:52	-	No	No	No	No	No	No	No	No
PJ51 S	2023-05-16 09:42:47	500±300	No	Yes	No	No	No	No	Yes	No

continued...

Table 5.2: Juno-UVS cases used in this work.

Perijove	Date	Exp. (km)	Fig. 5.5	Fig. 5.6	Fig. 5.7	Fig. 5.9 IFP	Fig. 5.9 EFP	Fig. 5.9 GFP	Fig. 5.10 ME	Fig. 5.10 GFP
PJ53 N	2023-07-31 09:29:34	-	No	No	No	No	No	No	No	No
PJ53 S	2023-07-31 11:50:11	-100±300	No	Yes	No	No	No	No	Yes	No
PJ54 N	2023-09-07 12:05:54	-	No	No	No	No	No	No	No	No
PJ54 S	2023-09-07 14:39:53	-1300±300	No	Yes	Yes	No	Yes	No	Yes	No

"Perijove" gives the perijove number and hemisphere for each case. "Date" gives the time of the central spin of the master UVS image in the format YYYY-MM-DD hh:mm:ss. "Exp." refers to the global expansion of the ME relative to the reference contour. Expansions are given as positive where the detected ME is, on average, equatorward of the reference contour. Negative values indicate global contraction of the ME compared to the reference contour. Columns of the type "Fig. X" state whether a particular case was used in the analysis associated with the numbered figure.

The detection of arcs in a series of auroral images performed in this work proceeds in three phases:

- Preprocessing: this step comprises the processing performed from the collection of the images by HST and UVS and before any detection-specific analysis is performed. Images are converted to a polar-projected format and smoothed to improve the efficiency of the arc-extraction algorithm.

- Extraction: this step comprises the detection of arcs in each preprocessed image. The image is template-matched with an artificial arc profile to detect those regions of the image that show 'arc-like' shapes. The results of this template matching are used to determine the skeleton of the aurora, from where individual arcs can be extracted.

- Characterisation: this step involves the extraction of a number of key properties of the detected arcs (brightness, position, ...). These properties are stored in a database,

which allows auroral arcs to be more quickly analysed than directly from image data.

5.1.1 Preprocessing

For this work, images from Juno-UVS and HST were first transformed into a 1024×1024-pixel Cartesian polar projection, that is, as though viewed from above the northern geographical pole of Jupiter, with a System-III longitude of 0° toward the top of the image and 90° toward the right. In the case of the southern aurora, the aurora is still displayed as though seen from the northern geographical pole 'through the planet', as this allows for more intuitive comparison of images of the northern and southern aurora. A 1024×1024-pixel projection was chosen to ensure parity between the polar-projected images and the maps from which they are made; these maps have a resolution of 0.1° in both latitude and longitude, which is roughly equivalent to 100 km on the globe of Jupiter and hence consistent with the approximate 100-km-per-pixel resolution of the polar-projected image. During this projection, it was assumed that the aurora be located at an altitude of 400 km; this projection altitude is a compromise between the moon footprints at 900 km and the ME at 250-400 km (Vasavada et al., 1999; Bonfond et al., 2015b). The advantages of this for large-scale image analysis are essentially twofold: firstly, the projection of each pixel to System-III coordinates is consistent between polar-projected images; and, secondly, the true size of features is preserved near the pole. Since the aurorae of Jupiter remain largely fixed in System-III coordinates (e.g. Clarke et al., 2004b) and are located near the geographical poles of Jupiter, the comparison of the aurora between any

two images is greatly simplified. The difference between the projection altitude and actual altitude of auroral features will introduce an error into the projected position of the aurora; however, for a typical Juno-UVS emission angle of 30° and an altitude difference of 200 km (i.e. projected vs assumed altitude of the ME), an error of some 115 km is introduced, which is equivalent to around one pixel in the polar-projected images used in this work. In conjunction with the fact that Juno views the aurora from many different positions and hence that the errors are not systematic, the error introduced by the projection was considered negligible.

In the case of image data collected using STIS, collected photons are frequently collated into 10-second image frames to investigate the evolution of auroral features over short timescales. However, for this work, each STIS exposure was instead collated into a single frame, representing the pixelwise median of all 10-second frames within the exposure. This has the disadvantage of reducing the signal from short-lived features; however, the use of median averaging is preferred over mean-averaging as it has the added advantage of reducing noise in the image and highlighting the morphology of the comparatively steady main emission, important when attempting automated analysis, as is done in this work. Features not in corotation (that move in System-III and hence also in the polar-projected images), such as the moon footprints, are not strongly filtered by this collation, provided they move sufficiently slowly.

5.1.2 Extraction of auroral arcs

The aurorae of Jupiter are composed of multiple smaller discrete features (Grodent, 2015), many of which show arc-like

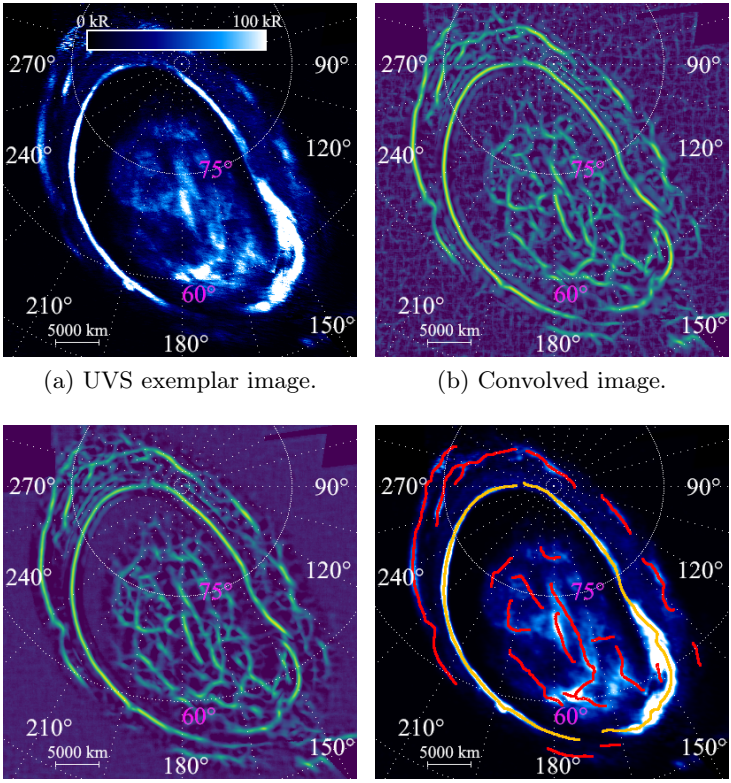

(a) UVS exemplar image.

(b) Convolved image.

(c) Convolved image with noise removal.

(d) Detected auroral arcs. ME arcs in yellow.

Figure 5.1: Arc-detection algorithm applied to the UVS exemplar image from PJ6-N. A 15°-by-15° grid in System-III longitude and planetocentric latitude is overlain on the aurora. The System-III longitude of certain gridlines are given in white, and the planetocentric latitudes of certain gridlines in magenta.

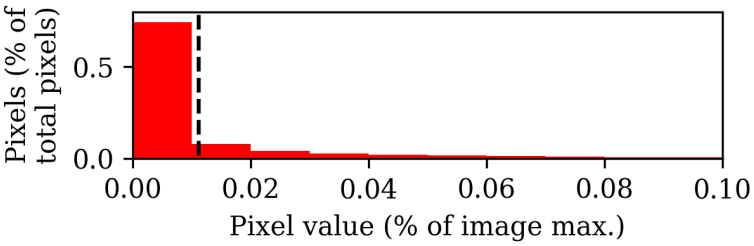

(a) Juno-UVS.

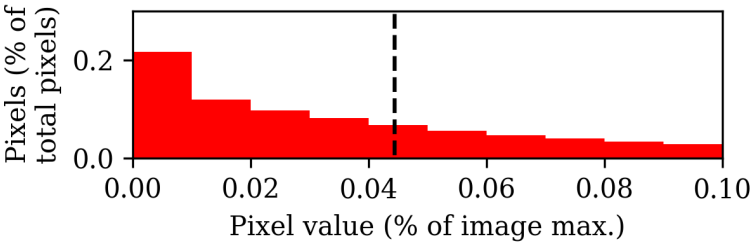

(b) HST-STIS.

Figure 5.2: Histograms of the average pixel-brightness distributions for the (a) UVS and (b) STIS images used in this work. The position of the 75th (UVS) or 50th (HST) percentile cut-off has been annotated with a dashed black line. The plot has been truncated at a percentage pixel value of 0.1 to highlight the position of the cut-off.

morphologies. Previous work (e.g. Vogt et al., 2022b; Rutala et al., 2022) tends to employ techniques that use the position of the peak in the approximately Gaussian profile of the ME around some central location in the aurora or predefined statistical oval to determine its position in the images. A nat-

ural extension of this technique would be an arc-detection algorithm that works for all arc-like structures in the aurora, even undetected arcs for which a suitable 'central point' has not been determined. The goal of this arc-detection algorithm, therefore, was the automatic extraction and characterisation of these auroral arcs, without bias toward brighter arcs, such as those found in the ME. To this end, template matching with an artificial auroral-arc profile can be used to provide a measure of 'arcness' for each pixel in the polar-projected images. In the interest of completeness, the polar-projected images used in this work are of the non-absorbed emission rather than the extrapolated full H_2 emission, though the auroral morphology is identical and the difference is merely a scaling factor of 8.1. The template element was a 13×13-pixel kernel, with a normalised Gaussian profile with a FWHM of 8 px centred along the vertical axis of the kernel. By rotating the image between 0° and 180° in 1° increments, performing the template matching against the vertical arc-profile kernel using the `match_template` function in Python3's `scikit-image` library (van der Walt et al., 2014) on each rotated image, and taking the maximum normalised response to the template matching at each pixel over all the rotations, an arcness map of the original auroral image could be obtained that is not dependent on the brightness of the auroral arcs, as in Figure 5.1b. However, background shot noise in the auroral images leads to the presence of an unwanted background pattern in the convolved arcness maps. Since the template matching produces normalised responses, the intensity of this background pattern was comparable to the intensity of the 'true' auroral arcs, despite the considerably greater brightness of the latter in the auroral images, and would interfere with the results of

later arc-detection procedures. This background pattern is dependent on the distribution of the shot noise, and, as such, neither a change in the parameters of convolution element nor repeating the template matching will diminish its presence. To remove this background pattern, the background noise level of the polar-projected auroral images was estimated by taking either the 50th-percentile (HST) or 75th-percentile (UVS) pixel value of those pixels with values greater than 0; the choice of percentile is a consequence of the different typical coverages of HST and UVS polar-projected images. As shown in Figure 5.2, these cut-offs provide a suitable boundary between background pixels (which make up the majority of any given image) and brighter pixels that form part of the aurora. HST images have much flatter distributions of pixel value due to different detector throughput, which makes the placement of the cut-off a little less obvious; nevertheless, the chosen cut-off allows the autodetection procedure to reliably detect arcs in HST images. By inserting random Gaussian noise with a mean of 0 and a standard deviation equivalent to this background level, the distribution of the background shot noise can be modified without disturbing the much-brighter auroral arcs. The template matching was performed 30 times with different random background noise profiles, and the final arcness map of an auroral image was the pixelwise median of these 30 iterations; see Figure 5.1c, where the background pattern is clearly diminished compared to Figure 5.1b. Some noise could still be seen in brighter parts of the aurora. For this work, which concentrates on the clear arc-like profiles of the ME with a considerable manual element, this noise did not materially impact the results; however, if dimmer arcs, such as the polar filaments (Nichols et al., 2009a), were to be investigated using

this algorithm, the background-noise removal process would be refined to remove this pattern from the relevant regions of the aurora.

In the case of the aurora, it is more sensible to extract the central axes of the auroral arcs via skeletonisation, rather than attempt to define the bounding shape, as auroral arcs are not structures with well-defined borders. To this end, a suitable threshold was applied to the arcness maps; it was determined a posteriori that estimating the background level BG using the same pixel-value percentile as before, this time applied to the arcness maps, then calculating $BG + 0.25(1 - BG)$ provides a suitable threshold to distinguish between true arcs and background noise. Applying this threshold to the arcness map returned a mask of the approximate arc locations in the aurora, which could be further reduced to a skeleton of the aurora through the use of the `skeletonize` function included in the `scikit-image` Python library (van der Walt et al., 2014). This auroral skeleton can be interpreted in the form of a mathematical graph, with nodes and edges, using the `sknw` Python library under the `ImagePy` framework (Wang et al., 2018), which allows for easier modification and processing of the detected auroral arcs. A number of processing steps were applied to this skeleton graph to extract individual instances of auroral arc:

- Very short arcs (fewer than 10 pixels) were removed, as these are likely to be background noise.
- Graph nodes between three edges were assumed to be the intersection between one larger arc and one smaller arc, as it is unlikely that three independent auroral arcs would meet in the same location in the aurora. To this end, the

two edges that best align at the node were associated to the same auroral arc and are hence merged together.

- Edges that exhibit very small local radii of curvature (<5 px) were assumed to consist of two auroral arcs that have been mistakenly included in the same edge, since auroral arcs are presumed to curve relatively gradually. As such, these edges were split into two arcs at the point of minimum radius of curvature.

- If two arcs were well aligned (<30° difference between straight-line fits to the arcs) and their ends close to one another (<5 px), they were assumed to form part of one larger arc than has been mistakenly split into two arcs and were hence merged together.

At the end of this processing, the set of detected individual auroral-arc instances was returned; see Figure 5.1d. Detected arcs are given in red, with those that are considered to belong to the ME highlighted in orange.

5.1.3 Characterisation of auroral arcs

To perform further analysis on arc-like structures in Jupiter's aurorae, it is necessary to extract key properties of the detected arcs. Many of these properties (such as arc brightness, position, ...) can be trivially retrieved by reprojecting the detected arcs onto the polar-projected auroral images. However, several arc properties have slightly more involved derivations.

In much the same way that a representative 'exemplar' auroral brightness map can be constructed for each perijove, as in section 5.1.1, an exemplar auroral colour-ratio map can be

established from the ratio between the radiance at 155-162 nm and at 125-130 nm (Bonfond et al., 2017c). Whereas the auroral brightness contains information about the flux of the precipitating electrons, the colour ratio can be used as a proxy for the electron energy; higher-energy electrons are expected to be able to penetrate further into Jupiter's atmosphere, where flux in the 125-130 nm band is more strongly attenuated by the CH_4 layer, thus leading to a higher ('redder') colour ratio.

In this work, the JRM33 internal-magnetic-field model of Jupiter (Connerney et al., 2022) was used together with the Con2020 model of the external (ECS) magnetic field (Connerney et al., 2020) to model the total magnetic field, and to provide mappings between ionospheric and presumed ECS locations of detected auroral arcs. An 18th-order JRM33 magnetic-field fit is used to ensure the best-possible correspondence between the modelled and observed positions of the moon footprints, particularly that of Ganymede (Moirano et al., 2024). These models are contained within the `JupiterMag` Python wrapper (James et al., 2022) as part of the Magnetospheres of the Outer Planets Community Code project (Wilson et al., 2023).

The Con2020 model does not take into account local-time variations in the configuration of the magnetic field, and so an error is introduced. By using a model of the external field that does take into account this local-time variation, notably the KK2005 model of Khurana and Schwarzl (2005), the magnitude of this error can be estimated. A mapping was performed from 10 positions in the magnetosphere (30 R_J, evenly distributed in longitude) to the ionosphere using JRM33 + Con2020, then back to the magnetosphere using JRM33 + KK2005 (Rabia et al., 2024) at two times separated by 5 hours (half a Jovian rotation). In both the northern and southern

hemispheres, this introduces a median radial error of 5 R_J and a median longitudinal error of 1°. In this work, magnetic mapping is mainly used to obtain the magnetospheric longitude (and hence local time) of points in the main emission, with a resolution of one hour. A 1° longitude difference is equivalent to 4 minutes in local time, and hence the use of Con2020, as a more recent model that uses measurements from Juno and more accurately reflects the behaviour of the magnetic field in the inner magnetosphere (Rabia et al., 2024), is justified.

Of particular importance to this work is the correct identification of those auroral arcs that comprise the main auroral emission. The ME is broadly associated with the innermost semi-continuous bright arc in the aurora, though, as discussed above, this definition is empirical and does not prescribe a single shared magnetospheric origin to the entire ME. This morphology can be strongly disrupted by the presence of bridges (Palmaerts et al., 2024), strong injection signatures (Grodent et al., 2018), or dawn storms (Bonfond et al., 2021), among other causes. The ME can therefore have starkly different sizes and morphologies between any two images of the aurora, and, as such, designation of the approximate region of the polar-projected images that contain the ME was performed manually. This manual designation was based on the convolved images (such as Figure 5.1c) with reference to the original brightness images (Figure 5.1a) to ensure that only bright regions (typically those with brightnesses exceeding 200 kR, the upper threshold in the reference images used during the manual designation) showing strong arc-like profiles (or dimmer continuations of the same bright arc) were attributed to the ME. For each detected auroral arc, the part of the skeleton that fell within this manually designated region was taken to

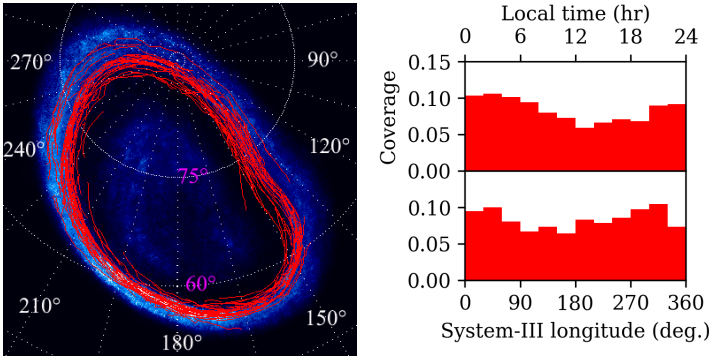

(a) North.

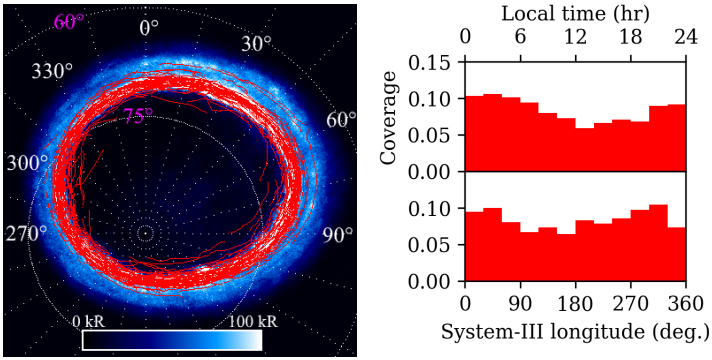

(b) South.

Figure 5.3: Detected ME arcs for perijoves 1 through 54, shown in red, overlain on the pixelwise median-average aurora for each hemisphere. Annotation is as per Figure 5.1. A histogram of the distribution of detected ME arcs in both local time (top) and System-III longitude (bottom) is given for both hemispheres.

belong to the ME. This method has the benefit of the unbiased detection of auroral arcs from the automatic arc-detection algorithm as well as the certainty that only the ME is considered for further analysis. An automatic ME designation containing those arcs within a certain distance of the average UVS main oval was a posteriori determined to be inadequate; a distance limit from the reference contour sufficiently large to capture the full range of contraction and expansion of the ME would also result in the inclusion of many detected poleward and equatorward arcs that do not form part of the ME, due to their insufficient length, misalignment with the ME reference contour, or being obviously pole- or equatorward of an ME arc. Manual designation also allows for the exclusion of the most heavily disrupted regions of the ME, where the arc-detection algorithm performs most poorly.

The results of this semi-automatic ME-detection process are given in Figure 5.3. The majority of the detected ME arcs were located on or near the reference contour for perijoves 1 to 54 (see section 5.2.1). Figure 5.3 also shows that the ME was evenly sampled in System-III longitude; there are no portions of the ME that were distinctly under- or over-sampled. This is as expected, as many features that would prevent proper detection of portions of the ME (the presence of bridges, dusk-side disruption, dawn storms) are not fixed in System-III longitude. Indeed, the typically more disrupted morphology of the ME at dusk is reflected in the slightly poorer coverage of the detected ME arcs close to 18:00, though this asymmetry is very slight and is not expected to materially affect the results of this work. Additionally, the average aurorae shown in Figure 5.3 would, at first glance, not appear to demonstrate the empirical result that approximately one third of the total auroral power can

be attributed to each of the three regions of the aurora (ME, polar emission, outer emission) (Grodent et al., 2018). This is due to the median averaging performed to obtain the average aurorae; for example, bright but transient features that dominate the power output of the polar region are disproportionately diminished by median averaging. Median averaging is used here to ensure that the ME, the main subject of this work, is as clear as possible, free from the unwanted effects of transient elements such as dawn storms.

5.2 Results and discussion

5.2.1 New reference oval for the main emission

Any investigation of the variable size of the ME must necessarily define a reference ME profile against which individual images of the ME can be compared. There exist previously defined ME reference ovals in the literature (e.g. Bonfond et al., 2012); however, for this work, new reference ovals were defined based on the average position of the ME in the UVS exemplar images between perijoves 1 and 54. These exemplar images were stacked and the pixelwise median brightness (for those pixels with UVS coverage) taken to produce an average ME profile, separately for both the northern and southern hemispheres; see Figure 5.4. This average ME profile was then convolved with a Gaussian kernel, as described in section 5.1.2, to provide a smooth and continuous contour for the average ME. A central reference point was defined for each hemisphere (left-handed System-III longitude $\phi_{S3} = 185°$, planetocentric latitude $\theta = 74°$ in the north; $\phi_{S3} = 32°$, $\theta = -82°$ in the south; taken from Bonfond et al. (2012)) and used to define

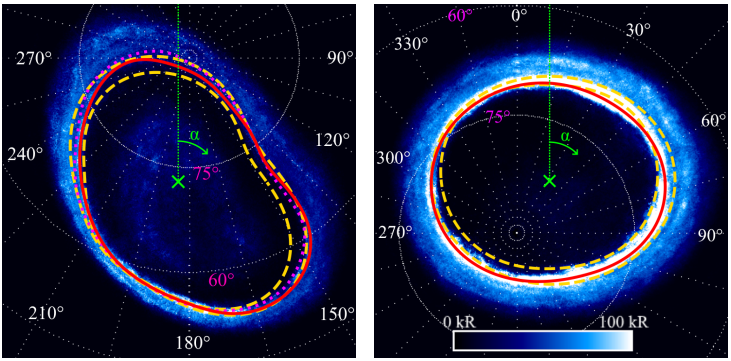

(a) North. (b) South.

Figure 5.4: ME reference ovals defined in this work, overlain on the pixelwise median-average aurora for each hemisphere. The new UVS reference oval is shown as a solid red line. The expanded and contracted HST ME reference ovals from Bonfond et al. (2012), shown as dashed yellow lines, and the northern reference oval from Nichols et al. (2017), shown as a magenta dotted line, are included for comparison. The pseudo-magnetic-coordinate reference point is denoted by a green cross, alongside the sense of pseudo-magnetic angle α. Annotation is as per Figure 5.1.

a pseudo-magnetic coordinate (radius and angle around the reference point) for each point in the ME profile. A univariate spline was fitted through the pseudo-magnetic coordinates of the pixels in the average ME contour, then converted to left-handed System-III longitude and planetocentric latitude to provide the final ME reference oval for each hemisphere. The use of pseudo-magnetic coordinates is preferred here over

System-III longitude and planetocentric latitude to ensure a sensible spline fitting that evenly samples the contour of the ME, most necessary in the northern hemisphere where the ME deviates noticeably from its idealised circular shape.

It can be seen in Figure 5.4 that the new reference ovals well describe the average position of the ME between perijoves 1 and 54 in both the northern and southern hemispheres. In some locations, such as near 30° longitude in the south, the reference oval appears to favour the inner edge of the observed average ME. This is likely a visual illusion induced by the choice of brightness threshold in the images; the quasi-Gaussian brightness profile of the ME is typically wider on the equatorward side, due to the presence of the moderately bright diffuse equatorward emission, which, when combined with the relatively low brightness threshold in the images, appears to move the arc of the ME equatorward. For the most part, they also fall within the range of ME positions determined from HST data by Bonfond et al. (2012). The UVS reference ovals differ from the Bonfond et al. (2012) and Nichols et al. (2017) reference ovals most notably at high latitudes; this is to be expected, as these previous reference ovals are based on HST observations of the ME, in which the high-latitude aurora is rendered unobservable by the typical viewing geometry. The Bonfond et al. (2012) and Nichols et al. (2017) ME reference ovals also notably underestimate the size of the average UVS ME in the northern hemisphere in the region of the magnetic anomaly along the 150° System-III meridian (Grodent et al., 2008). This normally corresponds to the dusk-side hemisphere in HST images, in which the ME tends to be contracted (Grodent et al., 2003a). It is therefore unsurprising that the HST-based reference ovals underestimate the size of the ME in this

sector. In the southern hemisphere, the ME in the 15°-to-75° longitude range normally corresponds to the dawn-side hemisphere in HST images, and it is thus equally unsurprising that the Bonfond et al. (2012) reference ovals overestimate the size of the ME in this sector.

5.2.2 Global behaviour of the main emission

Using the UVS reference oval and the automatically detected ME arcs as described in section 5.1, it is possible to calculate the average global expansion of the ME for each perijove hemisphere. Using the same central reference point as shown in Figure 5.4, the detected ME arcs for each perijove hemisphere were converted to pseudo-magnetic coordinates as per section 5.2.1. For each pixel in the ME arcs, the point on the reference oval with the same pseudo-magnetic angle was used to calculate the pixelwise expansion of the ME, since it is assumed that, for sufficiently small shifts, the aurora expands perpendicularly from the reference oval under conditions of global expansion or contraction. This expansion was calculated in kilometres by projecting the ME pixel and the reference oval to the globe of Jupiter. By taking the median pixelwise expansion of every pixel in each ME arc, an average ME expansion can be defined for each perijove hemisphere. This expansion is positive for an equatorward expansion of the ME and negative for a poleward contraction. To estimate the uncertainty in this measure of expansion, the standard deviation of the calculated pixelwise expansions was taken. To test the assumption that the ME expand perpendicularly from its reference contour, the UVS ME reference contour was expanded and contracted by 20 pixels (approximately equivalent to 2000 km, comparable

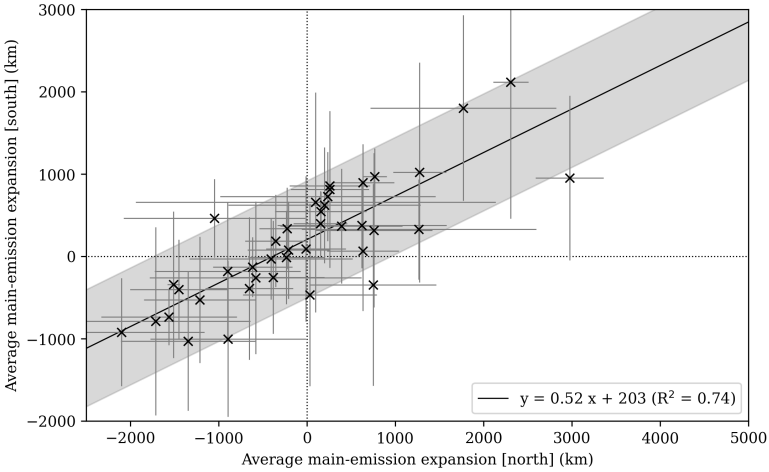

Figure 5.5: Median-averaged global ME expansion from the UVS reference oval in the north vs in the south for perijoves 1 through 54. The fitted relationship is given by a solid black line; its form and R-squared goodness-of-fit value are given in the legend. The 1σ confidence level of the fit is given by the shaded region. The position of the origin is denoted by two dotted black lines. Negative (positive) values of ME expansion indicate a global contraction (expansion) of the ME.

to the range of ME expansion seen in Figure 5.5), achieved by holding α constant and increasing or decreasing the distance from the central reference point by 20 pixels. Each point on the original ME reference contour was linked to a point on the expanded or contracted reference contour by taking the pixel with the nearest pseudo-magnetic angle. The expansion or contraction of each point was calculated. The same was

performed taking the pixel with the closest mapped magnetospheric System-III longitude and the expansion or contraction once again calculated. The median difference between these two estimations of expansion or contraction for each point on the original reference contour was less than 200 km in both the northern and southern hemispheres, which is less than the estimated uncertainty of the expansion of the ME, and so the use of pseudo-magnetic coordinates to calculate the expansion of the ME is reasonable.

Figure 5.5 provides a comparison of the global expansion of the ME between the northern and southern hemispheres. Perijoves with sufficiently poor coverage in the northern hemisphere such that the position of no part of the ME can be reliably determined have been omitted. The standard deviations of the pixelwise expansions of the detected ME for each perijove are included in Figure 5.5 as errorbars. These error bars appear considerable; however, they are dominated by the expected dawn-dusk asymmetry in ME expansion. This is evidenced by the significantly smaller average standard deviations in ME expansion when only the dawn or dusk sectors are considered: in the north, the median standard deviation is 600 km, which drops to 300 km and 400 km in the dawn and dusk sectors, and in the south, the median standard deviation is 700 km, which drops to 200 km and 400 km in the dawn and dusk sectors respectively. Figure 5.5 shows a clear (R^2 = 74%) positive correlation between the global expansion of the ME in the north and the south during a given perijove. This positive gradient indicates that expansions or contractions of the ME occur in conjunction between the two hemispheres and that the physical origin of the variability in ME expansion is a global phenomenon that affects the aurorae in both hemi-

spheres in the same manner, and indicates therefore that the process(es) giving rise to the ME are magnetospheric, and not ionospheric, in nature. The processes controlling the expansion of the ME must therefore also vary over timescales no shorter than the time required for Juno to pass from the northern to the southern hemisphere during a perijove (∼2.5 hours). The fact that the relation passes close to the origin indicates that the average position of the ME in the two hemispheres corresponds to the same magnetospheric state. Figure 5.5 also shows that the expansion of the northern ME varies around twice as much as the southern ME in absolute terms. This is as expected given the presence of the low-field-strength magnetic anomaly in the north (Bonfond et al., 2015a) and thus the same relative expansion of the ME would typically result in a larger absolute-distance expansion in the north than in the south. There is also a similar region of elevated field strength in the northern hemisphere; however, an argument based on the conservation of magnetic flux indicates that low-field anomalies will more greatly affect the movement of the ME than high-field anomalies. The reader is asked to imagine an event in the magnetosphere that stretches the field lines outward. A series of field lines will pass through an arbitrary section of the ME source region; these field lines can be thought of as a flux tube, and hence the total tube magnetic flux is conserved between the ECS and the ionosphere (IS), as

$$\Phi = B_{\mathrm{ECS}} S_{\mathrm{ECS}} = B_{\mathrm{IS}} S_{\mathrm{IS}}, \tag{5.1}$$

where Φ is the total magnetic flux in the flux tube, B_{ECS} and B_{IS} refer to the magnetic field strength, and S_{ECS} and S_{IS} to the flux-tube foot surface area in the ECS and ionosphere respectively. We are free to choose rectangular flux-tube ends,

such that

$$S_{\mathrm{ECS}} = \Delta r_{\mathrm{ECS}} l_{\mathrm{ECS}},\ S_{\mathrm{IS}} = \Delta r_{\mathrm{IS}} l_{\mathrm{IS}}, \tag{5.2}$$

where Δr refers to the radial shift of the magnetic field lines connecting the ME in the ionosphere to the ECS and l refers to an arbitrary (small) flux-tube end width. Since we are introducing an arbitrarily small radial stretch in the magnetic field lines in the ECS (such that B_{ECS} remains essentially unchanged and r_{ECS} is a small constant that we define),

$$B_{\mathrm{IS}} S_{\mathrm{IS}} = \mathrm{Const}, \tag{5.3}$$

and hence

$$\Delta r_{\mathrm{IS}} \propto B_{\mathrm{IS}}^{-1}. \tag{5.4}$$

Given this relation, and that the northern-hemisphere weak-field and strong-field anomalies are approximately half and twice as strong as the average surface magnetic field (Moirano et al., 2024), it is therefore reasonable to assume that the weak-field anomaly affects the expansion of the northern ME twice as much as the strong-field anomaly in absolute distance, and hence that the northern ME would show a greater expansion in ionospheric distance than the southern ME for a given state of the magnetosphere.

The expansion of the ME from its reference oval can also be investigated separately for regions of the ME that magnetically map to the day-side (06:00 to 18:00 local time) and night-side (18:00 to 06:00 local time) magnetosphere. Figure 5.6 shows that, in both the northern and southern hemispheres, the correspondence between the expansion of the night-side ME and the expansion of the day-side ME can be well described by a positive linear relation (91% and 73% of the total variance in

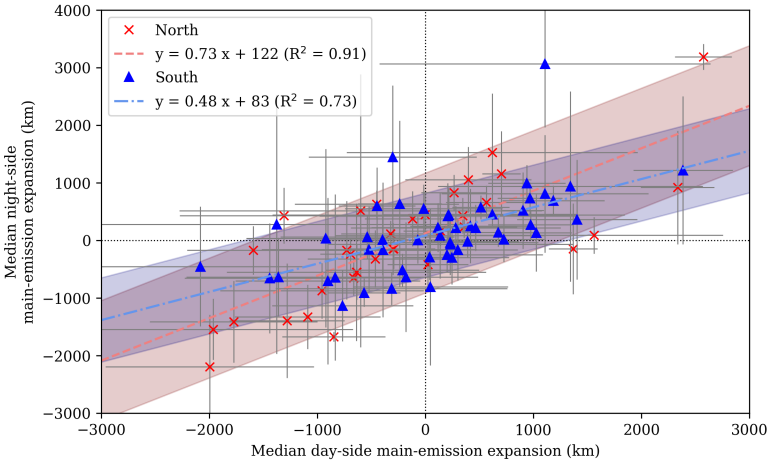

Figure 5.6: Median-averaged global ME expansion from the UVS reference oval in the day-side hemisphere vs in the night-side hemisphere for perijoves 1 through 54, for the northern (red crosses) and southern (blue triangles) aurorae. The fitted relationships are given by a red dashed line and a blue dot-dashed line for the northern and southern hemisphere respectively; their forms and R-squared goodness-of-fit values are given in the legend. The 1σ confidence levels of the fits are given by the red and blue shaded regions, for the northern and southern hemispheres respectively. The position of the origin is denoted by two dotted black lines. Negative values of ME expansion indicate a global contraction of the ME.

the data can be described by a linear relation, for the northern and southern hemisphere respectively). When the day-side ME is contracted, so too is the night-side ME. In both hemispheres, the day-side ME expands more than the night-side ME; in the southern hemisphere, the day-side ME expands and contracts more than twice as much as the night-side ME in absolute distance. The fitted relations pass through the (0,0) origin in both hemispheres to within the error of the data (approximately $\pm$400 km). In all, these results indicate that processes that work to contract the ME affect both hemispheres simultaneously, though the day-side ME is frequently affected to a greater extent.

The use of the automatic arc-detection algorithm in this work permits the systematic comparison of the global ME expansion with other parameters, such as the brightness of the ME. In this work, the median-average brightness of all pixels in the automatically detected arcs of the ME was taken as a characteristic measurement of ME brightness. We note that the median brightness of the detected ME cannot be directly related to any 'average' emitted auroral power measured by Juno-UVS and depends on the pixel binning of the polar projections; however, it does allow for the straightforward comparison of a characteristic brightness of the ME between images, or between different regions of the ME in the same image. To ensure a sensible comparison, only those perijoves with a pseudo-magnetic ME coverage greater than 80% were taken, which amounts to 8 cases in the north and 25 cases in the south. We note that 'coverage' refers to the total pseudo-magnetic angular coverage of detected arcs that can be reliably associated with the ME; it is possible that the entire aurora be imaged by UVS yet the coverage be less than 100% if, for example,

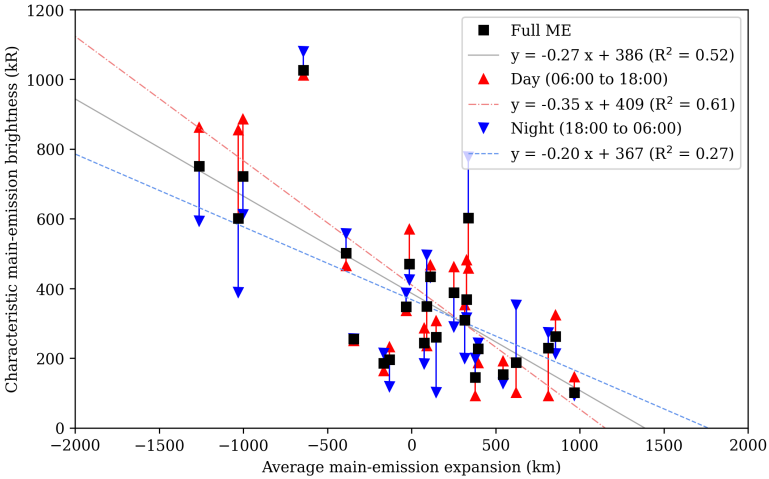

Figure 5.7: Characteristic ME brightness vs the median-averaged global ME expansion from perijoves 1 through 54, in the southern hemisphere. The characteristic brightness of the entire ME is given by black squares, and the characteristic brightness of only the day- and night-side hemispheres by red and blue triangles respectively. Linear fits to the data have been calculated and shown as a black solid line (full ME), a red dashed line (day), or a blue dotted line (night). The form and R-squared goodness-of-fit value of these fits are given in the legend.

parts of the ME are too dim or morphologically disrupted to be unquestionably identified as belonging to the ME. Figure 5.7 shows that, in the southern hemisphere, the characteristic ME brightness increases with contraction (negative expansion) of the ME. The R^2 value of this relationship indicates that a

linear response in ME brightness to ME contraction can account for 52% of the variance in the data; given the frequent presence of additional features on the ME that can contribute significantly to the detected brightness (dawn storms, disrupted morphologies), it is noteworthy that more than half of this brightness variability can be attributed to a simple response to ME contraction. Therefore, in an ideal ME, one without additional features superimposed, it would be expected that the contraction-brightness relationship be even clearer. The brightness of the ME is typically within the expected range of 50 to 500 kR as measured by HST (Grodent et al., 2003a). The results for the northern hemisphere have been omitted from Figure 5.7 for the sake of clarity and the comparatively few perijoves (8) with the necessary 80% coverage of the ME by UVS. Although a coverage of 80% was selected as a suitable threshold, the same relationships between ME expansion and brightness are present for coverage thresholds between 50% and 99%, though the strength of this relationship decreases at lower coverage thresholds. The observed relation between ME expansion and brightness is therefore not merely an artefact of the selected cases.

Additionally, Figure 5.7 displays separately the characteristic brightnesses of the day-side and night-side ME, the regions of the ME that magnetically map to the ECS from 06:00 to 18:00 and from 18:00 to 06:00, respectively. This shows that the positive dependence of the brightness of the ME on the contraction (negative expansion) of the ME is far more striking in the day-side hemisphere, with a given ME contraction increasing the day-side brightness by almost twice as much as the night-side brightness. If the global contraction of the ME can be associated with an increased solar-wind ram pres-

sure, as indicated by models (Promfu et al., 2022), this result stands in opposition to the expected behaviour of a FAC-driven ME; both magnetohydrodynamical simulations (Chané et al., 2017; Sarkango et al., 2019; Feng et al., 2022) and observations (Lorch et al., 2020) agree that solar-wind compression more greatly increases the density of FACs on the night-side hemisphere. This is discussed in greater detail and in the context of further results below in section 5.2.7.

5.2.3 Local-time dependence of the morphology of the main emission

In addition to investigating the global behaviour of the ME, it is equally possible to analyse how the properties of the ME change in local time, as shown in Figure 5.8. The arcs of the ME were projected to the ECS using the JRM33 internal-field and Con2020 external-field models, as described in section 5.1.3, to allow for more meaningful comparison between the northern and southern aurorae. The projected ME arcs were binned in ECS local time in three-hour bins separated by one hour, and then the median average of each bin taken; this overlap between bins serves to smooth the data shown in Figure 5.8.

It can be seen in Figure 5.8 that, in the north as well as the south, the ME tends to be contracted on the dusk side and expanded on the dawn side compared to the ME reference position, which is produced from the average ME position in many different images of the aurora (with many different subsolar longitudes) in which dawn-dusk asymmetries are smoothed out. This is in broad agreement with the local-time dependence of the ME mapping of Vogt et al. (2011),

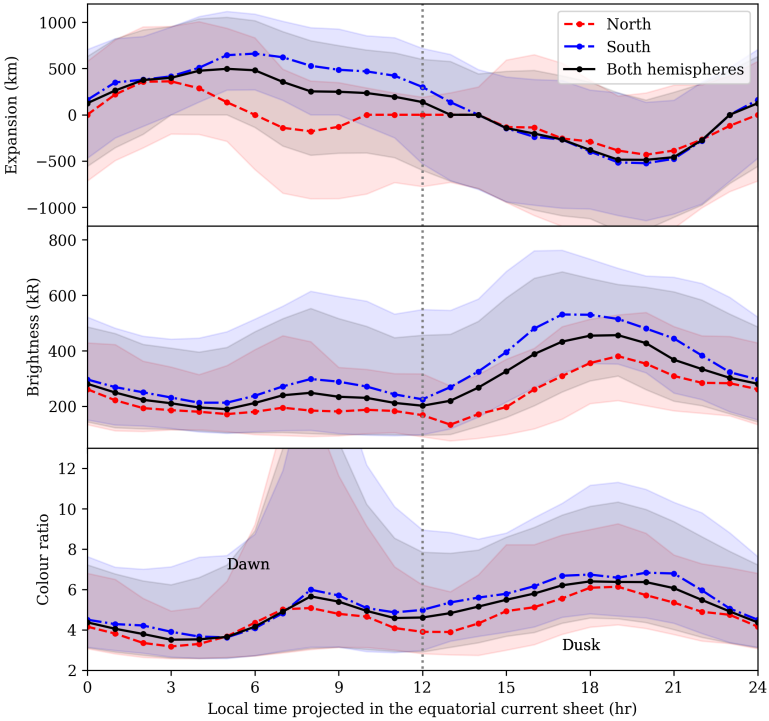

Figure 5.8: Median-averaged expansion, characteristic brightness, and colour ratio of the ME as a function of projected local time in the ECS. The northern hemisphere is given by a red dashed line, the southern hemisphere by a blue dot-dashed line, and both hemispheres by a solid black line. The interval spanned by the 25th-to-75th percentile range has been shaded for each series.

which was associated with a corotation-enforcement current or plasma outflow rate that is local-time dependent. The range given by the 25th-to-75th-percentile values in each bin, given by the shaded regions in Figure 5.8, is comparable between both hemispheres and is approximately uniform around the median value. The northern hemisphere is less locally variable in expansion than the southern hemisphere, which appears to stand in contrast to the global variability discussed previously. However, one must be careful to distinguish between the local-time dependence of the expansion of the ME, which may be understood as a consequence of its local-time-dependent mapping to the ECS (Vogt et al., 2022b), and the global expansion of the ME relative to the reference oval, which has previously been linked to the effect of solar-wind pressure or the varying strength of the ECS magnetic field (Promfu et al., 2022). Here, it may be said that the expansion of the dawn-side northern ME depends slightly less strongly on local time than the conjugate ME in the south, though the comparatively poor coverage of UVS in the north (only 8 perijoves with northern ME coverages >80%, against 25 in the south) limits the strength of this conclusion.

The characteristic brightness of the ME also shows a strong dependence on local time. As in the discussion around Figure 5.7, the characteristic brightness is defined as the median-average brightness of all pixels in the detected arcs of the ME, now binned in local time. The dusk-side ME is typically twice as bright as the dawn-side ME, with this difference being more pronounced in the south than in the north, which is in agreement with previous observations (Bonfond et al., 2015a; Groulard et al., 2024). These works noted that the power emitted from the dusk-side ME is around four times

greater than that from the dawn-side ME. This is consistent with the result presented here, since emitted power is a consequence of both ME brightness and ME width, and the dusk-side ME is known to be around twice as wide as the dawn-side ME (Grodent et al., 2003a). The simulations performed by Chané et al. (2017) also predicted this dawn-dusk ME brightness asymmetry. They also predicted a far greater day-night asymmetry in ME brightness; however, the dawn-dusk asymmetry in brightness in Figure 5.8 is more striking than a day-night asymmetry, if one is indeed present. In contrast to the dusk-side ME, neither the day- nor night-side ME show consistently disrupted morphologies, so this lack of obvious day-night asymmetry is unlikely to be a result of poor sampling by the arc-detection algorithm. The lack of obvious day-night asymmetry in the brightness of the ME is difficult to reconcile with the modelled (Chané et al., 2017) and observed (Lorch et al., 2020) predominance of FACs in the night-side magnetosphere, if FACs give rise to the ME, as is the case in the explanation related to corotation-enforcement; this is discussed in more depth in section 5.2.7. The colour ratio of the ME also peaks at dusk; this is likely a consequence of the established dependence of ME colour ratio on ME brightness (Gérard et al., 2016). The brightness and, more clearly, the colour ratio also show a secondary peak around 09:00. This may be attributed to the presence of dawn storms, transient auroral features that appear on the dawn-side ME that show increased brightnesses and colour ratios (Bonfond et al., 2021) and lead to a peak in electron deposition at dawn (Rutala et al., 2024). The strong peak in the 75th-percentile colour ratio around 09:00 supports the presence of a number of discrete, high-colour-ratio structures at dawn, which are very likely to be dawn storms. Dawn

storms disrupt the clear arc-like nature of the ME, and thus are usually not included in the detected ME arcs. If they were included, both the brightness and colour ratio would show strong peaks between 06:00 and 12:00, since dawn storms are bright, high-colour-ratio features that appears in around one-third of the UVS images used in this work, in line with previous estimates (Bonfond et al., 2021). However, it is possible that smaller, less disruptive pseudo-dawn storms (Bonfond et al., 2021), frequently observed in the aurora (Rutala et al., 2022), are included in the dataset, which are the likely origin of this secondary peak. These are small features that lie on the ME and so are unlikely to affect the measure of ME expansion, both locally and globally.

5.2.4 Comparison with the Ganymede footprint

Expansion or contraction of the ME can be potentially understood as the consequence of two physical processes. Firstly, the magnetic-field-line mapping between the ECS and the ionosphere may be variable. For a fixed ME source region in the ECS, a variable magnetic mapping would move the ME poleward (contraction) if the field lines themselves were compressed, and equatorward (expansion) if the field lines were expanded. Alternatively, it may be that the ME source region itself varies in position in the magnetosphere, which would translate to a variable global ME expansion. It is possible to use the position of the Ganymede footprint (GFP), as the moon closest to the presumed ME source region at 30 R_J with a consistently visible auroral footprint (Hue et al., 2023), to distinguish between the relative contributions of these two parameters (Vogt et al., 2022b). Since the magnetospheric source

region of the GFP, Ganymede, is unlikely to vary its distance from Jupiter as a function of, for example, magnetospheric compression, a correlation between the global ME expansion and the movement of the GFP relative to a fixed reference path would imply that a change in the magnetic mapping is largely responsible for the variable expansion of the ME. If the two show little or no correlation, it is likely that the movement of the ME magnetospheric source region plays a larger role. Additionally, since the effect of a variable ECS magnetic field on the mapping of auroral features would become more prominent with distance into the magnetosphere, the latitudinal shift of the GFP is expected to correlate more strongly than the shift of the Europa footprint (EFP) with the ME expansion, which itself would correlate more strongly than the Io footprint (IFP).

In this work, the position of the IFP, EFP, and GFP were (where visible) manually identified in each of the UVS exemplar images. The position of these spots were compared with the magnetic-field-line mapping (as per section 5.1.3) of the orbit of their respective moons to an altitude of 900 km (Hue et al., 2023) from the one-bar level to determine the shift of the moon footprint from a fixed reference path, in much the same way as the UVS ME reference was used in section 5.2.1. Here, the use of the magnetically mapped moon-footprint path is preferred over the use of the latest empirical paths based on UVS observations (Hue et al., 2023) since it is precisely the shift in position of the footprints in UVS images that is being measured in this work, and so comparison with a path independent of UVS image data is more sensible. The moon footprints are, in fact, made of multiple discrete spots (Bonfond et al., 2013b,a), but only the brightest of these spots, which is

frequently but not always the Main-Alfvén-Wing (MAW) spot (Hue et al., 2022), was considered in this work. Since only the shift in magnetic latitudes of the footprints (perpendicular to the footprint path) are considered in this work, rather than any shift in longitude (along the footprint path), there is no need to distinguish between the various spots that compose the moon footprints. Indeed, previous work has noted that the latitudinal positions of the MAW spot and the footprint tail do not show any meaningful deviation (Moirano et al., 2024), and so the position of the footprint tail is a suitable measure of the latitudinal shift of the moon footprint.

As shown in Figure 5.9, the latitudinal shift of the southern GFP relative to the magnetically mapped reference contour shows a reasonable ($R^2 = 0.42$) correlation with the ME expansion, in agreement with early results based on limited data (Grodent et al., 2008). It is also in agreement with more recent work which found a moderate agreement between expansion of the day-side ME and latitudinal shift of the GFP (Vogt et al., 2022b), though the relation found in this work is both stronger and applicable over a wider range of ME expansions. The uncertainty in the position of the moon footprints in Figure 5.9 has been estimated from their average apparent radius of 3 px. This result indicates that it is likely to be a changing magnetic mapping between the ME source region and the ionosphere that best explains the variability in the global expansion of the ME. This may be due to a changing current intensity in the magnetodisc, and hence a changing contribution to the total magnetic field of Jupiter, which works to stretch the magnetic field lines outward. This would correspond to an expansion of the ME when the magnetodisc current intensity is elevated, which can occur during periods of increased plasma outflow

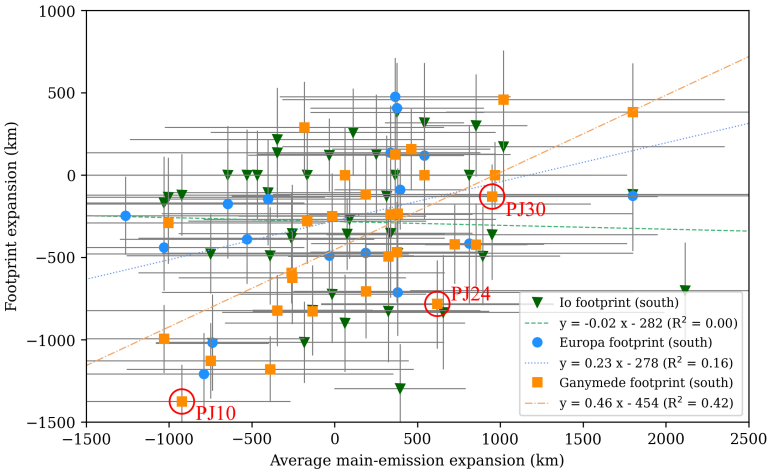

Figure 5.9: Median-averaged expansion of the southern ME relative to the UVS reference oval vs the expansion of the Io, Europa, and Ganymede auroral footprints relative to their magnetically mapped contours at 900 km. The expansion of the Io footprint is denoted by green triangles, that of the Europa footprint by blue circles, and that of the Ganymede footprint by orange squares. The fitted relation between the Io-footprint expansion and the ME expansion is denoted by a green dashed line, that between the Europa-footprint location and the ME expansion by a blue dotted line, and that between the Ganymede-footprint location and the ME expansion by an orange dot-dashed line. The forms and R-squared goodness-of-fit coefficients of these relations are given in the legend. Cases at similar System-III longitudes have been annotated and highlighted with red circles.

from the Io torus (Nichols, 2011). The magnetic-field mapping to the ionosphere from the ME source region and Ganymede, both at a greater distance from Jupiter than Io, would be influenced by the changing ECS magnetic field. However, the mapping between the ionosphere and Io itself, where the magnetic field is essentially dipolar (Promfu et al., 2022), would remain relatively unaffected; indeed, Figure 5.9 shows that the footprint of Io does not demonstrate any correlation with the expansion of the ME ($R^2 = 0.00$). The latitudinal shift of the EFP, as expected of an intermediary moon, shows a correlation with the ME expansion that has both a gradient and R^2 goodness-of-fit between those of the IFP and the GFP. This indicates that the effect of the variable field-line stretching on the latitudinal shift of auroral features becomes more prominent with distance from Jupiter, as expected. The majority of the cases in Figure 5.9 show GFP latitudinal shifts in line with predictions from models (±650 km) (Moirano et al., 2024). Nevertheless, the IFP does show variations from its reference contour of comparable magnitude to those of the GFP. This may be in part due to the weaker magnetic field in the ionosphere at lower latitudes, which amplifies even the smaller magnetic variations expected at Io to be of similar magnitude to those of the higher-latitude GFP in absolute (km) terms. Overall, the ME moves twice as much compared to its reference contour than the GFP. This is as expected, since the ME source region is around twice as far into the magnetosphere as Ganymede, where Jupiter's internal magnetic field is weaker, and thus the ME magnetic mapping is affected to a greater extent by an increased magnetodisc field than that of the GFP.

There exists a considerable scatter in the GFP data around their fitted relation, which is possibly due, in part, to system-

atic under- or over-estimation of the average GFP latitude by parts of the magnetically mapped reference contour. Given the comparatively few detections of the GFP in this dataset, it is not possible to robustly determine which parts of the reference contour show systematic inaccuracies and where the GFP shows a genuine deviation from its nominal location. Nevertheless, the variation of the latitudinal shift of the GFP within a small region of the reference contour can be analysed in an effort to quantify this systematic error. In Figure 5.9, three cases with similar GFP System-III longitudes in a region of the reference contour that is suspected to underestimate the latitude of the GFP have been highlighted: PJ10 ($\phi_{S3} = 272°$), PJ24 ($\phi_{S3} = 283°$), and PJ30 ($\phi_{S3} = 267°$). All three cases appear to show poleward GFP shifts despite the considerable range in ME expansion that they encompass, which indicates that the reference contour is indeed underestimating the latitude of the GFP in this range. Additionally, these three cases show the same positive relation between the expansion of the ME and the latitudinal shift of the GFP, suggesting that some portion of the scatter around the fitted linear relation is due to systematic errors in the reference contour.

In all, the results indicate that a changing magnetic-field mapping, likely due to a variable contribution to the total magnetic field by the ECS, can largely account for the variable expansion of the ME. Its R-squared value indicates that a linear relation between the expansions of the ME and the GFP can account for 46% of the variability in the data. Care must be taken, however, when using this goodness-of-fit value to make physical conclusions. The conclusion offered, that a changing magnetic mapping largely accounts for the variable expansion of the ME, is not based simply on the relation between the

expansion of the ME and the GFP, but rather on the combination of the linear relation between the expansion of the ME and the GFP, and the lack of linear relation between the expansion of the ME and the IFP. In this, therefore, the statistical strength of this conclusion does not allow itself to be easily deduced from the goodness-of-fits of the two relations. One can imagine the case where the two relations shown in Figure 5.9 perfectly describe the data; in this case, both R-squared values would be unity, and the changing-magnetic-mapping model would be strongly supported. However, if the relation between the ME and IFP expansions instead showed a positive gradient comparable with the relation between the ME and GFP expansions, the proposed conclusion would be less strongly supported, despite the R-squared values of unity, as it would no longer agree with the premise that the magnetic field at Io depends much less strongly on the state of the ECS. Thus, the credibility of the proposed conclusion depends on a combination of the parameters of the linear relations, their R-squared values, and the accompanying physical interpretation. This does not exclude other explanations for this variability, such as a moving ME source region, instead only indicating that the changing magnetic mapping implied by the relation shown in Figure 5.9 accounts for a large portion of the variability in the data. Indeed, in one set of HST images, the GFP was detected poleward of the ME (Bonfond et al., 2012), which indicates that the ME source region can move. This displacement of the ME source region was linked to an increased mass outflow rate from the orbit of Io, which would also work to stretch the magnetic field lines. Thus, it is possible that this variability in position of the ME source region can partially account for the spread of the data in Figure 5.9.

5.2.5 Comparison with magnetodisc current strength

Indeed, the relationship between the ECS magnetic-field strength and the expansion of the ME can be more directly studied using the magnetodisc current constants fitted to each perijove (Vogt et al., 2022a), as shown in Figure 5.10a. The global expansion of the ME shows a positive correlation with the magnetodisc current constant, which is consistent with an outward stretching of the magnetic field lines by the magnetodisc (Vogt et al., 2022b) and hence with the conclusions drawn from Figure 5.9. The same relationship is also present in the perpendicular shift in the GFP, as expected from Figure 5.9. In both cases, a linear relation with the magnetodisc current constant accounts for around one third of the variation in the data. This relationship was not previously found in a similar analysis of HST data (Vogt et al., 2022b), though this is possibly due to the large uncertainty in the limb fitting of Jupiter in HST images (Bonfond et al., 2017c). Vogt et al. (2022a) estimated an average magnetodisc current constant $\mu_0 I_{MD}$ of 288 nT; the fitted relationship for the southern ME in Figure 5.10a predicts a very small global ME expansion of 92 km (less than one pixel in the polar-projected images) at this value of magnetodisc current constant, which supports the use of the ME reference oval defined in this work as the average position of the ME. This relationship can be interpreted in the context of an outward stretching of the global magnetic field when the azimuthal current in the magnetodisc, and hence the ECS contribution to the magnetic field, is elevated, which leads to the mapping of the fixed ME magnetospheric source region to a smaller M-shell and therefore an expansion of the ME (Vogt et al., 2017). Field-line tracing using the JRM33 + Con2020 magnetic-field

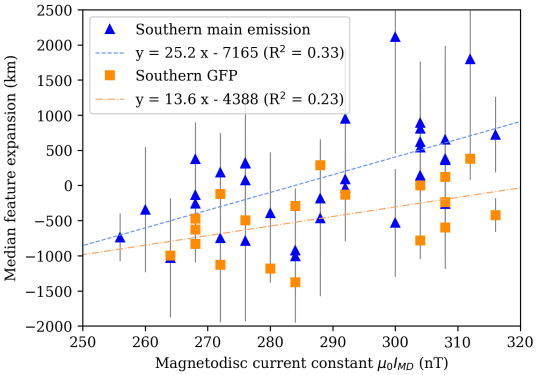
Southern main emission
y = 25.2 x - 7165 (R² = 0.33)
Southern GFP
y = 13.6 x - 4388 (R² = 0.23)
Median feature expansion (km)
Magnetodisc current constant $\mu_0 I_{MD}$ (nT)

(a)

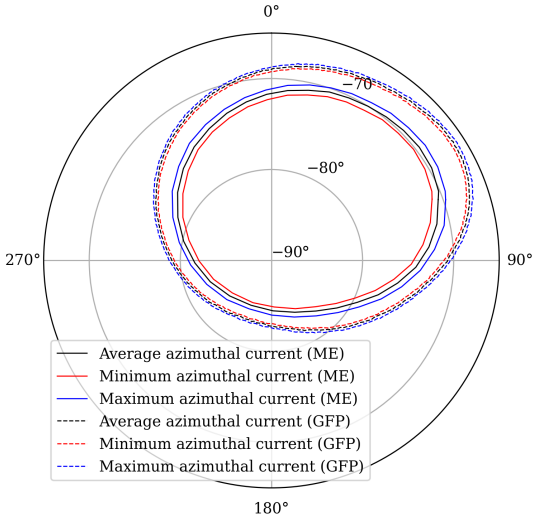
0°
−70°
−80°
−90°
270°
90°
180°
Average azimuthal current (ME)
Minimum azimuthal current (ME)
Maximum azimuthal current (ME)
Average azimuthal current (GFP)
Minimum azimuthal current (GFP)
Maximum azimuthal current (GFP)

(b)

Figure 5.10: (a) Magnetodisc current constant fitted to perijoves 1 through 34 after Vogt et al. (2022a) vs the median-averaged global expansion of the ME relative to the UVS reference oval and the expansion of the Ganymede auroral footprint relative to its mapped contour at 900 km, in the southern hemisphere. The global ME expansion in the south is denoted by blue triangles, and the expansion of the southern Ganymede footprint by orange squares. The fitted relation between the ME expansion and the current constant is denoted by a blue dashed line, and that between the Ganymede-footprint location and the current constant by an orange dot-dashed line. The form and R-squared goodness-of-fit values of the fitted relations are given in the legend. (b) Auroral mapping of the southern UVS ME reference oval (solid lines) and the southern GFP (dashed lines) using the JRM33 + Con2020 magnetic-field model with azimuthal current constants equivalent to the average (288 nT, black), minimum (256 nT, red, innermost), and maximum (316 nT, blue, outermost) values shown in (a). The System-III longitudes of gridlines are annotated around the outside of the plot, and the planetocentric latitudes next to circular gridlines.

model (Figure 5.10b) indicates that an increased magnetodisc current constant should indeed lead to an expansion of the ME. The model predicts an ME contraction of -650 km at the minimum magnetodisc current constant and an expansion of 660 km at the maximum, which is in agreement with the fitted relation in Figure 5.10a to within the uncertainty of the data. Figure 5.10b also shows that the GFP is expected to ex-

pand or contract with the ME but to a smaller absolute extent (±310 km vs ±660 km for the ME), which is in quantitative agreement with the fitted relation shown in Figure 5.9.

This variability in azimuthal current may be the result of variable plasma mass outflow from the Io torus, which works to stretch the magnetic field lines outward and hence move the ME and GFP equatorward (Nichols et al., 2009b). Additionally, compression of the magnetosphere by the solar wind has been observed increase current-sheet intensity (Xu et al., 2023) and to move the GFP (Promfu et al., 2022) and the day-side ME (see section 5.2.6 below) poleward, which may explain some portion of the variance in the data shown in Figure 5.10. Therefore, the variability in the expansion of the ME is likely a combination of both internal (mass loading from the Io torus) and external (solar wind) sources. To distinguish between these two sources, information regarding the timescale of the change in the ME expansion is required. Changes due to solar-wind pressure are expected to occur over periods of several hours (Chané et al., 2017), whereas those changes due to increased plasma outflow from the Io torus are expected to happen over longer timescales of several weeks (Bagenal and Delamere, 2011; Nichols et al., 2017; Tao et al., 2018).

5.2.6 Comparison with magnetospheric compression state

As Juno passes through the magnetopause, it is possible to determine the state of compression of the magnetosphere (Yao et al., 2022). This is accomplished via the detection of trapped low-frequency radio continuum radiation, which indicates the crossing of the magnetosheath by Juno; were the magneto-

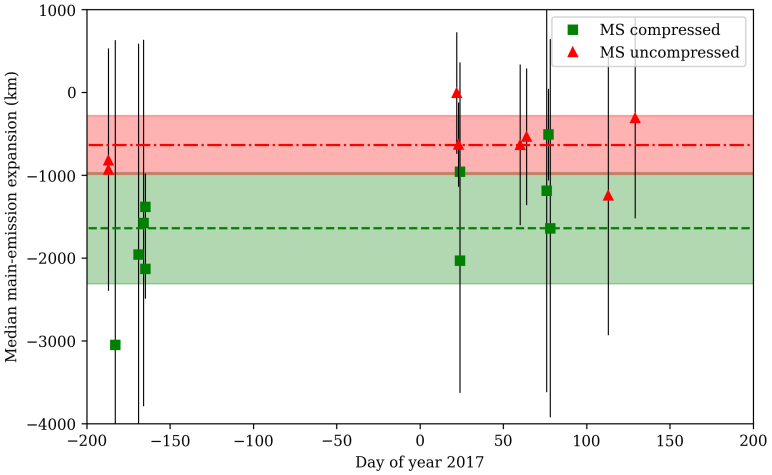

Figure 5.11: Imaging date (as day-of-year 2017) vs the median-averaged global ME expansion from the UVS reference oval for those northern-hemisphere HST image series with known magnetospheric (MS) compression states, after Yao et al. (2022). An uncompressed magnetosphere is denoted by a red square and a compressed magnetosphere by a green triangle. The average ME expansion in the uncompressed-magnetosphere case (-600 km) is denoted by a red dot-dashed line, and that in the compressed-magnetosphere case (-1600 km) by a green dashed line. The shaded regions around each average-value line denote the 1σ range.

sphere compressed, this crossing would occur at a lower altitude. Since Juno is necessarily far from the planet when this occurs, no UVS image data are collected for comparison with the compression state of the magnetosphere. However, in many cases, HST image data are available during the period that Juno crosses the magnetopause. These HST data come with two caveats: firstly, that only the day-side ME can be imaged by HST; and secondly, that HST-STIS images have relatively large uncertainties in the centring of Jupiter (± 8 px $\sim$ 800 km) (Bonfond et al., 2017c). Additionally, only northern-hemisphere cases have been considered due to their favourable viewing geometry and a paucity of suitable HST image series imaging the southern hemisphere.

As shown in Figure 5.11, the average global ME contraction in the northern hemisphere shows a strong correlation with the compression state of the magnetosphere; when the magnetosphere is compressed, the day-side ME is also contracted. This behaviour is in line with results from modelling work, which indicate that increased solar-wind dynamic pressure compresses the day-side field lines, moving the day-side ME poleward, and that increased plasma mass outflow from the Io torus stretches the day-side magnetic field lines outwards, moving the day-side ME equatorward (Promfu et al., 2022). The errorbars in Figure 5.11 may look substantial, but they do not represent a true error or uncertainty in the calculated ME expansions, but rather show the distribution of pixelwise expansions along the detected ME, subject to the significant but expected dawn-dusk asymmetry in the size of the ME. The 1σ ranges of the two data series overlap only very slightly, indicating that the difference in the average contraction of the ME in magnetosphere-compressed and magnetosphere-uncompressed cases is of reas-

onable statistical significance. It should be noted here that, due to the typically more disrupted morphology of the dusk-side ME during magnetospheric compression (Yao et al., 2022) and its resulting unsuitability for the arc-detection algorithm, the compressed-magnetosphere cases in Figure 5.11 are likely biased toward the dawn-side ME. However, this is not necessarily an issue when interpreting Figure 5.11. It has been previously shown (Figure 5.8) that the dawn-side ME tends to undergo expansion from the average ME position, and that, conversely, the dusk-side ME tends to be contracted; did the dusk-side ME not show this disruption during magnetospheric compression, and were it hence more consistently included when determining the global ME expansion, it would likely only serve to make the distinction between magnetosphere-compressed and magnetosphere-uncompressed cases more striking. Additionally, in HST images of the northern hemisphere, the dusk-side ME is located in the region of the low-strength magnetic anomaly and therefore moves more in kilometre terms than the dawn-side ME for a given change in the magnetic field, which would lead to an even greater distinction between the magnetosphere-compressed and magnetosphere-uncompressed cases if the dusk-side ME was more consistently included.

5.2.7 Interpreting the results in the context of theories of ME generation

Existing models of ME generation under both FAC-based and Alfvénic frameworks are not entirely sufficient to explain the appearance and behaviour of the ME. We consider three recent models of the distribution of FACs in the Jovian magnetosphere:

- The model of Chané et al. (2017) predicts a steady-state ME that is brightest at night and dimmest during the day, with a slight dawn-dusk asymmetry in favour of the dusk-side emission. In response to a solar-wind compression, the ME undergoes a dramatic brightening in night-side sector, a lesser brightening at dusk, and a slight dimming in the day-side ME.

- The model of Sarkango et al. (2019) predicts a steady-state ME that is brightest at night and dimmer during the day, but with no observable dawn-dusk asymmetry. In response to a forward solar-wind shock, the ME undergoes a brightening in night-side sector and a slight dimming in the day-side sector. In the presence of a Parker-spiral-type shock, the dusk-side ME also undergoes a strong brightening.

- The FAC-based model presented in Feng et al. (2022) predicts a steady-state ME that is brightest during the day and at dawn, in contrast to the two models above. Additionally, during solar-wind compression, the ME is to increase in brightness in a uniform way.

Two of the three models given above predict FACs, responsible for generating the ME in the corotation-enforcement-current model (Cowley and Bunce, 2001), that are stronger at night, which has been observed by Juno (Lorch et al., 2020). If these currents give rise to the ME, it would be expected that the steady-state ME be brighter at night than during the day. However, as previously discussed in section 5.2.3, the dominant asymmetry in the ME is a dawn-dusk asymmetry; only the model of (Chané et al., 2017) predicts a (slight) dawn-dusk

asymmetry, and this is overshadowed by the far-greater day-night asymmetry predicted by the model, which is not found in this work. Feng et al. (2022) also predicts a dawn-dusk asymmetry, but one where the dawn-side ME is brighter than the dusk-side ME, inconsistent with the other models and Figure 5.8. FAC density is also predicted to be far greater during the day than at night in this model, which is inconsistent with the other models and observation (Lorch et al., 2020).

Additionally, the responses to solar-wind compression of the magnetosphere, which has been shown to contract the ME, that are predicted by these models do not well align with the observed behaviour. Firstly, to link a global contraction of the ME with compression of the magnetosphere, several steps are required. Firstly, it has been determined that the day-side ME and the night-side ME expand and contract together (Figure 5.6); under conditions of global contraction of the ME, both the day- and night-side are also contracted from their average location. Secondly, under conditions of magnetospheric compression, the day-side ME was observed to be consistently contracted (Figure 5.11). These two results suggest that compression of the magnetosphere results in a global contraction of the ME. Under global contraction, the ME is observed to undergo global brightening. This brightening is both more prominent and better correlated with ME contraction in the day-side ME (Figure 5.7). The brightness of the night-side ME is both less prominent and shows a poorer (though still present) correlation with global ME contraction than the brightness of the ME as a whole. This is in disagreement with the modelled response of the FACs to solar-wind compression by Chané et al. (2017) and Sarkango et al. (2019), in which the night-side FACs increase in strength and the day-side FACs remain approximately con-

stant or undergo a slight reduction. The model of Feng et al. (2022) does predict an increase in the strength of the day-side FACs during solar-wind compression, though this accompanied by a night-side increase of equal magnitude, which is not supported by this work.

An Alfvénic model for the generation of the ME may better explain these results. It has been previously estimated that the Alfvénic Poynting flux is of the order of 62 to 620 mW m^{-2} in the auroral acceleration region (Pan et al., 2021), which is consistent with the downward energy fluxes, thought to give rise to the Jovian aurorae, measured by the JEDI instrument aboard Juno (Mauk et al., 2017c). The dusk-side middle magnetosphere is known, from Galileo magnetometer measurements, to have a greater degree of turbulence than the dawn-side middle magnetosphere; under the Alfvénic framework of Saur et al. (2003), this would correspond to a greater generation of Alfvén waves in the dusk-side magnetosphere and hence a brighter dusk-side ME, as demonstrated in this work.

Feng et al. (2022) also includes the results of an Alfvénic model of the ME. During periods of compression of the magnetosphere by the solar wind, this predicts an increase in auroral Alfénic power, most notably in the day-side aurora, which is broadly consistent with the findings of this work. However, in their simulation, this increase in day-side Alfvénic power is also accompanied by an increase in the day-side FACs, and so this model does not necessarily support an Alfvénic framework over a FAC framework. Solar-wind compression of the magnetosphere also leads to an expansion of the ME in this model, in both the FAC and Alfvénic frameworks, which is inconsistent with the results of this work. The peak in the intensity of the FACs does not correspond to exactly the same location in

the aurora nor does it occur at exactly the same time after the solar-wind shock as the peak in the Alfvénic Poynting flux. Additionally, this model would indicate that, in the steady state, the aurora is brightest in the day- and dawn-side sectors, which is not consistent with other models nor observations.

As it stands, neither the proposed FAC-based nor Alfvénic ME-generation mechanisms are fully consistent with observation, and deeper analysis of turbulence within the magnetosphere is required. Additionally, information regarding the timescale of the changes in the expansion of the ME is necessary to distinguish between the response of the ME to solar-wind compression and torus-mass-outflow inflation of the magnetosphere, as well as to distinguish between the response of a FAC-based and Alfvénic ME to solar-wind compression.

5.3 Conclusion

The findings of this work can be summarised as follows:

1. In Juno-UVS image data between perijoves 1 and 54, Jupiter's main auroral emission was observed to globally expand and contract by as much as $\pm$2000 km from its average position. There is excellent correlation between the expansion in the northern and southern hemispheres, which indicates that the process(es) causing this expansion or contraction are global within the magnetosphere, as well as between the expansion of the day-side and night-side ME, suggesting that the processes that work to contract the ME affect both hemispheres simultaneously and are stable over timescales of several hours.

2. The global expansion of the ME is anti-correlated with its brightness in both the northern and southern hemispheres; a contracted ME is usually brighter than an expanded ME. This brightening is more pronounced in the day-side ME.

3. Additionally, the local morphology of the ME is asymmetric in local time; the dawn-side ME is typically expanded, and the dusk-side ME is contracted, compared to the average ME position.

4. The perpendicular shift of the auroral footprint of Ganymede from its magnetically mapped reference path is positively correlated with the global expansion of the ME, while the shift of the IFP from its reference position shows no correlation, which indicates that a variable magnetodisc magnetic field can account for a considerable part of the variability of the expansion of the ME. The behaviour of the EFP was found to be intermediate to that of the IFP and GFP, which is consistent with this interpretation.

5. The equatorward expansion of the ME for perijoves 1 to 32 correlates well with increased magnetodisc current constant, reinforcing the previous conclusion that the current-sheet magnetic field is an important factor in determining the expansion of the ME.

6. An analysis of the day-side expansion of the ME in HST images of the aurora showed a clear distinction in day-side expansion of the ME between the cases with compressed and uncompressed magnetospheres; when the magnetosphere is compressed, the day-side ME is contracted. When combined with the correlation between the

day-side and night-side expansion of the ME, this indicates that an increased compression of the magnetosphere works to compress the magnetic field lines and hence globally contract the ME.

7. The combination of these results suggests that solar-wind compression of the Jovian magnetosphere works to increase the global brightness of the ME, though predominantly that of the day-side ME. This result stands in opposition to models and observations of the field-aligned currents in the middle magnetosphere, which are expected to give rise to the ME in the corotation-enforcement-current framework.

Similar techniques can be applied to the study of similar arc-like features in the Jovian aurora, as well as to understand how the morphology of the ME varies over shorten timescales in response to the solar wind.

Chapter 6

The UV auroral bridge

Well, no, but I don't... Seal off the bridge!

Nute Gunray, *Star Wars Episode I: The Phantom Menace*

Jupiter's ultraviolet aurora frequently shows a number of arcs between the dusk-side polar region and the main emission, which are denoted as "bridges". Despite frequently being present in the aurora, these bridges have yet to be the subject of large-scale investigation of their properties and origins. This work presents a largely automated detection and statistical analysis of bridges over 248 Hubble-Space-Telescope observations, alongside a multi-instrument study of crossings of magnetic field lines connected to bridges by the Juno spacecraft during its first 30 perijoves. The results from these two investigations are then combined to discuss the bridge in the context of existing auroral frameworks. Bridges are observed to arise on timescales of $\sim$2 hours, can persist over a full Jupiter rotation,

and are conjugate between hemispheres. The appearance of bridges is associated with compression of the magnetosphere, likely by the solar wind. Low-altitude bridge crossings are associated with upward-dominated, broadband electron distributions, consistent with Zone-II aurorae, as well as with plasma-wave emission observed by Juno-Waves, in agreement with existing theoretical models for the generation of polar-region aurorae. Main-emission crossings where no bridges are visible also show characteristics associated with bridges (more upward electron flux, plasma-wave emission), which is not the case for main-emission crossings with visible bridges, as though bridges remain present but spatially indistinguishable from the main emission in the former case. In all, compression of the magnetosphere may work to spatially separate the Zone-I and Zone-II regions of the main emission, in the form of Zone-II bridges.

This section on the bridge features in Jupiter's UV aurora follows from Head et al. (2025), published by Astronomy and Astrophysics on 2025-08-19, of which I was first author. The most relevant sections of the introduction are sections 2.6 (main emission) and 2.7 (polar emission).

6.1 Methods

6.1.1 Observations

In the first part of this work, HST-STIS UV observations between 2012 and 2023 are considered, notably those from the campaigns GO-11649, 12883, 13035, 14105, 14634, 15638, 16193, and 16675. For the automated bridge detection discussed in section 6.1.2, only northern-hemisphere visits are considered,

due to the favourable viewing geometry in the northern hemisphere for observation of the dusk-side polar region (where bridges are located) from Earth orbit, equivalent to 248 unique HST-STIS visits or 143 hours of observation. HST-STIS image data were collated into 10-second frames as per section 3.1.2. Composite UV images from Juno-UVS (68-210 nm; Gladstone et al. 2017) are also used in this work. Details

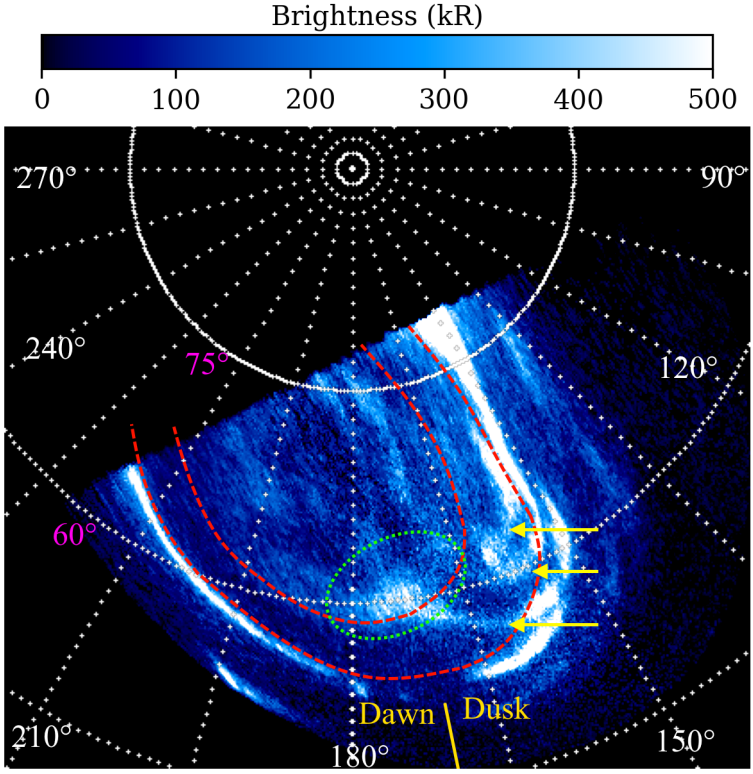

Figure 6.1: An 300-second image of the northern jovian UV aurora captured by HST during the GO-15638 campaign (exposure ID: odxc01okq). A 15°-by-15° grid in System-III longitude and planetocentric latitude is included; the System-III longitude of certain meridians are given in white, and certain planetocentric latitudes in magenta. The average subsolar longitude during this exposure (170°) is denoted by a solid yellow line, and the positions of the dawn and dusk hemispheres are included to guide the reader. The approximate location of the polar collar is enclosed by red dashed lines, and that of the noon active region by a green dashed ellipse. Bridges are highlighted with yellow arrows.

on the production of these composite images are given in section 3.1.1. This results in a representative view of the aurora in each hemisphere during each perijove. In total, this corresponds to 58 images of the aurora for the first 30 perijoves, two per perijove excluding PJ2, when Juno was placed into safe mode. In addition to image data from Juno-UVS, data from other Juno instruments are used in this work, notably from the FluxGate Magnetometer (MAG-FGM; Connerney et al. 2017b), the Juno Energetic-particle Detector Instrument (JEDI; Mauk et al. 2017a), and the Waves instrument (Kurth et al., 2017). Technical details of each instrument are described within their associated reference.

6.1.2 Automatic detection of bridge-like arcs

In the first part of this work, an automated method is employed to detect bridge-like arcs in 248 HST-STIS images of

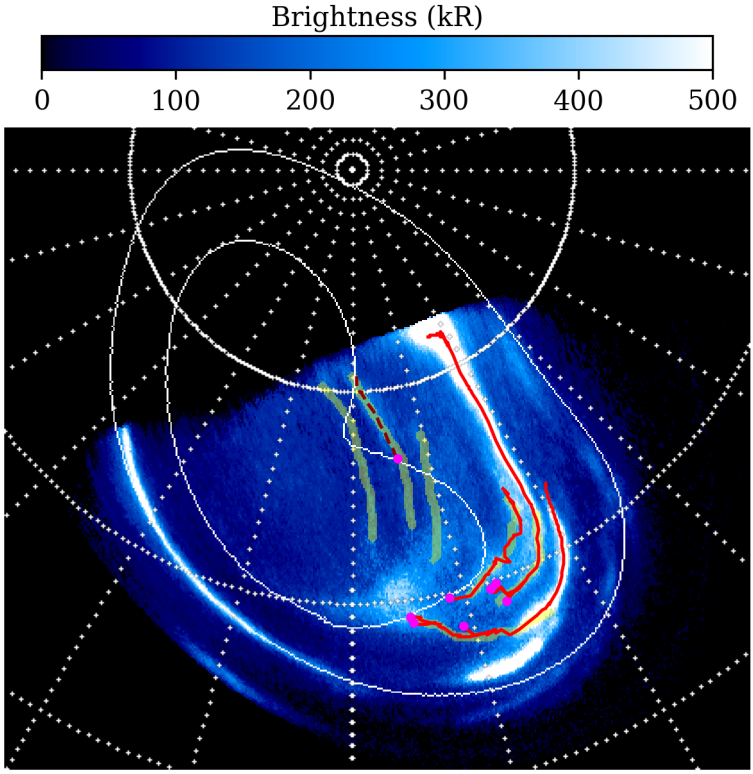

Figure 6.2: Results of the bridge-detection algorithm after filtering. Red solid lines denote detected arcs identified as bridges. Dark-red dashed lines denote arcs identified as PAFs. The seed point of each arc is in magenta. Manually designated arcs are in green. White contours give the region of validity of the Vogt et al. (2011) JRM33 flux-equivalence mapping along closed field lines.

the northern aurora. Each STIS time-tag image series is typically split into 30-second frames, which presents a compromise between image noise reduction and preservation of auroral dynamics. These images are first mapped into a polar projection - as though observed from directly above the axis of rotation of Jupiter, with a System-III longitude of 0° to the top of the image and 90° to the right - to ensure ease of comparison between images whilst preserving the physical size of features in the aurora. For this work, each STIS image series was collated into a single frame by taking the pixelwise median of the image stack; since prior investigations have indicated that bridge morphology does not greatly change over the 40 minutes of a HST exposure (Nichols et al., 2009b), this reduces the required computational effort whilst ensuring that each image represents a unique instance of auroral morphology. Though bridges have been observed to remain fixed in local time (Pardo-Cantos, 2019) rather than in System-III longitude (and thus are observed to slowly advance in longitude over the course of a STIS exposure), they remain clearly visible in the collated images, as shown in Figure 6.1. To more clearly highlight the arc-like form of the bridges and hence to make automatic detection of these structures more feasible, each collated image was convolved with a Gaussian-arc kernel to produce an "arcness" map of the aurora, as in Figure 6.3a; see section 3.2 of Head et al. (2024) for a thorough description of this method.

Bridges are defined as arcs that connect the day-side active region to the main emission via the polar collar (though they may not span this gap fully). This implies that they traverse a significant radial distance in the magnetosphere, since the main emission is surmised to originate from a region between 20 and 40 R_J(Cowley and Bunce, 2001), whereas the active re-

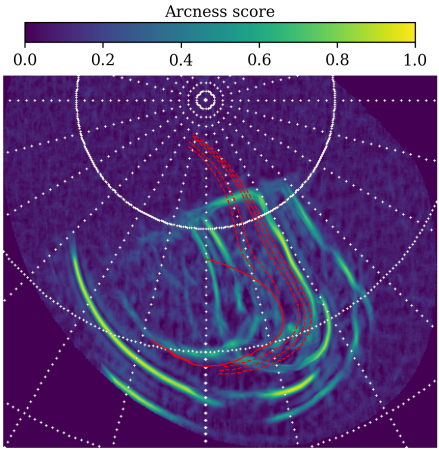
Arcness score
0.0
0.2
0.4
0.6
0.8
1.0

(a)

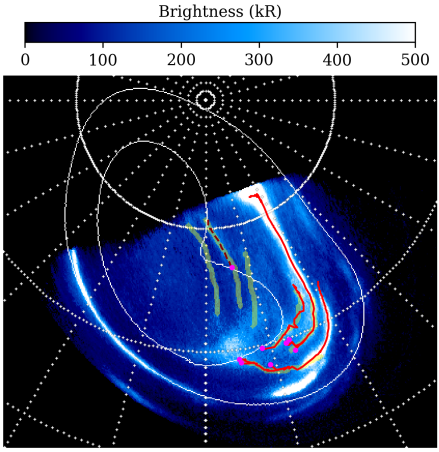
Brightness (kR)
0
100
200
300
400
500

(b)

Figure 6.3: (a) Arc convolution of the auroral image shown in Figure 6.1. Red lines denote the mapped magnetopause (solid) and fixed-radius contours (dashed) described in the text. (b) Results of the bridge-detection algorithm after filtering. Red solid lines denote detected arcs identified as bridges. Dark-red dashed lines denote arcs identified as PAFs. The seed point of each arc is in magenta. Manually designated arcs are in green. White contours give the region of validity of the Vogt et al. (2011) JRM33 flux-equivalence mapping along closed field lines.

gion is firmly within the polar aurora and hence maps to more distant regions of the magnetosphere. This behaviour can be leveraged to automatically detect auroral arcs that are likely to be bridges. Hence, a number of fixed-radius contours were projected to the ionosphere (75, 80, 85, 100, and 110 R_J), as well as the Joy et al. (2002) expanded magnetopause (stand-off distance 92 R_J; used as the outer boundary of validity in the Vogt et al. 2011 flux-equivalence model) which was observed to approximately coincide with the boundary between the polar collar and the day-side active region; see red contours in Figure 6.3a. Here, the flux-equivalence mapping of Vogt et al. (2011) was used with the JRM33 magnetic-field model (Connerney et al., 2022) since it is expected to be more reliable than field-line tracing in the polar aurora, though the choice of mapping method was a posteriori determined to not affect the conclusions of this work. The brightness along these mapped contours was determined and a broad uniform filter (0.3 MLT) applied. Peaks in the smoothed brightness were presumed to

coincide with arcs that cross these contours. For each of these "seed" points, the arc was propagated in a stepwise fashion, by taking all pixels within a 11×11-pixel area around the seed pixel, calculating an effective path brightness for each pixel by averaging the brightness of all pixels between the seed and the target pixel (to ensure that the arc propagation algorithm does not jump over regions of dark pixels to arrive at a bright pixel), and adding the pixel with the greatest effective path brightness to the arc. This process is repeated for all seed pixels until one of the following conditions is met: the new best target pixel is already part of a different arc, at which point the two arcs can be merged; the target pixel maps to a magnetospheric radius that is more than 10 R_J from the radius of the previous pixel, which was determined to often coincide with a failure of the algorithm; the target pixel maps to a radius less than 50 R_J in the magnetosphere, at which point the algorithm is at risk of simply detecting the main emission; the target pixel has an arcness score below 0.2.

To ensure that the algorithm is indeed detecting bridges, manual designations were created (thick yellow arcs in Figure 6.3b) for the northern-hemisphere image series in the STIS campaign GO-15638, which contains a total of 66 manually identified bridges over 42 image series. At this stage, the bridge-detection algorithm performs poorly; it does detect 90% of the manually identified bridges, but only 16% of the automatically detected bridges have a manual equivalent. Using the `scikit-learn` Python library, a random-forest classifier with a typical train-test split of 8:2 was trained on a number of detected-arc parameters (seed magnetosphere radial distance, seed magnetosphere local time, average arc brightness, average arc "arcness" value, total projected length of the arc in the

magnetosphere). The optimal hyperparameters were determined using a randomised search with tree counts between 10 and 1000 and maximum tree depths between 3 and 50; a tree count of 912 and a maximum tree depth of 42 were found to be optimal, and resulted in a model test accuracy of 0.82 when applied to the test data. This classifier was then applied to the full set of automatically detected bridges as a filter, which increased the proportion of detected arcs with manual equivalents (of those cases where arcs had been identified manually) from 16% to 96%. An example of the filtered bridge arcs is given in Figure 6.3b.

To estimate the uncertainty in the detected bridge count introduced by this method, a sensitivity analysis was performed by varying the cutoff arcness score between 0.1 and 0.3. The uncertainties in the detected bridge count shown in Figure 6.10 indicate the range of detected bridge counts introduced by varying this cutoff parameter.

6.1.3 Juno multi-instrument analysis

In the second part of this work, data from multiple Juno instruments are combined to build a full picture of the bridge. These quantities are determined as follows:

- Field-aligned currents: calculated from FGM data compared against the latest JRM33 magnetic-field model (Connerney et al., 2022) (implemented using the `JupiterMag` Python wrapper; James et al. 2022, Wilson et al. 2023) and extrapolated via magnetic-flux conservation to the assumed auroral altitude of 400 km, after Al Saati et al. (2022); see below.

- Alfvénic Poynting flux: from FGM data, extrapolated via magnetic-flux conservation to the assumed auroral altitude of 400 km, after the method presented by Gershman et al. (2019).

- Electron energy and pitch-angle distribution: from JEDI measurements (Mauk et al., 2017a), where data from all detectors have been stacked.

- Juno-Waves spectrum: from Juno-Waves data; in this work, only data from the LFR-Lo channel (50 Hz to 20 kHz) is presented.

Non-UVS data are sourced from the Automated Multi-Dataset Analysis (AMDA) database maintained by the Centre des Données de la Physique des Plasmas (Génot et al., 2021) and accessed using the `speasy` Python library (Jeandet and Schulz, 2024), with the exception of JEDI data which were downloaded using the JMIDL tool provided by John Hopkins University.

The method used to estimate the field-aligned-current (FAC) densities close to Jupiter uses data from the Juno FluxGate Magnetometer (FGM) instrument and is essentially an application of the method described in Al Saati et al. (2022). The interested reader is invited to consult the thorough description of this method provided in the supporting material of Al Saati et al. (2022). The method makes several key assumptions. Firstly, the ionosphere/auroral layer is modelled as an infinitely thin shell; this is a reasonable approximation given the thickness of this layer compared to the scale of the jovian magnetosphere. Jupiter's magnetic field is assumed to be dipolar, and hence the magnetic field lines radial close to the planet. The main emission is taken to run (locally) along a contour of

constant magnetic latitude, and that magnetospheric-coupling parameters are (locally) constant along the field line and along the main emission, and only vary in the direction perpendicular to the contour of the main emission. Juno is assumed to be moving roughly perpendicularly to the background magnetic field, and perturbations in this magnetic field are assumed to be spatial, not temporal, since Juno cannot distinguish between the two (Sulaiman et al., 2023). Under these assumptions, Ampère's law (in a vacuum and in the absence of a time-varying electric field)

$$\vec{J} = \frac{1}{\mu_0}\vec{\nabla} \times \vec{B}, \tag{6.1}$$

where $\vec{J}$ is the current density at Juno, μ_0 is the permeability of free space, and $\vec{B}$ is the magnetic field at Juno, can be reduced to

$$J_{\parallel} = \frac{1}{\mu_0}\frac{\partial(\sin\theta\delta B_{\phi})}{r\sin\theta\partial\theta}, \tag{6.2}$$

where $\delta\vec{B}$ denotes the magnetic-field residuals obtained by subtracting a magnetic-field model from the FGM magnetic-field measurements (JRM09 in Al Saati et al. (2022), JRM33 in this work). By conservation of magnetic flux,

$$J_{\parallel,iono} = \frac{|B_{iono}|}{|B|}J_{\parallel}, \tag{6.3}$$

where X_{iono} refers to values determined for the ionosphere. Al Saati et al. (2022) also perform a Fourier filtering on their magnetic-field residuals to remove superfluous frequencies that lay far from the frequency of their signal(s) of interest.

This work makes the same assumptions as Al Saati et al. (2022), barring the assumption of a dipolar magnetic field. Instead, the full magnetic field is taken into account when calculating $\vec{\nabla} \times \delta\vec{B}$, and so the field-aligned currents are given by

$$J_{\parallel} = (\frac{1}{\mu_0}\vec{\nabla} \times \delta\vec{B}) \cdot \hat{B}_{JRM33}. \tag{6.4}$$

This does not greatly increase the computational effort required to estimate the field-aligned currents. Additionally, no Fourier filtering is performed on the magnetic-field residuals since so particular signal frequency is targeted by this work. The implementation of this method was checked against the results presented in Al Saati et al. (2022) and found to agree exactly in all cases, and thus the method used in this work is considered to be verified against Al Saati et al. (2022), though the assumptions used in this work risk misrepresenting the true state of the auroral currents and should be investigated more thoroughly in a dedicated work.

Due to the relatively low number of cases (58 over 30 PJs), the determination of the positions of bridges in each exemplar image, and hence the Juno bridge traversal timestamps, was done manually (using the arc-convolved exemplar images, similar to Figure 6.2a, to highlight arc locations) to avoid the introduction of artefacts or the omission of bridges by the automatic detection algorithm. The Juno footprint is considered to cross a manually identified arc when within 5 px (∼600 km); this is a relatively broad threshold to ensure that the full arc crossing is included. However, since the auroral morphology in the base image is determined from stacked UVS spectral scan centred at a particular time, it may not be representative of the auroral morphology at the time of a supposed Juno

bridge traversal. This effect can be counteracted by looking at the instantaneous UVS map of the aurora at the time of the suspected bridge crossing to ensure that the bridge is approximately in the same position as in the exemplar image, and making adjustments to the crossing timestamps if necessary. The mean (and standard deviation) difference between the exemplar-map time and bridge crossings is 44 minutes (±23 minutes), so most bridge crossings are reliably determined from the initial manual estimates. Additionally, since the auroral arcs of bridges and the ME are typically crossed perpendicularly, the instantaneous UVS Juno-footprint brightness should show a peak during the supposed crossings, which can be used as an additional timestamp-validity check. In this work, the first 30 perijoves are considered, since after the 30th orbit, Juno's orbit is such that incomplete maps of the northern aurora become more and more common, making it difficult to identify mesoscale features like bridges, and passes over the southern aurora occur at increasingly greater altitudes, lowering the resolution of southern auroral maps and again making identification of the bridge challenging. Details of the automatically detected bridge and ME crossings are given in Table 6.1.

Table 6.1: Perijoves used in this work.

Perijove	Crossings	Figure 6.17, 6.21 crossings
PJ1-N	2016-08-27 12:08:56 - 12:10:26	-
	2016-08-27 12:09:56 - 12:11:01	
PJ1-S	2016-08-27 13:30:00 - 13:32:00	2016-08-27 13:30:00 - 13:32:00
	2016-08-27 13:33:00 - 13:36:00	2016-08-27 13:33:00 - 13:36:00
PJ3-N	2016-12-11 16:23:35 - 16:24:35	2016-12-11 16:23:35 - 16:24:35
	2016-12-11 16:25:30 - 16:26:20	
PJ3-S	2016-12-11 17:37:27 - 17:38:27	2016-12-11 17:37:27 - 17:38:27
PJ4-N	2017-02-02 11:43:10 - 11:50:25	-
	2017-02-02 12:24:10 - 12:25:15	

continued...

Table 6.1: Perijoves used in this work.

Perijove	Crossings	Figure 6.17, 6.21 crossings
PJ4-S	2017-02-02 13:38:16 - 13:39:51	-
	2017-02-02 15:14:11 - 15:34:01	
	2017-02-02 15:44:36 - 16:04:26	
	2017-02-02 16:09:51 - 16:10:16	
	2017-02-02 16:10:56 - 16:11:26	
	2017-02-02 16:24:51 - 16:32:31	
	2017-02-02 16:34:56 - 16:35:41	
	2017-02-02 16:36:21 - 16:38:26	
	2017-02-02 16:39:06 - 16:40:01	
	2017-02-02 16:40:36 - 16:44:36	
	2017-02-02 17:12:01 - 17:31:56	
PJ5-N	2017-03-27 07:35:58 - 07:42:53	2017-03-27 08:27:18 - 08:28:43
	2017-03-27 08:27:18 - 08:28:43	2017-03-27 08:29:18 - 08:30:28
	2017-03-27 08:29:18 - 08:30:28	
PJ5-S	2017-03-27 09:41:49 - 09:43:59	2017-03-27 09:41:49 - 09:43:59
	2017-03-27 09:44:49 - 09:48:49	2017-03-27 09:44:49 - 09:48:49
	2017-03-27 12:27:39 - 12:47:34	
PJ6-N	2017-05-19 02:28:24 - 02:48:19	-
	2017-05-19 03:16:14 - 03:34:04	
	2017-05-19 03:35:54 - 03:55:44	
	2017-05-19 05:27:39 - 05:30:39	
PJ6-S	2017-05-19 06:51:01 - 06:55:11	2017-05-19 06:51:01 - 06:55:11
	2017-05-19 06:56:56 - 06:59:11	2017-05-19 06:56:56 - 06:59:11
	2017-05-19 10:39:51 - 10:59:46	
PJ7-N	2017-07-11 01:13:00 - 01:15:00	2017-07-11 01:13:00 - 01:15:00
	2017-07-11 01:15:15 - 01:16:39	
PJ7-S	2017-07-11 02:33:16 - 02:35:19	2017-07-11 02:40:05 - 02:46:03
	2017-07-11 02:40:05 - 02:46:03	
PJ8-N	2017-09-01 21:16:43 - 21:17:33	-
PJ8-S	2017-09-01 22:27:24 - 22:28:49	2017-09-01 22:27:24 - 22:28:49
PJ9-N	2017-10-24 16:41:07 - 16:44:22	2017-10-24 17:17:37 - 17:18:47
	2017-10-24 17:17:37 - 17:18:47	
PJ9-S	2017-10-24 18:34:08 - 18:36:08	2017-10-24 18:34:08 - 18:36:08
	2017-10-24 18:37:13 - 18:39:43	2017-10-24 18:37:13 - 18:39:43
	2017-10-24 18:40:58 - 18:43:38	2017-10-24 18:40:58 - 18:43:38
	2017-10-24 18:44:58 - 18:48:13	2017-10-24 18:44:58 - 18:48:13
	2017-10-24 21:09:03 - 21:27:53	
	2017-10-24 21:28:23 - 21:28:53	
	2017-10-24 21:34:08 - 21:35:33	
	2017-10-24 21:36:08 - 21:38:28	
	2017-10-24 21:40:03 - 21:54:58	
	2017-10-24 22:00:03 - 22:09:43	
	2017-10-24 22:10:18 - 22:10:43	
	2017-10-24 22:12:13 - 22:12:58	
	2017-10-24 22:19:08 - 22:44:28	
PJ10-N	2017-12-16 16:53:58 - 16:57:48	-
PJ10-S	2017-12-16 18:49:00 - 18:51:00	2017-12-16 18:49:00 - 18:51:00
PJ11-N	2018-02-07 08:50:15 - 08:56:35	-
	2018-02-07 09:23:15 - 09:28:15	
	2018-02-07 12:53:45 - 12:59:10	
	2018-02-07 13:31:50 - 13:32:55	

continued...

Table 6.1: Perijoves used in this work.

Perijove	Crossings	Figure 6.17, 6.21 crossings
PJ11-S	2018-02-07 14:43:53 - 14:46:13	2018-02-07 14:43:53 - 14:46:13
	2018-02-07 14:46:13 - 14:49:13	2018-02-07 14:46:13 - 14:49:13
	2018-02-07 17:48:48 - 17:50:18	
	2018-02-07 18:09:03 - 18:28:53	
PJ12-N	2018-04-01 06:29:37 - 06:31:17	-
	2018-04-01 06:32:47 - 06:34:27	
	2018-04-01 06:35:02 - 06:36:17	
	2018-04-01 07:02:32 - 07:13:47	
	2018-04-01 07:15:22 - 07:35:17	
	2018-04-01 08:34:37 - 08:52:37	
	2018-04-01 09:05:17 - 09:09:02	
PJ12-S	2018-04-01 10:45:19 - 10:48:54	2018-04-01 10:45:19 - 10:48:54
	2018-04-01 10:48:58 - 10:53:00	
PJ13-N	2018-05-24 05:05:51 - 05:06:41	2018-05-24 05:05:51 - 05:06:41
PJ13-S	2018-05-24 06:27:39 - 06:29:54	-
	2018-05-24 06:31:29 - 06:33:29	
PJ14-N	2018-07-16 03:03:14 - 03:23:09	-
	2018-07-16 03:30:14 - 03:36:09	
	2018-07-16 04:38:24 - 04:39:49	
	2018-07-16 04:40:24 - 04:42:59	
PJ14-S	2018-07-16 06:09:33 - 06:14:28	-
PJ15-N	2018-09-07 00:36:22 - 07:37:40	2018-09-07 00:36:22 - 07:37:40
PJ15-S	2018-09-07 01:57:13 - 02:00:08	2018-09-07 01:57:13 - 02:00:08
	2018-09-07 02:00:43 - 02:02:58	
PJ16-N	2018-10-29 20:16:22 - 20:18:47	2018-10-29 20:44:22 - 20:45:17
	2018-10-29 20:44:22 - 20:45:17	
PJ16-S	2018-10-29 21:57:49 - 21:58:50	2018-10-29 21:57:49 - 21:58:50
PJ17-N	-	-
PJ17-S	2018-12-21 18:05:14 - 18:07:59	-
PJ18-N	2019-02-12 16:51:06 - 16:52:56	-
PJ18-S	2019-02-12 18:33:57 - 18:36:27	2019-02-12 18:33:57 - 18:36:27
	2019-02-12 18:38:27 - 18:42:07	
	2019-02-12 20:41:47 - 20:57:02	
	2019-02-12 21:40:47 - 21:42:32	
	2019-02-12 21:43:02 - 21:43:27	
	2019-02-12 21:45:12 - 21:45:42	
	2019-02-12 21:46:17 - 21:46:42	
	2019-02-12 21:47:52 - 21:48:47	
	2019-02-12 22:03:47 - 22:23:37	
	2019-02-12 22:22:52 - 22:23:32	
	2019-02-12 22:25:07 - 22:28:17	
	2019-02-12 22:28:47 - 22:29:52	
PJ19-N	2019-04-06 09:16:41 - 09:27:46	-
	2019-04-06 09:28:46 - 09:29:11	
	2019-04-06 09:44:16 - 09:45:36	
	2019-04-06 09:46:06 - 09:58:06	
	2019-04-06 09:58:46 - 10:07:41	
	2019-04-06 10:43:31 - 10:47:56	
PJ19-S	2019-04-06 13:23:05 - 13:28:20	-
PJ20-N	2019-05-29 07:27:51 - 07:28:52	2019-05-29 07:27:51 - 07:28:52
	2019-05-29 07:29:00 - 07:30:00	2019-05-29 07:29:00 - 07:30:00
	2019-05-29 07:31:55 - 07:32:56	2019-05-29 07:31:55 - 07:32:56

continued...

Table 6.1: Perijoves used in this work.

Perijove	Crossings	Figure 6.17, 6.21 crossings
PJ20-S	2019-05-29 08:57:26 - 08:59:31	-
	2019-05-29 12:57:51 - 13:10:41	
PJ21-N	2019-07-21 03:07:54 - 03:09:59	-
	2019-07-21 03:37:29 - 03:38:19	
PJ21-S	2019-07-21 04:59:29 - 05:01:29	-
	2019-07-21 08:48:04 - 09:07:09	
PJ22-N	2019-09-12 02:28:45 - 02:32:00	2019-09-12 03:11:25 - 03:12:20
	2019-09-12 03:11:25 - 03:12:20	2019-09-12 03:13:55 - 03:14:40
	2019-09-12 03:13:55 - 03:14:40	
PJ22-S	2019-09-12 04:28:55 - 04:30:40	-
PJ23-N	-	-
PJ23-S	2019-11-03 23:25:35 - 23:29:20	-
	2019-11-04 01:14:55 - 01:25:00	
	2019-11-04 02:54:05 - 03:13:55	
PJ24-N	2019-12-26 14:46:42 - 14:48:57	-
PJ24-S	2019-12-26 18:52:07 - 19:01:07	-
PJ25-S	2020-02-17 22:22:44 - 22:37:29	-
PJ26-N	-	-
PJ26-S	2020-04-10 15:13:02 - 15:25:42	-
	2020-04-10 15:26:17 - 15:26:52	
PJ27-N	2020-06-02 09:13:35 - 09:21:05	-
PJ27-S	2020-06-02 14:47:40 - 15:07:30	-
PJ28-N	-	-
PJ28-S	2020-07-25 07:15:20 - 07:17:40	-
	2020-07-25 09:30:35 - 09:31:55	
	2020-07-25 09:42:40 - 10:02:35	
	2020-07-25 10:13:30 - 10:14:10	
	2020-07-25 10:36:00 - 10:36:35	
	2020-07-25 10:37:10 - 10:37:40	
	2020-07-25 10:47:35 - 11:07:30	
PJ29-N	-	-
PJ29-S	2020-09-16 03:26:32 - 03:30:07	-
	2020-09-16 06:18:52 - 06:32:12	
	2020-09-16 07:07:22 - 07:11:32	
PJ30-N	2020-11-08 01:20:16 - 01:21:41	-
PJ30-S	2020-11-08 02:52:37 - 02:55:47	-

"Perijove" gives the perijove number and hemisphere. "Crossings" give the timestamps of the semi-automatically detected arc crossings by Juno; red denotes bridge crossings and green denotes main-emission crossings; note that cases with many apparent traversals of the main emission are those cases where the Juno footprint passes along the main-emission arc. "Figure 6.17, 6.21 crossings" further specify those low-altitude, dusk-side crossings used in the analysis presented in Figure 6.17 and 6.21; red denotes bridge crossings, green denotes crossings of the main emission with associated bridges, and orange those main-emission crossings without obvious bridges, in line with the key of Figure 6.17.

6.2 Results

6.2.1 HST-STIS large-scale analysis

Detected bridges in the ionosphere were magnetically mapped to the equatorial plane in the magnetosphere using the Vogt et al. (2011) flux-equivalence mapping. As can be seen in Figure 6.4, the majority of detected bridges (light red) map to the dusk-side magnetosphere between 10 and 20 MLT, as expected from previous work (Pardo-Cantos, 2019). Detected arcs that map to the magnetopause beyond 16 MLT are considered to be PAFs and excluded from this analysis, to be discussed separately later in this work, though a continuum of arcs exist between bridges and PAFs and hence the choice of this cutoff is approximate.

To aid understanding of the average properties of these bridges, "average-bridge" contours (dark red, and blue for PAFs, in Figure 6.4) were calculated by taking a number of starting points on the magnetopause (black in Figure 6.4), following the average orientation of detected bridges (weighted by the inverse square of the distance to the point to produce a "local-average" orientation), and continuing this process to propagate each contour into the magnetosphere. These contours indicate that bridges typically curve duskward and radially inwards toward Jupiter. The bridge mapping shown in Figure 6.4 depends on the magnetic field model used to map poleward of the ME. Although the quantitative details are affected by the choice of such model (compare Figure 6.4 with Figure 6.5 using field-line tracing instead of flux-equivalence mapping), our results are broadly consistent with the expected location of the bridges. Bridges are thus named because they (at least par-

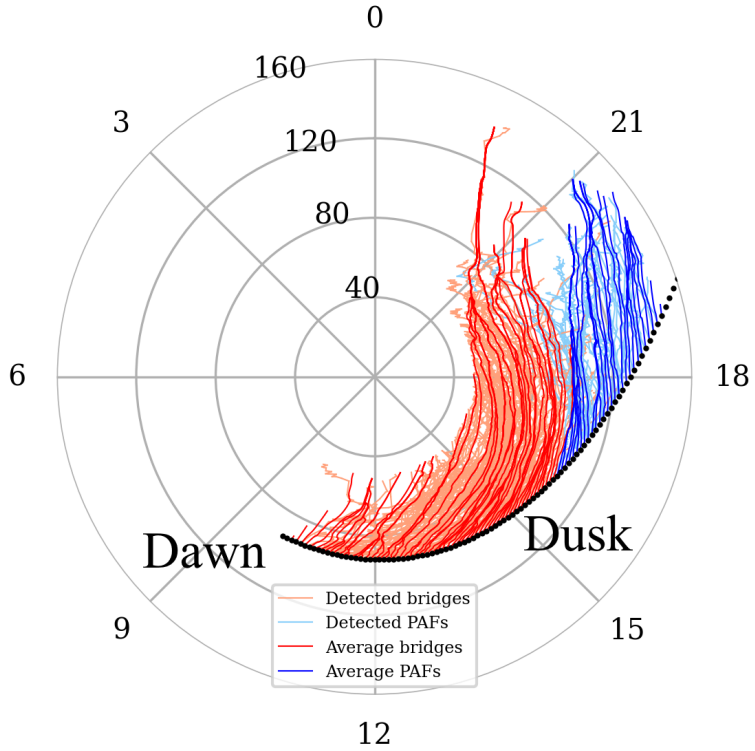

Figure 6.4: Automatically detected bridge/PAF-like arcs (in pale red/blue) in all northern-hemisphere HST-STIS observations considered in this work, mapped via flux-equivalence mapping to the magnetospheric equator (radius, local time). Radii are given in R_J. A set of average bridge/PAF contours are given in dark red/blue; their starting locations on the Joy et al. (2002) expanded magnetopause (solar-wind ram pressure = 0.039 nPa; stand-off distance 92 R_J) are given in black.

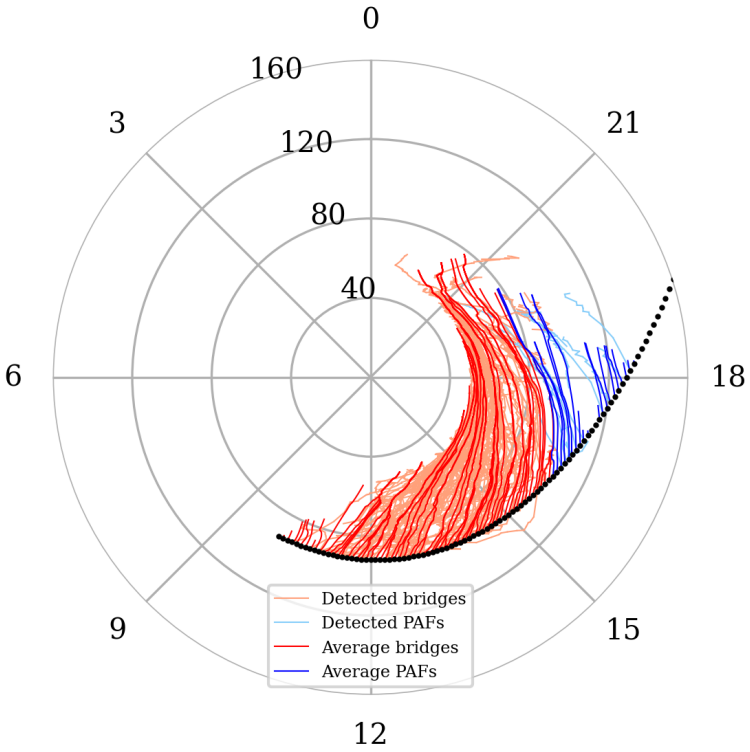

Figure 6.5: As Figure 6.4, but using field-line tracing of JRM33 (Connerney et al., 2022) and Con2020 (Connerney et al., 2020) to map the bridges from the aurora to the magnetosphere.

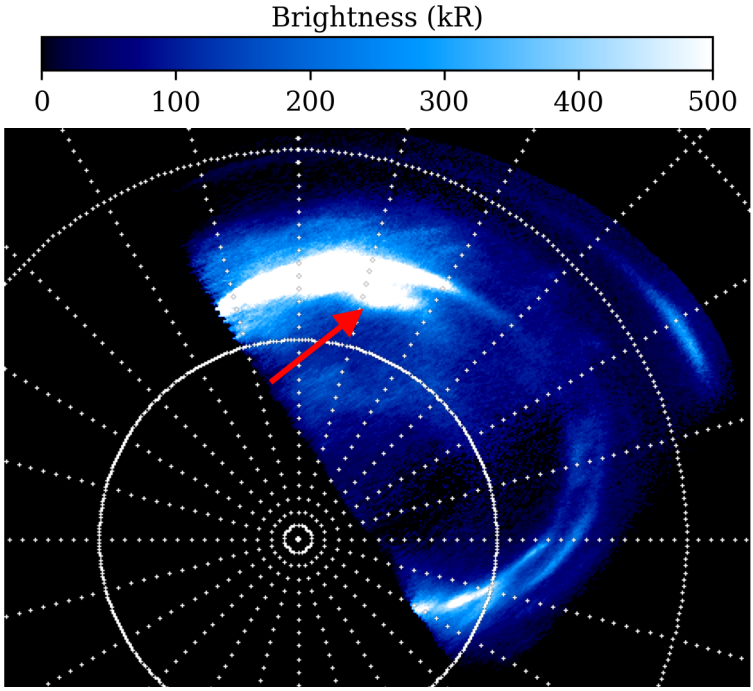

Figure 6.6: Observation of a persistent bridge-like arc over a full Jupiter rotation in the southern aurora during the GO-14634 HST campaign (2017-05-19 02:37:37). Bridge location is highlighted by the red arrow. This bridge is also present in the intervening HST and UVS (PJ6) observations.

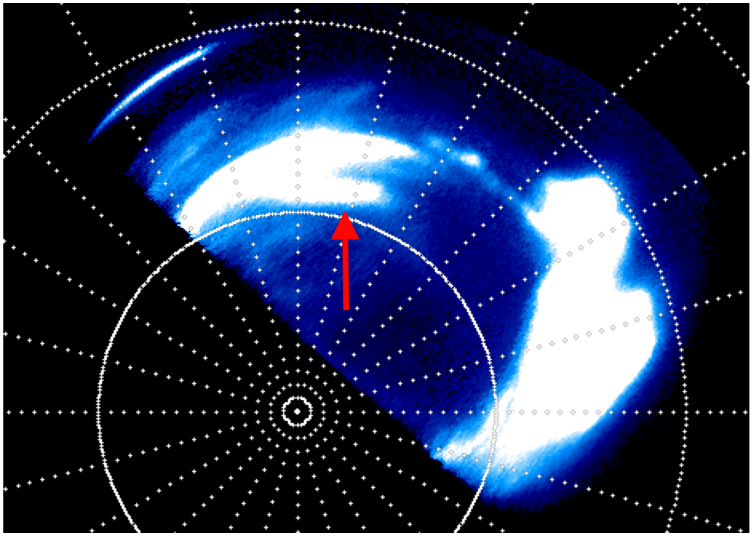

Figure 6.7: As Figure 6.6 but ∼10 hours later at 2017-05-19 12:09:43.

tially) bridge the polar collar between the active region (which can be assumed to relate to the magnetopause, or at least to large radial distance in the day-side magnetosphere; Nichols et al. 2007) and the ME (which is expected to arise much closer to Jupiter, at ∼30 R_J; Cowley and Bunce 2001).

Of all the HST cases analysed in this work, there exists only one quasi-continuous set of observations (notably, surrounding PJ6) that tracks the evolution of a bridge over a full Jupiter rotation; the start and end series of this set are shown in Figures 6.6 and 6.7. The bridge has persisted over the ∼10-hr span of this set of observations with very little change in morphology, having moved only slightly equatorward. This result is con-

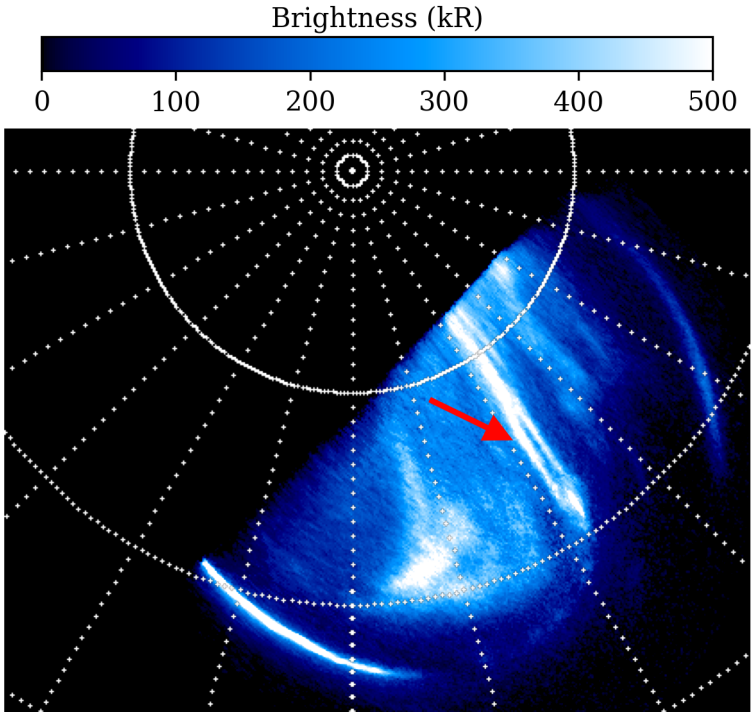

Figure 6.8: Observation of the growth of a bridge-like arc in the northern aurora during the GO-15638 HST campaign at 2019-02-13 21:16:57. Bridge location is highlighted by the red arrow.

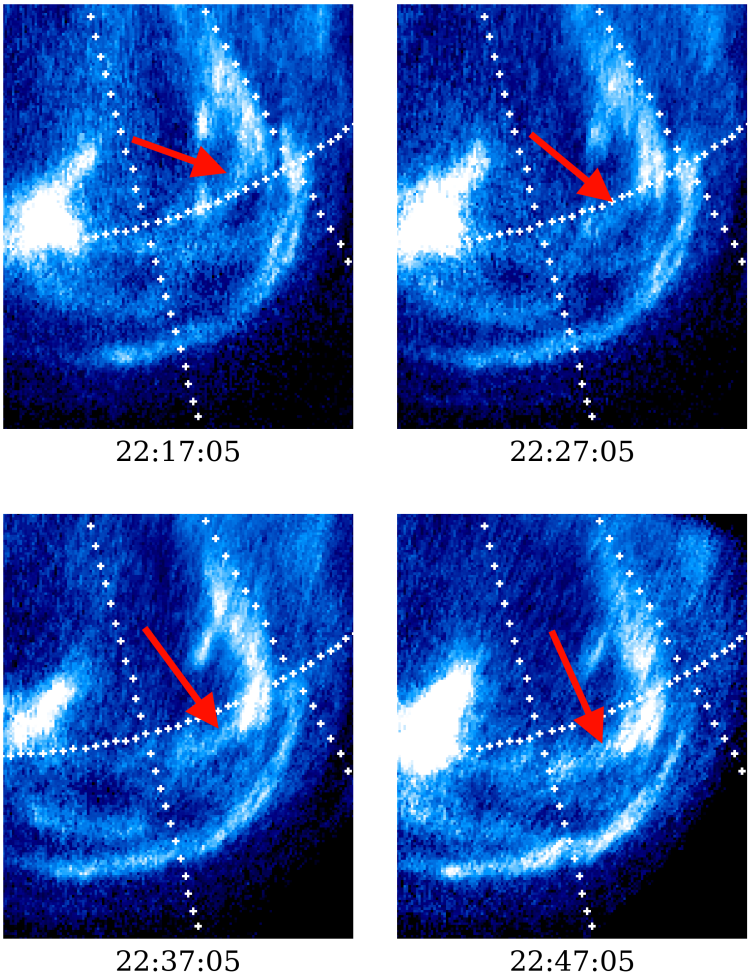

Figure 6.9: As Figure 6.8 but later in the sequence.

sistent with the findings of Palmaerts et al. (2024) and Nichols et al. (2009b) in which bridges are observed to be stable over at least 3 hours. This latter work also associated the appearance of bridges with magnetospheric compression by the solar wind, noted to be maintained over several days, which is consistent with bridges that can survive a full Jupiter rotation. A case in which a bridge was observed to develop between two HST observations is given in Figures 6.8 and 6.9. In this case, the ME was observed to first exist as two parallel arcs, which had evolved into a clear bridge-like arc separate from the ME one hour later, though this interpretation assumes that the two double-arc phenomena are related, impossible to confirm in the absence of intervening observations. In any case, this hour-scale onset is consistent with the suggested solar-wind influence on the presence of bridges (Nichols et al., 2017), since it is expected to vary on timescales of hours (Chané et al., 2017); however, some internal processes (such as dawn storms) are also known to vary over hour timescales (Bonfond et al., 2021) and so this timescale cannot be used as a confirmation of the influence of the solar wind without further supporting evidence.

The appearance of bridges can also be directly related to the compression of the magnetosphere. Figure 6.10 shows the expansion of the ME against the total detected bridge count for each northern HST series considered in this work, where "expansion" refers to the average equatorward distance (in km) of the ME from its average position, as per Head et al. (2024). The use of bridge count over e.g. total projected bridge length in the magnetosphere may potentially misrepresent the aurora in the case where many small bridges are detected; as shown in Figure 6.12, there exists a broadly lin-

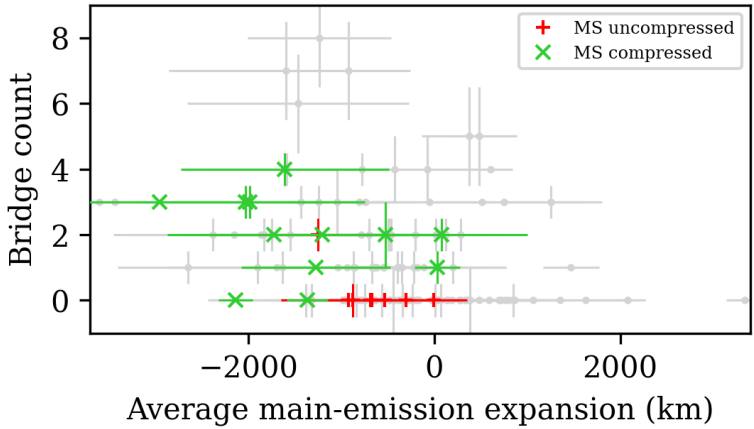

Figure 6.10: Detected average expansion of the ME from Head et al. (2024) vs. the total detected bridge count for each northern HST-STIS series considered in this work. Negative expansions imply a contracted ME. Bridge-count error bars are determined as described in section 6.1.2. Green crosses denote those cases where the magnetosphere was compressed, and red pluses those cases where the magnetosphere was uncompressed; grey points denote cases where the compression state of the magnetosphere is unknown.

ear relation between detected bridge count and total projected bridge length, and so we conclude that both parameters are reasonable measures of the quantity of bridges in the aurora. Figure 6.10 shows no clear relation between bridge count and ME expansion. However, by isolating those cases where the state of compression of the magnetosphere is known from Juno magnetopause-crossing altitudes (Yao et al., 2022;

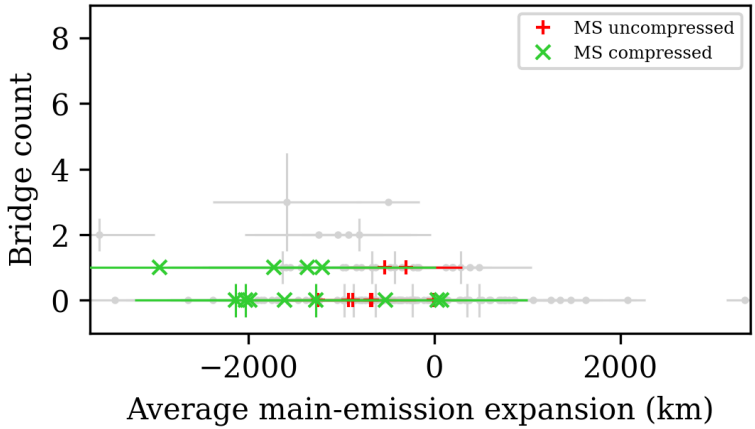

Figure 6.11: Detected average expansion of the ME from Head et al. (2024) vs the detected PAF count for each northern HST-STIS series considered in this work. Negative expansions imply a contracted ME. Green crosses denote those cases with a compressed magnetosphere, and red pluses those cases with an uncompressed magnetosphere (Yao et al., 2022); grey points denote cases where the compression state of the magnetosphere is unknown.

Louis et al., 2023), a clear distinction between cases with compressed and uncompressed magnetospheres is apparent. A Pearson-χ^2 test on these points with categories [bridge count > 0, bridge count $= 0$] and [compressed magnetosphere, uncompressed magnetosphere] indicates that compression of the magnetosphere is associated with the presence of bridges beyond the 99th-percentile level ($\chi^2 = 9.73$, p-value 0.002). This association between magnetospheric compression and bridge

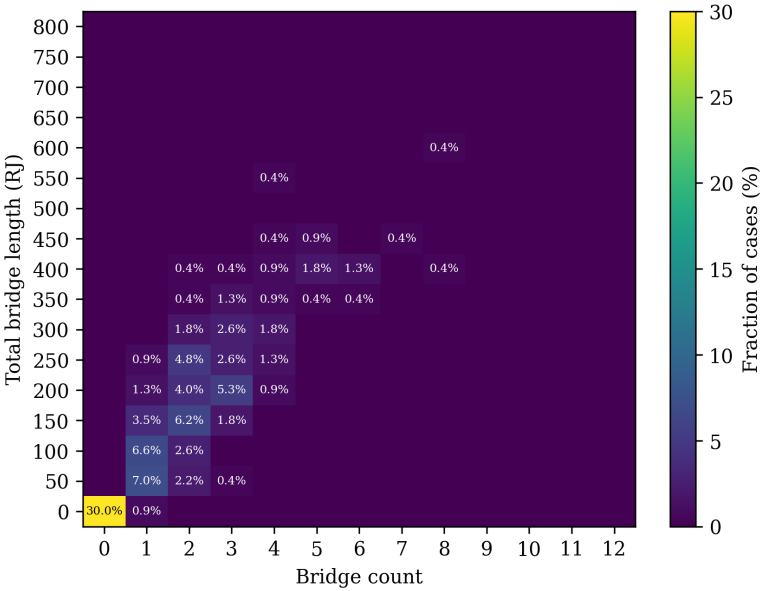

Figure 6.12: Detected bridge count vs total detected bridge magnetosphere-mapped length for the HST-STIS northern-hemisphere cases considered in section 6.2.1, expressed as a percentage of the total cases. There is an approximately linear relationship between bridge count and total bridge length.

count is evident even from a cursory inspection of the aurora in these cases, given in Figure 6.13. While the size of the magnetosphere may vary due to a number of factors, such as the solar-wind dynamic pressure (Chané et al., 2017) and the mass-outflow rate from Io (Bagenal and Delamere, 2011), this result, combined with the previously determined hour-scale variability of bridge morphology, is compatible with the idea that the

solar wind exerts some measure of influence on the appearance of bridges in the aurora, which is in line with the results of Nichols et al. (2017). However, this scenario cannot be robustly confirmed without simultaneous measurement of the solar wind near Jupiter, which is left to a future work. The

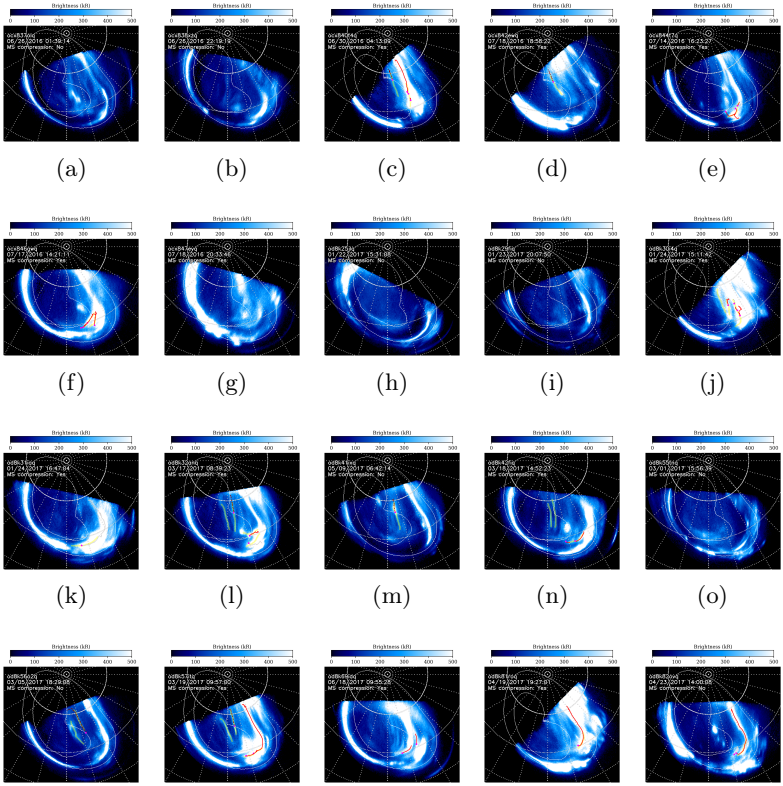

(a) (b) (c) (d) (e)

(f) (g) (h) (i) (j)

(k) (l) (m) (n) (o)

(p) (q) (r) (s) (t)

Figure 6.13: Results of the bridge-detection algorithm after filtering for cases where the compression state of the magnetosphere is known (Yao et al., 2022; Louis et al., 2023). Red lines denote bridge-candidate arcs that correspond to manual designations, and grey the arcs that do not but are nevertheless accepted by the random-forest filter. Dark-red dashed lines are those arcs that are identified as PAFs rather than bridge candidates. The seed point of each arc is given in magenta. Manually designated arcs are given in yellow. White contours give the region of validity of the Vogt et al. (2011) JRM33 flux-equivalence mapping along closed field lines. HST exposure identifiers, central timestamps, and the compression state of the magnetosphere are given in the top left.

arcs used in the above analysis were those with magnetopause local times less than 16 MLT; these arcs can be confidently said to be bridges, whereas there is some ambiguity with PAFs in those arcs that map to the distant magnetosphere beyond 16 MLT. A similar analysis was performed separately for the assumed PAFs (blue in Figure 6.4) and no difference was found in the total detected arc length for compressed and uncompressed magnetospheres (see Figure 6.11). This suggests that PAFs are not exactly the same feature as the auroral bridge and that they do not show a dependence on the solar wind, in agreement with Nichols et al. (2009a). However, the methods presented in this work are not necessarily suited to the analysis of these polar-cap features, which are often found within the region of open magnetic flux after Vogt et al. (2011), and so more specialised work should be carried out to confirm this

conclusion.

6.2.2 Juno multi-instrument analysis

Case study - PJ9-S

By comparing the projected Juno ionospheric footprint against manually determined bridge positions in the base image of each hemisphere during each perijove, approximate bridge-crossing timestamps can be determined and compared against data and derived parameters from Juno. Note that mapping of the Juno footprint in the ionosphere was performed using field-line tracing of the JRM33 field model rather than flux-equivalence mapping, since Juno is at low altitude, minimising the effect of model inaccuracies in the polar region, and this method can map the footprint within the entire polar region. An example of this analysis is given in Figures 6.14 and 6.15 for PJ9-S, in which Juno passed first over the ME (green) and then over three clear bridge-like structures in the dusk-side polar collar (red) at low altitude ($\sim$2 R_J), where the positions of these features are determined as per section 6.1.3. The crossing showed the expected FAC inversion (Al Saati et al., 2022; Mauk et al., 2020); Juno observed upward FACs (majority downward-travelling electrons) as it first passed through the ME, then downward FACs (majority upward-travelling electrons) as it continued into the polar collar. It is notable that the ME crossing was associated with uniquely upward FACs, rather than an inversion, indicating that the ME was a uniquely ZI feature during this crossing (Mauk et al., 2020). Unlike the ME crossing of PJ7-N described in (Kurth et al., 2018), there was no significant Waves-E emission; instead, we see that Juno started to observe significant plasma-wave emission once it entered

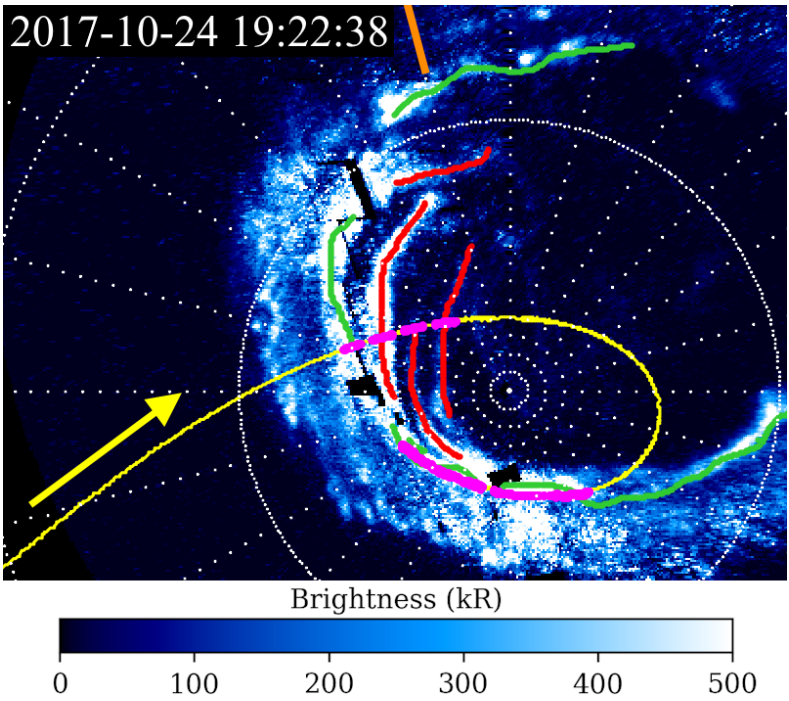

Figure 6.14: Mapped Juno-footprint trajectory for PJ9-S overlain on the UVS exemplar image (central spin timestamp in top-left). The yellow arrow indicates the direction of travel of Juno. The sun position is marked by a solid orange line. Bridges are given in red, and the ME in green; Juno crossings of these arcs are given in magenta.

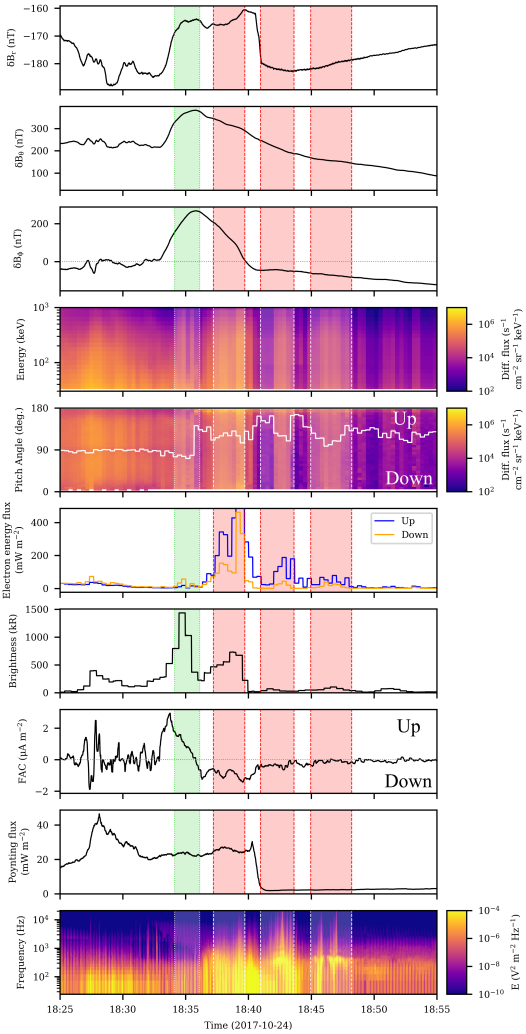
δB_r (nT)
δB_θ (nT)
δB_φ (nT)
Energy (keV)
Diff. flux (s⁻¹ cm⁻² sr⁻¹ keV⁻¹)
Pitch Angle (deg.)
Up
Down
Electron energy flux (mW m⁻²)
Brightness (kR)
FAC (μA m⁻²)
Poynting flux (mW m⁻²)
Frequency (Hz)
E (V² m⁻² Hz⁻¹)
18:25
18:30
18:35
18:40
18:45
18:50
18:55
Time (2017-10-24)

Figure 6.15: Juno instrument data for PJ9-S. The ME crossing is first (green, dotted) followed by three bridge crossings (red, dashed). From top to bottom: residual magnetic field components (FGM data - JRM33); JEDI electron energy; JEDI electron pitch-angle distribution (average given by solid white line); JEDI field-aligned (0°-20°, 160°-180°) electron energy flux; UVS footprint brightness; calculated ionospheric FACs; calculated ionospheric Alfvénic Poynting flux (the "step" in the flux is related to a change in operating range of the FGM instrument); Waves-E LFR-Lo spectral density.

into the polar collar, with high-frequency peaks occurring during bridge crossings, which then abated after the third bridge. The calculated FACs remained downward for all three of these bridge crossings, though no particular peaks or signatures were observed that can be associated with the bridge. In particular, the lack of FAC inversion signatures during the bridge crossings suggests two things: firstly, that bridges are mechanically distinct from the ME, although they are morphologically related insofar as they can disrupt the morphology of the ME (Nichols et al., 2009a); and secondly, that vorticity in the dusk-side magnetosphere is likely not the source of the bridges, as had been previously suggested (Fukazawa et al., 2006; Pardo-Cantos, 2019), since this would be expected to give rise to noticeable FAC signatures (Delamere et al., 2013; Johnson et al., 2021). Additionally, there was no bridge-crossing signature in the derived Alfvénic Poynting flux which indicates that the mechanisms responsible for auroral moon footprints (Gershman et al., 2019) are not responsible for the bridges. Dur-

ing the first bridge crossing, Juno observed a clearly broadband, bidirectional, field-aligned electron distribution, though the upward electron energy flux was greater than the downward flux. This trend is stronger for the latter two crossings; while the electron distributions remain field-aligned and broadband, there is a clear preference for upward-travelling electrons. However, only a small downward electron flux would be required to produce the low auroral brightnesses associated with these bridge crossings, regardless of the upward electron flux; peaks in the downward electron energy flux are present and coincide with the peaks in auroral brightness. It is notable that, while plasma-wave emission can clearly be associated with these bridge crossings (and not with the ME crossing), the intensity of this emission does not appear to correlate with the auroral brightness seen during the bridge crossings. The plasma-wave emission is also not constant during the crossings, though these peaks are not associated with any flaring behaviour in the bridges. This may indicate a more complex relationship between these plasma waves and generation of the aurora, if they are indeed related to the processes that give rise to bridges, rather than merely coincident.

Analysis of the first 30 perijoves

A similar analysis was performed for the first 30 perijoves, equivalent to 58 auroral crossings. Bridges are present in the dusk-side polar collar during 39 of these traversals, and Juno passes over at least one arc in 26 of these cases. 11 of these traversals show aurorae with no clear bridges. The remaining 8 cases are those with large gaps in UVS coverage and are ignored. Bridges are present in a large fraction (at least 67%)

of the first 30 perijoves. Of these perijoves, the presence or absence of bridges is mostly maintained between the northern and southern crossing; if Juno observes bridges in the northern aurora, it also typically sees bridges in the southern aurora ∼2 hours later. This is in line with previous work, which suggested that bridges are stable over timescales of several hours (Nichols et al., 2009b), and indicates that the processes that give rise to bridges are conjugate between hemispheres and thus likely occur on closed field lines. These bridges are noted to occur at similar local times and have comparable geometries, though more accurate magnetic-field models are required to determine whether the bridges lie along the same field lines in the north and south. Only two perijoves (PJ4, PJ9) showed bridges that appeared or disappeared over the course of a perijove. During PJ4, a long, faint bridge was visible in the northern aurora around 21 MLT, which had disappeared completely by Juno's pass over the southern aurora. During PJ9, the dusk-side polar collar was free of bridges (though the dusk-side ME was slightly non-continuous) during the northern pass; by the time of Juno's southern pass, three distinct bridges had developed. This, combined with the result that bridges usually appear conjugate between the two hemispheres, indicates that the process that causes bridges can occur over hour-long timescales, consistent with the result shown in Figures 6.8 and 6.9.

Bridge crossings at low altitudes were also generally associated with downward FACs (average for cases with altitudes below 3 R_J = -0.1±0.3 μA m^{-2}) but without a particular signature (a peak during the crossing, for example), as well as broadband upward-dominated bidirectional electron distributions, as suggested by the results from PJ9-S. ME crossings, however, were more usually associated with upward FACs (av-

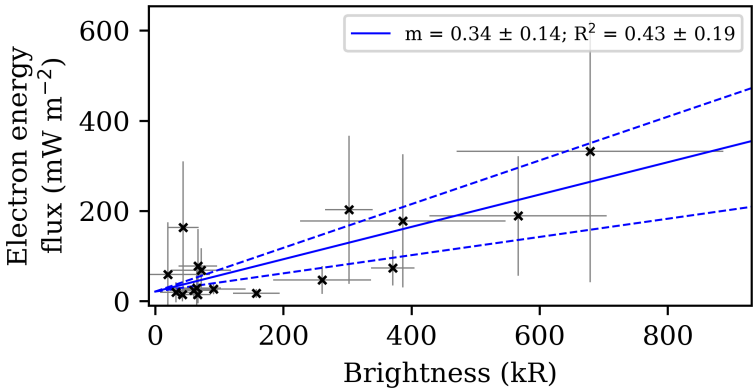

Figure 6.16: Mean Juno-footprint UV auroral brightness vs. mean JEDI downward electron energy flux observed during low-altitude (<3 R_J) bridge crossings between PJ1 and PJ30. Uncertainties (grey) are estimated using the 50th and 100th-percentile values observed during crossings. The gradient and R^2 value of the least-squares linear relation (solid blue line) is given in the legend.

erage for cases with altitudes below 3 R_J = 0.2±0.7 μA m^{-2}) or FAC inversions, though the large uncertainties make it challenging to differentiate the two features from their average currents alone.

Figure 6.16 shows an approximately linear relationship (that passes through the origin) between the mean UV auroral brightnesses and downward electron energy fluxes seen by Juno during bridge crossings. This is an indication that the downward electrons seen by Juno are indeed the source of the auroral emission associated with bridges. An electron energy flux of 1

mW m^{-2} is equivalent to an auroral brightness of 2.9 kR. This is a slightly lower brightness than previous estimates for the aurora (Mauk et al., 2017c; Nichols and Cowley, 2022). This may be due to subtle implementation differences with previous work, or a genuine difference from the canonical "1 mW m^{-2} = 10 kR" in the case of bridges. This also assumes that the entire electron energy flux seen by Juno at the typical crossing altitude of ∼2 R_J contributes toward the auroral brightness of the bridge. In the presence of a vertically extended acceleration region at or below the altitude of Juno (e.g. Sulaiman et al., 2022), some of the downward electron flux may be bidirectionally re-accelerated, reducing the downward flux that reaches the auroral layer.

In addition to the above relation between bridge auroral brightness and downward electron flux, the typical electron pitch-angle profiles seen during bridge and ME crossings (red in Figure 6.17) are also noteworthy; the crossings used in this analysis are given in Figures 6.18 to 6.20 and Table 6.1. These pitch-angle distributions are the average normalised profiles of bridge/ME crossings rather than the average distribution, to account for large differences in total electron flux, since the profile is the aspect of interest. Bridges are dominated by upward-travelling, field-aligned electrons, though with a considerable downward component. ME crossings have been split into cases where the ME crossing is immediately preceded/succeeded by a bridge (whether this is crossed by Juno or not) and cases with no bridges in the vicinity of the ME crossing. ME crossings with bridges (green) show electron distributions that are dominated by downward-going electrons. Cases without bridges (orange) have broadly symmetrical field-aligned electron populations, though there is a preference toward upward-travelling

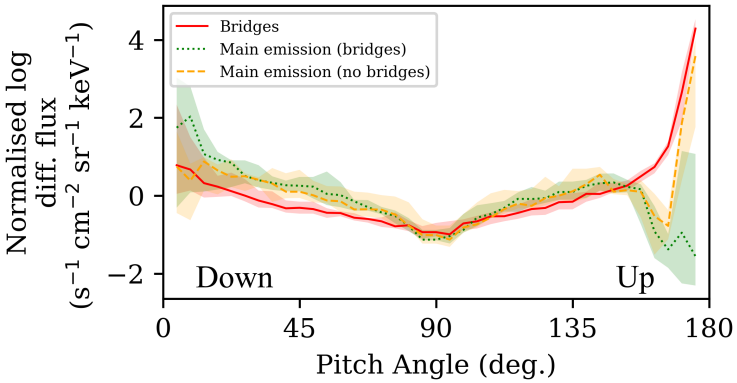

Figure 6.17: Median-average JEDI electron flux vs. pitch angle profiles during low-altitude (<3 R_J) bridge crossings (red, solid) and ME crossings, both with (green, dotted) and without (orange, dashed) local bridges, observed by Juno. The shaded regions denote the 25-to-75th percentile range.

electrons. It is first worth noting that the presence or absence of bridges affects the properties of the ME auroral-electron population, not simply its morphology. Secondly, in the absence of a bridge, the ME electron population takes on a more "bridge-like" character, with a greater proportion of upward-travelling electrons. This hints that the "bridge" is still present within the aurora but indistinguishable from the ME.

The three types of crossing also differ in the observed Waves-E LFR-Lo intensity, especially at higher frequencies; see Figure 6.21, where only the higher frequency portion (>1000 Hz) of the Waves-E LFR-Lo spectra has been used to capture the "spiking" behaviour of the Waves-E signal seen in Figure 6.15.

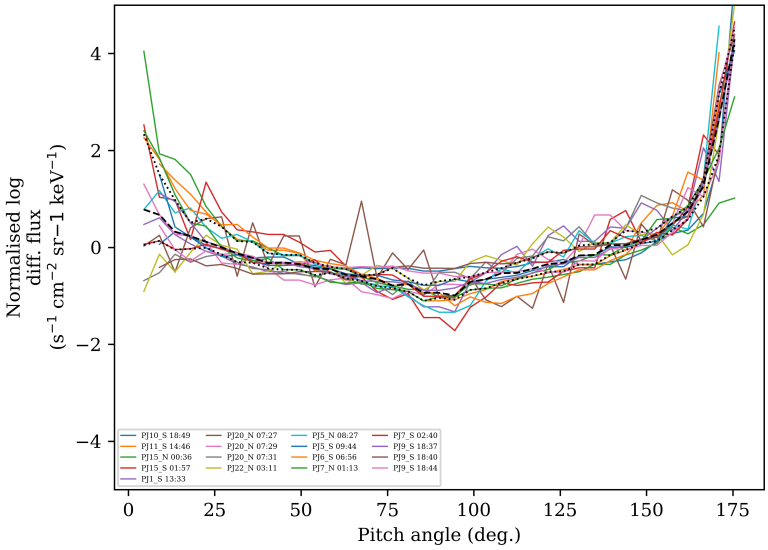

Figure 6.18: The normalised log JEDI electron differential flux pitch-angle profiles used to produce the average profile for bridge crossings in Figure 6.17 (red). The median-average profile is given as a black dashed line. The 25th- and 75th-percentile values are given as black dotted lines.

The high-frequency Waves-E intensity is noticeably elevated compared to the polar-region background level (dotted grey line) for bridge crossings (red), in line with previous results (Sulaiman et al., 2022), and crossings of the ME when no bridges are present (orange). ME crossings with bridges present (green) have noticeably lower high-frequency Waves-E LHR-Lo intensities comparable with the background, as seen in PJ9-S, and there is a clear distinction (in the 25-to-75th-percentile range)

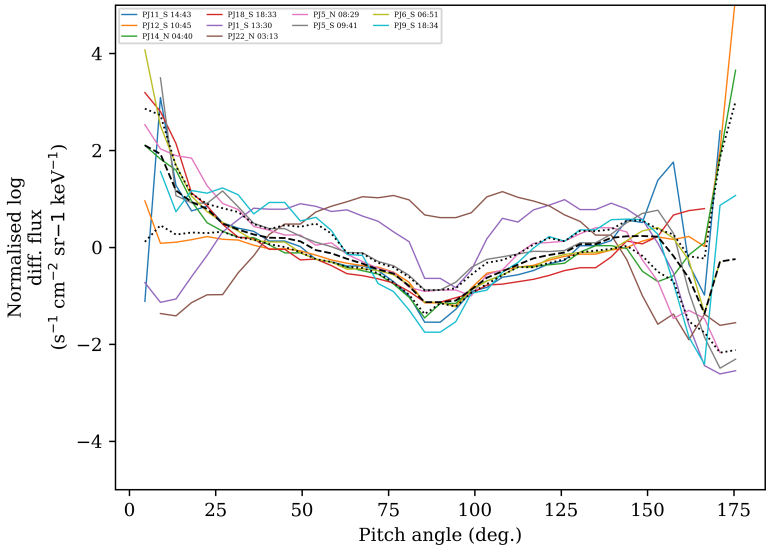

Figure 6.19: The normalised log JEDI electron differential flux pitch-angle profiles used to produce the average profile for main-emission crossings with nearby bridges in Figure 6.17 (green). The median-average profile is given as a black dashed line. The 25th- and 75th-percentile values are given as black dotted lines.

from the other two crossing types. If increased Waves-E intensity can be associated with bridge crossings, as seen during PJ9-S and as indicated by Figure 6.21, then the ME appears to take on bridge-like traits in the absence of a discernable bridge, again indicating that the "bridge" emission is still present within the ME. As in PJ9-S, although this Waves-E intensity is increased during bridge crossings, it is not correl-

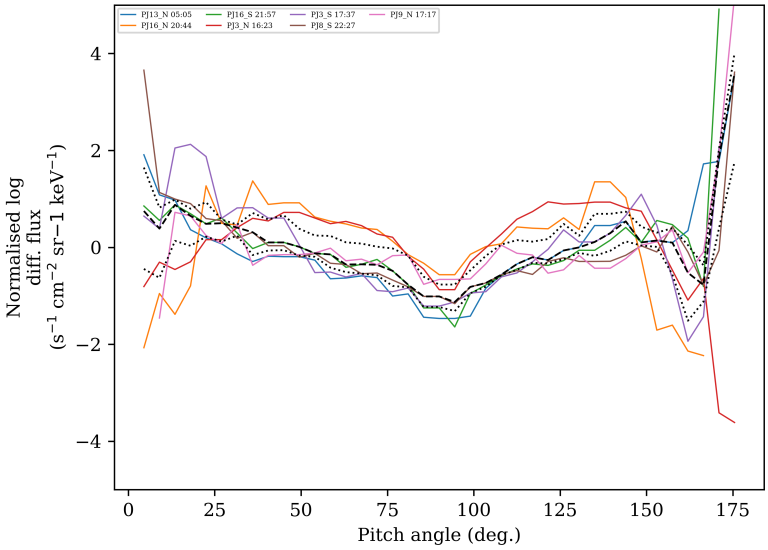

Figure 6.20: The normalised log JEDI electron differential flux pitch-angle profiles used to produce the average profile for main-emission crossings without nearby bridges in Figure 6.17 (orange). The median-average profile is given as a black dashed line. The 25th- and 75th-percentile values are given as black dotted lines.

ated with auroral brightness, which may be due to a strong dependence on altitude or a genuine complex non-linearity in the associated acceleration process(es).

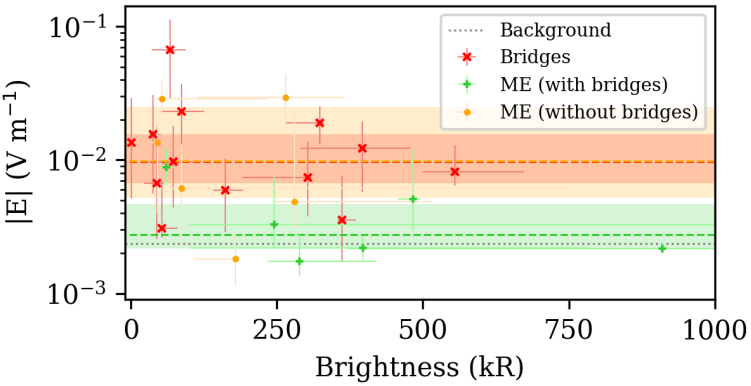

Figure 6.21: Median high-frequency (>1000 Hz) Waves-E LFR-Lo intensity vs median UV Juno-footprint brightness during dusk-side (12<MLT<18), low-altitude (<3 R_J) bridge crossings (red, cross) and ME crossings, both with (green, plus) and without (orange, dot) local bridges, observed by Juno. Error bars give the 25th- and 75th-percentile values during each crossing. The median Waves-E intensity of each distribution is given by a dashed line, and the 25-to-75th percentile range by the shaded areas. The background intensity is given by a dotted grey line.

6.3 Discussion

The results of this work indicate that bridges show similarities with ZII aurora, as defined by Mauk et al. (2020). They preferentially coincide with the downward-FAC region poleward of the ME and they show bidirectional electron distributions dominated by upward-travelling electrons, as in Figure 6.17. This

tentative association between ZII aurora and bridges is notable because it would imply that the spacing between ZI (upward FAC) and ZII (downward FAC) aurora is variable, to such an extent that there is sometimes a considerable gap between the two (in this case, between the bridge and the rest of the ME). The presence or absence of bridges is also suggested to affect the properties of the ME. When bridges are present, the ME is dominated by downward-travelling electrons (see Figure 6.17), as expected of ZI aurora. When bridges are instead absent, the ME electron distribution is typically more symmetric. The proposed interpretation is that bridges are ZII aurora that have become spatially separated from the ZI aurora, such that, in the absence of bridges, the ZII aurora is spatially indistinguishable from the ZI ME, leading to a more symmetric electron distribution during these ME crossings. This hypothesis is further supported by the stronger broadband plasma-wave signatures (considered to be a signature of ZII aurora; Sulaiman et al. 2022) seen during ME crossings in the absence of bridges (compared to those where bridges are present), as though the ZI and ZII aurorae are spatially adjacent (the "typical" configuration; Mauk et al. 2020). Even if future work weakens the association between bridges and ZII aurora, the fact that the presence of bridges affects not only the morphology but also the electron populations of the ME is itself notable.

Pending sampling of the low-altitude dawn aurora by Juno, the distinction between ZI and ZII aurora is expected to be a phenomenon that is present in the entire ME, though perhaps with some considerable local-time dependence (Sulaiman et al., 2022), which may seem at odds with the idea that the bridge, a uniquely pre-dusk feature, can be identified as ZII aurora. It is suggested that the process that gives rise to the separation

between ZI and ZII in the case of bridges may occur more easily or to a greater extent in the pre-dusk magnetosphere. This is compatible with analysis by Jenkins et al. (2024), in which the Alfvén radius is shown to be greater than 60 R_J only between 10 and 20 MLT, limiting the information that can be conveyed to the aurora from the distant magnetosphere beyond 60 R_J via Alfvén waves outside of these sectors; the bridge source process may similarly be hampered in the dawn and night sectors, explaining the lack of observed bridges in these regions of the aurora. This interpretation is tentative and would require both modelling work and further data from Juno, as well as a better understanding of the processes that give rise to bridges.

The results of this work also support the ZII auroral-generation scenario described by Elliott et al. (2018) and Sulaiman et al. (2022). In this scenario, electric-potential structures above the ionosphere create upward electron beams that generate large-amplitude ESWs, as has been demonstrated (Elliott et al., 2020). These ESWs provoke bidirectional broadband electron acceleration that leads to auroral emission. This scenario explains the presence of high-frequency Waves-E emission observed by Juno-Waves during bridge crossings (frequency-domain representations of large-amplitude ESWs; Sulaiman et al. 2022) and upward-dominated bidirectional broadband electrons observed by JEDI (the combination of upward electron beams and stochastic acceleration from ESWs). The association of enhanced Waves-E emission with bridge crossings indicated in this work, rather than with signatures in the FACs or Alfvénic Poynting flux, supports this scenario. ESWs, observed as enhanced Waves-E emission, are also associated with ME crossings in the absence of bridges, but not when bridges are present,

again supporting the hypothesis that the "bridge" aurora remains present even when spatially indistinguishable from the ME, consistent with the association between bridges and ZII. While ESWs appear to be associated with bridge crossings, the expected acceleration processes are poorly understood and highly non-linear and, though Waves-E intensity peaks are systematically seen during bridge crossings, there is a lack of correlation between auroral brightness and Waves-E intensity, and so the above scenario remains speculative.

The results of this work also suggest that the solar wind exerts some influence on the morphology of the ZI and ZII aurorae. If magnetospheric compression can be predominantly attributed to the solar wind (rather than a variable plasma-outflow rate from Io), the agreement between bridge count and the compression state of the magnetosphere, shown in Figure 6.10, is consistent with the result of Nichols et al. (2017), in which a bridge-like morphology was observed in the dusk-side polar collar during a solar-wind shock measured by Juno during its approach to Jupiter. The results regarding the onset times and lifetimes for bridges (that they can arise within a few hours and can last for longer than a Jupiter rotation) also fit this hypothesis, since hour-scale variations are compatible with simulations of the effect of solar-wind shocks on the magnetosphere (Chané et al., 2017). Therefore, if ZI aurora can be spatially associated with upward Birkeland currents and ZII aurorae with the downward currents necessary to close the loop (Sulaiman et al., 2022), then the solar wind is suggested to affect the local ionospheric or magnetospheric conditions required for current-loop closure, thus affecting the morphology of the ZI and ZII aurorae. It may, to some extent, do this by modifying the magnetic topology within Jupiter's middle magnetosphere. Com-

pression of the magnetosphere by the solar wind has already been shown to play a significant role in contracting the ME via modification of the current sheet and associated magnetic-field contribution, rather than by modifying the ME magnetospheric source radius (Nichols et al., 2009a; Head et al., 2024). This present work may indicate that magnetospheric compression by the solar wind pushes the magnetic field lines inward, which would move ME features poleward as well as increase the ionospheric separation between adjacent features in the magnetosphere. This scenario, though tentative, is consistent with bridges that "grow" from the ME rather than from the active region (Figures 6.8 and 6.9). Additionally, three ME crossings (PJ3-N, PJ14-N, PJ22-N) were identified by Al Saati et al. (2022) in which the ZII (downward FAC) region was located equatorward of the ZI region. These three cases all also show expanded MEs (Head et al. 2024; supporting material), associated with an uncompressed magnetosphere, which may work in the opposite direction to pull the ZII aurorae equatorward of the ZI aurora, in contrast with previous predictions (Cowley et al., 2007). More work is required to investigate the exact mechanisms for the variation in morphology of the ZI and ZII aurorae, but, in all, this work suggests that the solar wind may exert an indirect yet significant influence on Jupiter's aurorae.

6.4 Conclusions

The findings of this work can be summarised as follows:

1. Bridges, observed as dusk-side polar-collar arcs in Jupiter's UV aurora, are frequently seen in both hemispheres, in both HST-STIS and Juno-UVS images.

2. They are observed to appear and disappear on timescales of hours and have been seen to persist over a full Jupiter rotation, in line with previous conclusions made using limited data.

3. The appearance of bridges in the aurora is associated with compression of the magnetosphere.

4. Crossings of bridges by Juno are preferentially associated with downward FACs and broadband field-aligned electron distributions dominated by upward-travelling electrons, indicating that bridges are possibly ZII aurorae, as defined by Mauk et al. (2020), that have become noticeably separated from the (ZI) ME. Where Juno passes at low (<3 R_J) altitude over the aurora, bridge crossings are also often associated with ESWs observed by Juno-Waves. This aligns with the scenario presented by Elliott et al. (2018) and Sulaiman et al. (2022), in which upward-travelling ESWs induce bidirectional broadband auroral electron acceleration.

5. The ME is typically associated with ESWs and largely symmetric, bidirectional electron distributions when bridges are absent from the aurora, and with predominantly downward electron populations without considerable ESWs when bridges are present. This suggests that the ME may exist as either an adjacent ZI/ZII aurora, or as a uniquely ZI aurora when the ZII aurora has become spatially separated in the form of bridges.

6. Finally, the identification of the bridge as ZII aurora spatially separated from the ME, alongside the observed dependence of the appearance of bridges on the state of

compression of the magnetosphere, implies that the solar wind can exert influence on the morphology of Jupiter's UV aurora.

Future numerical experiments are required to investigate the effect of various types of solar-wind compression on auroral morphology and provide a theoretical explanation for the results described in this work.

Chapter 7

Injection signatures

It was just before dawn. They came out of nowhere.

Cliegg Lars, *Star Wars Episode II: Attack of the Clones*[1]

Discrete features in Jupiter's ultraviolet aurora have been interpreted as signatures of plasma injections in the middle magnetosphere. There exists some ambiguity whether magnetodisc scattering or high-latitude Alfvénic acceleration best describes the observed properties of these injection signatures, and also to what extent arcs in the outer emission are related to injections. Many injection signatures are the result of the evolution of dawn storms; there is, however, limited evidence that non-dawn-storm injection signatures are sometimes present in the aurora. The outstanding questions in the literature that

[1]The author is grateful to B. Bonfond, who suggested that quotes should be sourced from films other than Star Wars Episode I: The Phantom Menace. I hope that the reader appreciates this new variety.

this work aims to tackle are thus the following:

- Can injection signatures be classed into two types (dawn-storm and non-dawn-storm) based on their behaviour and characteristics?
- Are injection signatures predominantly driven by scattering in the magnetodisc or high-latitude Alfvénic acceleration?
- Is there a phenomenological difference between (blob-like) injection signatures and arcs in the outer emission?

We use automatic detection of these discrete features, alongside data from Juno-UVS and in-situ measurements by other Juno instruments, to show that pitch-angle scattering in the equatorial plane likely accounts for most of the electron precipitation associated with injection signatures. Additionally, there is evidence that injection signatures can be classified into two types: dawn-storm and non-dawn-storm. Arc-like features in the outer emission show very similar properties to traditional blob-like injection signatures and may consist of sequences of injection signatures that have broadened into an arc via energy-dependent electron drift. Finally, both Alfvénic and current-based generation mechanisms are not supported by this work despite the presence of both field-aligned currents and Alfvénic flux during Juno crossings of injection signatures; it is suggested that these are secondary products of the pitch-angle scattering process and do not meaningfully contribute towards auroral injection signatures.

This section on injection signatures in Jupiter's UV aurora follows from Head et al. (2026), published by Astronomy and Astrophysics on 2026-03-13, of which I was first author. The

most relevant section of the introduction is section 2.8 (outer emission).

7.1 Methods

In order to determine the location of potential injection signatures in maps of the aurora, an algorithm was developed that combines manual feature designations with an automatic random-forest classifier. This combines the accuracy of manual designation of which features constitute probable injection signatures with the objectivity of the automatic random-forest classifier. A random-forest classifier is a classification model that uses a large number of decision trees to assign labels to data points (Ho, 1998). Each decision tree is trained on a random subset of the data and assigns a label to each data point by taking the most common result from the ensemble of decision trees (a "forest"). The total number of decision trees in the forest and their length (number of branches/decisions in the tree) can be varied to produce labellings of varying accuracy to the original labels. Random-forest classifiers can be applied to assign labels to unseen data in a partially labelled dataset or, as is the case in this work, to improve the objectivity of a set of manual labels. By varying the number and length of the decision trees in the forest, the "coarseness" of the generated labelling can be modified, from unusably coarse for very small forests of very short trees up to a perfect recreation of the original labelling for very large forests of very tall trees. Somewhere between these two extremes lies a middle ground that will return a labelling that is more objective than the original manual labelling while still approximating it in a broad sense.

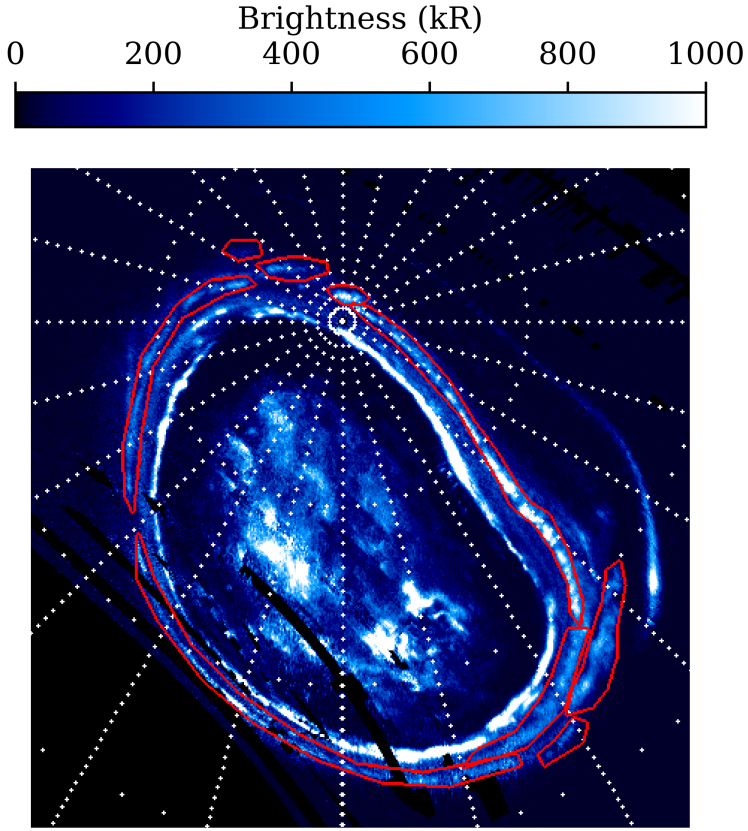

Figure 7.1: Exemplar map of UV brightness for PJ11-N. Manually designated features in the outer emission have been highlighted in red.

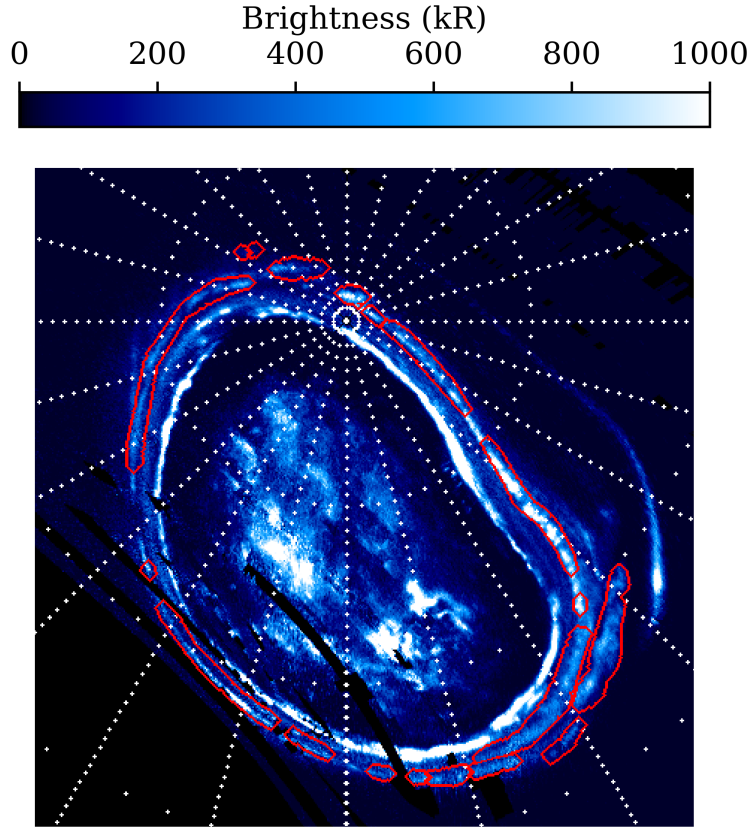

Figure 7.2: Same as Figure 7.1 but instead with automatically detected features.

A more general description of random-forest classification is given in section 3.2.2.

Manual labelling of potential injection signatures was performed by designating polygons on maps of the aurora. Since the colour-bar limits of these maps was set at (0, 250) kR, these manual designations are likely insensitive to injection signatures with maximum brightnesses below ∼50 kR, though this brightness is comparable with the background brightness of the diffuse aurora and thus injection signatures with this maximum brightness are, in any case, not likely to be easily differentiable from the rest of the aurora. These polygons were designed to comfortably contain the entire injection signature rather than to follow its border exactly, since it was expected that further refinement of the injection-signature masks would be performed by the random-forest classifier. Since these designations were performed "by eye", they are naturally more sensitive to injection signatures that are large in the ionosphere, and thus to regions of weak surface magnetic field. This is not expected to significantly affect the results of this work as Juno performs its perijoves without any bias in subsolar longitude, and hence a particular local time will correspond to many System-III longitudes during the first 40 perijoves.

The random-forest classifier used in this work takes the pixel masks generated by the above manual-designation process and combines them with the pixelwise brightness, colour ratio, and projected radial distance, System-III longitude, and local time in the equatorial magnetosphere to produce automatic pixelwise masks of potential injection signatures. Each data point to be assigned a label by the random-forest classifier is thus a polar-projected-image pixel represented as a vector with five properties. The projected location in the mag-

netosphere is used alongside the (ionospheric) brightness and colour ratio to refine the behaviour of the detector; the brightness of injection features or the background aurora may vary based on local magnetic-field strength, local time, or distance from the main emission, and so it is important to encode these parameters for the detector. It was a posteriori determined that the random-forest classifier does a very poor job of creating masks for injection signatures when only the brightness and colour ratio are used as inputs. A standard 4:1 train-test split was used to train the classifier and assess its accuracy. A 50-tree forest with tree depth of 100 was determined to adequately perform the classification. Smaller forest sizes or shorter trees gave far less precise injection-signature masks, whereas increasing these parameters above these values, even by orders of magnitude, did not materially alter the performance of the classifier; the results of the 50-tree, 100-depth random-forest classifier represent a settled solution for this dataset. The training of this classifier was performed using the `scikit-learn` Python package, and resulted in a model accuracy of 97%. Qualitatively, the masks produced by the automatic classifier strongly resemble the manual designations but smoother and more granular. Some injection signatures are split or merged, some are absent, and extra injections have been identified, as expected from an automatic method, but it fundamentally identifies the same population of potential injection signatures as the manual designation. An example of manual designations of potential injection signatures and their automatically determined equivalents is given in Figures 7.1 and 7.2. The trained classifier is available for download at `https://zenodo.org/records/17751841`.

These detected discrete features were further sub-divided

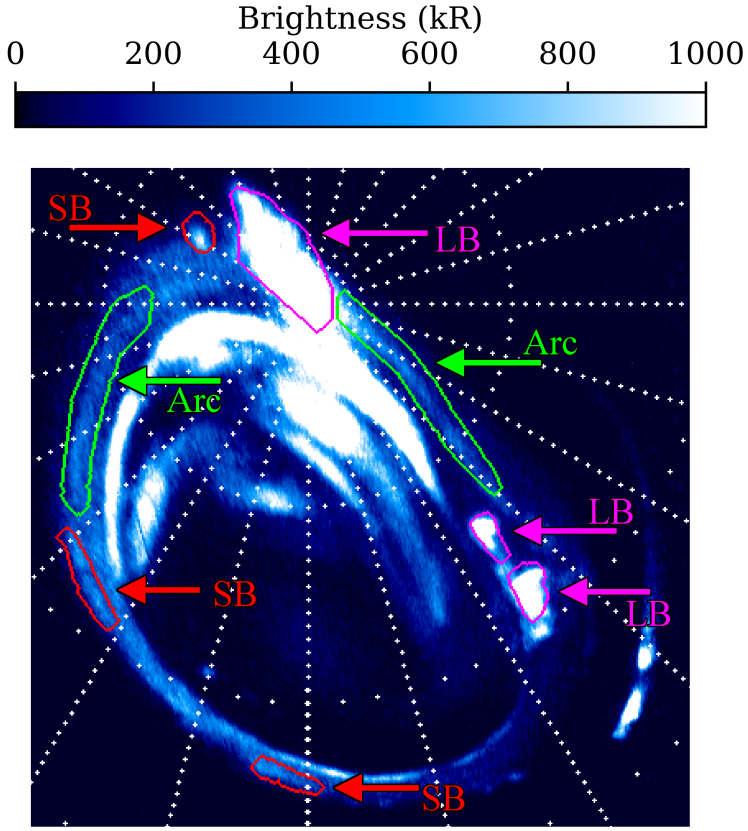

Figure 7.3: Exemplar map of UV brightness from PJ7-N. Automatically detected features in the outer emission have been highlighted according to their feature type as defined in the text: red = small blob (SB), magenta = large blob (LB), green = arc. Gridlines are in jovicentric coordinates and are spaced by 15° in latitude and longitude.

into three categories based on their shape when projected from the ionosphere into the magnetosphere equatorial plane:

- Small blobs: longitudinal extent $< 30°$, radial extent < 5 R_J;
- Large blobs: longitudinal extent $< 30°$, radial extent > 5 R_J;
- Arcs: longitudinal extent $> 30°$, radial extent < 5 R_J.

The radial-extent cutoff of 5 R_J was chosen to coincide with the "compact-structure" latitudinal-width cutoff (3°; 1° latitude $\sim$ 1.75 R_J in the outer emission) used in Dumont et al. (2014). The longitudinal-extent cutoff was selected qualitatively to differentiate between obvious arcs and more compact structures. A case showing the three types of feature morphology is given in Figure 7.3.

A sensitivity analysis was performed to support the use of this cutoff. It can been seen in Figures 7.4 and 7.5 that varying the longitudinal-extent cutoff between automatically detected blob-like and arc-like features in the outer emission by $\pm 10°$ has little effect on the distribution shown in Figure 7.6 (longitudinal-extent cutoff = 30°). In all cases, the small-blob features and arc-like features are both concentrated around a projected radial distance of $\sim$11 R_J, with arc-like features being more concentrated in the dusk sector than the noticeably more uniformly distributed small-blob features. The choice of a 30° longitudinal-extent cutoff, while chosen as an approximate cutoff between the longitudinal spans of blob-like and arc-like features, is thus not expected to materially affect the conclusions of this work. Indeed, the fact that Figures 7.4 and 7.5 show such similar distributions is itself indicative that most

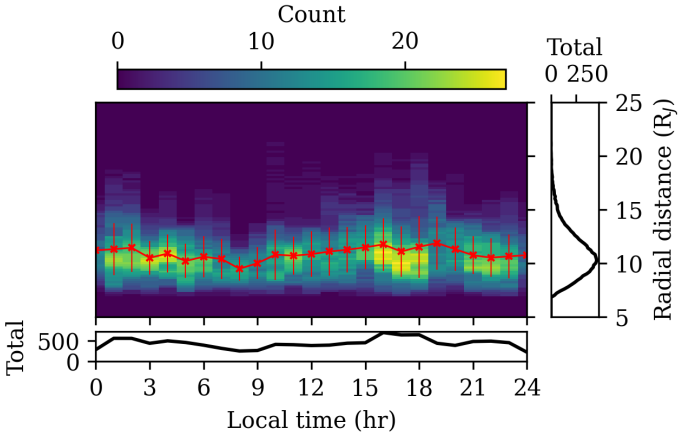
Count
0
10
20
Total
0 250
25
20
15
10
5
Radial distance (Rj)
Total
500
0
0
3
6
9
12
15
18
21
24
Local time (hr)

(a)

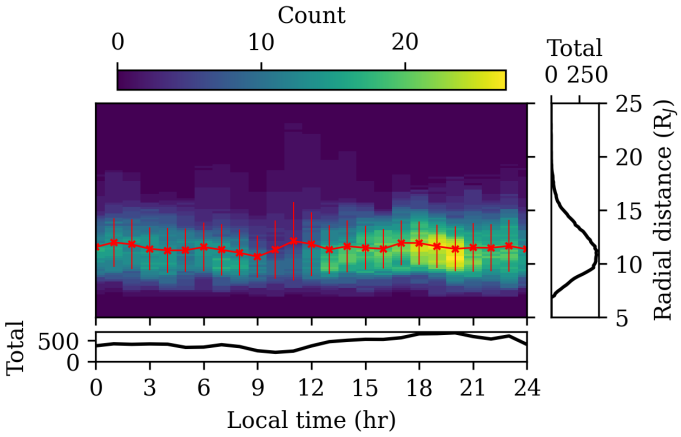
Count
0
10
20
Total
0 250
25
20
15
10
5
Radial distance (Rj)
Total
500
0
0
3
6
9
12
15
18
21
24
Local time (hr)

(b)

Figure 7.4: Histogram in radial distance and local time of the projected position in the equatorial plasma sheet of (a) small blobs and (b) arcs (longitudinal-extent cutoff = 20°) in the outer emission. The mean-average location for each local-time bin is given by the red line; error bars denote the standard deviation. Histograms flattened in local time and radial distance are given to the bottom and right of the main plot, respectively.

blob-like features have longitudinal extents less than 20°, as assumed by Dumont et al. (2014), and that arc-like features mostly have longitudinal extents greater than 40°.

Perijoves 1 to 40 are considered in this work. The evolution of Juno's orbit is such that passes over the northern aurora occur at increasing speed and passes over the southern aurora at increasing altitude toward later perijoves. This results in a diminishing UVS coverage of the aurora in the north and a diminishing resolution in the south, both of which hamper the reliable identification of injection signatures. As such, perijove 40 represents a reasonable cutoff for this work. In total, this corresponds to 78 exemplar maps of the aurora, one per hemisphere per perijove excluding PJ2, when Juno was placed into safe mode. Exemplar maps of auroral brightness B in the non-absorbed (145-165 nm) band in Rayleigh are converted to maps of estimated emitted power P in watts by determining the surface area subtended by each pixel A and applying

$$P = 10^{10} \cdot \frac{1}{4} \cdot \frac{hc}{|\lambda|} \cdot A \cdot B \cdot 4.4, \tag{7.1}$$

derived from the definition of the Rayleigh, where h is the Planck constant, c the speed of light, and 4.4 an empirical

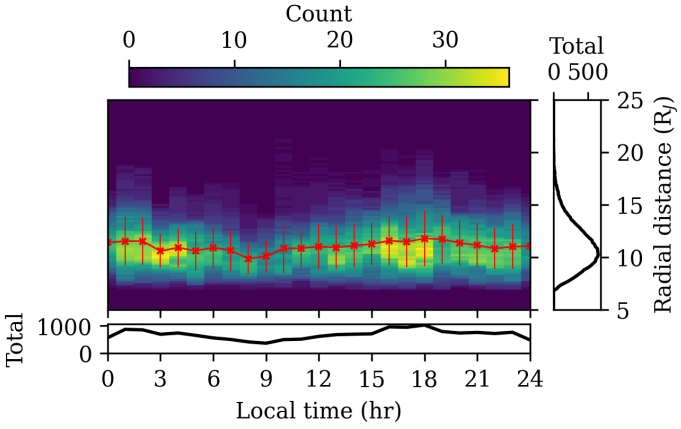
Count
0
10
20
30
Total
0 500
25
20
15
10
5
Radial distance (R$_J$)
Total
1000
0
0
3
6
9
12
15
18
21
24
Local time (hr)

(a)

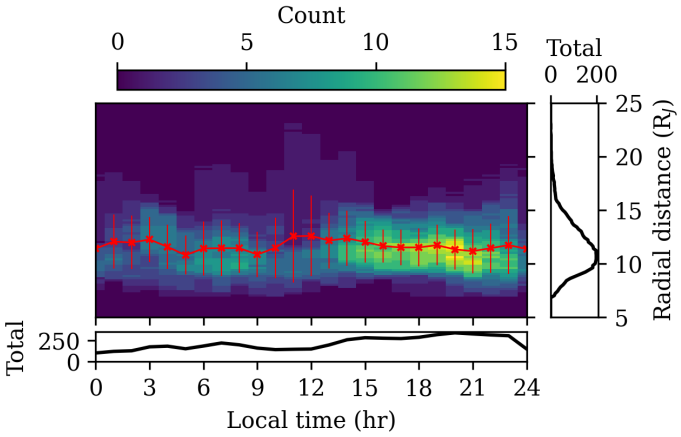
Count
0
5
10
15
Total
0 200
25
20
15
10
5
Radial distance (R$_J$)
Total
250
0
0
3
6
9
12
15
18
21
24
Local time (hr)

(b)

Figure 7.5: As Figure 7.4 (a: small blobs, b: arcs) but with a longitudinal-extent cutoff of 40°.

factor to convert the non-absorbed brightness into the full UV brightness (Groulard et al., 2024), calculated from a synthetic spectrum of H_2 (Gustin et al., 2013; Hue et al., 2019a). In this work, the non-absorbed band is preferred over the more typical Lyman-α band (155-162 nm) because of its wider spectral range and hence greater signal-to-noise, especially to detect dimmer injection signatures. This estimation of emitted power in this wavelength band is very approximate and assumes that all UV photons have the same wavelength of $|\lambda| = 160$ nm. In this work, emitted power is only ever considered as the ratio of emitted power in the northern and southern hemispheres, and so the accuracy of the conversion is not essential as long as it is consistent between hemispheres.

In addition to maps of the auroral UV brightness, colour-ratio maps are also used in this work. The (methane) colour ratio is used to probe the average energy of precipitating electrons, which we take as the ratio of the intensity in the 155-162 nm and 135-140 nm bands, since this definition has been shown to be less sensitive to known calibration issues in Juno-UVS (Vinesse et al., 2026) than the typical (155-162)/(125-130) nm definition (Gustin et al., 2013). In any case, Vinesse et al. (2026) indicate that the two colour ratios deviate mainly for very bright features (such as the main emission and dawn storms) and so the effect of this new colour ratio on our conclusions is expected to be slight, especially since the absolute value of the colour ratio is not used to draw conclusions in this

work.

The auroral brightness at the Juno footprint is determined separately from the exemplar maps to ensure that the instantaneous brightness of the aurora below Juno is captured, since the exemplar maps represent a single snapshot of the aurora during Juno's traversal of each hemisphere. For the peak brightnesses (embodied by the 90th-percentile brightness seen during Juno crossings of a discrete feature), an additional geometric correction of r^2, where r is the radial distance from the centre of Jupiter in R_J, has been applied. This is to compensate for the effect that Juno's altitude has on peak brightness; while the loss of resolution at higher altitudes should not affect the total power of an injection signature, the peak brightness value will decrease as r^{-2}.

The downward (planetward), upward, and perpendicular electron energy flux is determined from JEDI data accessed via the JMIDL tool provided by John Hopkins University. Typically, JEDI data would be taken in conjunction with JADE data, which can sample lower-energy electrons than JEDI; however, since we use detected electron properties to calculate the total energy flux, JEDI higher-energy electrons contribute far more to the energy flux than the JADE lower-energy electrons, and so we consider this a reasonable simplification, used in previous work (e.g. Clark et al., 2018). Nevertheless, it should be stated that the electron energy fluxes presented in this work therefore represent lower limits, as per Clark et al. (2018). The downward and upward fluxes take electrons within 20° of the local magnetic-field vector, whereas the perpendicular flux takes electrons in the 45-135° range. This is to ensure that the loss cone is never sampled by the "perpendicular" electron flux, since a loss-cone angle of 45° corresponds to an altitude

of ∼0.26 R_J, below the minimum Juno-crossing altitude for the injection signatures presented in this work. An approximate loss-cone angle of 20° is reasonable for Juno's low-altitude passes over the aurora (Mauk et al., 2017c), though the exact angle varies with altitude and local surface magnetic field. Since it would be prohibitively time-consuming to download electron-flux data within the exact loss-cone angle for each timestamp during each perijove, a geometric correction is applied by multiplying the 20° electron energy flux by the ratio between the calculated loss-cone angle at each point during Juno's traversal and 20°. This is a simple correction that does not take into account e.g. the potential inhomogeneity of the flux within the loss cone, but it is necessary to get reasonable estimates of the loss-cone electron flux from JMIDL data. In any case, perfect estimation of the loss-cone electron flux is difficult due to the lack of sampling by the most-field-aligned JEDI channels (Mauk et al., 2017c; Clark et al., 2018).

Alfvénic Poynting flux is determined from Juno-FGM data extrapolated via magnetic-flux conservation to the assumed auroral altitude of 400 km to ensure that the flux within the flux tube is correctly compared between perijoves regardless of Juno's observing altitude, after the method presented by Gershman et al. (2019). A bandpass frequency filter with limits of (0.2, 5) Hz is applied to high-resolution (64 Hz; Connerney et al. 2017b) Juno-FGM data; these filter frequencies are chosen to investigate Alfvén waves that could potentially give rise to auroral electron precipitation (Lorch et al., 2022). This filtered magnetic-field data is compared to the JRM33 magnetic-field model to determine the field residual δB and hence estimate the Alfvénic Poynting flux in this frequency

range

$$F_{\mathrm{Alf}} = \frac{(\delta B)^2 \, c}{\mu_0}, \tag{7.2}$$

where μ_0 is the permeability of free space, as per Gershman et al. (2019).

Magnetic-field-line tracing is performed using the 18th-order JRM33 internal-field model (Connerney et al., 2022) combined with the Con2020 external-field model (Connerney et al., 2020), via routines made available by the `JupiterMag` Python library (James et al., 2022; Wilson et al., 2023).

Field-aligned currents were calculated from FGM data compared against the above magnetic-field model and extrapolated via conservation of current to the assumed auroral altitude of 400 km as per Al Saati et al. (2022); a full description is given in appendix A.2 of Head et al. (2025).

7.2 Results

7.2.1 Juno-UVS analysis

Via magnetic mapping into the equatorial plasma sheet, the magnetospheric location of injection signatures can be investigated, as shown in Figure 7.6; "Count" denotes the number of different signatures that cover a given bin, though a single signature can cover multiple bins in the magnetosphere. Figure 7.6a indicates that large-blob features predominantly map to the dusk-side magnetosphere between 10 and 20 R_J from Jupiter. This radial distance is compatible with the preferred distance for young plasma injections identified by Juno ($\sim$17 R_J; Daly et al. 2024). The location of these large-blob features in the dusk-side magnetosphere is consistent with their

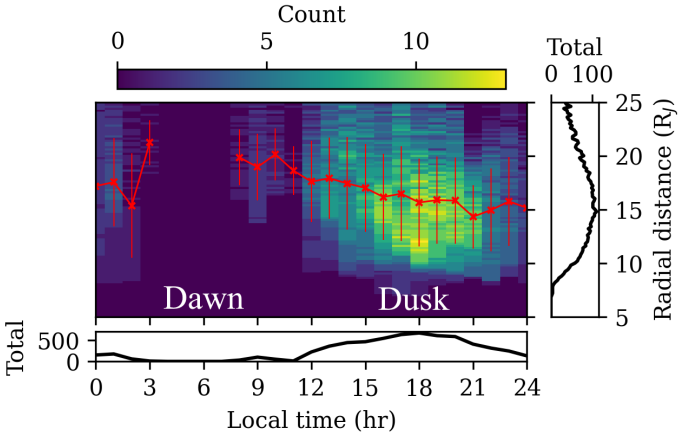
Count
0
5
10
Total
0 100
25
20
15
10
5
Radial distance (Rj)
Dawn
Dusk
Total
500
0
0 3 6 9 12 15 18 21 24
Local time (hr)

(a)

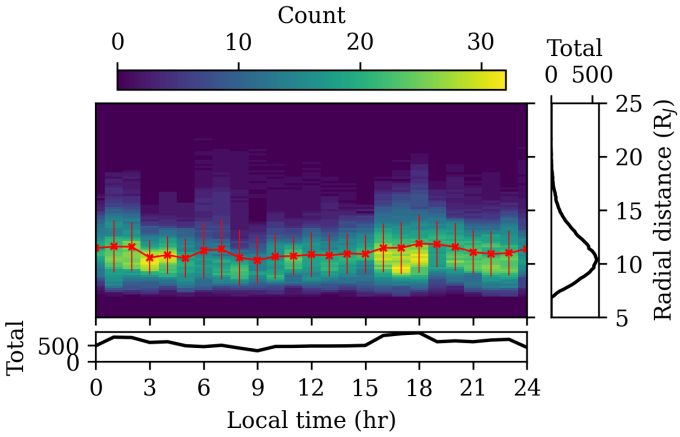
Count
0
10
20
30
Total
0 500
25
20
15
10
5
Radial distance (Rj)
Total
500
0
0 3 6 9 12 15 18 21 24
Local time (hr)

(b)

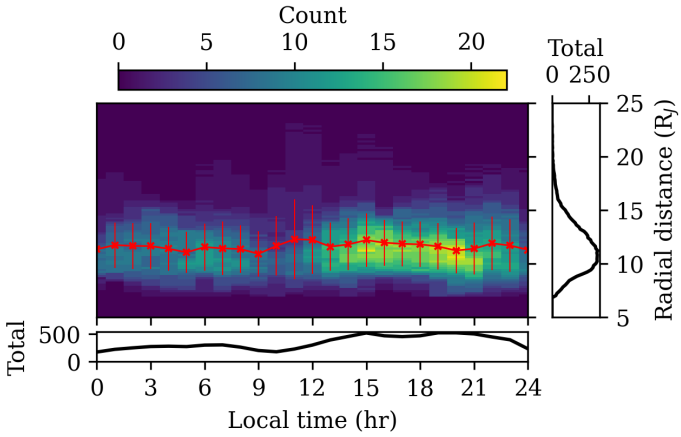

(c)

Figure 7.6: Histogram in radial distance and local time of the projected extent in the equatorial plasma sheet of (a) large blobs, (b) small blobs, and (c) arcs in the outer emission. The mean-average location for each local-time bin is given by the red line; error bars denote the standard deviation. Histograms flattened in local time and radial distance are given to the bottom and right of the main plot, respectively.

interpretation as evolved dawn storms (Bonfond et al., 2021); as dawn storms evolve, they move duskward and equatorward, transforming into injection signatures in the dusk-side outer emission. This interpretation is strengthened by the fact that the average projected radial distance of the features decreases when moving from midday into dusk, as dawn storms leave the main emission and move equatorward in the midday sector (Bonfond et al., 2021). The absence of these features in

the dawn-side outer emission therefore strengthens the link between large injection signatures and evolved dawn storms, which remain coincident with the main emission in the dawn sector and only transform into large injection signatures once they leave the main emission in the post-noon sector (Bonfond et al., 2021).

As shown in Figure 7.6b, small-blob features are observed much more uniformly at all magnetic local times (MLT), though there is still a slight preference for the dusk- and night-side aurora. Additionally, their projected radial distance is closer to Jupiter than that of big-blob features, forming a dense population around 11 R_J in agreement with earlier work (Dumont et al., 2014). It is curious that a significant portion of the small-blob population is located in the dawn side aurora, since dawn storms are expected to give rise to injections in the post-noon, dusk, and night sectors (Bonfond et al., 2021). This may be the result of a second class of injections that occur at all MLT. Arc-like features in the outer emission show a very similar distribution as small-blob features (Figure 7.6c), being concentrated around a radial distance of 11 R_J. Their distribution in MLT, while more uniform than the large-blob injection signatures, is decidedly biased toward the dusk-side aurora when compared with the small-blob features. The consequences of these results are discussed further in section 7.3.

In addition to the example given by Bonfond et al. (2017a), this work identifies several further cases of injection signatures that appear in the absence of a preceding dawn storm; some examples are given in Figures 7.7 to 7.9. In Figure 7.7, at 06:51, the injection signature is barely present in the aurora, with a brightness comparable to the background brightness provided by the diffuse emission. Later, at 07:17, the power of

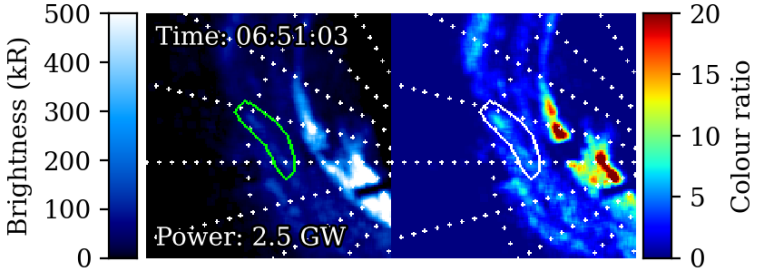

(a)

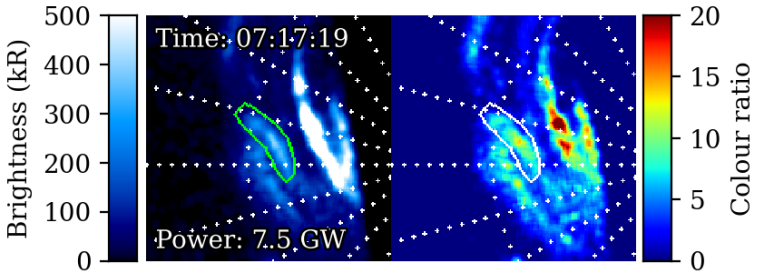

(b)

Figure 7.7: An injection signature observed on 2017-05-19 at (a) 06:51:03 and (b) 07:17:19 by Juno-UVS during PJ6-S, highlighted in green. The brightness map is given on the left and the colour-ratio map on the right. The main emission is present to the right of the injection signature.

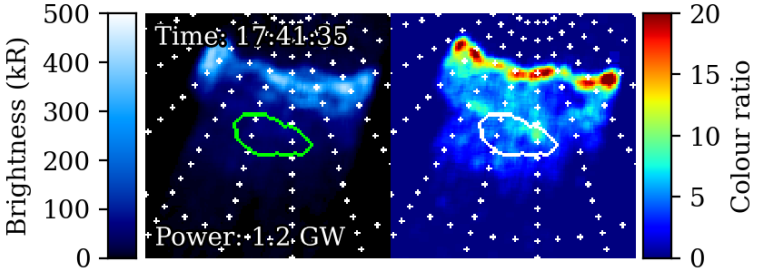

(a)

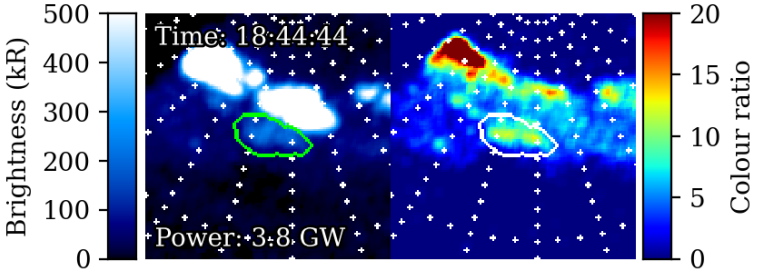

(b)

Figure 7.8: An injection signature observed on 2016-12-11 at (a) 17:41:35 and (b) 18:44:44 by Juno-UVS during PJ3-S, highlighted in green. The brightness map is given on the left and the colour-ratio map on the right. The main emission is present above the injection signature.

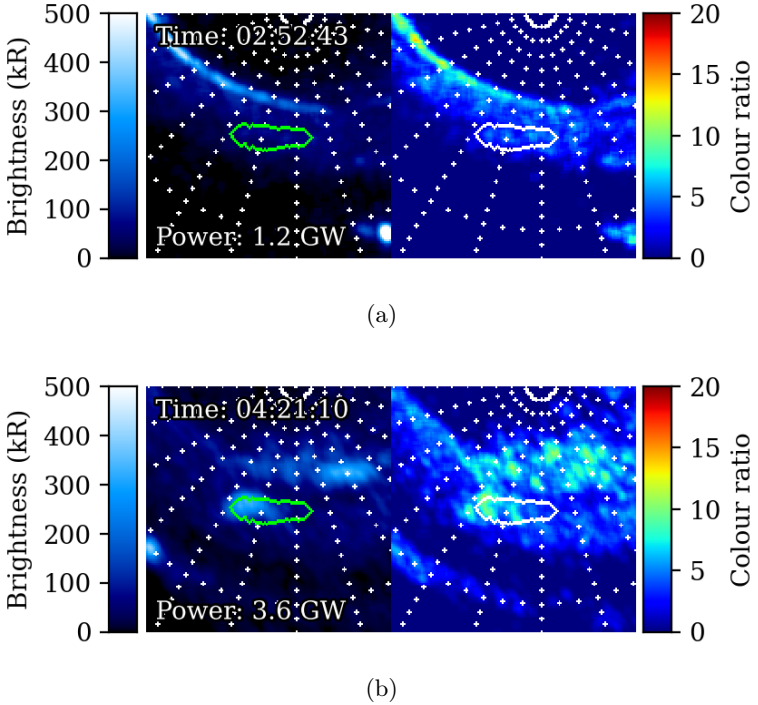

Figure 7.9: An injection signature observed on 2017-07-11 at (a) 02:52:48 and (b) 04:21:10 by Juno-UVS during PJ7-S, highlighted in green. The brightness map is given on the left and the colour-ratio map on the right. The main emission is present above the injection signature.

the injection signature has increased threefold and now forms a clear, discrete structure distinct from the diffuse emission. This example is present in the post-noon aurora (∼13 MLT); the two further examples in Figures 7.8 and 7.9 are located at ∼9 MLT and ∼11 MLT respectively, indicating that non-dawn-storm injections may occur at a variety of local times.

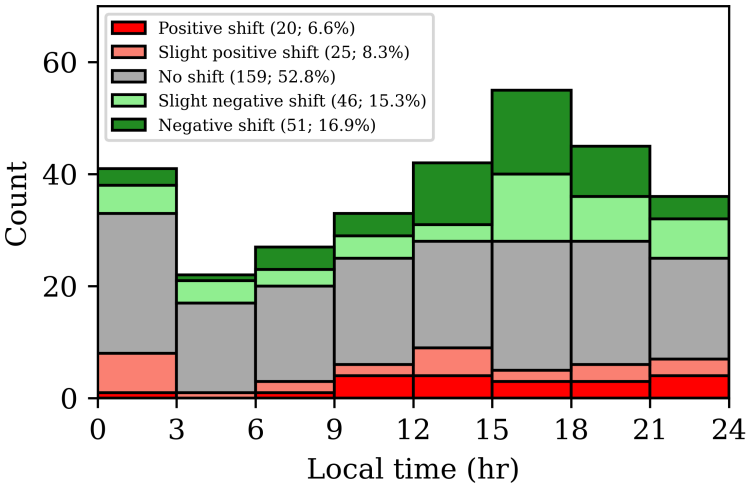

Figure 7.10: Histogram in magnetospheric local time of (small and large) blob-like injection features in the outer emission. Features are categorised by the magnetospheric longitude shift between the brightness peak and colour-ratio peak: no shift (<0.5°), slight shift (0.5° to 1°), and shift (>1°), from positive (red, bottom) through to negative (green, top) shifts.

Figure 7.10 shows the shift between the brightness peak and colour-ratio peak for blob-like injection signatures. A positive

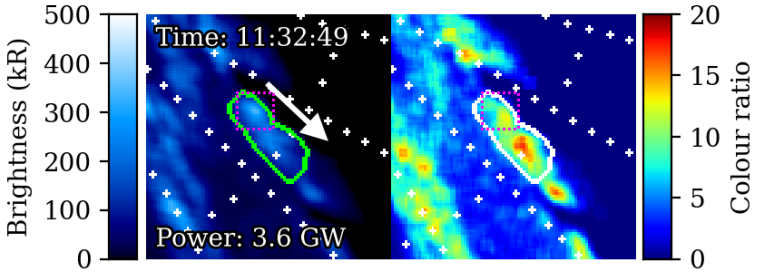

Figure 7.11: An injection signature observed at UTC 2019-04-06 11:32:49 by Juno-UVS during PJ19-N, highlighted in green. The brightness map is given on the left and the colour-ratio map on the right. The main emission is present to the left of the injection signature. The direction of increasing magnetospheric System-III longitude is indicated by the white arrow. The position of the brightness peak is given by a dotted magenta square in both maps for the sake of comparison.

(negative) shift indicates that the brightness peak is at higher (lower) System-III longitude than the colour-ratio peak. These shifts are calculated from the 10 highest-resolution (lowest-altitude) consecutive Juno-UVS spins that captured at least 90% of the injection signature; signatures with fewer than 10 consecutive spins are ignored. This is to avoid spurious shift measurements in cases where the injection signature is not sufficiently sampled by Juno-UVS, either spatially or temporally. This method is preferred over the use of the exemplar maps to avoid introducing artefact brightness or colour-ratio peaks, since the exemplar maps are built from spins that may sometimes differ considerably in time. Around half of detected injec-

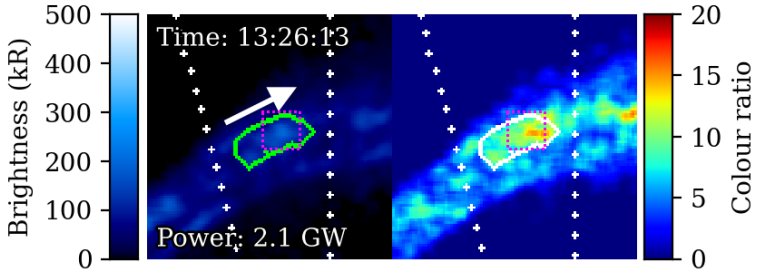

Figure 7.12: An injection signature observed at UTC 2019-04-06 13:26:13 by Juno-UVS during PJ19-S, highlighted in green. The brightness map is given on the left and the colour-ratio map on the right. The main emission is present below the injection signature. The direction of increasing magnetospheric System-III longitude is indicated by the white arrow. The position of the brightness peak is given by a dotted magenta square in both maps for the sake of comparison.

tion signatures show no discernible shift between the brightness and colour-ratio peaks (absolute shift $< 0.5°$). These features are relatively uniformly distributed in MLT, and a homogeneity test (a two-sided t-test) between the feature counts in the dawn sector (3 MLT to 12 MLT; this choice is motivated by the empty region in Figure 7.6a where large-blob signatures are absent) and the dusk/night sector (12 MLT to 3 MLT) returns a p-value of 0.16. This is insufficient to indicate non-homogeneity at the 95% confidence level. Cases with noticeable shift have been separated into slight shifts ($0.5° \leq$ shift $< 1°$) and considerable shifts (shift $\geq 1°$) to increase the granularity of the analysis. The negative-shift cases, which col-

lectively account for 32% of all detected features, appear to be concentrated in the dusk sector between 12 and 21 MLT; the same homogeneity test indicates a probability of 95% that the negative-shift cases are not homogenous between the dawn and dusk/night sectors, which is a stronger indication of non-homogeneity than for the no-shift cases. Positive-shift cases only account for 15% of the detected injection signatures. Of the 20 cases with strong positive shifts (>1°), 18 were found to be due to misdetection by the peak-finding algorithm, typically because the closest colour-ratio peak to the brightness peak was significantly smaller than a more distant peak (or vice versa), or because a single brightness peak presents as two slightly separated colour-ratio peaks (or vice versa). This leaves only two signatures with strong (>1°) positive shifts that are not obviously the consequence of algorithmic failure. In both of these cases, however, the widths of the brightness and colour-ratio peaks show significant overlap. A similar inspection of the strong-negative-shift cases provides many more examples (36 out of 51 signatures, or 70%) of convincing negative shift; some examples are given in Figures 7.11 and 7.12. This is as expected, since negative-shift cases correspond to injections where energy-dependent drift has forced the high-energy electrons (that give rise to the colour-ratio peak) ahead in System-III longitude of the lower-energy electrons (that, through a greater population, give rise to the brightness peak). Positive-shift cases are therefore difficult to describe in this framework, since our current understanding supposes that energy-dependent drift always pushes the high-energy electrons ahead of the low-energy electrons (Mauk et al., 2002) due to the properties of the energy-dependent drift imposed by curvature and gradients in the magnetic field

(Mauk et al., 1999; Dumont et al., 2018). If we assume that all positive-shift cases are due to a deficiency in the algorithm, and that this deficiency works to introduce positive and negative artefacts symmetrically, we can subtract the positive-shift counts from the negative-shift counts to estimate the "true" distribution. This returns a population of 75% no-shift features, 9% slight-negative-shift features, and 15% negative-shift features. Thus, even after we compensate for the deficiencies of the peak-detection algorithm, negative-shift cases still make up a significant portion (24%) of all injection signatures. Note that exact proportions of each shift type are dependent on the implementation of the peak-detection algorithm; nevertheless, it can be said that negative-shift cases likely constitute a non-negligible portion of all injection signatures.

One of the key observable differences between the magnetodisc-scattering and high-latitude-acceleration scenarios to precipitate electrons into injection signatures is the relation between injection-signature power and the local magnetic-field strength present for the injection signature within the ionosphere. In the latter case, a greater precipitating electron flux is expected in regions of higher surface field strength, due to increased efficiency of the Alfvénic acceleration process (Hess et al., 2013). For the isotropic-scattering case, the precipitating electron flux is controlled by the loss-cone angle α in the ionosphere (at least in the simplified case; in practice, the atmospheric profile and energy-dependent cross-sections of the various atmospheric components will modify the altitude at which electrons are expected to interact), which goes as

$$\alpha = \sin^{-1}\left(\left(\frac{B_{MS}}{B_{IS}}\right)^{\frac{1}{2}}\right), \tag{7.3}$$

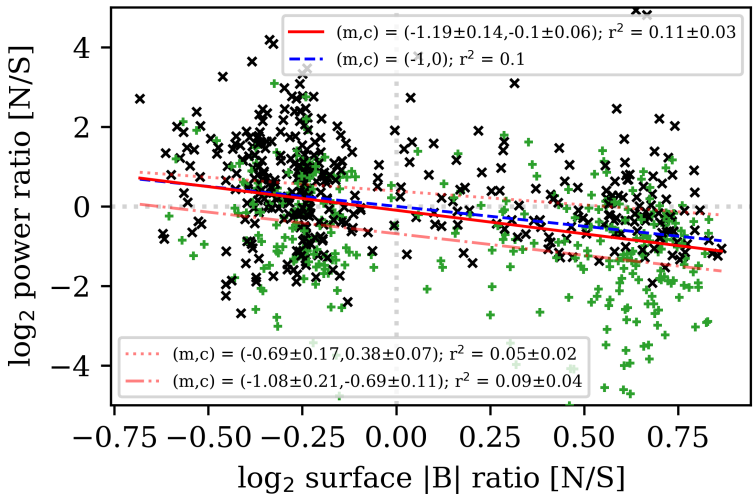

Figure 7.13: North-to-south UV auroral power ratio vs surface magnetic-field-magnitude ratio for injection signatures detected by Juno-UVS during the first 40 perijoves. The N→S projections are denoted by black ×, and the S→N projections by green +. The best-fit linear relation for all points is given by a solid red line, and separate fitted relations for the N→S and S→N case by dotted and dash-dot lines respectively. The theoretical pitch-angle-scattering relation is given by a dashed blue line.

where B_{IS} is the magnetic-field strength in the ionosphere (or rather, for simplicity's sake, the strength at the surface) and B_{MS} the magnetic-field strength at the source of the scattering

in the magnetosphere (Mauk et al., 2017c), or

$$\alpha \simeq \left(\frac{B_{MS}}{B_{IS}}\right)^{\frac{1}{2}}, \tag{7.4}$$

since $B_{IS} \gg B_{MS}$. If we assume, based on the area subtended by the loss cone for a given loss-cone angle, that the power $P \propto \alpha^2$, then

$$P \propto \frac{B_{MS}}{B_{IS}} \tag{7.5}$$

and hence the ratio of power in the northern and southern hemispheres, assuming that injection signatures are conjugate between hemispheres and hence arise from the same location in the magnetosphere,

$$\frac{P_N}{P_S} = \frac{B_S}{B_N} \tag{7.6}$$

or equivalently

$$\log_2\left(\frac{P_N}{P_S}\right) = -\log_2\left(\frac{B_N}{B_S}\right), \tag{7.7}$$

where B is the ionospheric field strength and P the emitted power in the northern (N) and southern (S) hemispheres. This relation assumes that the variability of the intrinsic "intensity" or the average electron energy of the plasma injection has little effect on the ratio of hemispheric auroral power. Different penetration depths (and hence different absorption profiles) between hemispheres may slightly affect this relation and hence account for some of the scatter in Figure 7.13. Here, the ratio of auroral power between hemispheres is preferred to a direct comparison of auroral power with surface field strength

to remove the influence of the intrinsic intensity of the plasma injection, the same for the injection signature in the northern and southern aurora, since this may otherwise mask the influence of surface field strength on injection-signature power. This analysis also supposes that conjugate injection signatures are sufficiently long-lived to remain visible in the southern hemisphere even after the approximately three-hour traversal of Juno between hemispheres, which is supported by previous work (Gérard et al., 2013; Dumont et al., 2018).

This theoretical relation is plotted in Figure 7.13 alongside the observed north/south power ratios for the injection signatures analysed in this work. Here, the pixel masks covered by the detected injection signatures (see section 7.1) in one hemisphere are projected along magnetic field lines to the other hemisphere, which creates a similar pixel mask in the other hemisphere. The total projected power can be calculated from this projected mask and compared to the total power in the original mask, though this assumes that the injection is in full corotation and produces conjugate signatures in both hemispheres. This means that most injections have two points in Figure 7.13 (N→S, S→N), but both points are included to account for cases where the injection signature is detected in only one hemisphere. The projection of a detected injection signature into the other hemisphere is also preferred over a comparison of two conjugate detected signatures because the areas returned by the signature-detection algorithm may not be exactly conjugate between the two hemispheres, and some signatures may be missed entirely in one hemisphere. It is nevertheless expected that injection signatures be magnetically conjugate (Gérard et al., 2013), as seen frequently by Juno (e.g. Bonfond et al., 2017a; Palmaerts et al., 2024). Of the injection

signatures detected in this work, 33% were found to have at least 50% of their conjugate area covered by another detected injection signature. It is expected that this relatively low conjugate-detection fraction is a consequence of algorithmic failure and the longitude precession of the injections, rather than a genuine lack of hemispheric conjugacy.

It can be seen that the linear relation fitted to these points is very close to the theoretical scattering relation. However, there exists significant scatter in the data points, as evidenced by the low R^2 value of 0.11. Firstly, a t-test was performed with the null hypothesis that the power ratios of points with (negative $\log_2$) field-strength ratios above zero are higher than those below zero. This led to a rejection of the null hypothesis with a probability of 10^{-13}, indicating that the clustered population of points on the left of Figure 7.13 are strongly suggested to have greater power ratios than those points on the right. This is not incompatible with the large scatter in Figure 7.13; though the data in the left and right clusters show reasonable overlap in their (presumed Gaussian) power-ratio distributions, these distributions are sufficiently well-sampled by the data to say with considerable certainty that data on the right are taken from a population with a lower average power ratio than the data on the left. Secondly, injections are known to slightly sub-corotate (Gérard et al., 2013; Dumont et al., 2018), and so will have moved slightly between Juno's northern and southern pass. The north-to-south auroral power ratio of injection signatures is typically greater than one for N→S projections (i.e. where the injection signature is detected in the northern hemisphere and magnetically projected to the south) and less than one for S→N projections. In other words, the emitted power in the detected injection signature is larger than

the emitted power in the projection of the injection signature in the other hemisphere. This may be due to the slight sub-corotation of injections, which would mean that, for a given injection signature, the conjugate signature in the other hemisphere would be located slightly ahead or behind the original signature in magnetospheric System-III longitude, since Juno has a hour-scale travel time between hemispheres. To test this hypothesis, we consider a hypothetical injection signature with Gaussian power profile

$$p = p_0 \cdot \exp\left(-\frac{(\theta-\mu)^2}{2\sigma^2}\right), \tag{7.8}$$

where p_0 is the peak power, θ is the System-III longitude of a given point, μ is the central longitude, and σ is the RMS width of the injection signature. To calculate the total power P of the injection signature, we integrate within a set of reasonable bounds for our detected signature, which we take to be $\mu \pm 2\sigma$, and so

$$\begin{aligned} P &= p_0 \int_{\mu-2\sigma}^{\mu+2\sigma} d\theta \cdot \exp\left(-\frac{(\theta-\mu)^2}{2\sigma^2}\right) \\ &= p_0 \cdot \left[\sqrt{\frac{\pi}{2}} \cdot \sigma \cdot \operatorname{erf}\left(\frac{\mu-\theta}{\sqrt{2}\sigma}\right)\right]_{\mu-2\sigma}^{\mu+2\sigma}. \end{aligned} \tag{7.9}$$

For the power P_{proj} contained in the projected injection-signature bounds, we assume that the injection signature has moved by $\dot{\theta}t$, where $\dot{\theta}$ is the sub-corotation rate in degrees per hour and t the Juno hemisphere traversal time in hours, and hence

$$P_{\text{proj}} = p_0 \cdot \left[\sqrt{\frac{\pi}{2}} \cdot \sigma \cdot \operatorname{erf}\left(\frac{\mu-\theta}{\sqrt{2}\sigma}\right)\right]_{\mu-2\sigma+\dot{\theta}t}^{\mu+2\sigma+\dot{\theta}t}. \tag{7.10}$$

Since the Gaussian function is symmetrical about its mean, this expression is valid for both N→S and S→N projections, i.e. whether the conjugate injection signature is ahead or behind of its expected (fully corotational) projected location. The ratio of these two powers is thus

$$\frac{P}{P_{\text{proj}}} = \frac{\left[\text{erf}\left(\frac{\mu-\theta}{\sqrt{2}\sigma}\right)\right]_{\mu-2\sigma}^{\mu+2\sigma}}{\left[\text{erf}\left(\frac{\mu-\theta}{\sqrt{2}\sigma}\right)\right]_{\mu-2\sigma+\dot{\theta}t}^{\mu+2\sigma+\dot{\theta}t}} \tag{7.11}$$

or equivalently

$$\frac{P}{P_{\text{proj}}} = \frac{2 \cdot \text{erf}\left(\sqrt{2}\right)}{\text{erf}\left(\frac{\dot{\theta}t+2\sigma}{\sqrt{2}\sigma}\right) - \text{erf}\left(\frac{\dot{\theta}t-2\sigma}{\sqrt{2}\sigma}\right)}. \tag{7.12}$$

The average vertical shift between the full linear relation in Figure 7.13 and the linear relation for the N→S and S→N cases separately is 0.57±0.1, or equivalently, since Figure 7.13 is given in $\log_2$ space,

$$\frac{P}{P_{\text{proj}}} = 1.49 \pm 0.1 \tag{7.13}$$

and hence, by assuming that the Juno hemisphere traversal time $t = 3$ hr, that injection signatures are approximately of longitudinal width $\sigma = 10°$, and solving equation 7.12 numerically,

$$\dot{\theta} = 5.4 \pm 0.4° \text{ hr}^{-1} \tag{7.14}$$

which is equivalent to a corotation fraction of 85±1%. This is within the 80-to-90% corotation fraction given by Dumont et al. (2018) and hence we suggest that the slight sub-corotation

of injection signatures combined with Juno's hour-scale traversal from the northern to the southern hemisphere may account for a significant proportion of the scatter present in Figure 7.13.

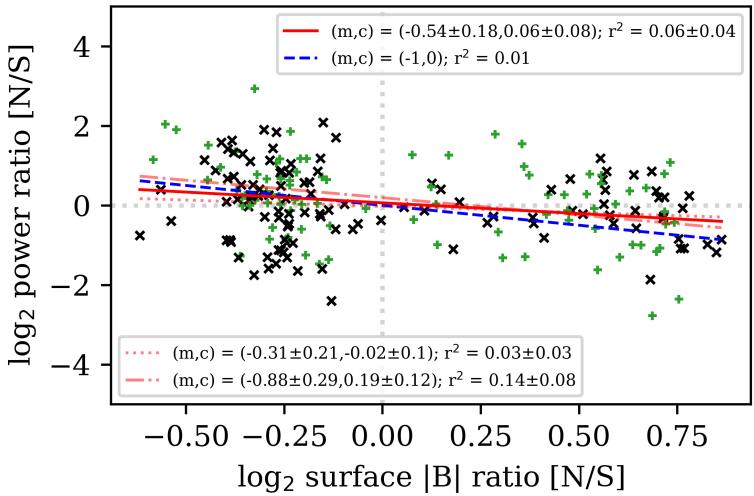

Figure 7.14: North-to-south UV auroral power ratio (conjugate area only) vs surface magnetic-field-magnitude ratio for injection signatures detected by Juno-UVS during the first 40 perijoves. The N→S projections are denoted by black ×, and the S→N projections by green +. The best-fit linear relation for all points is given by a solid red line, and separate fitted relations for the N→S and S→N case by dotted and dash-dot lines respectively. The theoretical pitch-angle-scattering relation is given by a dashed blue line.

To test this hypothesis, a modified version of the analysis

of Figure 7.13 was performed in which only those injection signatures with a detected conjugate signature in the other hemisphere were used. If the injection-signature polygon projected into the other hemisphere has less than 50% of its area covered by a (presumed conjugate) detected injection signature, it is ignored. Additionally, only the area of the two conjugate injection signatures that maps within the area of the other signature is considered when calculating the total emitted power ratio. In principle, this should greatly reduce the effect of a slight sub-corotation on the emitted power ratio. The results of this analysis are shown in Figure 7.14. There remains some significant scatter in the data; however, the fitted linear relations for the N→S and S→N projections are no longer distinct from the overall linear relation. In other words, the notion that the original detected injection signature always emits more power than its projected conjugate in the other hemisphere (present in Figure 7.13) is not present in Figure 7.14. We thus conclude that the slight sub-corotation of injections likely plays a significant role in explaining the distribution of points in Figure 7.13, in line with the mathematical argument presented above. It should be noted that injection signatures that are small enough to have no overlap in their detection polygons between hemispheres because of this sub-corotation are necessarily ignored by this analysis. This is expected to correspond to injection signatures less than 15° in longitudinal extent (since a feature moving at 85% of corotation moves ∼15° in the ∼3 hours between Juno passes of the two hemispheres), which may slightly affect the results in Figure 7.14.

These analyses increase confidence that the fitted relation in Figure 7.13 reflects physical reality, though the extent to which this scatter can be accounted for by the results of these

analyses is difficult to estimate. It should be noted that, while these caveats exist for the interpretation of the fitted relation in Figure 7.13, positive correlation between increased field-strength ratio and power ratio, and hence high-latitude Alfvénic acceleration within injection signatures, is not supported by Figure 7.13.

7.2.2 Juno multi-instrument analysis

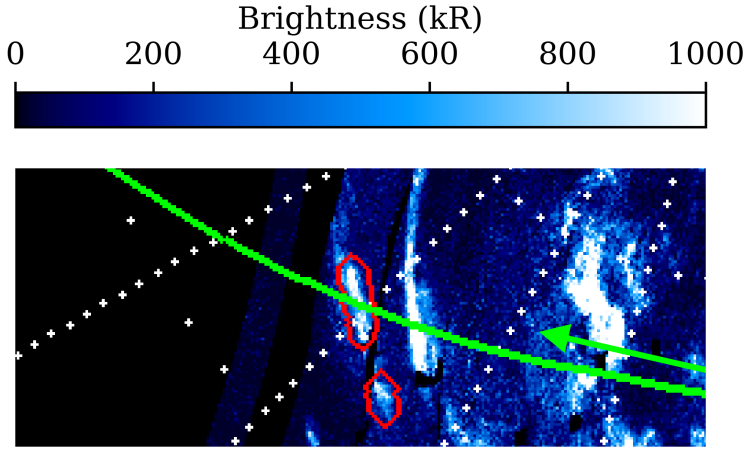

Figure 7.15: The Juno footprint path (green) overlaid on the exemplar map of the aurora for PJ21-N. An automatically detected small-blob-type discrete feature crossed by Juno is highlighted in red. The direction of travel of Juno is denoted by the green arrow.

In addition to the analysis of auroral maps made by Juno-

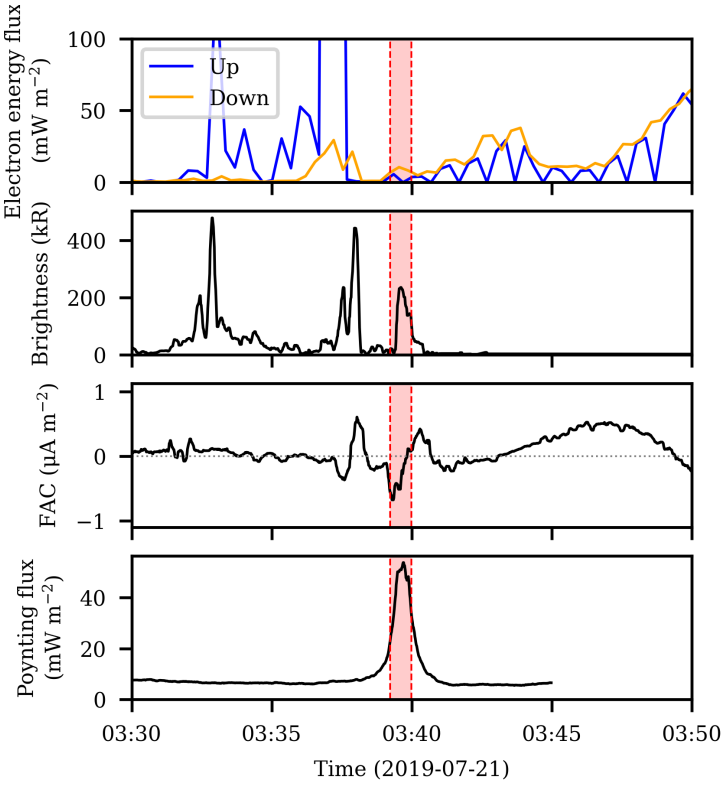

Figure 7.16: Juno instrument data for PJ21-N. The crossing of the discrete feature in Figure 7.15 is given in red. From top to bottom: JEDI field-aligned (0°-20° upward, 160°-180° downward) electron energy flux; UVS footprint brightness; calculated ionospheric field-aligned electrical current; calculated ionospheric Alfvénic Poynting flux.

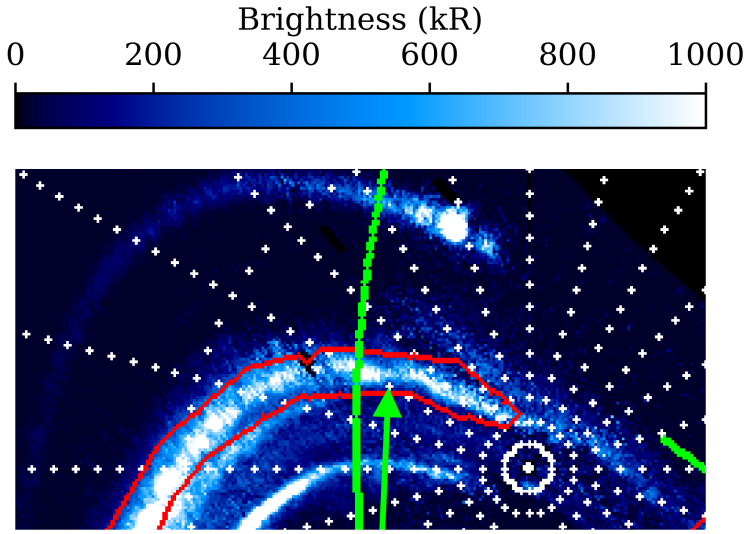

Figure 7.17: The Juno footprint path (green) overlaid on the exemplar map of the aurora for PJ13-N. An automatically detected arc-type discrete feature crossed by Juno is highlighted in red. The direction of travel of Juno is denoted by the green arrow.

UVS, the properties of injection signatures can be investigated using other instruments on board Juno. Figures 7.15 and 7.16 show the evolution of several calculated parameters as the Juno footprint passed through a blob-like injection signature during PJ21-N. The footprint UVS brightness was observed to peak within the range attributed to the feature crossing, which increases confidence that this feature is being properly detected. The field-aligned downward electron energy flux shows a

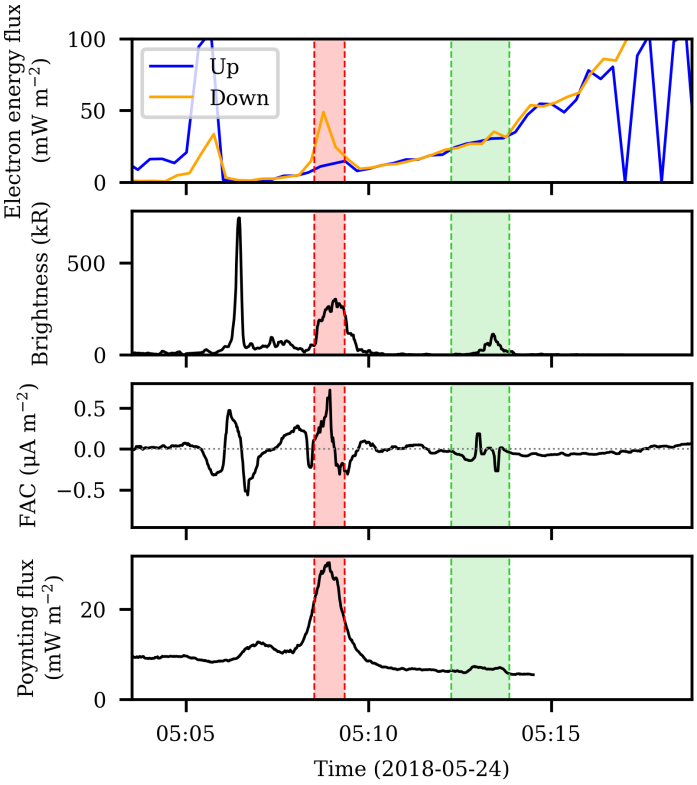

Figure 7.18: Juno instrument data for PJ13-N. The crossing of the discrete feature in Figure 7.17 is given in red, and the crossing of the Io footprint tail in green. From top to bottom: JEDI field-aligned (0°-20°, 160°-180°) electron energy flux; UVS footprint brightness; calculated ionospheric field-aligned electrical current; calculated ionospheric Alfvénic Poynting flux.

small peak ($\sim$15 mW m^{-2}) during the feature crossing, which is slightly below the energy flux expected to produce an auroral brightness of $\sim$200 kR (20 mW m^{-2}; Gérard et al. 2016). The dissipative Alfvénic flux also shows a clear peak far above the background level. A similar case where Juno instead flew over an arc-like feature (Figures 7.17 and 7.18) shows very similar behaviour.

When considering Juno crossings of both blob-like and arc-like discrete features in the outer emission during the first 40 perijoves, there exists a noticeable correlation between the downward electron-energy flux measured by JEDI and the instantaneous Juno-footprint auroral brightness, as given by the solid black line in Figure 7.19. However, while high electron-energy flux ($\gtrsim$ 80 mW m^{-2}) can be robustly associated with high auroral brightness ($\gtrsim$ 800 kR), the R^2 value of only 0.32 does not strongly support the fitted linear relation, and there exist several injection-signature crossings where high auroral brightness was coincident with only modest downward electron flux. Several mitigating factors exist that may partially explain this discrepancy. Firstly, the most field-aligned electrons are often poorly sampled by the JEDI instrument (Mauk et al., 2017c). This can lead to an underestimation of the field-aligned electron energy flux, and one that is inconsistent between injection-signature crossings. Secondly, while, for a typical average electron energy of 100 keV, the expected relation between electron energy flux and auroral brightness is 1 mW m^{-2} $\sim$ 10 kR, this relation can vary slightly with electron energy (Gustin et al., 2016), which may work to disrupt any linear relation that would otherwise be expected in Figure 7.19. Finally, the loss-cone correction applied to the electron flux (described in section 7.1), while necessary to extrapolate

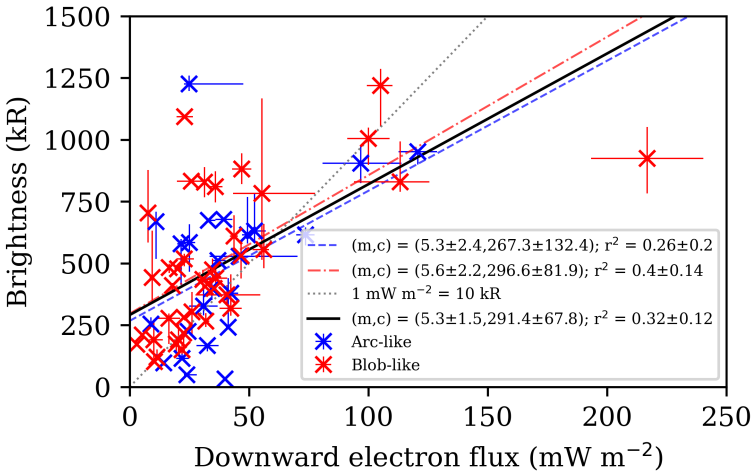

Figure 7.19: The 90th-percentile brightness vs 90th-percentile precipitating energy flux based on downward JEDI electrons (25-1000 keV) observed by Juno during crossings of arc-like (blue) and blob-like (red) features in the outer emission. Error bars denote the 80th-100th percentile range. The best-fit linear relation is given by a solid black line, as well as separate best-fit relations for the arc-like (dashed) and blob-like (dash-dot) features. The theoretical relation after Gérard et al. (2016) is given by the dotted grey line.

the electron flux within 20° to the loss-cone electron flux at Juno, may also introduce some artificial error, especially when this relatively coarse correction is applied where the loss-cone angle differs significantly from 20°, though it should be noted that this correction improves the strength of the linear relation in Figure 7.19 ($R^2 = 0.11 \rightarrow 0.32$). With these caveats

in mind, the principle that an increased downward electron energy flux leads to a higher auroral brightness is somewhat supported by Figure 7.19. Figure 7.19 also shows no meaningful separation between blob-like and arc-like discrete features in the outer emission. Both morphologies occupy the same regions of the plot, and the fitted linear relations are identical within the calculated uncertainties. This indicates that blob-like and arc-like outer-emission features have similar typical brightness/electron-flux ratios and hence a similar range of typical electron energies.

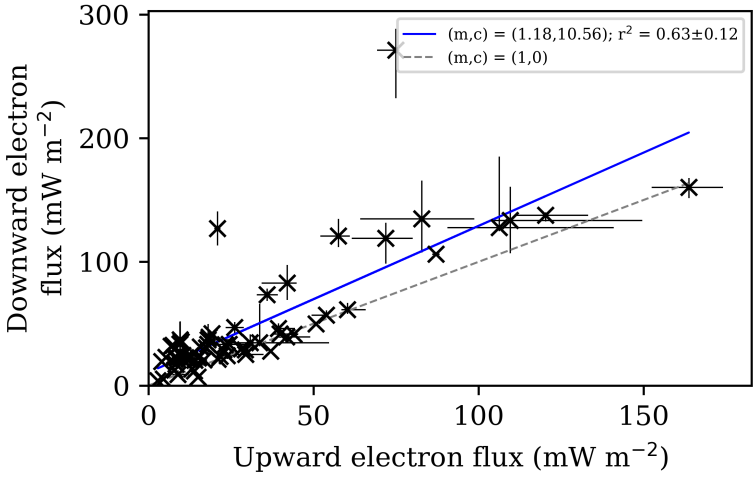

Figure 7.20: The 90th-percentile upward vs downward electron energy flux observed by JEDI during crossings of discrete features in the outer emission. Error bars denote the 80th-100th percentile range. The best-fit linear relation is given by a solid blue line, and the 1:1 relation by a dashed grey line.

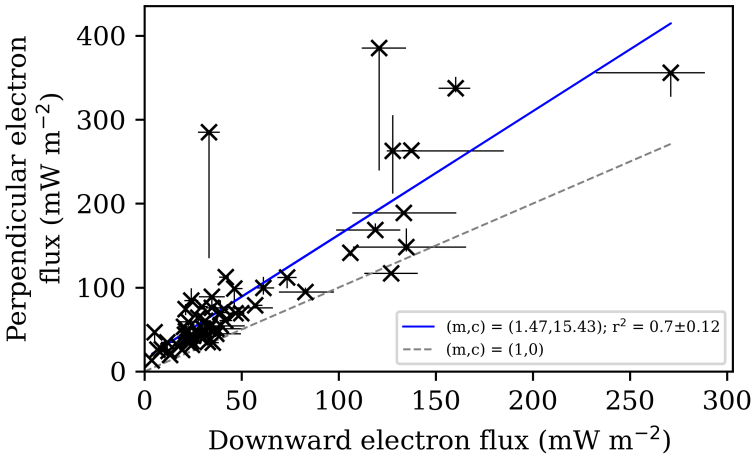

Figure 7.21: As Figure 7.20 but for the downward vs perpendicular electron energy flux.

As shown in Figures 7.20 and 7.21, there exist also moderately strong linear relations between the upward and downward, and downward and perpendicular, electron energy fluxes. Here, "upward" and "downward" refer to the electron population within 20° of the local magnetic-field vector, without the loss-cone correction as described in section 7.1. "Perpendicular" electrons have pitch angles between 45° and 135°. The lack of loss-cone-angle correction is to be able to compare the (fixed-angular-width) perpendicular electron flux with other parts of the pitch-angle profile, rather than to compare the auroral brightness with the precipitating electrons that give rise to it, as in Figure 7.19. In any case, the effect of this correction on Figures 7.20 and 7.21 is minimal. The reasonable

correlation between all three portions of the directional electron flux indicates that the electron acceleration is likely to be, for the most part, isotropic and not simply bidirectional and field-aligned. This is more compatible with magnetodisc scattering to provoke auroral electron precipitation (Li et al., 2017), rather than high-latitude field-aligned acceleration, discussed further in section 7.3.

The full average electron pitch-angle profiles (in $\log_{10}$ to highlight order-of-magnitude differences and normalised to prevent dominance of the greatest absolute electron flux in the average profile) for both blob-like and arc-like features (Figure 7.22) show butterfly distributions (Ma et al., 2017), which indicate the same loss-cone depletion as pancake distributions (Salveter et al., 2022) but also include a "notch" at 90°. This notch is tentatively associated with a slight parallelisation of a pancake distribution via Landau damping of electrostatic waves at low altitude (Ma et al., 2017). Alternatively, Sulaiman et al. (2022) suggest that this notch be likely unphysical and related to spacecraft shadowing effects (Sulaiman et al., 2022). From Figure 7.22, it would appear that there is no significant difference in the average electron pitch-angle profiles of blob-like and arc-like features in the outer emission. Additionally, the pancake-like butterfly distribution shown by both types of feature is indicative of partial refilling of the loss cones by isotropic scattering (Salveter et al., 2025), which implies that the two corresponding source processes are at least comparable, if not the same process.

Similarly, the Alfvénic Poynting flux (in the potentially dissipative frequency range of 0.2 to 5 Hz; Lorch et al. 2022) observed during Juno crossings of injection signatures shows a reasonable linear correlation with auroral brightness, as in

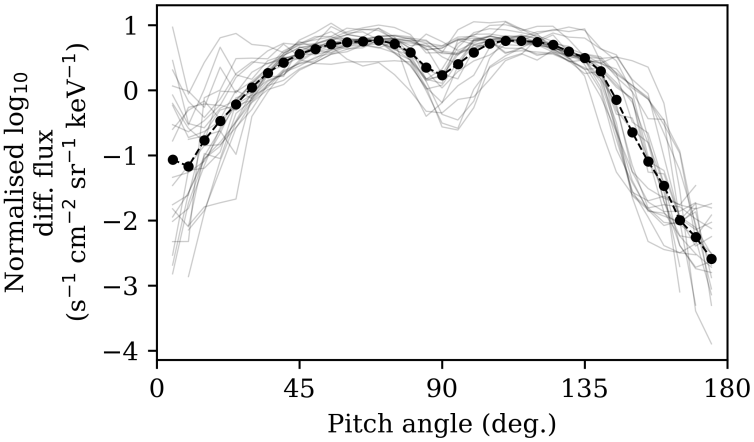
Normalised log10
diff. flux
(s−1 cm−2 sr−1 keV−1)
1
0
−1
−2
−3
−4
0
45
90
135
180
Pitch angle (deg.)

(a)

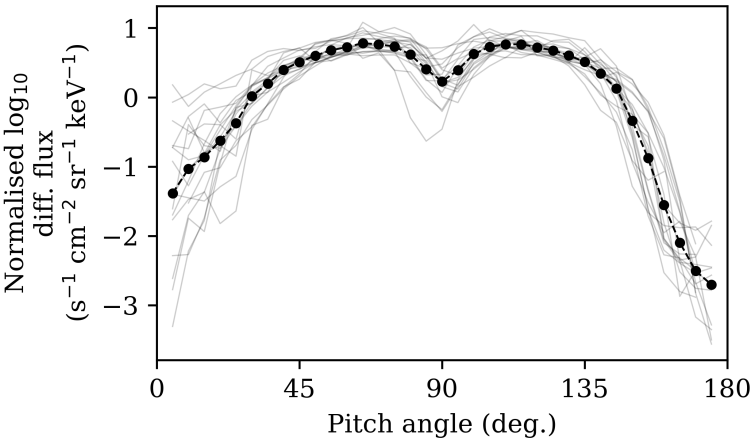
Normalised log10
diff. flux
(s−1 cm−2 sr−1 keV−1)
1
0
−1
−2
−3
0
45
90
135
180
Pitch angle (deg.)

(b)

Figure 7.22: The average electron pitch-angle distribution observed by JEDI during crossings of (a) blob-like and (b) arc-like features in the outer emission. Pitch-angle distributions from individual crossings are given in light grey. 0° (180°) denotes downward (upward) field-aligned electron flux.

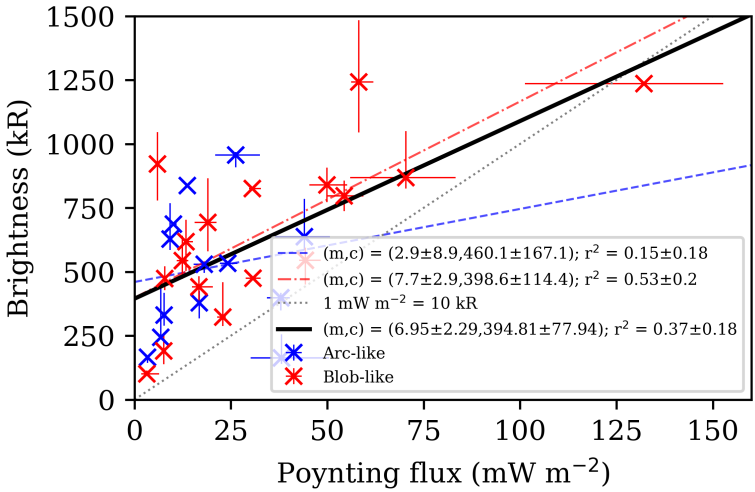

Figure 7.23: The 90th-percentile brightness vs 90th-percentile ionospheric Alfvénic flux extrapolated from Juno(-UVS, -FGM) observations below an altitude of 1 R_J during crossings of arc-like (blue) and blob-like (red) features in the outer emission. Error bars and best-fit relations are denoted as per Figure 7.19.

Figure 7.23. It should be noted that Figure 7.23 only includes cases where the Juno crossing occurred below an altitude of 1 R_J, since no peaks in the Alfvénic flux were observed above this altitude. Additionally, to ensure a sensible comparison between data points, cases where the Juno crossing occurred in a region of magnetic field strength above 0.1 mT (where Juno-FGM has a higher operational range than during the rest of a pass over the aurora; Connerney et al. 2017b) have been ignored. Here, unlike in Figure 7.19, there appears to be a separation between arc-like and blob-like features, with the high-flux, high-brightness populated predominantly by blob-like features. Given the lack of such a separation in Figure 7.19, it is anticipated that this is a result of the stricter filters for feature crossings in Figure 7.23 and low-number statistics rather than a physical effect. In any case, there remains a reasonable ($R^2 = 0.52$) correlation between Alfvénic Poynting flux below 1 R_J and feature brightness for "traditional" blob-like injection signatures. Since this Alfvénic flux is still observable at low altitudes, and therefore not consumed by wave-particle interactions as expected for the main emission (Sulaiman et al., 2022), we suggest that it does not contribute significantly to the electron precipitation associated with injection signatures and may instead be a by-product of the pitch-angle scattering process.

Similar to the Alfvénic flux, the magnitude of the upward electrical currents (that correspond to a majority of downward-travelling electrons) also show some measure ($R^2 = 0.32$) of correlation with observed auroral brightness for the discrete outer-emission features investigated in this work. This is as expected for plasma injections; a parcel of plasma moving within a magnetic field will naturally lead to the production of elec-

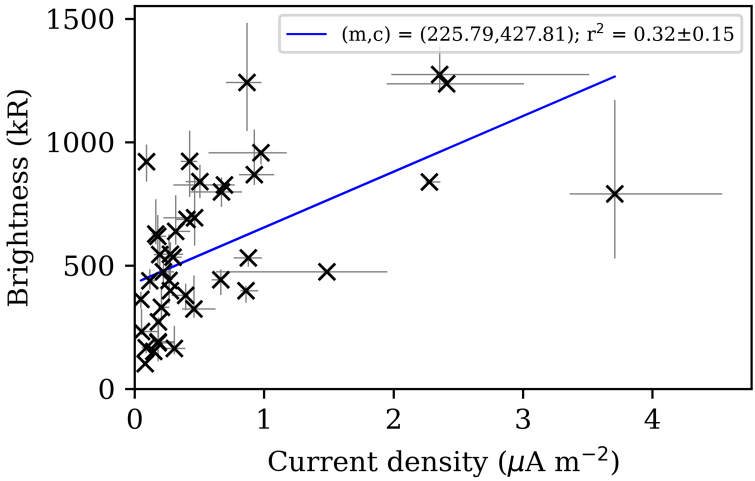

Figure 7.24: The 90th-percentile brightness vs 90th-percentile upward ionospheric current density extrapolated from Juno(-UVS, -FGM) observations during crossings of discrete features below an altitude of 1 R_J in the outer emission. Error bars denote the 80th-100th percentile range. The best-fit linear relation is given by a solid blue line.

trical currents (Radioti et al., 2010). We may also expect that whichever property (or properties) of the plasma injection governs the brightness of the corresponding injection signature may also govern the intensity of the produced electrical currents. However, similarly to the Alfvénic flux discussed above, correlation between upward current density and auroral brightness does not necessarily imply a current-based origin for injection signatures, as discussed further in section 7.3.

7.3 Discussion

This work presents evidence that there may exist two classes of auroral injection signature, and hence two classes of injection. The first, which we refer to as dawn-storm injections, is that of dawn storms which evolve through the large-blob phase and become smaller injection signatures. We would expect these injection signatures to be found in the post-noon, dusk, and night sectors (Bonfond et al., 2021) as the (sub-)corotating dawn storms move duskward as they evolve. We would also expect these dusk-side injection signatures to show signs of ageing via energy-dependent electron drift (Bonfond et al., 2017a). The second is injection signatures that arise even in the absence of dawn storms. The onset of a non-dawn-storm injection signature has been observed in only a single case prior to this work (Bonfond et al., 2017a), perhaps owing to their relatively short onset time compared to the typical lifetime of an injection signature. This work (Figures 7.7, 7.8, 7.9) provides further examples of this phenomenon, indicating that the case presented by Bonfond et al. (2017a) was not a one-off event. Indeed, the example given in Figure 7.7 is a small feature with no discernable shift between the brightness and colour-ratio peaks, indicative of a "young" injection. We suggest that these smaller non-dawn-storm injection signatures arise at all MLT and therefore account for the considerable population of injection signatures in the dawn-side aurora; the dusk-side aurora thus consists of a mixture of the two types of injection signature. This interpretation is consistent with the local-time distribution of injection signatures (Figure 7.6). Large-blob injection signatures are found exclusively at dusk because dawn storms evolve into injection sig-

natures in this sector (Bonfond et al., 2021), and small-blob injection signatures show a uniform distribution of non-dawn-storm injection signatures overlain by dusk-side dawn-storm injection signatures. This is compatible with the distribution of brightness/colour-ratio shifts (Figure 7.10), which shows a uniform no-shift baseline for the "young" non-dawn-storm injections and a dusk-side concentration of negative-shift cases for the aged dawn-storm injection signatures. The existence of non-dawn-storm injections at any local time may be consistent with a finger-like, interchange-dominated magnetodisc structure (Feng et al., 2023; Yao et al., 2025) and/or the presence of reconnection events identified at all local times in the magnetodisc (Guo and Yao, 2024; Zhao et al., 2024). Alternatively, the dawn-side population of no-shift injection signatures may be explained by the existence of significantly aged dawn-storm injections which have remained detectable and sub-corotated into the dawn-side aurora; in this scenario, the high-energy electron population may be completely depleted, which would bring the colour-ratio peak back in line with the brightness peak. However, the threefold increase in auroral power over a timescale of hours for the dawn-side examples given in Figures 7.7, 7.8, and 7.9 is not easily compatible with significantly aged injection signatures arising from later-stage injections, since we would not expect these to increase in brightness at such a late stage in their evolution. More work is required regarding the distribution, properties, and evolution of injections to be able to differentiate between these two scenarios.

The results of this work do not support high-latitude Alfvénic acceleration as the dominant mechanism for the production of injection signatures. Firstly, the butterfly pitch-angle distributions (Figure 7.22) and the correlation between the down-

ward, upward, and perpendicular flux in the low-altitude electron populations above injection signatures (Figures 7.20 and 7.21) are consistent with an isotropic acceleration process, such as pitch-angle scattering in the magnetodisc, rather than a largely field-aligned process, as high-latitude Alfvénic acceleration (and, indeed, acceleration via electrical currents; Ebert et al. 2021) is expected to be. This interpretation is strengthened by the lack of a positive correlation between hemispheric surface-field and auroral-power ratios for injection signatures, as would be expected for high-latitude Alfvénic acceleration. Indeed, Figure 7.13 shows some evidence for the inverse-log proportionality expected of isotropic scattering, though the dispersion in the data prevents us from drawing concrete conclusions from this analysis alone. Finally, the existence of injection signatures with upstream drift of their colour-ratio peak (Figure 7.10) is far more consistent with the isotropic scattering of an energy-differentiated (aged) plasma injection than with high-latitude Alfvénic acceleration (Dumont et al., 2018). Dumont (2023) suggests that more no-shift (young) injection signatures are detectable at higher surface field strength in the north, whereas this distribution is more uniform in the south, which was suggested to be the consequence of Alfvénic acceleration and its positive correlation between surface magnetic-field strength and auroral brightness. We suggest instead that no-shift injection signatures are biased at high surface field strength (the maximum surface field strength is higher in the north) because a stronger surface field reduces the size of features in the ionosphere and thus makes it more difficult to identify non-zero brightness/colour-ratio peak shifts with the finite spatial resolution of Juno-UVS. It has also been suggested that modification of the local magnetic-field topology by

a plasma injection may produce Alfvén waves (Gray et al., 2017), which may be the source of the Alfvénic-flux peaks seen by Juno during traversals of injection signatures. However, since the evidence presented in this work indicates that pitch-angle scattering is the dominant acceleration process, it is unlikely that this Alfvénic flux, which is expected to produce field-aligned acceleration, contributes significantly to electron acceleration above injection signatures. Indeed, the fact that Alfvénic flux in the potentially dissipative regime (Lorch et al., 2022) is observable at low altitude above injection signatures at all indicates that this flux does not significantly contribute to electron acceleration. For example, the main emission, which is more frequently attributed to Alfvénic acceleration in recent years (e.g. Sulaiman et al., 2022; Head et al., 2024; Kruegler et al., 2025), is not associated with significant Alfvénic flux at low altitude (Sulaiman et al., 2022); instead, dissipative Alfvénic flux is observable at $\sim$10 R_J (Lorch et al., 2022) which is then efficiently converted into electron acceleration at low altitude, resulting in bidirectional field-aligned electron distributions but no low-altitude Alfvénic flux. A similar scenario does not appear to be valid for injection signatures. The moderate correlation between Alfvénic flux and auroral brightness (Figure 7.23) is perhaps indicative that the source process that isotropically scatters electrons in the equatorial plane also produces Alfvénic perturbations, the strength of which scales with the strength of the scattering process. Overall, the results of this work support pitch-angle scattering as the dominant mechanism for electron precipitation by plasma injections, consistent with previous work (e.g. Li et al., 2017; Dumont et al., 2018; Devinat et al., 2025).

Similarly, the correlation between upward electrical current

density and auroral brightness shown in Figure 7.24 reminds us that correlation between two parameters does not imply causality. Electrical currents, despite this correlation, are unlikely to be significant contributors to the electron precipitation associated with injection signatures; as discussed above, the ubiquity of electron pitch-angle distributions associated with isotropic scattering, as well the absence of inverted-V structures (Salveter et al., 2022), above injection signatures is inconsistent with precipitation from currents induced by quasi-static electrical potentials. We propose instead that plasma injections that give rise to injection signatures also produce field-aligned electrical currents due to charge accumulation on their flanks, as has previously been suggested (Radioti et al., 2010), but that these currents do not result in significant auroral precipitation. This interpretation reminds us that an in-situ signature of some process (e.g. field-aligned currents) does not immediately imply causation, and in-situ signatures must be interpreted in the context of other observations before they can be considered causative rather than simply coincident. Indeed, in the case of main-emission Alfvénic flux discussed above, it is precisely the absence of an in-situ signature (at low altitude) that supports Alfvénic generation of the main emission (Lorch et al., 2022; Sulaiman et al., 2022) when combined with other in-situ measurements (e.g. particle distributions; Mauk et al., 2017b, 2018) and the observed behaviour of the main emission (Head et al., 2024).

This work also presents evidence that blob-like and arc-like discrete features in the outer emission are both governed by the same fundamental processes. Both feature types present comparable relations between downward electron flux/Alfvénic flux and auroral brightness (Figures 7.19 and 7.23) and show

near-identical average electron pitch-angle distributions (Figure 7.22). Additionally, small blob-like and arc-like features are both projected to a preferred radial distance of ∼11 R_J in the equatorial magnetosphere (Figure 7.6). This indicates that there is some measure of similarity between blob-like and arc-like features in the outer emission. One key difference is that arc-like features seem to be less common in the dawn-side aurora. We suggest that these results may be explained if arc-like features are interpreted as sequences of broadened or "smeared-out" blob-like features under the influence of energy-dependent electron drift, as is expected to occur (Dumont et al., 2018). Dawn storms are known to sometimes produce sequences of injection signatures in the post-noon sector (Bonfond et al., 2021). If these injections are sufficiently closely packed, energy-dependent electron drift may make it difficult to ascertain where one injection signature ends and the next begins. Importantly, only dawn-storm injection signatures would be expected to show sufficient dispersion during the aged small-blob phase to broaden into an arc, since we anticipate that non-dawn-storm small-blob injection signatures would decay below the detection threshold before sufficient broadening had occurred; in any case, it is not presently clear why these non-dawn-storm injection signatures should occur in a sequence. This interpretation explains why arc-like and small blob-like injection signatures preferentially occur at the same radial distance, but why arc-like signatures are less forthcoming in the dawn-side aurora, where dawn-storm injection signatures are absent. The extended "second auroral oval" in the dawn-side aurora reported by Gray et al. (2017) observed five days after a series of exceptionally bright injection signatures may be explained if the exceptional brightness of these sequential injec-

tion signatures allows them to remain detectable even once they have sub-corotated into the dawn aurora, at which point they would be expected to have undergone significant energy-dependent drift and hence have formed an extended arc. The requirement for injection signatures to be initially exceptionally bright if they are to remain detectable once they reach the dawn-side aurora may explain the reduced (though still present) population of dawn-side arc-like features in Figure 7.6c.

7.4 Conclusions

In response to the three questions tackled by this work, presented in the introduction, we present the following results:

1. There is some evidence to suggest that injection signatures (and consequently injections) may be classified into two types: dawn-storm and non-dawn-storm. Dawn-storm injections occur primarily in the dusk and night sector and present as large, bright injection signatures that decay into smaller injection signatures that show ageing via energy-dependent electron drift. Non-dawn-storm injections can occur at any local time and present as small, unaged injection signatures. Dawn-storm injections occur over a range of radial distances (10-20 R_J), whereas non-dawn-storm injections appear to occur predominantly below 15 R_J, with a peak at 11 R_J.

2. Injection signatures appear to be dominated by pitch-angle scattering of electrons in the magnetospheric equatorial plane rather than by field-aligned currents or Alfvénic

acceleration at high latitude. The low-altitude auroral electron energy flux increases isotropically with injection-signature brightness, and higher surface magnetic-field strength typically leads to a dimmer injection signature, consistent with pitch-angle scattering.

3. Arc-like discrete features in the outer emission may consist of sequences of dawn-storm injection signatures that have undergone broadening via energy-dependent electron drift. Juno crossings of both types of feature revealed no significant difference in their typical electron populations or Alfvénic flux. They map to the same radial distance as small blob-like features but are more preferentially located in the dusk-side aurora, consistent with injection signatures resulting from dawn storms.

Further work should aim to identify further examples of non-dawn-storm injection signatures and test whether they are truly uniformly distributed in local time, an analysis that is not possible at present due to the low number of conclusively identified non-dawn-storm injection signatures. Confirmed Juno crossings of non-dawn-storm injection signatures would also allow us to investigate whether the two classes of injection signature differ in their particle/wave/current properties, which would likely require a combination of in-situ measurement and remote observation. A more extensive comparison of blob-like and arc-like discrete features, perhaps looking at the average energy of the precipitating electrons or an extended sequence of observations, may provide further evidence that arc-like features in the outer emission consist of sequences of broadened injection signatures.

Chapter 8

Conclusions and perspectives

> *But Master Yoda said I should be mindful of the future.*
>
> Obi-Wan Kenobi, *Star Wars Episode I: The Phantom Menace*

This thesis contains the results of four complementary investigations, each targeted at a different part of the Jupiter-moon-magnetosphere system. Despite not being focused on one particular aspect of this system, there are nevertheless several overarching conclusions that can be drawn from this work. I would say that the main conclusion of this thesis is that

there is a growing body of evidence that mechanisms based on large-scale stationary field-aligned currents are insufficient to explain the behaviour and properties of the jovian UV main auroral emission,

a body of evidence to which, I hope, this thesis has contributed. Though only chapter 5 discussed the main emission directly, chapters 6 and 7 also provide evidence that the main emission is fundamentally Alfvénic and does not principally arise from field-aligned currents ensuing from the breakdown of plasma corotation:

- Chapter 5: This section dealt with the main emission most directly and, as such, presents the most evidence inconsistent with a fully current-based generation of the main emission. It was shown that the predominant asymmetry in the main emission is a dawn-dusk asymmetry, with the dusk-side aurora emitting, on average, four times as much power as the dawn-side aurora. Both models (Chané et al., 2017; Sarkango et al., 2019) and observations (Lorch et al., 2020) of field-aligned currents indicate that they are strongest in the night-side aurora and magnetosphere. This disagreement between the distribution of field-aligned currents and auroral emission indicates that the former does not straightforwardly contribute to the later. Conversely, observations of turbulence in the middle magnetosphere (responsible for the generation of the main emission in the competing Alfvénic framework; Saur et al. 2003) have indicated a higher degree of turbulence in the dusk-side magnetosphere (Tao et al., 2015), which would be more consistent with the average distribution of auroral power that I presented. Additionally, early models of field-aligned currents during periods of solar-wind compression of the magnetosphere indicated that the aurora should reduce in brightness during compression (Southwood and Kiv-

elson, 2001), which is entirely incompatible with the results presented in chapter 5 in which the main emission undergoes a consistent global brightening when the magnetosphere is compressed. Later models indicate that the total field-aligned current density should increase during solar-wind compression, but not in a global fashion; the night-side field-aligned currents undergo the greatest increase in intensity, whereas the day-side currents are frequently found to reduce in intensity during solar-wind compression (Chané et al., 2017; Sarkango et al., 2019), which is again inconsistent with the results presented in this thesis. Results of models of the main emission in the Alfvénic scenario are unfortunately rare, with the latest model indicating a stronger main emission in the dawn sector, an asymmetry that becomes even stronger during solar wind compression (Feng et al., 2022). This is also inconsistent with the results of this thesis, and also, curiously, with observations of turbulence in the middle magnetosphere, indicating that Alfvénic models require further development before they can truly explain the properties and behaviour of the main emission.

- Chapter 6: This section discussed the "bridge" aurora that is frequently present in the dusk-side polar region. Nevertheless, it was shown that there is some evidence that these bridges are, in fact, part of the main emission, or, more precisely, that they are the Zone-II aurora (Mauk et al., 2020) that have become noticeably separated from the Zone-I main emission. This behaviour is difficult to explain with a uniquely current-loop main emission. Indeed, in the current-loop model of Cowley

and Bunce (2001), no auroral emission would be expected in the downward-current (Zone-II) region, since electrons would be flowing away from Jupiter and back into the magnetosphere. This is analogous to the upward-electron "black aurora" on Earth (Marklund et al., 2001). However, the fundamentally bidirectional nature of Alfvénic acceleration is more compatible with a region of downward current (and hence a majority of upward-travelling electrons) that nevertheless shows appreciable auroral emission (from a minority of downward-travelling electrons). Additionally, given the lack of current signatures during bridge crossings (which were seen to occur in regions of downward current but with no accompanying "peak"), it is difficult to understand why currents would produce discrete bridges rather than a broad, diffuse aurora in the downward-current region. Nevertheless, it is not impossible a current-based generation of the main emission proceeds in a more complicated fashion than a simple current loop, which may make it possible to explain the Zone-II aurora and bridges under a current-based framework, though I am not aware of any existing current models that do so. As discussed in chapter 6, it is currently unclear how the Zone-II aurora would spatially separate from the Zone-I aurora to form bridges, even under an Alfvénic framework, though this is, in large part, due to the lack of published results from Alfvénic models of the main emission and especially from models that deal with compression of the magnetosphere by the solar wind.

- Chapter 7: This chapter investigated signatures of plasma

injection in the aurora. While these injection signatures are phenomenologically distinct from the main emission, we can nevertheless use them to draw conclusions about the main emission and the interpretation of in-situ data. One of the key conclusions of chapter 7 is that the evidence suggests overwhelmingly that pitch-angle scattering in the equatorial plane gives rise to injection signatures, and not field-aligned currents nor Alfvénic acceleration at low altitude. This conclusion was based on remote sensing of the aurora and the thence-extracted properties of injection signatures, and not uniquely from in-situ data collected during crossings of these features by Juno. Indeed, chapter 7 presents a reasonable correlation between the brightness of crossed injection signatures and both the calculated Alfvénic Poynting flux and upward field-aligned current density. Naively, one may take these correlations as evidence for an Alfvénic or current-based generation of these injection signatures. However, the properties of injection signatures (inverse relation between brightness and surface magnetic-field strength, evidence for isotropic electron acceleration in the particle distributions, presence of longitudinal shifts between the peak in brightness and colour ratio) are best described by pitch-angle scattering in the equatorial plane, and are comparatively difficult to describe using Alfvénic or current-based models. The correlations between brightness and Alfvénic flux or current density should therefore best be understood as secondary products of the process that produces injection signatures that themselves do not appear to contribute to auroral emission in a meaningful way. Concerning the Alfvénic flux in particular: if Juno is

able to detect considerable Alfvénic flux even at very low altitude, we may conclude either that the Alfvénic acceleration region is located at even lower altitude (which is unlikely since the other properties of injection signatures appear to be incompatible with low-altitude Alfvénic acceleration) or that the observed Alfvénic flux is not being "consumed" by wave-particle interactions and hence not meaningfully contributing toward acceleration of auroral electrons. We may also apply this logic to the main emission, which, importantly, does not show meaningful Alfvénic flux at low altitude (Sulaiman et al., 2022; Head et al., 2025) but does at higher altitude (Lorch et al., 2022). If there is sufficient supporting evidence to suggest that the main emission be largely Alfvénic in origin (e.g. Tao et al., 2015; Mauk et al., 2017c, 2018; Saur et al., 2018; Clark et al., 2018; Kotsiaros et al., 2019; Gershman et al., 2019; Bonfond et al., 2020; Pan et al., 2021; Lorch et al., 2022; Salveter et al., 2022; Sulaiman et al., 2022; Head et al., 2024, 2025; Kruegler et al., 2025), then we may interpret this lack of Alfvénic Poynting flux at low altitude as evidence that it has been efficiently transformed into acceleration of auroral electrons though resonant and/or non-resonant particle interactions.

In all, the work presented in this thesis supports an Alfvénic origin for the main emission over a current-based origin. However, despite the evidence presented here and elsewhere (e.g. Bonfond et al., 2020), a full understanding of how Alfvénic processes could explain every aspect and observation of the main emission remains elusive and considerable work, both from an experimental and simulatory standpoint, is yet required before

the Alfvénic model can be said to have triumphed over the traditional current-based model. In any case, even if evidence suggests that Alfvénic acceleration is the dominant generation mechanism for the main emission, it may, by no means, be the sole contributing process, and auroral acceleration by quasi-static potentials may itself also participate to a lesser extent (e.g. Mauk et al., 2018).

The work presented in chapters 6 and 7 includes the interpretation of Juno in-situ data alongside image data from Juno-UVS. Naturally, many other publications exist that use Juno data from UVS or the other in-situ instruments, and indeed many that use both (e.g. Gérard et al., 2019; Haewsantati et al., 2023). However, this work has demonstrated the usefulness, and indeed the necessity, of considering UVS images when analysing Juno in-situ data. This gives important context to in-situ measurements, such as knowing exactly which auroral morphology is found at the Juno magnetic footprint at a given time, which is frequently more useful to the interpretation of in-situ data than simply assuming that Juno is flying over a particular part of the aurora based on e.g. M-shell. For example, the work presented in chapter 7 highlighted the importance of disentangling the properties of the diffuse aurora (essentially ubiquitous in local time in the outer emission) from those of injection signatures, which are limited in spatial extent but sufficiently common that Juno very rarely crosses a "pristine" diffuse aurora. It is therefore essential to only select cases without injection signatures if the properties of the diffuse aurora are to be investigated. Likewise, chapter 5 demonstrates that the size of the main emission can vary both globally with the state of compression of the magnetosphere and locally with local time. Simply using a magnetic-field model like JRM33,

which does not take either of these effects into account, introduces a variation of the order of 20-to-40 R_J into the apparent mapped location of the main emission in the magnetosphere. Therefore, simply assuming that the main emission is located along an M-shell of e.g. 40 according to JRM33 may introduce significant error that could influence the interpretation of in-situ data. Besides it being important to consider UVS data when interpreting Juno in-situ measurements, I hope that this work has demonstrated the value of a large-scale, simultaneous, automated analysis of in-situ data from multiple Juno instruments, without which it would have been impossible to draw the conclusions presented in chapters 6 and 7.

One final conclusion of this work is that more advanced and more automated analysis techniques are a powerful tool in the investigation of the Jupiter-moon-magnetosphere system. This work, it is hoped, has provided several examples of how these more-advanced image-analysis techniques can be applied to the ever-growing amount of data associated with Jupiter, its moons, its aurora, or its magnetosphere, though the applications presented in chapters 4 to 7 is by no means exhaustive. The large-scale analysis of tens to thousands of images of Io or the aurora that form the basis of this thesis, and the scientific conclusions that these analyses have allowed, would not have been possible without these largely automated image-analysis techniques. Chapter 4 presented the automatic detection of neutral-sodium jets around Io, even in cases where these latter features were not clear to the human eye. This automatic detection allowed for the more-objective sampling of jet properties and helped to show that is no systematic or statistical link between the brightness or appearance of a jet and the brightness of the wider neutral-sodium environment.

Chapter 5 presents the automatic detection of the main emission in Juno-UVS images of the aurora taken during the first 54 perijoves. This task would have been tedious and mired by human bias if performed manually. This automatic detection produced new average reference contours for the main emission which show key differences from previous reference contours based on HST observations (including, importantly, a much-reduced local-time bias) which have already been used in other work (Kruegler et al., 2025). This automatic analysis also allowed for the unbiased determination of the size of the main emission and its subsequent comparison with other properties (brightness, magnetospheric compression, ...). Since automatic methods allow for easy application to a large number of auroral images, this work was limited to analysis of the (relatively small) dataset of 108 images from the first 54 perijoves (one per hemisphere) but could also be applied to the much-larger HST dataset (comprising thousands of images). This latter analysis permitted the identification of a strong link between compression of the magnetosphere (as determined from Juno crossings of the main emission) and a globally contracted (and brighter) main emission (from HST images), which would have been prohibitively time-consuming if performed manually. Chapter 6 presents the automatic detection of bridges in thousands of HST images, which, again, would be essentially impossible without automatic methods. This again allowed for the association of the appearance of bridges in the aurora with compression of the magnetosphere in much the same way as in chapter 5, as well as to present a statistical view of their distribution in the magnetosphere. Chapter 7 used random-forest classification to extract the locations of injection signatures in Juno-UVS data from the first 40 perijoves,

which again allowed for a statistical analysis of their locations and the distribution of brightness and colour ratio within each feature. In all, it is hoped that this thesis may serve as inspiration for future applications of automated techniques to the analysis of the Jupiter-moon-magnetosphere system as well as those of other planets, such as Saturn. As our datasets continue to increase in size, especially with the impending simultaneous presence of two spacecraft (JUICE and Europa Clipper) at Jupiter, it is expected that automatic analysis techniques will continue to grow in importance to the field.

Beyond a general push towards a wider application of advanced image-analysis techniques to the study of Jupiter, this thesis also makes recommendations and suggestions for future avenues of study of Jupiter and its magnetosphere:

- More advanced models of the Alfvénic generation of the main emission: One of the largest outstanding problems when discussing the Alfvénic generation of the main emission is the relative dearth of published results from simulations, and, even more so, published results that adequately corroborate the ever-growing observational evidence for an Alfvénic main emission. In particular, the brighter dusk-side main emission is, as yet, not well described by simulations, nor is the behaviour of the main emission during solar-wind compression. It is suggested that the dipolar and axisymmetric nature of many simulations is insufficient to adequately model the main emission, and that the effect of the solar wind (and, indeed, internal sources of variation such as the mass outflow rate from Io) must be taken into account, even when modelling the middle magnetosphere, since this

thesis demonstrates that the size of the magnetopause can have considerable effects on auroral processes even in this region. A simulation of magnetospheric turbulence and the thence-ensuing auroral Alfvénic acceleration that demonstrates the dawn-dusk asymmetry and global contraction (and brightening) during magnetospheric compression from chapter 5, and perhaps even the Zone-I-II separation from chapter 6, would be an excellent result that would support both the results of this thesis and the Alfvénic framework for the main emission.

- Further study of the auroral bridges: Chapter 6 suggested that bridges be generated via previously known mechanisms involving upward electron beams and large-amplitude electrostatic waves, but this does not fully explain their appearance or observed properties. If bridges are indeed a spatially separated Zone-II main emission, why do they preferentially appear during magnetospheric compression? Why do they take the form of discrete "feathered" arcs (i.e. that appear to "bridge" the gap between the main emission and active region) rather than a simple double arc parallel to the Zone-I main emission? Why do they only appear at dusk? Is it possible to observe the full evolution of a bridge starting with a splitting of the main emission (if indeed this is how they evolve, as suggested by the single case discussed in chapter 6)? How do they end? Do they fade away or split from the main emission entirely and move into the active region? Is their discrete nature truly a consequence of a magnetospheric effect or could it be that low-altitude processes (such as pressure waves in the ionosphere) give

them their arc-like appearance? How do bridges relate to flashes in the polar collar, which are known to be coincident with bridges but remain in phase over enormous mapped distances in the magnetosphere? It is hoped that this illustrates that bridges are an enigmatic and understudied part of Jupiter's UV aurora and hence fertile ground for future study.

- Investigation of the two classes of injection signature: Chapter 7 presented evidence that there exist two classes of injection signature, dawn-storm and non-dawn-storm. Dawn-storm injections are typically brighter, found in the post-noon aurora, and show signs of ageing due to energy-dependent longitudinal electron drift. Non-dawn-storm injections are typically dimmer but not limited to any one local-time sector of the aurora. Non-dawn-storm injection signatures were (tentatively) associated with constant radial plasma interchange in a finger-like magnetodisc, though, ideally, this conclusion might be supported by future models. More detailed analysis of the in-situ properties of injection-signature crossings may also yield characteristic differences between the two classes of injection signature that may support the two-class system on phenomenological grounds. It is expected that more data will be required to perform this analysis, since only three convincing non-dawn-storm injection signatures (insofar as their onset was observed by Juno-UVS and not preceded by a dawn storm) were seen during the first 40 perijoves, though this is likely because there were only three non-dawn-storm injection signatures that were observed to appear during a perijove (and can therefore

unequivocally be said to be unrelated to dawn storms) and that many other observed injection signatures already present at the start of a perijove were also unrelated to dawn storms.

- Linking neutral-sodium jets to processes on Io or in its atmosphere: One of the largest mysteries that remains after the work presented in chapter 4 is how the (variable) neutral-sodium jet, which is expected to originate (directly or indirectly) from volcanic processes on Io, is produced. Io's atmosphere is remarkably stable, and so it is expected that the process(es) that give(s) rise to jets must somehow bypass the atmosphere. One possibility is that volcanic plumes "float" sodium-bearing molecules to sufficient altitude that they may interact directly with the plasma torus to become ionised and produce the jet without having any great effect on the atmosphere. However, this remains a hypothesis that requires direct observation to verify. High-resolution observation of Io during a period where a (bright) sodium jet is also present would potentially show a volcanic plume giving rise to the jet. It is expected that this plume be located toward higher latitudes where the thinner atmosphere facilitates direct interaction between the plume and the plasma torus. The lack of a particularly striking plume may indicate that the jet originates from a global enhancement of the atmosphere-torus interaction rather than from a specific plume.

This is, of course, a non-exhaustive list of potential avenues of study, and, if nothing else, it is my sincere hope that this thesis has demonstrated that even the most obvious and strik-

ing parts of Jupiter and its interaction with its moons and magnetosphere, after more than 70 years of study, remain exceptionally rich and intriguing subjects of scientific investigation. Though I hope that this thesis has contributed toward unravelling these mysteries, I expect that future generations of planetary scientists will have no shortage of interesting puzzles to solve and discussions to be had before we can truly say that we understand Jupiter and its aurora.

Bibliography

M. H. Acuña and N. F. Ness. The main magnetic field of Jupiter. *Journal of Geophysical Research (1896-1977)*, 81(16):2917–2922, 1976. ISSN 2156-2202. doi:10.1029/JA081i016p02917.

M. H. Acuña, F. M. Neubauer, and N. F. Ness. Standing Alfvén wave current system at Io: Voyager 1 observations. *Journal of Geophysical Research: Space Physics*, 86(A10): 8513–8521, 1981. ISSN 2156-2202. doi:10.1029/JA086iA10p08513.

S. Al Saati, N. Clément, C. Louis, M. Blanc, Y. Wang, N. André, L. Lamy, B. Bonfond, B. Collet, F. Allegrini, S. Bolton, G. Clark, J. E. P. Connerney, J.-C. Gérard, G. R. Gladstone, S. Kotsiaros, W. S. Kurth, and B. Mauk. Magnetosphere-Ionosphere-Thermosphere Coupling Study at Jupiter Based on Juno's First 30 Orbits and Modeling Tools. *Journal of Geophysical Research: Space Physics*, 127(10):e2022JA030586, 2022. ISSN 2169-9402. doi:10.1029/2022JA030586.

F. Allegrini, F. Bagenal, S. Bolton, J. Connerney, G. Clark, R. W. Ebert, T. K. Kim, W. S. Kurth, S. Levin, P. Louarn, B. Mauk, D. J. McComas, C. Pollock, D. Ranquist, M. Reno, J. R. Szalay, M. F. Thomsen, P. Valek, S. Weidner, R. J. Wilson, and J. L. Zink. Electron beams and loss cones in the auroral regions of Jupiter. *Geophysical Research Letters*, 44(14):7131–7139, 2017. ISSN 1944-8007. doi:10.1002/2017GL073180.

F. Allegrini, B. Mauk, G. Clark, G. R. Gladstone, V. Hue, W. S. Kurth, F. Bagenal, S. Bolton, B. Bonfond, J. E. P. Connerney, R. W. Ebert, T. Greathouse, M. Imai, S. Levin, P. Louarn, D. J. McComas, J. Saur, J. R. Szalay, P. W. Valek, and R. J. Wilson. Energy Flux and Characteristic Energy of Electrons Over Jupiter's Main Auroral Emission. *Journal of Geophysical Research: Space Physics*, 125(4):e2019JA027693, 2020. ISSN 2169-9402. doi:10.1029/2019JA027693.

B. A. Archinal, C. H. Acton, M. F. A'Hearn, A. Conrad, G. J. Consolmagno, T. Duxbury, D. Hestroffer, J. L. Hilton, R. L. Kirk, S. A. Klioner, D. McCarthy, K. Meech, J. Oberst, J. Ping, P. K. Seidelmann, D. J. Tholen, P. C. Thomas, and I. P. Williams. Report of the IAU Working Group on Cartographic Coordinates and Rotational Elements: 2015. *Celestial Mechanics and Dynamical Astronomy*, 130(3):22, Feb. 2018. ISSN 1572-9478. doi:10.1007/s10569-017-9805-5.

F. Bagenal. The magnetosphere of Jupiter: Coupling the equator to the poles. *Journal of Atmospheric and Solar-Terrestrial Physics*, 69(3):387–402, Mar. 2007. ISSN 1364-6826. doi:10.1016/j.jastp.2006.08.012.

F. Bagenal and P. A. Delamere. Flow of mass and energy in the magnetospheres of Jupiter and Saturn. *Journal of Geophysical Research: Space Physics*, 116(A5), 2011. ISSN 2156-2202. doi:10.1029/2010JA016294.

F. Bagenal and V. Dols. The Space Environment of Io and Europa. *Journal of Geophysical Research: Space Physics*, 125(5):e2019JA027485, 2020. ISSN 2169-9402. doi:10.1029/2019JA027485.

F. Bagenal and J. D. Sullivan. Direct plasma measurements in the Io torus and inner magnetosphere of Jupiter. *Journal of Geophysical Research: Space Physics*, 86(A10): 8447–8466, 1981. ISSN 2156-2202. doi:10.1029/JA086iA10p08447.

F. Bagenal, R. J. Wilson, S. Siler, W. R. Paterson, and W. S. Kurth. Survey of Galileo plasma observations in Jupiter's plasma sheet. *Journal of Geophysical Research: Planets*, 121 (5):871–894, 2016. ISSN 2169-9100. doi:10.1002/2016JE005009.

G. E. Ballester, J. T. Clarke, J. T. Trauger, W. M. Harris, K. R. Stapelfeldt, D. Crisp, R. W. Evans, E. B. Burgh, C. J. Burrows, S. Casertano, J. S. Gallagher, R. E. Griffiths, J. J. Hester, J. G. Hoessel, J. A. Holtzman, J. E. Krist, V. Meadows, J. R. Mould, R. Sahai, P. A. Scowen, A. M. Watson, and J. A. Westphal. Time-Resolved Observations of Jupiter's Far-Ultraviolet Aurora. *Science*, 274(5286):409–413, Oct. 1996. doi:10.1126/science.274.5286.409. Publisher: American Association for the Advancement of Science.

R. Bauske, M. R. Combi, and J. T. Clarke. Analysis of Midlatitude Auroral Emissions Observed during the Impact of Comet Shoemaker–Levy 9 with Jupiter. *Icarus*, 142(1): 106–115, Nov. 1999. ISSN 0019-1035. doi:10.1006/icar.1999.6198.

J. W. Belcher. The Jupiter-Io Connection: An Alfvén Engine in Space. *Science*, 238(4824): 170–176, Oct. 1987. doi:10.1126/science.238.4824.170.

J. W. Belcher, C. K. Goertz, and H. S. Bridge. The low energy plasma in the Jovian magnetosphere. *Geophysical Research Letters*, 7(1):17–20, Jan. 1980. ISSN 0094-8276, 1944-8007. doi:10.1029/GL007i001p00017.

B. Benmahi, B. Bonfond, B. Benne, D. Grodent, V. Hue, G. R. Gladstone, G. Gronoff, J. Lilensten, G. Sicorello, L. A. Head, M. Barthélemy, C. S. Wedlund, R. S. Giles, and T. K. Greathouse. Energy mapping of Jupiter's auroral electrons from Juno/UVS data using a new H2 UV emission model. *Astronomy & Astrophysics*, Feb. 2024a. ISSN 0004-6361, 1432-0746. doi:10.1051/0004-6361/202348634.

B. Benmahi, B. Bonfond, B. Benne, V. Hue, D. Grodent, M. Barthélemy, J. A. Sinclair, A. Moirano, L. A. Head, R. Gladstone, G. Gronoff, G. Sicorello, C. S. Wedlund, R. Giles, and T. K. Greathouse. Auroral 3D structure retrieval from the Juno/UVS data. *Astronomy & Astrophysics*, 691:A91, Nov. 2024b. ISSN 0004-6361, 1432-0746. doi:10.1051/0004-6361/202451439. Publisher: EDP Sciences.

J. A. Bennett. The longitude and the new science. *Vistas in Astronomy*, 28:219–225, Jan. 1985. ISSN 0083-6656. doi:10.1016/0083-6656(85)90029-7.

J. T. Bergstralh, D. L. Matson, and T. V. Johnson. Sodium D-line emission from Io: Synoptic observations from Table Mountain Observatory. *Astrophyical Journal*, 195:L131 – L135, 1975.

J.-L. Bertaux, F. Leblanc, O. Witasse, E. Quemerais, J. Lilensten, S. A. Stern, B. Sandel, and O. Korablev. Discovery of an aurora on Mars. *Nature*, 435(7043):790–794, June 2005. ISSN 1476-4687. doi:10.1038/nature03603.

B. Bhattacharya, R. M. Thorne, and D. J. Williams. On the energy source for diffuse Jovian auroral emissivity. *Geophysical Research Letters*, 28(14):2751–2754, July 2001. ISSN 1944-8007. doi:10.1029/2000GL012616.

D. Bhattacharyya, J. T. Clarke, J. Montgomery, B. Bonfond, J.-C. Gérard, and D. Grodent. Evidence for Auroral Emissions From Callisto's Footprint in HST UV Images. *Journal of Geophysical Research: Space Physics*, 123(1):364–373, 2018. ISSN 2169-9402. doi:10.1002/2017JA024791.

E. K. Bigg. Influence of the Satellite Io on Jupiter's Decametric Emission. *Nature*, 203(4949): 1008–1010, Sept. 1964. ISSN 1476-4687. doi:10.1038/2031008a0. Publisher: Nature Publishing Group.

A. B. Binder and D. P. Cruikshank. Evidence for an Atmosphere on Io. *Icarus*, 3:299–305, Nov. 1964. ISSN 0019-1035. doi:10.1016/0019-1035(64)90038-7. ADS Bibcode: 1964Icar....3..299B.

E. Blum. The computation of eigenvalues and eigenvector of a completely continuous self-adjoint operator. *Journal of Computer and System Sciences*, 1(4):362–370, 1967. ISSN 1090-2724. doi:10.1016/S0022-0000(67)80026-6.

A. Blöcker, J. Saur, L. Roth, and D. F. Strobel. MHD Modeling of the Plasma Interaction With Io's Asymmetric Atmosphere. *Journal of Geophysical Research: Space Physics*, 123(11):9286–9311, 2018. ISSN 2169-9402. doi:10.1029/2018JA025747.

S. J. Bolton, F. Bagenal, M. Blanc, T. Cassidy, E. Chané, C. Jackman, X. Jia, A. Kotova, N. Krupp, A. Milillo, C. Plainaki, H. T. Smith, and H. Waite. Jupiter's Magnetosphere: Plasma Sources and Transport. *Space Science Reviews*, 192(1):209–236, Oct. 2015. ISSN 1572-9672. doi:10.1007/s11214-015-0184-5.

B. Bonfond and A. Sulaiman. Alfvén Waves Related to Moon–Magnetosphere Interactions. In *Alfvén Waves Across Heliophysics*, pages 139–161. American Geophysical Union (AGU), 2024. ISBN 978-1-394-19598-5. doi:10.1002/9781394195985.ch7.

B. Bonfond, D. Grodent, J.-C. Gérard, A. Radioti, J. Saur, and S. Jacobsen. UV Io footprint leading spot: A key feature for understanding the UV Io footprint multiplicity? *Geophysical Research Letters*, 35(5), 2008. ISSN 1944-8007. doi:10.1029/2007GL032418.

B. Bonfond, D. Grodent, J.-C. Gérard, A. Radioti, V. Dols, P. A. Delamere, and J. T. Clarke. The Io UV footprint: Location, inter-spot distances and tail vertical extent. *Journal of Geophysical Research*, 114:A07224, 2009. doi:10.1029/2009JA014312.

B. Bonfond, M. F. Vogt, J.-C. Gérard, D. Grodent, A. Radioti, and V. Coumans. Quasi-periodic polar flares at Jupiter: A signature of pulsed dayside reconnections? *Geophysical Research Letters*, 38(2), 2011. ISSN 1944-8007. doi:10.1029/2010GL045981.

B. Bonfond, D. Grodent, J.-C. Gérard, T. Stallard, J. T. Clarke, M. Yoneda, A. Radioti, and J. Gustin. Auroral evidence of Io's control over the magnetosphere of Jupiter. *Geophysical Research Letters*, 39(1), 2012. ISSN 1944-8007. doi:10.1029/2011GL050253.

B. Bonfond, S. Hess, F. Bagenal, J.-C. Gérard, D. Grodent, A. Radioti, J. Gustin, and J. T. Clarke. The multiple spots of the Ganymede auroral footprint. *Geophysical Research Letters*, 40(19):4977–4981, 2013a. ISSN 1944-8007. doi:10.1002/grl.50989.

B. Bonfond, S. Hess, J. C. Gérard, D. Grodent, A. Radioti, V. Chantry, J. Saur, S. Jacobsen, and J. T. Clarke. Evolution of the Io footprint brightness I: Far-UV observations. *Planetary and Space Science*, 88:64–75, Nov. 2013b. ISSN 0032-0633. doi:10.1016/j.pss.2013.05.023.

B. Bonfond, J. Gustin, J.-C. Gérard, D. Grodent, A. Radioti, B. Palmaerts, S. V. Badman, K. K. Khurana, and C. Tao. The far-ultraviolet main auroral emission at Jupiter – Part 1: Dawn–dusk brightness asymmetries. *Annales Geophysicae*, 33(10):1203–1209, Oct. 2015a. ISSN 0992-7689. doi:10.5194/angeo-33-1203-2015.

B. Bonfond, J. Gustin, J.-C. Gérard, D. Grodent, A. Radioti, B. Palmaerts, S. V. Badman, K. K. Khurana, and C. Tao. The far-ultraviolet main auroral emission at Jupiter – Part 2: Vertical emission profile. *Annales Geophysicae*, 33(10):1211–1219, Oct. 2015b. ISSN 0992-7689. doi:10.5194/angeo-33-1211-2015.

B. Bonfond, D. Grodent, S. V. Badman, J.-C. Gérard, and A. Radioti. Dynamics of the flares in the active polar region of Jupiter. *Geophysical Research Letters*, 43(23):11,963–11,970, 2016. ISSN 1944-8007. doi:10.1002/2016GL071757.

B. Bonfond, G. R. Gladstone, D. Grodent, T. K. Greathouse, M. H. Versteeg, V. Hue, M. W. Davis, M. F. Vogt, J.-C. Gérard, A. Radioti, S. Bolton, S. M. Levin, J. E. P. Connerney, B. H. Mauk, P. Valek, A. Adriani, and W. S. Kurth. Morphology of the UV aurorae Jupiter during Juno's first perijove observations. *Geophysical Research Letters*, 44(10): 4463–4471, 2017a. ISSN 1944-8007. doi:10.1002/2017GL073114.

B. Bonfond, D. Grodent, S. V. Badman, J. Saur, J. C. Gérard, and A. Radioti. Similarity of the Jovian satellite footprints: Spots multiplicity and dynamics. *Icarus*, 292:208–217, Aug. 2017b. ISSN 0019-1035. doi:10.1016/j.icarus.2017.01.009.

B. Bonfond, J. Saur, D. Grodent, S. V. Badman, D. Bisikalo, V. Shematovich, J.-C. Gérard, and A. Radioti. The tails of the satellite auroral footprints at Jupiter. *Journal of Geophysical Research: Space Physics*, 122(8):7985–7996, 2017c. ISSN 2169-9402. doi:10.1002/2017JA024370.

B. Bonfond, Z. Yao, and D. Grodent. Six pieces of evidence against the corotation enforcement theory to explain the main aurora at Jupiter. *Journal of Geophysical Research: Space Physics*, 125:e2020JA028152, 2020. doi:10.1029/2020JA028152.

B. Bonfond, Z. H. Yao, G. R. Gladstone, D. Grodent, J.-C. Gérard, J. Matar, B. Palmaerts, T. K. Greathouse, V. Hue, M. H. Versteeg, J. A. Kammer, R. S. Giles, C. Tao, M. F. Vogt, A. Mura, A. Adriani, B. H. Mauk, W. S. Kurth, and S. J. Bolton. Are Dawn Storms Jupiter's Auroral Substorms? *AGU Advances*, 2(1):e2020AV000275, 2021. ISSN 2576-604X. doi:10.1029/2020AV000275.

F. Braga-Ribas, B. Sicardy, J. L. Ortiz, C. Snodgrass, F. Roques, R. Vieira-Martins, J. I. B. Camargo, M. Assafin, R. Duffard, E. Jehin, J. Pollock, R. Leiva, M. Emilio, D. I. Machado, C. Colazo, E. Lellouch, J. Skottfelt, M. Gillon, N. Ligier, L. Maquet, G. Benedetti-Rossi, A. R. Gomes, P. Kervella, H. Monteiro, R. Sfair, M. E. Moutamid, G. Tancredi, J. Spagnotto, A. Maury, N. Morales, R. Gil-Hutton, S. Roland, A. Ceretta, S.-h. Gu, X.-b. Wang, K. Harpsøe, M. Rabus, J. Manfroid, C. Opitom, L. Vanzi, L. Mehret, L. Lorenzini, E. M. Schneiter, R. Melia, J. Lecacheux, F. Colas, F. Vachier, T. Widemann, L. Almenares, R. G. Sandness, F. Char, V. Perez, P. Lemos, N. Martinez, U. G. Jørgensen, M. Dominik, F. Roig, D. E. Reichart, A. P. LaCluyze, J. B. Haislip, K. M. Ivarsen, J. P. Moore, N. R. Frank, and D. G. Lambas. A ring system detected around the Centaur (10199) Chariklo. *Nature*, 508(7494):72–75, Apr. 2014. ISSN 1476-4687. doi:10.1038/nature13155.

H. S. Bridge, J. W. Belcher, A. J. Lazarus, J. D. Sullivan, R. L. McNutt, F. Bagenal, J. D. Scudder, E. C. Sittler, G. L. Siscoe, V. M. Vasyliunas, C. K. Goertz, and C. M. Yeates. Plasma Observations Near Jupiter: Initial Results from Voyager 1. *Science*, 204(4396): 987–991, June 1979. doi:10.1126/science.204.4396.987.

A. L. Broadfoot, M. J. Belton, P. Z. Takacs, B. R. Sandel, D. E. Shemansky, J. B. Holberg, J. M. Ajello, S. K. Atreya, T. M. Donahue, H. W. Moos, J. L. Bertaux, J. E. Blamont, D. F. Strobel, J. C. McConnell, A. Dalgarno, R. Goody, and M. B. McElroy. Extreme ultraviolet observations from voyager 1 encounter with jupiter. *Science (New York, N.Y.)*, 204(4396):979–982, June 1979. ISSN 0036-8075. doi:10.1126/science.204.4396.979.

A. L. Broadfoot, F. Herbert, J. B. Holberg, D. M. Hunten, S. Kumar, B. R. Sandel, D. E. Shemansky, G. R. Smith, R. V. Yelle, D. F. Strobel, H. W. Moos, T. M. Donahue, S. K. Atreya, J. L. Bertaux, J. E. Blamont, J. C. McConnell, A. J. Dessler, S. Linick, and R. Springer. Ultraviolet Spectrometer Observations of Uranus. *Science*, 233(4759):74–79, July 1986. doi:10.1126/science.233.4759.74.

A. L. Broadfoot, S. K. Atreya, J. L. Bertaux, J. E. Blamont, A. J. Dessler, T. M. Donahue, W. T. Forrester, D. T. Hall, F. Herbert, J. B. Holberg, D. M. Hunter, V. A. Krasnopolsky, S. Linick, J. I. Lunine, J. C. McConnell, H. W. Moos, B. R. Sandel, N. M. Schneider, D. E. Shemansky, G. R. Smith, D. F. Strobel, and R. V. Yelle. Ultraviolet Spectrometer Observations of Neptune and Triton. *Science*, 246(4936):1459–1466, Dec. 1989. doi:10.1126/science.246.4936.1459.

M. E. Brown and A. H. Bouchez. The Response of Jupiter's Magnetosphere to an Outburst on Io. *Science*, 278(5336):268–271, Oct. 1997. doi:10.1126/science.278.5336.268.

R. A. Brown and F. H. Chaffee, Jr. High-Resolution Spectra of Sodium Emission from Io. *The Astrophysical Journal*, 187:L125, Feb. 1974. ISSN 0004-637X, 1538-4357. doi:10.1086/181413.

J. K. Burchill. What causes the magnetic curvature drift?, Apr. 2026. arXiv:2604.15354 [physics].

M. H. Burger and R. E. Johnson. Europa's neutral cloud: morphology and comparisons to Io. *Icarus*, 171(2):557–560, Oct. 2004. ISSN 0019-1035. doi:10.1016/j.icarus.2004.06.014.

B. F. Burke and K. L. Franklin. Observations of a variable radio source associated with the planet Jupiter. *Journal of Geophysical Research (1896-1977)*, 60(2):213–217, 1955. ISSN 2156-2202. doi:10.1029/JZ060i002p00213.

J. W. Chamberlain and D. M. Hunten. *Theory of planetary atmospheres. An introduction to their physics and chemistry.*, volume 36. Academic Press, Jan. 1987.

E. Chané, J. Saur, and S. Poedts. Modeling Jupiter's magnetosphere: Influence of the internal sources. *Journal of Geophysical Research: Space Physics*, 118(5):2157–2172, 2013. ISSN 2169-9402. doi:10.1002/jgra.50258.

E. Chané, J. Saur, R. Keppens, and S. Poedts. How is the Jovian main auroral emission affected by the solar wind? *Journal of Geophysical Research: Space Physics*, 122(2): 1960–1978, 2017. ISSN 2169-9402. doi:10.1002/2016JA023318.

E. Chané, B. Palmaerts, and A. Radioti. Periodic shearing motions in the Jovian magnetosphere causing a localized peak in the main auroral emission close to noon. *Planetary and Space Science*, 158:110–117, Sept. 2018. ISSN 0032-0633. doi:10.1016/j.pss.2018.04.023.

C. X. Chen and R. A. Wolf. Interpretation of high-speed flows in the plasma sheet. *Journal of Geophysical Research: Space Physics*, 98(A12):21409–21419, 1993. ISSN 2156-2202. doi:10.1029/93JA02080.

G. Clark, C. Tao, B. H. Mauk, J. Nichols, J. Saur, E. J. Bunce, F. Allegrini, R. Gladstone, F. Bagenal, S. Bolton, B. Bonfond, J. Connerney, R. W. Ebert, D. J. Gershman, D. Haggerty, T. Kimura, P. Kollmann, S. Kotsiaros, W. S. Kurth, S. Levin, D. J. McComas, G. Murakami, C. Paranicas, A. Rymer, and P. Valek. Precipitating Electron Energy Flux and Characteristic Energies in Jupiter's Main Auroral Region as Measured by Juno/JEDI. *Journal of Geophysical Research: Space Physics*, 123(9):7554–7567, 2018. ISSN 2169-9402. doi:10.1029/2018JA025639.

G. Clark, P. Kollmann, B. H. Mauk, C. Paranicas, D. Haggerty, A. Rymer, H. T. Smith, J. Saur, F. Allegrini, S. Duling, R. W. Ebert, W. S. Kurth, R. Gladstone, T. K. Greathouse, W. Li, F. Bagenal, J. E. P. Connerney, S. Bolton, J. R. Szalay, A. H. Sulaiman, C. J. Hansen, and D. L. Turner. Energetic Charged Particle Observations During Juno's Close Flyby of Ganymede. *Geophysical Research Letters*, 49(23):e2022GL098572, 2022. ISSN 1944-8007. doi:10.1029/2022GL098572.

J. T. Clarke, H. W. Moos, S. K. Atreya, and A. L. Lane. Observations from earth orbit and variability of the polar aurora on Jupiter. *The Astrophysical Journal*, 241:L179–L182, Nov. 1980. ISSN 0004-637X. doi:10.1086/183386. Publisher: IOP ADS Bibcode: 1980ApJ...241L.179C.

J. T. Clarke, R. Prange, G. E. Ballester, J. Trauger, R. Evans, D. Rego, K. Stapelfeldt, W. Ip, J.-C. Gerard, H. Hammel, M. Ballav, L. Ben Jaffel, J.-L. Bertaux, D. Crisp, C. Emerich, W. Harris, M. Horanyi, S. Miller, A. Storrs, and H. Weaver. HST Far-Ultraviolet Imaging of Jupiter During the Impacts of Comet Shoemaker-Levy 9. *Science*, 267:1302–1307, Mar. 1995. ISSN 0036-8075. doi:10.1126/science.7871427. ADS Bibcode: 1995Sci...267.1302C.

J. T. Clarke, G. E. Ballester, J. Trauger, R. Evans, J. E. P. Connerney, K. Stapelfeldt, D. Crisp, P. D. Feldman, C. J. Burrows, S. Casertano, J. S. Gallagher, R. E. Griffiths, J. J. Hester, J. G. Hoessel, J. A. Holtzman, J. E. Krist, V. Meadows, J. R. Mould, P. A. Scowen, A. M. Watson, and J. A. Westphal. Far-Ultraviolet Imaging of Jupiter's Aurora and the Io "Footprint". *Science*, 274(5286):404–409, Oct. 1996. doi:10.1126/science.274.5286.404.

J. T. Clarke, G. Ballester, J. Trauger, J. Ajello, W. Pryor, K. Tobiska, J. E. P. Connerney, G. R. Gladstone, J. H. Waite Jr., L. Ben Jaffel, and J.-C. Gérard. Hubble Space Telescope imaging of Jupiter's UV aurora during the Galileo orbiter mission. *Journal of Geophysical Research: Planets*, 103(E9):20217–20236, 1998. ISSN 2156-2202. doi:10.1029/98JE01130.

J. T. Clarke, J. Ajello, G. Ballester, L. Ben Jaffel, J. Connerney, J.-C. Gérard, G. R. Gladstone, D. Grodent, W. Pryor, J. Trauger, and J. H. Waite. Ultraviolet emissions from the magnetic footprints of Io, Ganymede and Europa on Jupiter. *Nature*, 415(6875): 997–1000, Feb. 2002. ISSN 1476-4687. doi:10.1038/415997a.

J. T. Clarke, D. Grodent, S. W. H. Cowley, E. J. Bunce, P. Zarka, J. E. P. Connerney, and T. Satoh. Jupiter's Aurora. In *Jupiter: The Planet, Satellites and Magnetosphere*. Cambridge University Press, Cambridge, 2004a.

J. T. Clarke, D. Grodent, S. W. H. Cowley, E. J. Bunce, P. Zarka, J. E. P. Connerney, and T. Satoh. Jupiter's aurora. In F. Bagenal, T. Dowling, and W. McKinnon, editors, *Jupiter: The Planet, Satellites and Magnetosphere*, chapter 26. Cambridge University Press, Cambridge, 2004b.

J. E. P. Connerney. Doing more with Jupiter's magnetic field. In *Proceedings of the 3rd International Workshop*, pages 13–33, Jan. 1992. ADS Bibcode: 1992pre3.conf...13C.

J. E. P. Connerney, R. Baron, T. Satoh, and T. Owen. Images of Excited H3+ at the Foot of the Io Flux Tube in Jupiter's Atmosphere. *Science*, 262(5136):1035–1038, Nov. 1993. doi:10.1126/science.262.5136.1035.

J. E. P. Connerney, M. H. Acuña, N. F. Ness, and T. Satoh. New models of Jupiter's magnetic field constrained by the Io flux tube footprint. *Journal of Geophysical Research: Space Physics*, 103(A6):11929–11939, 1998. ISSN 2156-2202. doi:10.1029/97JA03726.

J. E. P. Connerney, A. Adriani, F. Allegrini, F. Bagenal, S. J. Bolton, B. Bonfond, S. W. H. Cowley, J.-C. Gerard, G. R. Gladstone, D. Grodent, G. Hospodarsky, J. L. Jorgensen, W. S. Kurth, S. M. Levin, B. Mauk, D. J. McComas, A. Mura, C. Paranicas, E. J. Smith, R. M. Thorne, P. Valek, and J. Waite. Jupiter's magnetosphere and aurorae observed by the Juno spacecraft during its first polar orbits. *Science*, 356(6340):826–832, May 2017a. doi:10.1126/science.aam5928.

J. E. P. Connerney, M. Benn, J. B. Bjarno, T. Denver, J. Espley, J. L. Jorgensen, P. S. Jorgensen, P. Lawton, A. Malinnikova, J. M. Merayo, S. Murphy, J. Odom, R. Oliversen, R. Schnurr, D. Sheppard, and E. J. Smith. The Juno Magnetic Field Investigation. *Space Science Reviews*, 213(1):39–138, Nov. 2017b. ISSN 1572-9672. doi:10.1007/s11214-017-0334-z.

J. E. P. Connerney, S. Kotsiaros, R. J. Oliversen, J. R. Espley, J. L. Joergensen, P. S. Joergensen, J. M. G. Merayo, M. Herceg, J. Bloxham, K. M. Moore, S. J. Bolton, and S. M. Levin. A New Model of Jupiter's Magnetic Field From Juno's First Nine Orbits. *Geophysical Research Letters*, 45(6):2590–2596, 2018. ISSN 1944-8007. doi:10.1002/2018GL077312.

J. E. P. Connerney, S. Timmins, M. Herceg, and J. L. Joergensen. A Jovian Magnetodisc Model for the Juno Era. *Journal of Geophysical Research: Space Physics*, 125(10): e2020JA028138, 2020. ISSN 2169-9402. doi:10.1029/2020JA028138.

J. E. P. Connerney, S. Timmins, R. J. Oliversen, J. R. Espley, J. L. Joergensen, S. Kotsiaros, P. S. Joergensen, J. M. G. Merayo, M. Herceg, J. Bloxham, K. M. Moore, A. Mura, A. Moirano, S. J. Bolton, and S. M. Levin. A New Model of Jupiter's Magnetic Field at the Completion of Juno's Prime Mission. *Journal of Geophysical Research: Planets*, 127(2):e2021JE007055, 2022. ISSN 2169-9100. doi:10.1029/2021JE007055.

J. F. Cooper, R. E. Johnson, B. H. Mauk, H. B. Garrett, and N. Gehrels. Energetic Ion and Electron Irradiation of the Icy Galilean Satellites. *Icarus*, 149(1):133–159, Jan. 2001. ISSN 0019-1035. doi:10.1006/icar.2000.6498.

S. W. H. Cowley and E. J. Bunce. Origin of the main auroral oval in Jupiter's coupled magnetosphere–ionosphere system. *Planetary and Space Science*, 49:1067–1088, 2001. doi:10.1016/S0032-0633(00)00167-7.

S. W. H. Cowley, E. J. Bunce, T. S. Stallard, and S. Miller. Jupiter's polar ionospheric flows: Theoretical interpretation. *Geophysical Research Letters*, 30(5), 2003. ISSN 1944-8007. doi:10.1029/2002GL016030.

S. W. H. Cowley, J. D. Nichols, and D. J. Andrews. Modulation of Jupiter's plasma flow, polar currents, and auroral precipitation by solar wind-induced compressions and expansions of the magnetosphere: a simple theoretical model. *Annales Geophysicae*, 25(6): 1433–1463, June 2007. ISSN 0992-7689. doi:10.5194/angeo-25-1433-2007.

S. W. H. Cowley, G. Provan, E. J. Bunce, and J. D. Nichols. Magnetosphere-ionosphere coupling at Jupiter: Expectations for Juno Perijove 1 from a steady state axisymmetric physical model. *Geophysical Research Letters*, 44(10):4497–4505, 2017. ISSN 1944-8007. doi:10.1002/2017GL073129.

A. Daly, W. Li, Q. Ma, X.-C. Shen, P. H. Yoon, J. D. Menietti, W. S. Kurth, G. B. Hospodarsky, B. H. Mauk, G. Clark, F. Allegrini, J. E. P. Connerney, and S. J. Bolton. Plasma Wave and Particle Dynamics During Interchange Events in the Jovian Magnetosphere Using Juno Observations. *Geophysical Research Letters*, 50(23):e2023GL103894, 2023. ISSN 1944-8007. doi:10.1029/2023GL103894.

A. Daly, W. Li, Q. Ma, X.-C. Shen, L. Capannolo, S. Huang, W. S. Kurth, G. B. Hospodarsky, B. H. Mauk, G. Clark, F. Allegrini, and S. J. Bolton. Statistical Survey of Interchange Events in the Jovian Magnetosphere Using Juno Observations. *Geophysical Research Letters*, 51(19):e2024GL110300, 2024. ISSN 1944-8007. doi:10.1029/2024GL110300.

A. De Becker, L. A. Head, B. Bonfond, E. Jehin, J. Manfroid, Z. Yao, B. Zhang, D. Grodent, N. Schneider, and Z. Benkhaldoun. A study of Io's sodium jets with the TRAPPIST telescopes. *Astronomy & Astrophysics*, 680:A3, Dec. 2023. ISSN 0004-6361, 1432-0746. doi:10.1051/0004-6361/202347447. Publisher: EDP Sciences.

I. de Pater, K. de Kleer, and M. Ádámkovics. High Spatial and Spectral Resolution Observations of the Forbidden 1.707 μm Rovibronic SO Emissions on Io: Evidence for Widespread Stealth Volcanism. *The Planetary Science Journal*, 1:29, Sept. 2020. ISSN 2632-3338. doi:10.3847/PSJ/ab9eb1. ADS Bibcode: 2020PSJ.....1...29D.

I. de Pater, J. T. Keane, K. d. Kleer, and A. G. Davies. A 2020 Observational Perspective of Io. *Annual Review of Earth and Planetary Sciences*, 49(Volume 49, 2021):643–678, May 2021. ISSN 0084-6597, 1545-4495. doi:10.1146/annurev-earth-082420-095244.

I. de Pater, D. Goldstein, and E. Lellouch. The Plumes and Atmosphere of Io. In R. M. C. Lopes, K. de Kleer, and J. Tuttle Keane, editors, *Io: A New View of Jupiter's Moon*, Astrophysics and Space Science Library, pages 233–290. Springer International Publishing, Cham, 2023. ISBN 978-3-031-25670-7. doi:10.1007/978-3-031-25670-7_8.

A. de Spiegeleire. TRAPPIST observations of sodium jets from Io. Master's thesis, University of Liège, Liège, 2019.

P. A. Delamere, R. J. Wilson, S. Eriksson, and F. Bagenal. Magnetic signatures of Kelvin-Helmholtz vortices on Saturn's magnetopause: Global survey. *Journal of Geophysical Research: Space Physics*, 118(1):393–404, 2013. ISSN 2169-9402. doi:10.1029/2012JA018197.

M. Devinat, N. André, G. Vinci, M. Blanc, J. R. Szalay, Z.-Y. Liu, Q. Nénon, E. Penou, P. Louarn, F. Allegrini, R. W. Ebert, P. W. Valek, F. Bagenal, R. J. Wilson, J.-Z. Wang, W. S. Kurth, B. H. Mauk, Y. Wang, G. A. DiBraccio, J. E. P. Connerney, and S. J. Bolton. Ion Composition and Electron Pitch Angle Variations for Interchange Events in Jupiter's Inner Magnetosphere. *Geophysical Research Letters*, 52(20):e2025GL116114, 2025. ISSN 1944-8007. doi:10.1029/2025GL116114.

V. Dols, J. C. Gérard, F. Paresce, R. Prangé, and A. Vidal-Madjar. Ultraviolet imaging of the Jovian aurora with the Hubble Space Telescope. *Geophysical Research Letters*, 19 (18):1803–1806, 1992. ISSN 1944-8007. doi:10.1029/92GL02104.

V. Dols, P. A. Delamere, and F. Bagenal. A multispecies chemistry model of Io's local interaction with the Plasma Torus. *Journal of Geophysical Research: Space Physics*, 113(A9), 2008. ISSN 2156-2202. doi:10.1029/2007JA012805.

V. Dols, P. A. Delamere, F. Bagenal, W. S. Kurth, and W. R. Paterson. Asymmetry of Io's outer atmosphere: Constraints from five Galileo flybys. *Journal of Geophysical Research: Planets*, 117(E10), 2012. ISSN 2156-2202. doi:10.1029/2012JE004076.

M. K. Dougherty, A. Balogh, D. J. Southwood, and E. J. Smith. Ulysses assessment of the Jovian planetary field. *Journal of Geophysical Research: Space Physics*, 101(A11): 24929–24941, Nov. 1996. ISSN 0148-0227. doi:10.1029/96JA02385.

S. D. Drell, H. M. Foley, and M. A. Ruderman. Drag and propulsion of large satellites in the ionosphere: An Alfvén propulsion engine in space. *Journal of Geophysical Research (1896-1977)*, 70(13):3131–3145, 1965. ISSN 2156-2202. doi:10.1029/JZ070i013p03131.

M. Dumont. *Ultraviolet auroral emissions associated with plasma injections in Jupiter's magnetosphere*. PhD thesis, Université de Liège, Sept. 2023.

M. Dumont, D. Grodent, A. Radioti, B. Bonfond, and J.-C. Gérard. Jupiter's equatorward auroral features: Possible signatures of magnetospheric injections. *Journal of Geophysical Research: Space Physics*, 119(12):10,068–10,077, 2014. ISSN 2169-9402. doi:10.1002/2014JA020527.

M. Dumont, D. Grodent, A. Radioti, B. Bonfond, E. Roussos, and C. Paranicas. Evolution of the Auroral Signatures of Jupiter's Magnetospheric Injections. *Journal of Geophysical Research: Space Physics*, 123(10):8489–8501, 2018. ISSN 2169-9402. doi:10.1029/2018JA025708.

J. W. Dungey. Interplanetary Magnetic Field and the Auroral Zones. *Physical Review Letters*, 6(2):47–48, Jan. 1961. doi:10.1103/PhysRevLett.6.47.

W. R. Dunn, G. Branduardi-Raymont, R. F. Elsner, M. F. Vogt, L. Lamy, P. G. Ford, A. J. Coates, G. R. Gladstone, C. M. Jackman, J. D. Nichols, I. J. Rae, A. Varsani, T. Kimura, K. C. Hansen, and J. M. Jasinski. The impact of an ICME on the Jovian X-ray aurora. *Journal of Geophysical Research: Space Physics*, 121(3):2274–2307, 2016. ISSN 2169-9402. doi:10.1002/2015JA021888.

R. W. Ebert, T. K. Greathouse, G. Clark, V. Hue, F. Allegrini, F. Bagenal, S. J. Bolton, B. Bonfond, J. E. P. Connerney, G. R. Gladstone, M. Imai, S. Kotsiaros, W. S. Kurth, S. Levin, P. Louarn, B. H. Mauk, D. J. McComas, C. Paranicas, A. H. Sulaiman, J. R. Szalay, M. F. Thomsen, and R. J. Wilson. Simultaneous UV Images and High-Latitude Particle and Field Measurements During an Auroral Dawn Storm at Jupiter. *Journal of Geophysical Research: Space Physics*, 126(12):e2021JA029679, 2021. ISSN 2169-9402. doi:10.1029/2021JA029679.

S. S. Elliott, D. A. Gurnett, W. S. Kurth, B. H. Mauk, R. W. Ebert, G. Clark, P. Valek, F. Allegrini, and S. J. Bolton. The Acceleration of Electrons to High Energies Over the Jovian Polar Cap via Whistler Mode Wave-Particle Interactions. *Journal of Geophysical Research: Space Physics*, 123(9):7523–7533, 2018. ISSN 2169-9402. doi:10.1029/2018JA025797.

S. S. Elliott, D. A. Gurnett, P. H. Yoon, W. S. Kurth, B. H. Mauk, R. W. Ebert, G. Clark, P. Valek, F. Allegrini, S. J. Bolton, J. D. Menietti, P. Louarn, and A. H. Sulaiman. The Generation of Upward-Propagating Whistler Mode Waves by Electron Beams in the Jovian Polar Regions. *Journal of Geophysical Research: Space Physics*, 125(6): e2020JA027868, 2020. ISSN 2169-9402. doi:10.1029/2020JA027868.

A. Eviatar and C. Paranicas. The plasma plumes of Europa and Callisto. *Icarus*, 178(2): 360–366, Nov. 2005. ISSN 0019-1035. doi:10.1016/j.icarus.2005.06.007.

D. H. Fairfield. Average and unusual locations of the Earth's magnetopause and bow shock. *Journal of Geophysical Research (1896-1977)*, 76(28):6700–6716, 1971. ISSN 2156-2202. doi:10.1029/JA076i028p06700.

F. P. Fanale, R. H. Brown, D. P. Cruikshank, and R. N. Clake. Significance of absorption features in Io's IR reflectance spectrum. *Nature*, 280(5725):761–763, Aug. 1979. ISSN 1476-4687. doi:10.1038/280761a0.

F. P. Fanale, W. B. Banerdt, and D. P. Cruikshank. IO: Could SO2 condensation/sublimation cause the sometimes reported post-eclipse brightening? *Geophysical Research Letters*, 8(6):625–628, 1981. ISSN 1944-8007. doi:10.1029/GL008i006p00625.

L. M. Feaga, M. McGrath, and P. D. Feldman. Io's dayside SO 2 atmosphere. *Icarus*, 201: 570–584, June 2009. ISSN 0019-1035. doi:10.1016/j.icarus.2009.01.029. ADS Bibcode: 2009Icar..201..570F.

E. Feng, B. Zhang, Z. Yao, P. A. Delamere, Z. Zheng, O. J. Brambles, S.-Y. Ye, and K. A. Sorathia. Dynamic Jovian Magnetosphere Responses to Enhanced Solar Wind Ram Pressure: Implications for Auroral Activities. *Geophysical Research Letters*, 49(19): e2022GL099858, 2022. ISSN 1944-8007. doi:10.1029/2022GL099858.

E. Feng, B. Zhang, Z. Yao, P. A. Delamere, Z. Zheng, W. R. Dunn, and S.-Y. Ye. Variation of the Jovian Magnetopause Under Constant Solar Wind Conditions: Significance of Magnetodisc Dynamics. *Geophysical Research Letters*, 50(12):e2023GL104046, 2023. ISSN 1944-8007. doi:10.1029/2023GL104046.

L. Ferrarese, H. C. Ford, and W. Jaffe. Evidence for a Massive Black Hole in the Active Galaxy NGC 4261 from Hubble Space Telescope Images and Spectra. *The Astrophysical Journal*, 470:444, Oct. 1996. ISSN 0004-637X. doi:10.1086/177876. ADS Bibcode: 1996ApJ...470..444F.

J. L. Fox and A. I. F. Stewart. The Venus ultraviolet aurora: A soft electron source. *Journal of Geophysical Research: Space Physics*, 96(A6):9821–9828, 1991. ISSN 2156-2202. doi:10.1029/91JA00252.

W. L. Freedman, B. F. Madore, B. K. Gibson, L. Ferrarese, D. D. Kelson, S. Sakai, J. R. Mould, J. Robert C. Kennicutt, H. C. Ford, J. A. Graham, J. P. Huchra, S. M. G. Hughes, G. D. Illingworth, L. M. Macri, and P. B. Stetson. Final Results from the Hubble Space TelescopeKey Project to Measure the HubbleConstant*. *The Astrophysical Journal*, 553(1):47, May 2001. ISSN 0004-637X. doi:10.1086/320638.

H. U. Frey, S. B. Mende, T. J. Immel, S. A. Fuselier, E. S. Claflin, J. Gérard, and B. Hubert. Proton aurora in the cusp. *Journal of Geophysical Research: Space Physics*, 107(A7), July 2002. ISSN 0148-0227. doi:10.1029/2001JA900161.

K. Fukazawa, T. Ogino, and R. J. Walker. Configuration and dynamics of the Jovian magnetosphere. *Journal of Geophysical Research: Space Physics*, 111(A10), 2006. ISSN 2156-2202. doi:10.1029/2006JA011874.

E. Galanti, M. Smirnova, M. Ziv, M. Fonsetti, A. Caruso, D. R. Buccino, W. B. Hubbard, B. Militzer, S. J. Bolton, T. Guillot, R. Helled, S. M. Levin, M. Parisi, R. S. Park, P. Steffes, P. Tortora, P. Withers, M. Zannoni, and Y. Kaspi. The size and shape of Jupiter. *Nature Astronomy*, pages 1–9, Feb. 2026. ISSN 2397-3366. doi:10.1038/s41550-026-02777-x. Publisher: Nature Publishing Group.

P. E. Geissler and D. B. Goldstein. Plumes and their deposits. In *Io After Galileo: A New View of Jupiter's Volcanic Moon*, page 163. Springer, Jan. 2007. doi:10.1007/978-3-540-48841-5_8. ADS Bibcode: 2007iag..book..163G.

D. J. Gershman, J. E. P. Connerney, S. Kotsiaros, G. A. DiBraccio, Y. M. Martos, A. F. Viñas, V. Hue, G. Clark, F. Bagenal, S. Levin, and S. J. Bolton. Alfvénic Fluctuations Associated With Jupiter's Auroral Emissions. *Geophysical Research Letters*, 46(13): 7157–7165, 2019. ISSN 1944-8007. doi:10.1029/2019GL082951.

R. L. Gilliland and A. K. Dupree. First Image of the Surface of a Star with the Hubble Space Telescope*. *The Astrophysical Journal*, 463(1):L29, May 1996. ISSN 0004-637X. doi:10.1086/310043.

M. Gillon, E. Jehin, S. M. Lederer, L. Delrez, J. de Wit, A. Burdanov, V. Van Grootel, A. J. Burgasser, A. H. M. J. Triaud, C. Opitom, B.-O. Demory, D. K. Sahu, D. Bardalez Gagliuffi, P. Magain, and D. Queloz. Temperate Earth-sized planets transiting a nearby ultracool dwarf star. *Nature*, 533(7602):221–224, May 2016. ISSN 1476-4687. doi:10.1038/nature17448.

M. Gillon, A. H. M. J. Triaud, B.-O. Demory, E. Jehin, E. Agol, K. M. Deck, S. M. Lederer, J. de Wit, A. Burdanov, J. G. Ingalls, E. Bolmont, J. Leconte, S. N. Raymond, F. Selsis, M. Turbet, K. Barkaoui, A. Burgasser, M. R. Burleigh, S. J. Carey, A. Chaushev, C. M. Copperwheat, L. Delrez, C. S. Fernandes, D. L. Holdsworth, E. J. Kotze, V. Van Grootel, Y. Almleaky, Z. Benkhaldoun, P. Magain, and D. Queloz. Seven temperate terrestrial planets around the nearby ultracool dwarf star TRAPPIST-1. *Nature*, 542(7642):456–460, Feb. 2017. ISSN 1476-4687. doi:10.1038/nature21360.

G. R. Gladstone, S. C. Persyn, J. S. Eterno, B. C. Walther, D. C. Slater, M. W. Davis, M. H. Versteeg, K. B. Persson, M. K. Young, G. J. Dirks, A. O. Sawka, J. Tumlinson, H. Sykes, J. Beshears, C. L. Rhoad, J. P. Cravens, G. S. Winters, R. A. Klar, W. Lockhart, B. M. Piepgrass, T. K. Greathouse, B. J. Trantham, P. M. Wilcox, M. W. Jackson, O. H. W. Siegmund, J. V. Vallerga, R. Raffanti, A. Martin, J.-C. Gérard, D. C. Grodent, B. Bonfond, B. Marquet, and F. Denis. The Ultraviolet Spectrograph on NASA's Juno Mission. *Space Science Reviews*, 213(1):447–473, Nov. 2017. ISSN 1572-9672. doi:10.1007/s11214-014-0040-z.

C. K. Goertz and R. W. Boswell. Magnetosphere-ionosphere coupling. *Journal of Geophysical Research: Space Physics*, 1979. doi:10.1029/JA084iA12p07239.

P. Goldreich and D. Lynden-Bell. Io, a jovian unipolar inductor. *The Astrophysical Journal*, 156:59–78, Apr. 1969. ISSN 0004-637X. doi:10.1086/149947. Publisher: IOP ADS Bibcode: 1969ApJ...156...59G.

C. Grava, T. A. Cassidy, N. M. Schneider, H.-W. Hsu, J. P. Morgenthaler, F. Leblanc, V. Mangano, K. D. Retherford, M. H. Burger, and C. Barbieri. A Possible Dust Origin for an Unusual Feature in Io's Sodium Neutral Clouds. *The Astronomical Journal*, 162 (5):190, Nov. 2021a. ISSN 0004-6256, 1538-3881. doi:10.3847/1538-3881/ac1ff8.

C. Grava, R. M. Killen, M. Benna, A. A. Berezhnoy, J. S. Halekas, F. Leblanc, M. N. Nishino, C. Plainaki, J. M. Raines, M. Sarantos, B. D. Teolis, O. J. Tucker, R. J. Vervack, and A. Vorburger. Volatiles and Refractories in Surface-Bounded Exospheres in the Inner Solar System. *Space Science Reviews*, 217(5):61, June 2021b. ISSN 1572-9672. doi:10.1007/s11214-021-00833-8.

R. L. Gray, S. V. Badman, B. Bonfond, T. Kimura, H. Misawa, J. D. Nichols, M. F. Vogt, and L. C. Ray. Auroral evidence of radial transport at Jupiter during January 2014. *Journal of Geophysical Research: Space Physics*, 121(10):9972–9984, 2016. ISSN 2169-9402. doi:10.1002/2016JA023007.

R. L. Gray, S. V. Badman, E. E. Woodfield, and C. Tao. Characterization of Jupiter's secondary auroral oval and its response to hot plasma injections. *Journal of Geophysical Research: Space Physics*, 122(6):6415–6429, 2017. ISSN 2169-9402. doi:10.1002/2017JA024214.

T. Greathouse, R. Gladstone, M. Versteeg, V. Hue, J. Kammer, R. Giles, M. Davis, S. Bolton, S. Levin, J. Connerney, J.-C. Gérard, D. Grodent, B. Bonfond, E. Bunce, and M. F. Vogt. Local Time Dependence of Jupiter's Polar Auroral Emissions Observed by Juno UVS. *Journal of Geophysical Research: Planets*, 126(12):e2021JE006954, 2021. ISSN 2169-9100. doi:10.1029/2021JE006954.

D. Grodent. A brief review of ultraviolet auroral emissions on giant planets. *Space Science Review*, 187:23–50, 2015. doi:10.1007/s11214-014-0052-8.

D. Grodent, J. T. Clarke, J. Kim, J. H. Waite, and S. W. H. Cowley. Jupiter's main auroral oval observed with HST-STIS. *Journal of Geophysical Research*, 108:1389, 2003a. doi:10.1029/2003JA009921.

D. Grodent, J. T. Clarke, J. H. Waite Jr., S. W. H. Cowley, J.-C. Gérard, and J. Kim. Jupiter's polar auroral emissions. *Journal of Geophysical Research: Space Physics*, 108(A10), 2003b. ISSN 2156-2202. doi:10.1029/2003JA010017.

D. Grodent, J.-C. Gérard, A. Radioti, B. Bonfond, and A. Saglam. Jupiter's changing auroral location. *Journal of Geophysical Research: Space Physics*, 113(A1), 2008. ISSN 2156-2202. doi:10.1029/2007JA012601.

D. Grodent et al. Jupiter's aurora observed with HST during Juno orbits 3 to 7. *Journal of Geophysical Research: Space Physics*, 123:3299–3319, 2018. doi:10.1002/2017JA025046.

A. Groulard, B. Bonfond, D. Grodent, J. C. Gérard, T. K. Greathouse, V. Hue, G. R. Gladstone, and M. H. Versteeg. Dawn-dusk asymmetry in the main auroral emissions at Jupiter observed with Juno-UVS. *Icarus*, 413:116005, May 2024. ISSN 0019-1035. doi:10.1016/j.icarus.2024.116005.

R. Guo and Z. Yao. Magnetic reconnection in the magnetodisk of centrifugally dominated giant planets. *Reviews of Modern Plasma Physics*, 8(1):12, Apr. 2024. ISSN 2367-3192. doi:10.1007/s41614-024-00162-7.

J. Gustin, J.-C. Gérard, D. Grodent, S. W. H. Cowley, J. T. Clarke, and A. Grard. Energy-flux relationship in the FUV Jovian aurora deduced from HST-STIS spectral observations. *Journal of Geophysical Research: Space Physics*, 109(A10), 2004. ISSN 2156-2202. doi:10.1029/2003JA010365.

J. Gustin, B. Bonfond, D. Grodent, and J.-C. Gérard. Conversion from HST ACS and STIS auroral counts into brightness, precipitated power, and radiated power for H2 giant planets. *Journal of Geophysical Research: Space Physics*, 117(A7), 2012. ISSN 2156-2202. doi:10.1029/2012JA017607.

J. Gustin, J. C. Gérard, D. Grodent, G. R. Gladstone, J. T. Clarke, W. R. Pryor, V. Dols, B. Bonfond, A. Radioti, L. Lamy, and J. M. Ajello. Effects of methane on giant planet's UV emissions and implications for the auroral characteristics. *Journal of Molecular Spectroscopy*, 291:108–117, Sept. 2013. ISSN 0022-2852. doi:10.1016/j.jms.2013.03.010.

J. Gustin, D. Grodent, L. C. Ray, B. Bonfond, E. J. Bunce, J. D. Nichols, and N. Ozak. Characteristics of north jovian aurora from STIS FUV spectral images. *Icarus*, 268: 215–241, Apr. 2016. ISSN 0019-1035. doi:10.1016/j.icarus.2015.12.048.

V. Génot, E. Budnik, C. Jacquey, M. Bouchemit, B. Renard, N. Dufourg, N. André, B. Cecconi, F. Pitout, B. Lavraud, A. Fedorov, M. Ganfloff, I. Plotnikov, R. Modolo, N. Lormant, H. S. H. Mohand, C. Tao, B. Besson, D. Heulet, D. Boucon, J. Durand, N. Bourrel, Q. Brzustowski, N. Jourdane, R. Hitier, P. Garnier, B. Grison, N. Aunai, A. Jeandet, and F. Cabrolie. Automated Multi-Dataset Analysis (AMDA): An on-line database and analysis tool for heliospheric and planetary plasma data. *Planetary and Space Science*, 201:105214, July 2021. ISSN 0032-0633. doi:10.1016/j.pss.2021.105214.

J. C. Gérard, D. Grodent, V. Dols, R. Prangé, J. H. Waite, G. R. Gladstone, K. A. Franke, F. Paresce, A. Storrs, and L. B. Jaffel. A remarkable auroral event on jupiter observed in the ultraviolet with the hubble space telescope. *Science*, 266(5191):1675–1678, Dec. 1994. ISSN 0036-8075. doi:10.1126/science.266.5191.1675.

J. C. Gérard, D. Grodent, A. Radioti, B. Bonfond, and J. T. Clarke. Hubble observations of Jupiter's north–south conjugate ultraviolet aurora. *Icarus*, 226(2):1559–1567, Nov. 2013. ISSN 0019-1035. doi:10.1016/j.icarus.2013.08.017.

J. C. Gérard, B. Bonfond, D. Grodent, and A. Radioti. The color ratio-intensity relation in the Jovian aurora: Hubble observations of auroral components. *Planetary and Space Science*, 131:14–23, Oct. 2016. ISSN 0032-0633. doi:10.1016/j.pss.2016.06.004.

J. C. Gérard, A. Mura, B. Bonfond, G. R. Gladstone, A. Adriani, V. Hue, B. M. Dinelli, T. K. Greathouse, D. Grodent, F. Altieri, M. L. Moriconi, A. Radioti, J. E. P. Connerney, S. J. Bolton, and S. M. Levin. Concurrent ultraviolet and infrared observations of the north Jovian aurora during Juno's first perijove. *Icarus*, 312:145–156, Sept. 2018. ISSN 0019-1035. doi:10.1016/j.icarus.2018.04.020.

J.-C. Gérard, B. Bonfond, B. H. Mauk, G. R. Gladstone, Z. H. Yao, T. K. Greathouse, V. Hue, D. Grodent, L. Gkouvelis, J. A. Kammer, M. Versteeg, G. Clark, A. Radioti, J. E. P. Connerney, S. J. Bolton, and S. M. Levin. Contemporaneous Observations of Jovian Energetic Auroral Electrons and Ultraviolet Emissions by the Juno Spacecraft. *Journal of Geophysical Research: Space Physics*, 124(11):8298–8317, 2019. ISSN 2169-9402. doi:10.1029/2019JA026862.

K. Haewsantati, B. Bonfond, S. Wannawichian, G. R. Gladstone, V. Hue, T. K. Greathouse, D. Grodent, Z. Yao, J.-C. Gérard, R. Guo, S. Elliott, B. H. Mauk, G. Clark, D. Gershman, S. Kotsiaros, W. S. Kurth, J. Connerney, J. R. Szalay, and A. Phriksee. Juno's Multi-Instruments Observations During the Flybys of Auroral Bright Spots in Jupiter's Polar Aurorae. *Journal of Geophysical Research: Space Physics*, 128(8):e2023JA031396, 2023. ISSN 2169-9402. doi:10.1029/2023JA031396.

K. Haewsantati et al. Morphology of Jupiter's polar auroral bright spot emissions via Juno-UVS observations. *Journal of Geophysical Research: Space Physics*, 126: e2020JA028586, 2021. doi:10.1029/2020JA028586.

D. K. Haggerty, B. H. Mauk, C. P. Paranicas, G. Clark, P. Kollmann, A. M. Rymer, G. R. Gladstone, T. K. Greathouse, S. J. Bolton, and S. M. Levin. Jovian Injections Observed at High Latitude. *Geophysical Research Letters*, 46(16):9397–9404, 2019. ISSN 1944-8007. doi:10.1029/2019GL083442.

D. T. Hall, P. D. Feldman, M. A. McGrath, and D. F. Strobel. The Far-Ultraviolet Oxygen Airglow of Europa and Ganymede. *The Astrophysical Journal*, 499(1):475, May 1998. ISSN 0004-637X. doi:10.1086/305604. Publisher: IOP Publishing.

C. J. Hansen, S. Bolton, A. H. Sulaiman, S. Duling, F. Bagenal, M. Brennan, J. Connerney, G. Clark, J. Lunine, S. Levin, W. Kurth, A. Mura, C. Paranicas, F. Tosi, and P. Withers. Juno's Close Encounter With Ganymede—An Overview. *Geophysical Research Letters*, 49(23):e2022GL099285, 2022. ISSN 1944-8007. doi:10.1029/2022GL099285.

A. Hasegawa. Particle acceleration by MHD surface wave and formation of aurora. *Journal of Geophysical Research*, 1976. doi:10.1029/JA081i028p05083.

J. W. Head, L. S. Crumpler, J. C. Aubele, J. E. Guest, and R. S. Saunders. Venus volcanism: Classification of volcanic features and structures, associations, and global distribution from Magellan data. *Journal of Geophysical Research: Planets*, 97(E8):13153–13197, 1992. ISSN 2156-2202. doi:10.1029/92JE01273.

L. A. Head, D. Grodent, B. Bonfond, A. Moirano, B. Benmahi, G. Sicorello, J.-C. Gérard, M. F. Vogt, V. Hue, T. Greathouse, G. R. Gladstone, and Z. Yao. Effect of magnetospheric conditions on the morphology of Jupiter's ultraviolet main auroral emission as observed by Juno-UVS. *Astronomy & Astrophysics*, 688:A205, Aug. 2024. ISSN 0004-6361, 1432-0746. doi:10.1051/0004-6361/202450253.

L. A. Head, D. Grodent, B. Bonfond, A. Sulaiman, A. Moirano, G. Sicorello, S. Elliott, M. F. Vogt, C. K. Louis, N. Kruegler, J. Vinesse, and T. K. Greathouse. Ultraviolet auroral bridge of Jupiter - The effect of the solar wind on the morphology of the polar aurora. *Astronomy & Astrophysics*, 700:A142, Aug. 2025. ISSN 0004-6361, 1432-0746. doi:10.1051/0004-6361/202554759. Publisher: EDP Sciences.

L. A. Head, D. Grodent, B. Bonfond, A. Moirano, G. Sicorello, J. Vinesse, A. Mouton, M. Dumont, T. K. Greathouse, V. Hue, A. Sulaiman, B. H. Mauk, Z. H. Yao, R. L. Guo, and J. Y. Zhao. Characterising injection signatures in Jupiter's ultraviolet aurora using Juno observations. *Astronomy & Astrophysics*, 707:A209, Mar. 2026. ISSN 0004-6361, 1432-0746. doi:10.1051/0004-6361/202558607. Publisher: EDP Sciences.

S. Hess and P. A. Delamere. Satellite-Induced Electron Acceleration and Related Auroras. In *Auroral Phenomenology and Magnetospheric Processes: Earth And Other Planets*, pages 295–304. American Geophysical Union (AGU), 2012. ISBN 978-1-118-67028-6. doi:10.1029/2011GM001175.

S. L. G. Hess, P. Delamere, V. Dols, B. Bonfond, and D. Swift. Power transmission and particle acceleration along the Io flux tube. *Journal of Geophysical Research: Space Physics*, 115(A6):2009JA014928, June 2010. ISSN 0148-0227. doi:10.1029/2009JA014928.

S. L. G. Hess, B. Bonfond, V. Chantry, J. C. Gérard, D. Grodent, S. Jacobsen, and A. Radioti. Evolution of the Io footprint brightness II: Modeling. *Planetary and Space Science*, 88:76–85, Nov. 2013. ISSN 0032-0633. doi:10.1016/j.pss.2013.08.005.

T. Hill. Inertial limit on corotation. *Journal of Geophysical Research: Space Physics*, 84 (A11):6554–6558, 1979. ISSN 2156-2202. doi:10.1029/JA084iA11p06554.

T. W. Hill. The Jovian auroral oval. *Journal of Geophysical Research: Space Physics*, 106(A5):8101–8107, 2001. ISSN 2156-2202. doi:10.1029/2000JA000302.

T. W. Hill, A. J. Dessler, and C. K. Goertz. Magnetospheric models. In A. J. Dessler, editor, *Physics of the Jovian Magnetosphere*, Cambridge Planetary Science Old, pages 353–394. Cambridge University Press, Cambridge, 1983. ISBN 978-0-521-52006-5. doi:10.1017/CBO9780511564574.012.

D. P. Hinson, F. M. Flasar, A. J. Kliore, P. J. Schinder, J. D. Twicken, and R. G. Herrera. Jupiter's ionosphere: Results from the First Galileo Radio Occultation Experiment. *Geophysical Research Letters*, 24(17):2107–2110, 1997. ISSN 1944-8007. doi:10.1029/97GL01608.

D. P. Hinson, J. D. Twicken, and E. T. Karayel. Jupiter's ionosphere: New results from Voyager 2 radio occultation measurements. *Journal of Geophysical Research: Space Physics*, 103(A5):9505–9520, 1998. ISSN 2156-2202. doi:10.1029/97JA03689.

T. K. Ho. The random subspace method for constructing decision forests. *IEEE Transactions on Pattern Analysis and Machine Intelligence*, 20(8):832–844, Aug. 1998. ISSN 1939-3539. doi:10.1109/34.709601.

R. J. Hoch. Stable auroral red arcs. *Reviews of Geophysics*, 11(4):935–949, 1973. ISSN 1944-9208. doi:10.1029/RG011i004p00935.

R. B. Horne and R. M. Thorne. Electron pitch angle diffusion by electrostatic electron cyclotron harmonic waves: The origin of pancake distributions. *Journal of Geophysical Research: Space Physics*, 105(A3):5391–5402, 2000. ISSN 2156-2202. doi:10.1029/1999JA900447.

G. B. Hospodarsky. Spaced-based search coil magnetometers. *Journal of Geophysical Research: Space Physics*, 121(12):12,068–12,079, 2016. ISSN 2169-9402. doi:10.1002/2016JA022565.

G. B. Hospodarsky, W. S. Kurth, B. Cecconi, D. A. Gurnett, M. L. Kaiser, M. D. Desch, and P. Zarka. Simultaneous observations of Jovian quasi-periodic radio emissions by the Galileo and Cassini spacecraft. *Journal of Geophysical Research: Space Physics*, 109 (A9), 2004. ISSN 2156-2202. doi:10.1029/2003JA010263.

Hubble Reentry Tracker. Hubble reentry tracker, 2026. `https://hubblereentry.com/` [Accessed: 2026-05-05].

V. Hue, T. K. Greathouse, B. Bonfond, J. Saur, G. R. Gladstone, L. Roth, M. W. Davis, J.-C. Gérard, D. C. Grodent, J. A. Kammer, J. R. Szalay, M. H. Versteeg, S. J. Bolton, J. E. P. Connerney, S. M. Levin, P. C. Hinton, and F. Bagenal. Juno-UVS Observation of the Io Footprint During Solar Eclipse. *Journal of Geophysical Research: Space Physics*, 124(7):5184–5199, 2019a. ISSN 2169-9402. doi:10.1029/2018JA026431.

V. Hue, G. Randall Gladstone, T. K. Greathouse, J. A. Kammer, M. W. Davis, B. Bonfond, M. H. Versteeg, D. C. Grodent, J.-C. Gérard, S. J. Bolton, S. M. Levin, and B. D. Byron. In-flight Characterization and Calibration of the Juno-ultraviolet Spectrograph (Juno-UVS). *The Astronomical Journal*, 157(2):90, Feb. 2019b. ISSN 0004-6256, 1538-3881. doi:10.3847/1538-3881/aafb36.

V. Hue, J. R. Szalay, T. K. Greathouse, B. Bonfond, S. Kotsiaros, C. K. Louis, A. H. Sulaiman, G. Clark, F. Allegrini, G. R. Gladstone, C. Paranicas, M. H. Versteeg, A. Mura, A. Moirano, D. J. Gershman, S. J. Bolton, J. E. P. Connerney, M. W. Davis, R. W. Ebert, J.-C. Gérard, R. S. Giles, D. C. Grodent, M. Imai, J. A. Kammer, W. S. Kurth, L. Lamy, and B. H. Mauk. A Comprehensive Set of Juno In Situ and Remote Sensing Observations of the Ganymede Auroral Footprint. *Geophysical Research Letters*, 49(7): e2021GL096994, 2022. ISSN 1944-8007. doi:10.1029/2021GL096994.

V. Hue, G. R. Gladstone, C. K. Louis, T. K. Greathouse, B. Bonfond, J. R. Szalay, A. Moirano, R. S. Giles, J. A. Kammer, M. Imai, A. Mura, M. H. Versteeg, G. Clark, J.-C. Gérard, D. C. Grodent, J. Rabia, A. H. Sulaiman, S. J. Bolton, and J. E. P. Connerney. The Io, Europa, and Ganymede Auroral Footprints at Jupiter in the Ultraviolet: Positions and Equatorial Lead Angles. *Journal of Geophysical Research: Space Physics*, 128(5):e2023JA031363, 2023. ISSN 2169-9402. doi:10.1029/2023JA031363.

H. L. F. Huybrighs, A. Blöcker, E. Roussos, C. van Buchem, Y. Futaana, M. K. G. Holmberg, C. Goetz, and O. Witasse. Europa's Perturbed Fields and Induced Dipole Affect Energetic Proton Depletions During Distant Alfvén Wing Flybys. *Journal of Geophysical Research: Space Physics*, 128(9):e2023JA031420, 2023. ISSN 2169-9402. doi:10.1029/2023JA031420.

A. P. Ingersoll, A. R. Vasavada, B. Little, C. D. Anger, S. J. Bolton, C. Alexander, K. P. Klaasen, and W. K. Tobiska. Imaging Jupiter's Aurora at Visible Wavelengths. *Icarus*, 135(1):251–264, Sept. 1998. ISSN 0019-1035. doi:10.1006/icar.1998.5971.

A. P. Ingersoll, T. E. Dowling, P. J. Gierasch, and G. S. Orton. Dynamics of Jupiter's Atmosphere. *Jupiter. The Planet, Satellites and Magnetosphere*, 2004.

D. S. Intriligator and W. D. Miller. First evidence for a Europa plasma torus. *Journal of Geophysical Research: Space Physics*, 87(A10):8081–8090, 1982. ISSN 2156-2202. doi:10.1029/JA087iA10p08081.

G. Ioannidis and N. Brice. Plasma densities in the Jovian magnetosphere: Plasma slingshot or Maxwell demon? *Icarus*, 14(3):360–373, June 1971. ISSN 0019-1035. doi:10.1016/0019-1035(71)90007-8.

M. Ishii, M. Kubota, M. Conde, R. W. Smith, and M. Krynicki. Vertical wind distribution in the polar thermosphere during Horizontal E Region Experiment (HEX) campaign. *Journal of Geophysical Research: Space Physics*, 109(A12), 2004. ISSN 2156-2202. doi:10.1029/2004JA010657.

Issāršumuēreš. Untitled cuneiform tablet Rm211, 679 B.C.E. Preserved in the British Museum, The Reports of the Magicians and Astrologers of Nineveh and Babylon (RMA) 275.

R. A. Jacobsen. The orbits of the regular jovian satellites and the orientation of the pole of Jupiter, 2021. Private communcation to Horizons/NAIF.

S. Jacobsen, F. M. Neubauer, J. Saur, and N. Schilling. Io's nonlinear MHD-wave field in the heterogeneous Jovian magnetosphere. *Geophysical Research Letters*, 34(10), 2007. ISSN 1944-8007. doi:10.1029/2006GL029187.

M. K. James, G. Provan, A. Kamran, R. J. Wilson, M. F. Vogt, M. J. Brennan, and S. W. H. Cowley. JupiterMag, 2022. doi:10.5281/zenodo.6822191.

A. Jeandet and A. Schulz. Speasy, July 2024. doi:10.5281/zenodo.12656220.

E. Jehin, J. Manfroid, M. Gillon, D. Hutsemekers, and P. Magain. Occultation by (136199) Eris. *International Astronomical Union Circulars*, 9184, Nov. 2010. ISSN 0081-0304.

E. Jehin, M. Gillon, D. Queloz, P. Magain, J. Manfroid, V. Chantry, M. Lendl, D. Hutsemékers, and S. Udry. TRAPPIST: TRAnsiting Planets and PlanetesImals Small Telescope. *The Messenger*, 145:2–6, Sept. 2011. ISSN 0722-6691. ADS Bibcode: 2011Msngr.145....2J.

A. Jenkins, L. C. Ray, T. Fell, S. V. Badman, and C. T. S. Lorch. Revealing the Local Time Structure of the Alfvén Radius and Travel Times in Jupiter's Magnetosphere. *Journal of Geophysical Research: Planets*, 129(10):e2024JE008414, 2024. ISSN 2169-9100. doi:10.1029/2024JE008414.

K. L. Jessup, J. R. Spencer, G. E. Ballester, R. R. Howell, F. Roesler, M. Vigel, and R. Yelle. The atmospheric signature of Io's Prometheus plume and anti-jovian hemisphere: evidence for a sublimation atmosphere. *Icarus*, 169(1):197–215, May 2004. ISSN 0019-1035. doi:10.1016/j.icarus.2003.11.015.

J. R. Johnson, S. Wing, P. Delamere, S. Petrinec, and S. Kavosi. Field-Aligned Currents in Auroral Vortices. *Journal of Geophysical Research: Space Physics*, 126(2): e2020JA028583, 2021. ISSN 2169-9402. doi:10.1029/2020JA028583.

S. P. Joy, M. G. Kivelson, R. J. Walker, K. K. Khurana, C. T. Russell, and T. Ogino. Probabilistic models of the Jovian magnetopause and bow shock locations. *Journal of Geophysical Research: Space Physics*, 107(A10):SMP 17–1–SMP 17–17, 2002. ISSN 2156-2202. doi:10.1029/2001JA009146.

C. Kamath and E. Cantú-Paz. Creating ensembles of decision trees through sampling. In *Proceedings of the 33rd Symposium on the Interface: Computing Science and Statistics*, Costa Mesa, California, 2001. U.S. Department of Energy.

A. Kamran, E. J. Bunce, S. W. H. Cowley, M. K. James, J. D. Nichols, G. Provan, H. Cao, V. Hue, T. K. Greathouse, and G. R. Gladstone. Auroral Field-Aligned Current Signatures in Jupiter's Magnetosphere: Juno Magnetic Field Observations and Physical Modeling. *Journal of Geophysical Research (Space Physics)*, 127(12):e2022JA030431, Dec. 2022. doi:10.1029/2022JA030431.

R. M. Katsanis and M. A. McGrath. The Calstis IRAF Calibration Tools for STIS Data. Technical report, STScI, Apr. 1998.

L. Keszthelyi, A. S. McEwen, C. B. Phillips, M. Milazzo, P. Geissler, E. P. Turtle, J. Radebaugh, D. A. Williams, D. P. Simonelli, H. H. Breneman, K. P. Klaasen, G. Levanas, and T. Denk. Imaging of volcanic activity on Jupiter's moon Io by Galileo during the Galileo Europa Mission and the Galileo Millennium Mission. *Journal of Geophysical Research: Planets*, 106(E12):33025–33052, 2001. ISSN 2156-2202. doi:10.1029/2000JE001383.

K. K. Khurana. Influence of solar wind on Jupiter's magnetosphere deduced from currents in the equatorial plane. *Journal of Geophysical Research: Space Physics*, 106(A11): 25999–26016, 2001. ISSN 2156-2202. doi:10.1029/2000JA000352.

K. K. Khurana and M. G. Kivelson. Ultralow frequency MHD waves in Jupiter's middle magnetosphere. *Journal of Geophysical Research: Space Physics*, 94(A5):5241–5254, 1989. ISSN 2156-2202. doi:10.1029/JA094iA05p05241.

K. K. Khurana and H. K. Schwarzl. Global structure of Jupiter's magnetospheric current sheet. *Journal of Geophysical Research: Space Physics*, 110(A7), 2005. ISSN 2156-2202. doi:10.1029/2004JA010757.

K. K. Khurana, M. G. Kivelson, V. M. Vasyliunas, N. Krupp, J. Woch, A. Lagg, B. H. Mauk, and W. S. Kurth. The Configuration of Jupiter's Magnetosphere. In *Jupiter: The Planet, Satellites and Magnetosphere*. Cambridge University Press, 2004.

K. K. Khurana, X. Jia, M. G. Kivelson, F. Nimmo, G. Schubert, and C. T. Russell. Evidence of a Global Magma Ocean in Io's Interior. *Science*, 332(6034):1186–1189, June 2011. doi:10.1126/science.1201425.

T. Kimura, S. V. Badman, C. Tao, K. Yoshioka, G. Murakami, A. Yamazaki, F. Tsuchiya, B. Bonfond, A. J. Steffl, A. Masters, S. Kasahara, H. Hasegawa, I. Yoshikawa, M. Fujimoto, and J. T. Clarke. Transient internally driven aurora at Jupiter discovered by Hisaki and the Hubble Space Telescope. *Geophysical Research Letters*, 42(6):1662–1668, 2015. ISSN 1944-8007. doi:10.1002/2015GL063272.

T. Kimura, R. P. Kraft, R. F. Elsner, G. Branduardi-Raymont, G. R. Gladstone, C. Tao, K. Yoshioka, G. Murakami, A. Yamazaki, F. Tsuchiya, M. F. Vogt, A. Masters, H. Hasegawa, S. V. Badman, E. Roediger, Y. Ezoe, W. R. Dunn, I. Yoshikawa, M. Fujimoto, and S. S. Murray. Jupiter's X-ray and EUV auroras monitored by Chandra, XMM-Newton, and Hisaki satellite. *Journal of Geophysical Research: Space Physics*, 121(3):2308–2320, 2016. ISSN 2169-9402. doi:10.1002/2015JA021893.

H. Kita, T. Kimura, C. Tao, F. Tsuchiya, H. Misawa, T. Sakanoi, Y. Kasaba, G. Murakami, K. Yoshioka, A. Yamazaki, I. Yoshikawa, and M. Fujimoto. Characteristics of solar wind control on Jovian UV auroral activity deciphered by long-term Hisaki EXCEED observations: Evidence of preconditioning of the magnetosphere? *Geophysical Research Letters*, 43(13):6790–6798, 2016. ISSN 1944-8007. doi:10.1002/2016GL069481.

M. G. Kivelson and F. Bagenal. Planetary Magnetospheres. In *Encyclopedia of the Solar System*. Academic Press, 2006.

M. G. Kivelson and D. J. Southwood. Dynamical consequences of two modes of centrifugal instability in Jupiter's outer magnetosphere. *Journal of Geophysical Research: Space Physics*, 110(A12), 2005. ISSN 2156-2202. doi:10.1029/2005JA011176.

M. G. Kivelson, K. K. Khurana, R. J. Walker, J. Warnecke, C. T. Russell, J. A. Linker, D. J. Southwood, and C. Polanskey. Io's Interaction with the Plasma Torus: Galileo Magnetometer Report. *Science*, 274(5286):396–398, Oct. 1996. doi:10.1126/science.274.5286.396.

M. G. Kivelson, F. Bagenal, W. S. Kurth, F. M. Neubauer, C. Paranicas, and J. Saur. Magnetospheric Interactions with Satellites. In *Jupiter: The Planet, Satellites and Magnetosphere*. Cambridge University Press, Cambridge, 2004.

A. Kliore, D. L. Cain, G. Fjeldbo, B. L. Seidel, and S. I. Rasool. Preliminary results on the atmospheres of io and jupiter from the pioneer 10 s-band occultation experiment. *Science*, 183(4122):323–324, Jan. 1974. ISSN 0036-8075. doi:10.1126/science.183.4122.323.

A. J. Kliore, G. Fjeldbo, B. L. Seidel, D. N. Sweetnam, T. T. Sesplaukis, P. M. Woiceshyn, and S. I. Rasool. The atmosphere of Io from Pioneer 10 radio occultation measurements. *Icarus*, 24(4):407–410, Apr. 1975. ISSN 0019-1035. doi:10.1016/0019-1035(75)90057-3.

S. Knight. Parallel electric fields. *Planetary and Space Science*, 21(5):741–750, May 1973. ISSN 0032-0633. doi:10.1016/0032-0633(73)90093-7.

S. Kotsiaros, J. E. P. Connerney, G. Clark, F. Allegrini, G. R. Gladstone, W. S. Kurth, B. H. Mauk, J. Saur, E. J. Bunce, D. J. Gershman, Y. M. Martos, T. K. Greathouse, S. J. Bolton, and S. M. Levin. Birkeland currents in Jupiter's magnetosphere observed by the polar-orbiting Juno spacecraft. *Nature Astronomy*, 3(10):904–909, Oct. 2019. ISSN 2397-3366. doi:10.1038/s41550-019-0819-7.

N. S. Kruegler, A. H. Sulaiman, S. S. Elliott, W. S. Kurth, R. L. Lysak, and S. J. Bolton. Auroral Ionospheric Erosion at Jupiter. *Journal of Geophysical Research: Space Physics*, 130(8):e2025JA034156, 2025. ISSN 2169-9402. doi:10.1029/2025JA034156.

I. Kupo, Y. Mekler, Y. Mekler, and A. Eviatar. Detection of ionized sulfur in the Jovian magnetosphere. *The Astrophysical Journal*, 205:L51–L53, Apr. 1976. ISSN 0004-637X. doi:10.1086/182088. ADS Bibcode: 1976ApJ...205L..51K.

W. S. Kurth, J. D. Sullivan, D. A. Gurnett, F. L. Scarf, H. S. Bridge, and E. C. Sittler Jr. Observations of Jupiter's distant magnetotail and wake. *Journal of Geophysical Research: Space Physics*, 87(A12):10373–10383, 1982. ISSN 2156-2202. doi:10.1029/JA087iA12p10373.

W. S. Kurth, G. B. Hospodarsky, D. L. Kirchner, B. T. Mokrzycki, T. F. Averkamp, W. T. Robison, C. W. Piker, M. Sampl, and P. Zarka. The Juno Waves Investigation. *Space Science Reviews*, 213(1):347–392, Nov. 2017. ISSN 1572-9672. doi:10.1007/s11214-017-0396-y.

W. S. Kurth, B. H. Mauk, S. S. Elliott, D. A. Gurnett, G. B. Hospodarsky, O. Santolik, J. E. P. Connerney, P. Valek, F. Allegrini, G. R. Gladstone, S. J. Bolton, and S. M. Levin. Whistler Mode Waves Associated With Broadband Auroral Electron Precipitation at Jupiter. *Geophysical Research Letters*, 45(18):9372–9379, 2018. ISSN 1944-8007. doi:10.1029/2018GL078566.

W. S. Kurth, D. R. Wilkinson, G. B. Hospodarsky, O. Santolík, T. F. Averkamp, A. H. Sulaiman, J. D. Menietti, J. E. P. Connerney, F. Allegrini, B. H. Mauk, and S. J. Bolton. Juno Plasma Wave Observations at Europa. *Geophysical Research Letters*, 50(24): e2023GL105775, 2023. ISSN 1944-8007. doi:10.1029/2023GL105775.

V. Lainey, J.-E. Arlot, O. Karatekin, and T. Van Hoolst. Strong tidal dissipation in Io and Jupiter from astrometric observations. *Nature*, 459(7249):957–959, June 2009. ISSN 1476-4687. doi:10.1038/nature08108. Publisher: Nature Publishing Group.

E. Lellouch. Io's Atmosphere and Surface-Atmosphere Interactions. *Space Science Reviews*, 116:211–224, Jan. 2005. ISSN 0038-6308. doi:10.1007/s11214-005-1957-z. ADS Bibcode: 2005SSRv..116..211L.

E. Lellouch, M. Belton, I. de Pater, S. Gulkis, and T. Encrenaz. Io's atmosphere from microwave detection of SO2. *Nature*, 346:639–641, Aug. 1990. ISSN 0028-0836. doi:10.1038/346639a0. ADS Bibcode: 1990Natur.346..639L.

E. Lellouch, M. Belton, I. De Pater, G. Paubert, S. Gulkis, and T. Encrenaz. The structure, stability, and global distribution of Io's atmosphere. *Icarus*, 98(2):271–295, Aug. 1992. ISSN 0019-1035. doi:10.1016/0019-1035(92)90095-O.

E. Lellouch, M. A. McGrath, and K. L. Jessup. Io's atmosphere. In R. M. C. Lopez and J. R. Spencer, editors, *Io after Galileo*, chapter 10. Springer Berlin, Heidelberg, 2007.

W. Li, R. M. Thorne, N. P. Meredith, R. B. Horne, J. Bortnik, Y. Y. Shprits, and B. Ni. Evaluation of whistler mode chorus amplification during an injection event observed on CRRES. *Journal of Geophysical Research: Space Physics*, 113(A9), 2008. ISSN 2156-2202. doi:10.1029/2008JA013129.

W. Li, R. M. Thorne, Q. Ma, X.-J. Zhang, G. R. Gladstone, V. Hue, P. W. Valek, F. Allegrini, B. H. Mauk, G. Clark, W. S. Kurth, G. B. Hospodarsky, J. E. P. Connerney, and S. J. Bolton. Understanding the Origin of Jupiter's Diffuse Aurora Using Juno's First Perijove Observations. *Geophysical Research Letters*, 44(20):10,162–10,170, 2017. ISSN 1944-8007. doi:10.1002/2017GL075545.

W. Li, Q. Ma, X.-C. Shen, X.-J. Zhang, B. H. Mauk, G. Clark, F. Allegrini, W. S. Kurth, G. B. Hospodarsky, V. Hue, G. R. Gladstone, T. K. Greathouse, and S. J. Bolton. Quantification of Diffuse Auroral Electron Precipitation Driven by Whistler Mode Waves at Jupiter. *Geophysical Research Letters*, 48(19):e2021GL095457, 2021. ISSN 1944-8007. doi:10.1029/2021GL095457.

J. Lilensten, W. Kofman, J. Wisemberg, E. S. Oran, and C. R. DeVore. Ionization efficiency due to primary and secondary photoelectrons - A numerical model. *Annales Geophysicae*, 7:83–90, Feb. 1989. ISSN 0980-87520992-76891432-0576. ADS Bibcode: 1989AnGeo...7...83L.

C. T. S. Lorch, L. C. Ray, C. S. Arridge, K. K. Khurana, C. J. Martin, and A. Bader. Local Time Asymmetries in Jupiter's Magnetodisc Currents. *Journal of Geophysical Research: Space Physics*, 125(2):e2019JA027455, 2020. ISSN 2169-9402. doi:10.1029/2019JA027455.

C. T. S. Lorch, L. C. Ray, R. J. Wilson, F. Bagenal, F. Crary, P. A. Delamere, P. A. Damiano, C. E. J. Watt, and F. Allegrini. Evidence of Alfvénic Activity in Jupiter's Mid-To-High Latitude Magnetosphere. *Journal of Geophysical Research: Space Physics*, 127(6): e2021JA029853, 2022. ISSN 2169-9402. doi:10.1029/2021JA029853.

C. K. Louis, C. M. Jackman, G. Hospodarsky, A. O'Kane Hackett, E. Devon-Hurley, P. Zarka, W. S. Kurth, R. W. Ebert, D. M. Weigt, A. R. Fogg, J. E. Waters, S. C. McEntee, J. E. P. Connerney, P. Louarn, S. Levin, and S. J. Bolton. Effect of a Magnetospheric Compression on Jovian Radio Emissions: In Situ Case Study Using Juno Data. *Journal of Geophysical Research: Space Physics*, 128(9):e2022JA031155, 2023. ISSN 2169-9402. doi:10.1029/2022JA031155.

R. L. Lysak. Kinetic Alfvén waves and auroral particle acceleration: a review. *Reviews of Modern Plasma Physics*, 7(1):6, Jan. 2023. ISSN 2367-3192. doi:10.1007/s41614-022-00111-2.

R. L. Lysak and W. Lotko. On the kinetic dispersion relation for shear Alfvén waves. *Journal of Geophysical Research: Space Physics*, 101(A3):5085–5094, 1996. ISSN 2156-2202. doi:10.1029/95JA03712.

R. L. Lysak and Y. Song. Kinetic theory of the Alfvén wave acceleration of auroral electrons. *Journal of Geophysical Research: Space Physics*, 108(A4), 2003. ISSN 2156-2202. doi:10.1029/2002JA009406.

R. L. Lysak, Y. Song, S. Elliott, W. Kurth, A. H. Sulaiman, and D. Gershman. The Jovian Ionospheric Alfvén Resonator and Auroral Particle Acceleration. *Journal of Geophysical Research: Space Physics*, 126(12):e2021JA029886, 2021. ISSN 2169-9402. doi:10.1029/2021JA029886.

Q. Ma, R. M. Thorne, W. Li, X.-J. Zhang, B. H. Mauk, C. Paranicas, D. K. Haggerty, W. S. Kurth, J. E. P. Connerney, F. Bagenal, and S. J. Bolton. Electron butterfly distributions at particular magnetic latitudes observed during Juno's perijove pass. *Geophysical Research Letters*, 44(10):4489–4496, 2017. ISSN 1944-8007. doi:10.1002/2017GL072983.

R. J. MacDowall, M. L. Kaiser, M. D. Desch, W. M. Farrell, R. A. Hess, and R. G. Stone. Quasiperiodic Jovian Radio bursts: observations from the Ulysses Radio and Plasma Wave Experiment. *Planetary and Space Science*, 41:1059–1072, Nov. 1993. ISSN 0032-0633. doi:10.1016/0032-0633(93)90109-F. Publisher: Elsevier ADS Bibcode: 1993P&SS...41.1059M.

W. W. Macy and L. M. Trafton. Io's sodium emission cloud. *Icarus*, 25(3):432–438, July 1975. ISSN 0019-1035. doi:10.1016/0019-1035(75)90007-X.

H. Manners and A. Masters. The Global Distribution of Ultralow-Frequency Waves in Jupiter's Magnetosphere. *Journal of Geophysical Research: Space Physics*, 125(10): e2020JA028345, 2020. ISSN 2169-9402. doi:10.1029/2020JA028345.

F. Marchis, I. de Pater, A. G. Davies, H. G. Roe, T. Fusco, D. L. Mignant, P. Descamps, B. A. Macintosh, and R. Prangé. High-Resolution Keck Adaptive Optics Imaging of Violent Volcanic Activity on Io. *Icarus*, 160(1):124–131, Nov. 2002. ISSN 0019-1035. doi:10.1006/icar.2002.6955.

G. T. Marklund, N. Ivchenko, T. Karlsson, A. Fazakerley, M. Dunlop, P. A. Lindqvist, S. Buchert, C. Owen, M. Taylor, A. Vaivalds, P. Carter, M. André, and A. Balogh. Temporal evolution of the electric field accelerating electrons away from the auroral ionosphere. *Nature*, 414(6865):724–727, Dec. 2001. ISSN 0028-0836. doi:10.1038/414724a.

B. H. Mauk and J. Saur. Equatorial electron beams and auroral structuring at Jupiter. *Journal of Geophysical Research: Space Physics*, 112(A10), 2007. ISSN 2156-2202. doi:10.1029/2007JA012370.

B. H. Mauk, D. J. Williams, and R. W. McEntire. Energy-time dispersed charged particle signatures of dynamic injections in Jupiter's inner magnetosphere. *Geophysical Research Letters*, 24(23):2949–2952, 1997. ISSN 1944-8007. doi:10.1029/97GL03026.

B. H. Mauk, D. J. Williams, R. W. McEntire, K. K. Khurana, and J. G. Roederer. Storm-like dynamics of Jupiter's inner and middle magnetosphere. *Journal of Geophysical Research: Space Physics*, 104(A10):22759–22778, 1999. ISSN 2156-2202. doi:10.1029/1999JA900097.

B. H. Mauk, J. T. Clarke, D. Grodent, J. H. Waite, C. P. Paranicas, and D. J. Williams. Transient aurora on Jupiter from injections of magnetospheric electrons. *Nature*, 415 (6875):1003–1005, Feb. 2002. ISSN 0028-0836, 1476-4687. doi:10.1038/4151003a.

B. H. Mauk, D. K. Haggerty, S. E. Jaskulek, C. E. Schlemm, L. E. Brown, S. A. Cooper, R. S. Gurnee, C. M. Hammock, J. R. Hayes, G. C. Ho, J. C. Hutcheson, A. D. Jacques, S. Kerem, C. K. Kim, D. G. Mitchell, K. S. Nelson, C. P. Paranicas, N. Paschalidis, E. Rossano, and M. R. Stokes. The Jupiter Energetic Particle Detector Instrument (JEDI) Investigation for the Juno Mission. *Space Science Reviews*, 213(1):289–346, Nov. 2017a. ISSN 1572-9672. doi:10.1007/s11214-013-0025-3.

B. H. Mauk, D. K. Haggerty, C. Paranicas, G. Clark, P. Kollmann, A. M. Rymer, S. J. Bolton, S. M. Levin, A. Adriani, F. Allegrini, F. Bagenal, B. Bonfond, J. E. P. Connerney, G. R. Gladstone, W. S. Kurth, D. J. McComas, and P. Valek. Discrete and broadband electron acceleration in Jupiter's powerful aurora. *Nature*, 549(7670):66–69, Sept. 2017b. ISSN 1476-4687. doi:10.1038/nature23648. Publisher: Nature Publishing Group.

B. H. Mauk, D. K. Haggerty, C. Paranicas, G. Clark, P. Kollmann, A. M. Rymer, D. G. Mitchell, S. J. Bolton, S. M. Levin, A. Adriani, F. Allegrini, F. Bagenal, J. E. P. Connerney, G. R. Gladstone, W. S. Kurth, D. J. McComas, D. Ranquist, J. R. Szalay, and P. Valek. Juno observations of energetic charged particles over Jupiter's polar regions: Analysis of monodirectional and bidirectional electron beams. *Geophysical Research Letters*, 44(10):4410–4418, 2017c. ISSN 1944-8007. doi:10.1002/2016GL072286.

B. H. Mauk, D. K. Haggerty, C. Paranicas, G. Clark, P. Kollmann, A. M. Rymer, J. M. Peachey, S. J. Bolton, S. M. Levin, A. Adriani, F. Allegrini, F. Bagenal, B. Bonfond, J. E. P. Connerney, R. W. Ebert, G. R. Gladstone, W. S. Kurth, D. J. McComas, D. Ranquist, and P. Valek. Diverse Electron and Ion Acceleration Characteristics Observed Over Jupiter's Main Aurora. *Geophysical Research Letters*, 45(3):1277–1285, 2018. ISSN 1944-8007. doi:10.1002/2017GL076901.

B. H. Mauk, G. Clark, G. R. Gladstone, S. Kotsiaros, A. Adriani, F. Allegrini, F. Bagenal, S. J. Bolton, B. Bonfond, J. E. P. Connerney, R. W. Ebert, D. K. Haggerty, P. Kollmann, W. S. Kurth, S. M. Levin, C. P. Paranicas, and A. M. Rymer. Energetic Particles and Acceleration Regions Over Jupiter's Polar Cap and Main Aurora: A Broad Overview. *Journal of Geophysical Research: Space Physics*, 125(3):e2019JA027699, 2020. ISSN 2169-9402. doi:10.1029/2019JA027699.

M. B. McElroy, Y. L. Yung, and R. A. Brown. Sodium Emission from Io: Implications. *The Astrophysical Journal*, 187:L127, Feb. 1974. ISSN 0004-637X. doi:10.1086/181414. ADS Bibcode: 1974ApJ...187L.127M.

H. Melin, J. O'Donoghue, L. Moore, T. S. Stallard, L. N. Fletcher, M. T. Roman, J. Harkett, O. R. T. King, E. M. Thomas, R. Wang, P. I. Tiranti, K. L. Knowles, I. de Pater, T. Fouchet, P. H. Fry, M. H. Wong, B. J. Holler, R. Hueso, M. K. James, G. S. Orton, A. Mura, A. Sánchez-Lavega, E. Lellouch, K. de Kleer, and M. R. Showalter. Ionospheric irregularities at Jupiter observed by JWST. *Nature Astronomy*, 8(8):1000–1007, Aug. 2024. ISSN 2397-3366. doi:10.1038/s41550-024-02305-9.

M. Mendillo, J. Baumgardner, B. Flynn, and W. J. Hughes. The extended sodium nebula of Jupiter. *Nature*, 348(6299):312–314, Nov. 1990. ISSN 1476-4687. doi:10.1038/348312a0. Number: 6299.

M. Mendillo, J. Wilson, J. Spencer, and J. Stansberry. Io's volcanic control of Jupiter's extended neutral clouds. *Icarus*, 170(2):430–442, Aug. 2004. ISSN 0019-1035. doi:10.1016/j.icarus.2004.03.009.

M. Mendillo, S. Laurent, J. Wilson, J. Baumgardner, J. Konrad, and W. C. Karl. The sources of sodium escaping from Io revealed by spectral high definition imaging. *Nature*, 448(7151):330–332, July 2007. ISSN 1476-4687. doi:10.1038/nature06000.

J. D. Menietti, T. F. Averkamp, M. Imai, W. S. Kurth, G. B. Clark, F. Allegrini, J. B. Groene, J. B. Faden, and S. J. Bolton. Low-Latitude Whistler-Mode and Higher-Latitude Z-Mode Emission at Jupiter Observed by Juno. *Journal of Geophysical Research: Space Physics*, 126(2):e2020JA028742, 2021. ISSN 2169-9402. doi:10.1029/2020JA028742.

A. Moirano, A. Mura, B. Bonfond, J. Connerney, V. Dols, D. Grodent, V. Hue, J.-C. Gérard, F. Tosi, A. Migliorini, A. Adriani, F. Altieri, C. Castagnoli, A. Cicchetti, B. M. Dinelli, D. Grassi, M. L. Moriconi, R. Noschese, G. Piccioni, C. Plainaki, P. Scarica, G. Sindoni, R. Sordini, D. Turrini, and F. Zambon. Variability of the Auroral Footprint of Io Detected by Juno-JIRAM and Modelling of the Io Plasma Torus. *Journal of Geophysical Research: Space Physics*, n/a(n/a):e2023JA031288, 2023. ISSN 2169-9402. doi:10.1029/2023JA031288.

A. Moirano, A. Mura, V. Hue, B. Bonfond, L. A. Head, J. E. P. Connerney, A. Adriani, F. Altieri, C. Castagnoli, A. Cicchetti, B. M. Dinelli, D. Grassi, A. Migliorini, M. L. Moriconi, R. Noschese, G. Piccioni, C. Plainaki, P. Scarica, G. Sindoni, R. Sordini, F. Tosi, D. Turrini, and F. Zambon. The Infrared Auroral Footprint Tracks of Io, Europa and Ganymede at Jupiter Observed by Juno-JIRAM. *Journal of Geophysical Research: Planets*, 129 (3):e2023JE008130, 2024. ISSN 2169-9100. doi:10.1029/2023JE008130.

J. C. Momberg, A. N. Jaynes, S. N. F. Chepuri, A. Leali, J. A. Karl, and R. N. Troyer. The impact of drifting substorm-injected electrons on pulsating aurora initiation and intensification. *Frontiers in Astronomy and Space Sciences*, 11, Mar. 2024. ISSN 2296-987X. doi:10.3389/fspas.2024.1335562. Publisher: Frontiers.

M. Moncuquet, F. Bagenal, and N. Meyer-Vernet. Latitudinal structure of outer Io plasma torus. *Journal of Geophysical Research: Space Physics*, 107(A9):SMP 24–1–SMP 24–11, 2002. ISSN 2156-2202. doi:10.1029/2001JA900124.

L. A. Morabito, S. P. Synnott, P. N. Kupferman, and S. A. Collins. Discovery of Currently Active Extraterrestrial Volcanism. *Science*, 204(4396):972–972, June 1979. doi:10.1126/science.204.4396.972.a.

J. P. Morgenthaler, C. A. Schmidt, M. F. Vogt, N. M. Schneider, and M. Marconi. Jovian Sodium Nebula and Io Plasma Torus S+ and Brightnesses 2017–2023: Insights Into Volcanic Versus Sublimation Supply. *Journal of Geophysical Research: Space Physics*, 129(3):e2023JA032081, 2024. ISSN 2169-9402. doi:10.1029/2023JA032081.

F. Mottez and V. Génot. Electron acceleration by an Alfvénic pulse propagating in an auroral plasma cavity. *Journal of Geophysical Research: Space Physics*, 116(A1), 2011. ISSN 2156-2202. doi:10.1029/2010JA016367.

A. Moullet, M. A. Gurwell, E. Lellouch, and R. Moreno. Simultaneous mapping of SO2, SO, NaCl in Io's atmosphere with the Submillimeter Array. *Icarus*, 208(1):353–365, July 2010. ISSN 0019-1035. doi:10.1016/j.icarus.2010.02.009.

A. Mura, A. Adriani, J. E. P. Connerney, S. Bolton, F. Altieri, F. Bagenal, B. Bonfond, B. M. Dinelli, J.-C. Gérard, T. Greathouse, D. Grodent, S. Levin, B. Mauk, M. L. Moriconi, J. Saur, J. H. Waite, M. Amoroso, A. Cicchetti, F. Fabiano, G. Filacchione, D. Grassi, A. Migliorini, R. Noschese, A. Olivieri, G. Piccioni, C. Plainaki, G. Sindoni, R. Sordini, F. Tosi, and D. Turrini. Juno observations of spot structures and a split tail in Io-induced aurorae on Jupiter. *Science*, 361(6404):774–777, Aug. 2018. ISSN 0036-8075, 1095-9203. doi:10.1126/science.aat1450.

G. Murakami, K. Yoshioka, A. Yamazaki, F. Tsuchiya, T. Kimura, C. Tao, H. Kita, M. Kagitani, T. Sakanoi, K. Uemizu, Y. Kasaba, I. Yoshikawa, and M. Fujimoto. Response of Jupiter's inner magnetosphere to the solar wind derived from extreme ultraviolet monitoring of the Io plasma torus. *Geophysical Research Letters*, 43(24):12,308–12,316, 2016. ISSN 1944-8007. doi:10.1002/2016GL071675.

F. Neubauer. Nonlinear standing Alfvén wave current system at Io: Theory. *Journal of Geophysical Research: Space Physics*, 85(A3):1171–1178, 1980. ISSN 2156-2202. doi:10.1029/JA085iA03p01171.

F. M. Neubauer. The sub-Alfvénic interaction of the Galilean satellites with the Jovian magnetosphere. *Journal of Geophysical Research: Planets*, 103(E9):19843–19866, 1998. ISSN 2156-2202. doi:10.1029/97JE03370.

J. D. Nichols. Magnetosphere-ionosphere coupling in Jupiter's middle magnetosphere: Computations including a self-consistent current sheet magnetic field model. *Journal of Geophysical Research: Space Physics*, 116(A10), 2011. ISSN 2156-2202. doi:10.1029/2011JA016922.

J. D. Nichols and S. W. H. Cowley. Relation of Jupiter's Dawnside Main Emission Intensity to Magnetospheric Currents During the Juno Mission. *Journal of Geophysical Research: Space Physics*, 127(1):e2021JA030040, 2022. ISSN 2169-9402. doi:10.1029/2021JA030040.

J. D. Nichols, E. J. Bunce, J. T. Clarke, S. W. H. Cowley, J.-C. Gérard, D. Grodent, and W. R. Pryor. Response of Jupiter's UV auroras to interplanetary conditions as observed by the Hubble Space Telescope during the Cassini flyby campaign. *Journal of Geophysical Research: Space Physics*, 112(A2), 2007. ISSN 2156-2202. doi:10.1029/2006JA012005.

J. D. Nichols, J. T. Clarke, J. C. Gérard, and D. Grodent. Observations of Jovian polar auroral filaments. *Geophysical Research Letters*, 36(8), 2009a. ISSN 1944-8007. doi:10.1029/2009GL037578.

J. D. Nichols, J. T. Clarke, J. C. Gérard, D. Grodent, and K. C. Hansen. Variation of different components of Jupiter's auroral emission. *Journal of Geophysical Research: Space Physics*, 114(A6), 2009b. ISSN 2156-2202. doi:10.1029/2009JA014051.

J. D. Nichols, S. V. Badman, F. Bagenal, S. J. Bolton, B. Bonfond, E. J. Bunce, J. T. Clarke, J. E. P. Connerney, S. W. H. Cowley, R. W. Ebert, M. Fujimoto, J.-C. Gérard, G. R. Gladstone, D. Grodent, T. Kimura, W. S. Kurth, B. H. Mauk, G. Murakami, D. J. McComas, G. S. Orton, A. Radioti, T. S. Stallard, C. Tao, P. W. Valek, R. J. Wilson, A. Yamazaki, and I. Yoshikawa. Response of Jupiter's auroras to conditions in the interplanetary medium as measured by the Hubble Space Telescope and Juno. *Geophysical Research Letters*, 44(15):7643–7652, 2017. ISSN 1944-8007. doi:10.1002/2017GL073029.

J. D. Nichols, A. Kamran, and S. E. Milan. Machine Learning Analysis of Jupiter's Far-Ultraviolet Auroral Morphology. *Journal of Geophysical Research: Space Physics*, 124(11):8884–8892, 2019. ISSN 2169-9402. doi:10.1029/2019JA027120.

J. D. Nichols, F. Allegrini, F. Bagenal, E. J. Bunce, S. W. H. Cowley, R. W. Ebert, D. Grodent, E. Huscher, A. Kamran, W. S. Kurth, R. J. Wilson, and Z. Yao. An Enhancement of Jupiter's Main Auroral Emission and Magnetospheric Currents. *Journal of Geophysical Research: Space Physics*, 125(8):e2020JA027904, 2020. ISSN 2169-9402. doi:10.1029/2020JA027904.

J. D. Nichols, F. Allegrini, F. Bagenal, B. Bonfond, G. B. Clark, J. T. Clarke, J. E. P. Connerney, S. W. H. Cowley, R. W. Ebert, G. R. Gladstone, D. Grodent, D. K. Haggerty, B. Mauk, G. S. Orton, G. Provan, and R. J. Wilson. Jovian Magnetospheric Injections Observed by the Hubble Space Telescope and Juno. *Geophysical Research Letters*, 50 (20):e2023GL105549, 2023. ISSN 1944-8007. doi:10.1029/2023GL105549.

J. D. Nichols, O. R. T. King, J. T. Clarke, I. de Pater, L. N. Fletcher, H. Melin, L. Moore, C. Tao, and T. K. Yeoman. Dynamic infrared aurora on Jupiter. *Nature Communications*, 16(1):3907, May 2025. ISSN 2041-1723. doi:10.1038/s41467-025-58984-z.

J. O'Donoghue, L. Moore, T. Bhakyapaibul, H. Melin, T. Stallard, J. E. P. Connerney, and C. Tao. Global upper-atmospheric heating on Jupiter by the polar aurorae. *Nature*, 596 (7870):54–57, Aug. 2021. ISSN 1476-4687. doi:10.1038/s41586-021-03706-w. Publisher: Nature Publishing Group.

B. Palmaerts, A. Radioti, D. Grodent, E. Chané, and B. Bonfond. Transient small-scale structure in the main auroral emission at Jupiter. *Journal of Geophysical Research: Space Physics*, 119(12):9931–9938, 2014. ISSN 2169-9402. doi:10.1002/2014JA020688.

B. Palmaerts, D. Grodent, B. Bonfond, Z. H. Yao, R. L. Guo, J. C. Gérard, K. Haewsantati, G. R. Gladstone, T. K. Greathouse, V. Hue, and J. D. Nichols. Overview of a large observing campaign of Jupiter's aurora with the Hubble Space Telescope combined with Juno-UVS data. *Icarus*, 408:115815, Jan. 2024. ISSN 0019-1035. doi:10.1016/j.icarus.2023.115815.

D.-X. Pan, Z.-H. Yao, H. Manners, W. Dunn, B. Bonfond, D. Grodent, B.-Z. Zhang, R.-L. Guo, and Y. Wei. Ultralow-Frequency Waves in Driving Jovian Aurorae Revealed by Observations From HST and Juno. *Geophysical Research Letters*, 48(5):e2020GL091579, 2021. ISSN 1944-8007. doi:10.1029/2020GL091579.

C. Paranicas, B. H. Mauk, G. Clark, P. Kollmann, Q. Nénon, R. W. Ebert, J. R. Szalay, A. H. Sulaiman, J. E. P. Connerney, and S. Bolton. Energetic Charged Particle Measurements During Juno's Two Close Io Flybys. *Geophysical Research Letters*, 51(13): e2024GL109495, 2024. ISSN 1944-8007. doi:10.1029/2024GL109495.

C. P. Paranicas, B. H. Mauk, and S. M. Krimigis. Pressure anisotropy and radial stress balance in the Jovian neutral sheet. *Journal of Geophysical Research: Space Physics*, 96(A12):21135–21140, 1991. ISSN 2156-2202. doi:10.1029/91JA01647.

I. Pardo-Cantos. A new auroral structure on Jupiter: Jupiter's auroral bridge. Master's thesis, Université de Liège, 2019.

S. J. Peale, P. Cassen, and R. T. Reynolds. Melting of Io by Tidal Dissipation. *Science*, 203(4383):892–894, Mar. 1979. doi:10.1126/science.203.4383.892.

J. Pearl, R. Hanel, V. Kunde, W. Maguire, K. Fox, S. Gupta, C. Ponnamperuma, and F. Raulin. Identification of gaseous SO2 and new upper limits for other gases on Io. *Nature*, 280:755–758, Aug. 1979. ISSN 0028-0836. doi:10.1038/280755a0. ADS Bibcode: 1979Natur.280..755P.

M. A. Persinger and D. A. E. Vares. The Asteroid Belt as the Consequence of Resonance Density Convergence from Solar Velocity around the Galaxy and Universal Dynamic Pressure. *International Letters of Chemistry, Physics and Astronomy*, 34:73–79, 2014. ISSN 2299-3843. doi:10.56431/p-mmu107.

J. H. Piddington and J. F. Drake. Electrodynamic Effects of Jupiter's Satellite Io. *Nature*, 217(5132):935–937, Mar. 1968. ISSN 1476-4687. doi:10.1038/217935a0.

R. Prangé, D. Rego, D. Southwood, P. Zarka, S. Miller, and W. Ip. Rapid energy dissipation and variability of the lo-Jupiter electrodynamic circuit. *Nature*, 379:323–325, Jan. 1996. ISSN 0028-0836. doi:10.1038/379323a0. ADS Bibcode: 1996Natur.379..323P.

T. Promfu, J. D. Nichols, S. Wannawichian, J. T. Clarke, M. F. Vogt, and B. Bonfond. Ganymede's Auroral Footprint Latitude: Comparison With Magnetodisc Model. *Journal of Geophysical Research: Space Physics*, 127(12):e2022JA030712, 2022. ISSN 2169-9402. doi:10.1029/2022JA030712.

W. R. Pryor, A. M. Rymer, D. G. Mitchell, T. W. Hill, D. T. Young, J. Saur, G. H. Jones, S. Jacobsen, S. W. H. Cowley, B. H. Mauk, A. J. Coates, J. Gustin, D. Grodent, J.-C. Gérard, L. Lamy, J. D. Nichols, S. M. Krimigis, L. W. Esposito, M. K. Dougherty, A. J. Jouchoux, A. I. F. Stewart, W. E. McClintock, G. M. Holsclaw, J. M. Ajello, J. E. Colwell, A. R. Hendrix, F. J. Crary, J. T. Clarke, and X. Zhou. The auroral footprint of Enceladus on Saturn. *Nature*, 472(7343):331–333, Apr. 2011. ISSN 1476-4687. doi:10.1038/nature09928. Publisher: Nature Publishing Group.

J. Rabia, V. Hue, J. R. Szalay, N. André, Q. Nénon, M. Blanc, F. Allegrini, S. J. Bolton, J. E. P. Connerney, R. W. Ebert, G. R. Gladstone, T. K. Greathouse, P. Louarn, A. Mura, E. Penou, and A. H. Sulaiman. Evidence for Non-Monotonic and Broadband Electron Distributions in the Europa Footprint Tail Revealed by Juno In Situ Measurements. *Geophysical Research Letters*, 50(12):e2023GL103131, 2023. ISSN 1944-8007. doi:10.1029/2023GL103131.

J. Rabia, Q. Nénon, N. André, V. Hue, D. Santos-Costa, A. Kamran, and M. Blanc. Influence of the Jovian Current Sheet Models on the Mapping of the UV Auroral Footprints of Io, Europa, and Ganymede. *Journal of Geophysical Research: Space Physics*, 129(1): e2023JA032041, 2024. ISSN 2169-9402. doi:10.1029/2023JA032041.

J. Rabia, V. Hue, C. K. Louis, N. André, Q. Nénon, J. R. Szalay, R. Prangé, L. Lamy, P. Zarka, B. Collet, F. Allegrini, R. W. Ebert, T. K. Greathouse, B. Bonfond, G. R. Gladstone, A. H. Sulaiman, W. S. Kurth, J. E. P. Connerney, P. Louarn, E. Penou, A. Kamran, D. Santos-Costa, R. S. Giles, J. A. Kammer, M. H. Versteeg, and S. J. Bolton. In situ and remote observations of the ultraviolet footprint of the moon Callisto by the Juno spacecraft. *Nature Communications*, 16(1):7791, Sept. 2025. ISSN 2041-1723. doi:10.1038/s41467-025-62520-4.

J. Radebaugh, L. P. Keszthelyi, A. S. McEwen, E. P. Turtle, W. Jaeger, and M. Milazzo. Paterae on Io: A new type of volcanic caldera? *Journal of Geophysical Research: Planets*, 106(E12):33005–33020, 2001. ISSN 2156-2202. doi:10.1029/2000JE001406.

A. Radioti, J.-C. Gérard, D. Grodent, B. Bonfond, N. Krupp, and J. Woch. Discontinuity in Jupiter's main auroral oval. *Journal of Geophysical Research: Space Physics*, 113 (A1), 2008. ISSN 2156-2202. doi:10.1029/2007JA012610.

A. Radioti, D. Grodent, J.-C. Gérard, E. Roussos, C. Paranicas, B. Bonfond, D. G. Mitchell, N. Krupp, S. Krimigis, and J. T. Clarke. Transient auroral features at Saturn: Signatures of energetic particle injections in the magnetosphere. *Journal of Geophysical Research: Space Physics*, 114(A3), 2009. ISSN 2156-2202. doi:10.1029/2008JA013632.

A. Radioti, D. Grodent, J.-C. Gérard, and B. Bonfond. Auroral signatures of flow bursts released during magnetotail reconnection at Jupiter. *Journal of Geophysical Research: Space Physics*, 115(A7), 2010. ISSN 2156-2202. doi:10.1029/2009JA014844.

L. C. Ray, Y.-J. Su, R. E. Ergun, P. A. Delamere, and F. Bagenal. Current-voltage relation of a centrifugally confined plasma. *Journal of Geophysical Research: Space Physics*, 114(A4):2008JA013969, Apr. 2009. ISSN 0148-0227. doi:10.1029/2008JA013969.

L. C. Ray, R. E. Ergun, P. A. Delamere, and F. Bagenal. Magnetosphere-ionosphere coupling at Jupiter: Effect of field-aligned potentials on angular momentum transport. *Journal of Geophysical Research: Space Physics*, 115(A9), 2010. ISSN 2156-2202. doi:10.1029/2010JA015423.

L. C. Ray, N. A. Achilleos, M. F. Vogt, and J. N. Yates. Local time variations in Jupiter's magnetosphere-ionosphere coupling system. *Journal of Geophysical Research: Space Physics*, 119(6):4740–4751, 2014. ISSN 2169-9402. doi:10.1002/2014JA019941.

C. Raymond Hide. Zenographic longitude systems and Jupiter's differential rotation. *Notes and Records of the Royal Society of London*, 55(1):69–79, Jan. 2001. ISSN 0035-9149. doi:10.1098/rsnr.2001.0126.

K. D. Retherford, J. R. Spencer, S. A. Stern, J. Saur, D. F. Strobel, A. J. Steffl, G. R. Gladstone, H. A. Weaver, A. F. Cheng, J. W. Parker, D. C. Slater, M. H. Versteeg, M. W. Davis, F. Bagenal, H. B. Throop, R. M. C. Lopes, D. C. Reuter, A. Lunsford, S. J. Conard, L. A. Young, and J. M. Moore. Io's atmospheric response to eclipse: UV aurorae observations. *Science*, 318(5848):237–240, Oct. 2007. ISSN 1095-9203. doi:10.1126/science.1147594. Place: New York, N.Y.

E. Rickman and J. Brown. *STIS Instrument Handbook v.25.0.* STScI, Baltimore, 2025.

F. L. Roesler, J. L. Lowrance, P. Zucchino, D. Long, R. J. Oliversen, F. Scherb, J. Lattis, T. B. Williams, D. G. York, and E. B. Jenkins. Fabry-Perot/CCD observations of /S III/ and /S II/ emissions from the Jupiter plasma torus. *The Astrophysical Journal*, 259:900–907, Aug. 1982. ISSN 0004-637X. doi:10.1086/160223. ADS Bibcode: 1982ApJ...259..900R.

F. L. Roesler, H. W. Moos, R. J. Oliversen, R. C. Woodward, K. D. Retherford, F. Scherb, M. A. McGrath, W. H. Smyth, P. D. Feldman, and D. F. Strobel. Far-Ultraviolet Imaging Spectroscopy of Io's Atmosphere with HST/STIS. *Science*, 283(5400):353–357, Jan. 1999. doi:10.1126/science.283.5400.353. Publisher: American Association for the Advancement of Science.

L. Rokach. Ensemble-based classifiers. *Artificial Intelligence Review*, 33(1):1–39, Feb. 2010. ISSN 1573-7462. doi:10.1007/s10462-009-9124-7.

L. Roth, J. Saur, K. D. Retherford, D. F. Strobel, and J. R. Spencer. Simulation of Io's auroral emission: Constraints on the atmosphere in eclipse. *Icarus*, 214:495–509, Aug. 2011. ISSN 0019-1035. doi:10.1016/j.icarus.2011.05.014. Publisher: Elsevier ADS Bibcode: 2011Icar..214..495R.

L. Roth, J. Boissier, A. Moullet, A. Sánchez-Monge, K. de Kleer, M. Yoneda, R. Hikida, H. Kita, F. Tsuchiya, A. Blöcker, G. R. Gladstone, D. Grodent, N. Ivchenko, E. Lellouch, K. D. Retherford, J. Saur, P. Schilke, D. Strobel, and S. Thorwirth. An attempt to detect transient changes in Io's SO2 and NaCl atmosphere. *Icarus*, 350:113925, Nov. 2020. ISSN 0019-1035. doi:10.1016/j.icarus.2020.113925.

M. J. Rutala, J. T. Clarke, J. D. Mullins, and J. D. Nichols. Illuminating the Motions of Jupiter's Auroral Dawn Storms. *Journal of Geophysical Research: Space Physics*, 127 (6):e2022JA030448, 2022. ISSN 2169-9402. doi:10.1029/2022JA030448.

M. J. Rutala, J. T. Clarke, M. F. Vogt, and J. D. Nichols. Variation in the Pedersen Conductance Near Jupiter's Main Emission Aurora: Comparison of Hubble Space Telescope and Galileo Measurements. *Journal of Geophysical Research: Space Physics*, 129(3): e2023JA032122, 2024. ISSN 2169-9402. doi:10.1029/2023JA032122.

A. Salveter, J. Saur, G. Clark, and B. H. Mauk. Jovian Auroral Electron Precipitation Budget—A Statistical Analysis of Diffuse, Mono-Energetic, and Broadband Auroral Electron Distributions. *Journal of Geophysical Research: Space Physics*, 127(8): e2021JA030224, 2022. ISSN 2169-9402. doi:10.1029/2021JA030224.

A. Salveter, J. Saur, G. Clark, A. Sulaiman, B. H. Mauk, J. E. P. Connerney, and B. Bonfond. Investigating Magnetic Field Fluctuations in Jovian Auroral Electron Beams. *Journal of Geophysical Research: Space Physics*, 130(7):e2025JA033816, 2025. ISSN 2169-9402. doi:10.1029/2025JA033816.

B. R. Sandel and A. L. Broadfoot. Morphology of Saturn's aurora. *Nature*, 292(5825): 679–682, Aug. 1981. ISSN 1476-4687. doi:10.1038/292679a0.

B. R. Sandel and A. J. Dessler. Dual periodicity of the Jovian magnetosphere. *Journal of Geophysical Research: Space Physics*, 93(A6):5487–5504, 1988. ISSN 2156-2202. doi:10.1029/JA093iA06p05487.

Y. Sarkango, X. Jia, and G. Toth. Global MHD simulations of the Response of Jupiter's Magnetosphere and Ionosphere to Changes in the Solar Wind and IMF. *Journal of Geophysical Research: Space Physics*, 124(7):5317–5341, 2019. ISSN 2169-9402. doi:10.1029/2019JA026787.

J. Saur. A model of Io's local electric field for a combined Alfvénic and unipolar inductor far-field coupling. *Journal of Geophysical Research: Space Physics*, 109(A1), 2004. ISSN 2156-2202. doi:10.1029/2002JA009354.

J. Saur, D. F. Strobel, and F. M. Neubauer. Interaction of the Jovian magnetosphere with Europa: Constraints on the neutral atmosphere. *Journal of Geophysical Research: Planets*, 103(E9):19947–19962, 1998. ISSN 2156-2202. doi:10.1029/97JE03556.

J. Saur, F. M. Neubauer, D. F. Strobel, and M. E. Summers. Three-dimensional plasma simulation of Io's interaction with the Io plasma torus: Asymmetric plasma flow. *Journal of Geophysical Research: Space Physics*, 104(A11):25105–25126, 1999. ISSN 2156-2202. doi:10.1029/1999JA900304.

J. Saur, A. Pouquet, and W. H. Matthaeus. An acceleration mechanism for the generation of the main auroral oval on Jupiter. *Geophysical Research Letters*, 30(5), 2003. ISSN 1944-8007. doi:10.1029/2002GL015761.

J. Saur, S. Janser, A. Schreiner, G. Clark, B. H. Mauk, P. Kollmann, R. W. Ebert, F. Allegrini, J. R. Szalay, and S. Kotsiaros. Wave-Particle Interaction of Alfvén Waves in Jupiter's Magnetosphere: Auroral and Magnetospheric Particle Acceleration. *Journal of Geophysical Research: Space Physics*, 123(11):9560–9573, 2018. ISSN 2169-9402. doi:10.1029/2018JA025948.

F. L. Scarf. Possible traversals of Jupiter's distant magnetic tail by Voyager and by Saturn. *Journal of Geophysical Research: Space Physics*, 84(A8):4422–4424, 1979. ISSN 2156-2202. doi:10.1029/JA084iA08p04422.

N. M. Schneider and F. Bagenal. Io's neutral clouds, plasma torus, magnetospheric interaction. In R. M. C. Lopes and J. R. Spencer, editors, *Io After Galileo: A New View of Jupiter's Volcanic Moon*, pages 265–286. Springer, Berlin, Heidelberg, 2007. ISBN 978-3-540-48841-5. doi:10.1007/978-3-540-48841-5_11.

N. M. Schneider, J. T. Trauger, J. K. Wilson, D. I. Brown, R. W. Evans, and D. E. Shemansky. Molecular Origin of Io's Fast Sodium. *Science*, 253(5026):1394–1397, Sept. 1991. doi:10.1126/science.253.5026.1394. Publisher: American Association for the Advancement of Science.

R. Schreier, A. Eviatar, V. M. Vasyliūnas, and J. D. Richardson. Modeling the Europa plasma torus. *Journal of Geophysical Research: Space Physics*, 98(A12):21231–21243, Dec. 1993. ISSN 0148-0227. doi:10.1029/93JA02585.

J. J. Secosky and M. Potter. A Hubble Space Telescope Study of Posteclipse Brightening and Albedo Changes on Io. *Icarus*, 111(1):73–78, Sept. 1994. ISSN 0019-1035. doi:10.1006/icar.1994.1134.

P. K. Seidelmann and N. Divine. Evaluation of Jupiter longitudes in System III (1965). *Geophysical Research Letters*, 4(2):65–68, 1977. ISSN 1944-8007. doi:10.1029/GL004i002p00065.

G. Sicorello, D. Grodent, B. Bonfond, J.-C. Gérard, B. Benmahi, A. Salveter, A. Moirano, L. A. Head, J. Vinesse, T. Greathouse, G. R. Gladstone, and M. Barthélémy. The Pedersen and Hall conductances in the Jovian polar regions: New maps based on a broadband electron energy distribution. *Astronomy & Astrophysics*, 703:A69, Nov. 2025. ISSN 0004-6361, 1432-0746. doi:10.1051/0004-6361/202556176.

E. M. Sieveka and R. E. Johnson. Ejection of atoms and molecules from Io by plasmaion impact. *The Astrophysical Journal*, 287:418–426, Dec. 1984. ISSN 0004-637X. doi:10.1086/162701. Publisher: IOP ADS Bibcode: 1984ApJ...287..418S.

E. C. Sittler Jr., R. P. Lepping, B. H. Mauk, and S. M. Krimigis. Detection of a hot plasma component within the core regions of Jupiter's distant magnetotail. *Journal of Geophysical Research: Space Physics*, 92(A9):9943–9948, 1987. ISSN 2156-2202. doi:10.1029/JA092iA09p09943.

W. H. Smyth. Neutral cloud distribution in the jovian system. *Advances in Space Research*, 12:337–46, 1992. doi:10.1016/0273-1177(92)90408-P.

W. H. Smyth and M. R. Combi. A general model for Io's neutral gas clouds. II - Application to the sodium cloud. *The Astrophysical Journal*, 328:888, May 1988. ISSN 0004-637X, 1538-4357. doi:10.1086/166346.

W. D. Smythe, R. M. Nelson, and D. B. Nash. Spectral evidence for SO2 frost or adsorbate on Io's surface. *Nature*, 280(5725):766–766, Aug. 1979. ISSN 1476-4687. doi:10.1038/280766a0.

D. J. Southwood and M. G. Kivelson. A new perspective concerning the influence of the solar wind on the Jovian magnetosphere. *Journal of Geophysical Research: Space Physics*, 106(A4):6123–6130, 2001. ISSN 2156-2202. doi:10.1029/2000JA000236.

J. R. Spencer, K. L. Jessup, C. C. C. Tsang, N. Cunningham, and K. Retherford. Evidence for Volcanic Support of Io's Jupiter-Facing Atmosphere from Constraints on Post-Eclipse Atmospheric Changes. In *Proceedings of the 43rd Lunar and Planetary Science Conference*, page 2420, Mar. 2012. ADS Bibcode: 2012LPI....43.2420S.

T. S. Stallard, S. Miller, S. W. H. Cowley, and E. J. Bunce. Jupiter's polar ionospheric flows: Measured intensity and velocity variations poleward of the main auroral oval. *Geophysical Research Letters*, 30(5), 2003. ISSN 1944-8007. doi:10.1029/2002GL016031.

R. D. Starr, D. Schriver, L. R. Nittler, S. Z. Weider, P. K. Byrne, G. C. Ho, E. A. Rhodes, C. E. Schlemm II, S. C. Solomon, and P. M. Trávníček. MESSENGER detection of electron-induced X-ray fluorescence from Mercury's surface. *Journal of Geophysical Research: Planets*, 117(E12), 2012. ISSN 2156-2202. doi:10.1029/2012JE004118.

E. J. Stone and E. C. Zipf. Excitation of the Werner Bands of H2 by Electron Impact. *The Journal of Chemical Physics*, 56(9):4646–4650, May 1972. ISSN 0021-9606, 1089-7690. doi:10.1063/1.1677914.

R. G. Strom, N. M. Schneider, R. J. Terrile, A. F. Cook, and C. Hansen. Volcanic eruptions on Io. *Journal of Geophysical Research: Space Physics*, 86(A10):8593–8620, 1981. ISSN 2156-2202. doi:10.1029/JA086iA10p08593.

A. H. Sulaiman, B. H. Mauk, J. R. Szalay, F. Allegrini, G. Clark, G. R. Gladstone, S. Kotsiaros, W. S. Kurth, F. Bagenal, B. Bonfond, J. E. P. Connerney, R. W. Ebert, S. S. Elliott, D. J. Gershman, G. B. Hospodarsky, V. Hue, R. L. Lysak, A. Masters, O. Santolík, J. Saur, and S. J. Bolton. Jupiter's Low-Altitude Auroral Zones: Fields, Particles, Plasma Waves, and Density Depletions. *Journal of Geophysical Research: Space Physics*, 127(8):e2022JA030334, 2022. ISSN 2169-9402. doi:10.1029/2022JA030334.

A. H. Sulaiman, J. R. Szalay, G. Clark, F. Allegrini, F. Bagenal, M. J. Brennan, J. E. P. Connerney, V. Hue, W. S. Kurth, R. L. Lysak, J. D. Nichols, J. Saur, and S. J. Bolton. Poynting Fluxes, Field-Aligned Current Densities, and the Efficiency of the Io-Jupiter Electrodynamic Interaction. *Geophysical Research Letters*, 50(10):e2023GL103456, 2023. ISSN 1944-8007. doi:10.1029/2023GL103456.

A. H. Sulaiman, W. S. Kurth, J. E. P. Connerney, S. S. Elliott, G. B. Hospodarsky, N. S. Kruegler, R. L. Lysak, J. D. Menietti, J. R. Szalay, F. Allegrini, and S. J. Bolton. Io's Near-Field Alfvén Wings and Local Electron Beams Inferred From Juno/Waves. *Geophysical Research Letters*, 51(15):e2024GL110206, 2024. ISSN 1944-8007. doi:10.1029/2024GL110206.

M. E. Summers, D. F. Strobel, Y. L. Yung, J. T. Trauger, and F. Mills. The structure of Io's thermal corona and implications for atmospheric escape. *The Astrophysical Journal*, 343:468, Aug. 1989. ISSN 0004-637X, 1538-4357. doi:10.1086/167720.

D. G. Swanson. Plasma Waves (2nd edition). *Plasma Physics and Controlled Fusion*, 45 (6):1069, June 2003. ISSN 0741-3335. doi:10.1088/0741-3335/45/6/701.

D. W. Swift. Simulation of auroral electron acceleration by inertial Alfvén waves. *Journal of Geophysical Research: Space Physics*, 112(A12), 2007. ISSN 2156-2202. doi:10.1029/2007JA012423.

B. G. Swithenbank-Harris, J. D. Nichols, and E. J. Bunce. Jupiter's Dark Polar Region as Observed by the Hubble Space Telescope During the Juno Approach Phase. *Journal of Geophysical Research: Space Physics*, 124(11):9094–9105, 2019. ISSN 2169-9402. doi:10.1029/2019JA027306.

M. Syrjäsuo and T. Pulkkinen. Determining the skeletons of the auroras. In *Proceedings 10th International Conference on Image Analysis and Processing*, pages 1063–1066, Venice, Italy, 1999. IEEE Comput. Soc. ISBN 978-0-7695-0040-9. doi:10.1109/ICIAP.1999.797739.

M. T. Syrjäsuo and E. F. Donovan. Analysis of auroral images: Detection and tracking. *Geophysica*, 38:3–14, 2002.

J. R. Szalay, F. Allegrini, F. Bagenal, S. J. Bolton, B. Bonfond, G. Clark, J. E. P. Connerney, R. W. Ebert, D. J. Gershman, R. S. Giles, G. R. Gladstone, T. Greathouse, G. B. Hospodarsky, M. Imai, W. S. Kurth, S. Kotsiaros, P. Louarn, D. J. McComas, J. Saur, A. H. Sulaiman, and R. J. Wilson. Alfvénic Acceleration Sustains Ganymede's Footprint Tail Aurora. *Geophysical Research Letters*, 47(3):e2019GL086527, 2020. ISSN 1944-8007. doi:10.1029/2019GL086527.

C. Tao, F. Sahraoui, D. Fontaine, J. de Patoul, T. Chust, S. Kasahara, and A. Retinò. Properties of Jupiter's magnetospheric turbulence observed by the Galileo spacecraft. *Journal of Geophysical Research: Space Physics*, 120(4):2477–2493, 2015. ISSN 2169-9402. doi:10.1002/2014JA020749.

C. Tao, T. Kimura, F. Tsuchiya, G. Muirakami, K. Yoshioka, A. Yamazaki, S. V. Badman, H. Misawa, H. Kita, Y. Kasaba, I. Yoshikawa, and M. Fujimoto. Variation of Jupiter's Aurora Observed by Hisaki/EXCEED: 3. Volcanic Control of Jupiter's Aurora. *Geophysical Research Letters*, 45(1):71–79, 2018. ISSN 1944-8007. doi:10.1002/2017GL075814.

F. Taylor, S. Atreya, and D. Hunten. The Composition of the Atmosphere of Jupiter. *Jupiter. The Planet, Satellites and Magnetosphere*, Jan. 2004.

S. S. Tetrick, D. A. Gurnett, W. S. Kurth, M. Imai, G. B. Hospodarsky, S. J. Bolton, J. E. P. Connerney, S. M. Levin, and B. H. Mauk. Plasma waves in Jupiter's high-latitude regions: Observations from the Juno spacecraft. *Geophysical Research Letters*, 44(10):4447–4454, 2017. ISSN 1944-8007. doi:10.1002/2017GL073073.

N. Thomas. Optical observations of Io's neutral clouds and plasma torus. *Surveys in Geophysics*, 13(2):91–164, Mar. 1992. ISSN 0169-3298, 1573-0956. doi:10.1007/BF01903525.

N. Thomas, J. K. Wilson, F. Bagenal, and T. W. Hill. The Io Neutral Clouds and Plasma Torus. In *Jupiter: The Planet, Satellites and Magnetosphere*. Cambridge University Press, 2004.

J. G. Timothy. Review of multianode microchannel array detector systems. *Journal of Astronomical Telescopes, Instruments, and Systems*, 2(3):030901, July 2016. ISSN 2329-4124, 2329-4221. doi:10.1117/1.JATIS.2.3.030901. Publisher: SPIE.

L. Trafton. Detection of a potassium cloud near Io. *Nature*, 258(5537):690–692, Dec. 1975. ISSN 1476-4687. doi:10.1038/258690a0. Number: 5537.

L. Trafton, T. Parkinson, and W. Macy, Jr. The Spatial Extent of Sodium Emission around Io. *The Astrophysical Journal*, 190:L85, June 1974. ISSN 0004-637X. doi:10.1086/181512. ADS Bibcode: 1974ApJ...190L..85T.

L. M. Trafton, C. H. Moore, D. B. Goldstein, P. L. Varghese, and M. A. McGrath. HST/STIS observations and simulation of Io's emission spectrum in Jupiter shadow: Probing Io's Jupiter-facing eclipse atmosphere. *Icarus*, 220(2):1121–1140, Aug. 2012. ISSN 0019-1035. doi:10.1016/j.icarus.2012.06.025.

C. C. C. Tsang, J. R. Spencer, E. Lellouch, M. A. López-Valverde, M. J. Richter, and T. K. Greathouse. Io's atmosphere: Constraints on sublimation support from density variations on seasonal timescales using NASA IRTF/TEXES observations from 2001 to 2010. *Icarus*, 217(1):277–296, Jan. 2012. ISSN 0019-1035. doi:10.1016/j.icarus.2011.11.005.

C. C. C. Tsang, J. R. Spencer, E. Lellouch, M. A. López-Valverde, M. J. Richter, T. K. Greathouse, and H. Roe. Io's contracting atmosphere post 2011 perihelion: Further evidence for partial sublimation support on the anti-Jupiter hemisphere. *Icarus*, 226(1): 1177–1181, Sept. 2013. ISSN 0019-1035. doi:10.1016/j.icarus.2013.06.032.

C. C. C. Tsang, J. R. Spencer, E. Lellouch, M. A. Lopez-Valverde, and M. J. Richter. The collapse of Io's primary atmosphere in Jupiter eclipse. *Journal of Geophysical Research: Planets*, 121(8):1400–1410, 2016. ISSN 2169-9100. doi:10.1002/2016JE005025.

T. K. Tsubota, M. H. Wong, T. Stallard, X. Zhang, and A. A. Simon. UV-dark polar ovals on Jupiter as tracers of magnetosphere–atmosphere connections. *Nature Astronomy*, 9 (2):221–229, Feb. 2025. ISSN 2397-3366. doi:10.1038/s41550-024-02419-0.

F. Tsuchiya, K. Yoshioka, T. Kimura, R. Koga, G. Murakami, A. Yamazaki, M. Kagitani, C. Tao, F. Suzuki, R. Hikida, I. Yoshikawa, Y. Kasaba, H. Kita, H. Misawa, and T. Sakanoi. Enhancement of the Jovian Magnetospheric Plasma Circulation Caused by the Change in Plasma Supply From the Satellite Io. *Journal of Geophysical Research: Space Physics*, 123(8):6514–6532, 2018. ISSN 2169-9402. doi:10.1029/2018JA025316.

S. van der Walt, J. L. Schönberger, J. Nunez-Iglesias, F. Boulogne, J. D. Warner, N. Yager, E. Gouillart, T. Yu, and the scikit-image contributors. scikit-image: image processing in python. *PeerJ*, 2:e453, jun 2014. ISSN 2167-8359. doi:10.7717/peerj.453.

A. R. Vasavada, A. H. Bouchez, A. P. Ingersoll, B. Little, and C. D. Anger. Jupiter's visible aurora and Io footprint. *Journal of Geophysical Research: Planets*, 104(E11):27133–27142, 1999. ISSN 2156-2202. doi:10.1029/1999JE001055.

J. Vinesse, B. Bonfond, B. Benmahi, A. Moirano, D. Grodent, T. K. Greathouse, V. Hue, G. Sicorello, L. A. Head, G. R. Gladstone, and M. W. Davis. Spatial variability of CH4 and C2H2 absorptions in Jupiter's auroral regions from Juno-UVS observations. *Astronomy & Astrophysics*, 707:A330, Mar. 2026. ISSN 0004-6361, 1432-0746. doi:10.1051/0004-6361/202556908. Publisher: EDP Sciences.

M. F. Vogt, M. G. Kivelson, K. K. Khurana, R. J. Walker, B. Bonfond, D. Grodent, and A. Radioti. Improved mapping of Jupiter's auroral features to magnetospheric sources: IMPROVED MAPPING OF JUPITER'S AURORA. *Journal of Geophysical Research: Space Physics*, 116(A3), Mar. 2011. ISSN 01480227. doi:10.1029/2010JA016148.

M. F. Vogt, E. J. Bunce, J. D. Nichols, J. T. Clarke, and W. S. Kurth. Long-Term Variability of Jupiter's Magnetodisk and Implications for the Aurora. *Journal of Geophysical Research: Space Physics*, 122(12):12,090–12,110, 2017. ISSN 2169-9402. doi:10.1002/2017JA024066.

M. F. Vogt, F. Bagenal, and S. J. Bolton. Magnetic Field Conditions Upstream of Ganymede. *Journal of Geophysical Research: Space Physics*, 127(12):e2022JA030497, 2022a. ISSN 2169-9402. doi:10.1029/2022JA030497.

M. F. Vogt, M. Rutala, B. Bonfond, J. T. Clarke, L. Moore, and J. D. Nichols. Variability of Jupiter's Main Auroral Emission and Satellite Footprints Observed With HST During the Galileo Era. *Journal of Geophysical Research: Space Physics*, 127(2):e2021JA030011, 2022b. ISSN 2169-9402. doi:10.1029/2021JA030011.

J. H. Waite et al. An auroral flare at Jupiter. *Letters to Nature*, 410:787–789, 2001. doi:10.1038/35071018.

A. Wang, X. Yan, and Z. Wei. ImagePy: an open-source, Python-based and platform-independent software package for bioimage analysis. *Bioinformatics*, 34(18):3238–3240, Sept. 2018. ISSN 1367-4803. doi:10.1093/bioinformatics/bty313.

Q. Wang, H. Fang, and B. Li. Automatic Identification of Aurora Fold Structure in All-Sky Images. *Universe*, 9(2):79, Feb. 2023a. ISSN 2218-1997. doi:10.3390/universe9020079.

R. Wang, T. S. Stallard, H. Melin, K. H. Baines, N. Achilleos, A. M. Rymer, L. C. Ray, J. D. Nichols, L. Moore, J. O'Donoghue, M. N. Chowdhury, E. M. Thomas, K. L. Knowles, P. I. Tiranti, and S. Miller. Asymmetric Ionospheric Jets in Jupiter's Aurora. *Journal of Geophysical Research: Space Physics*, 128(12):e2023JA031861, 2023b. ISSN 2169-9402. doi:10.1029/2023JA031861.

Y. Wang, M. Blanc, C. Louis, C. Wang, N. André, A. Adriani, F. Allegrini, P.-L. Blelly, S. Bolton, B. Bonfond, G. Clark, B. M. Dinelli, J.-C. Gérard, R. Gladstone, D. Grodent, S. Kotsiaros, W. Kurth, L. Lamy, P. Louarn, A. Marchaudon, B. Mauk, A. Mura, and C. Tao. A Preliminary Study of Magnetosphere-Ionosphere-Thermosphere Coupling at Jupiter: Juno Multi-Instrument Measurements and Modeling Tools. *Journal of Geophysical Research: Space Physics*, 126(9):e2021JA029469, 2021. ISSN 2169-9402. doi:10.1029/2021JA029469.

D. A. Williams and R. R. Howell. Active volcanism: Effusive eruptions. In *Io After Galileo*, pages 133–161. Springer Berlin Heidelberg, 2007. ISBN 978-3-540-34681-4. doi:10.1007/978-3-540-48841-5_7. Series Title: Springer Praxis Books.

D. A. Williams, P. M. Schenk, and J. Radebaugh. Geology of Io. In R. M. C. Lopes, K. de Kleer, and J. Tuttle Keane, editors, *Io: A New View of Jupiter's Moon*, pages 147–172. Springer International Publishing, Cham, 2023. ISBN 978-3-031-25670-7. doi:10.1007/978-3-031-25670-7_5.

R. E. Williams, B. Blacker, M. Dickinson, W. V. D. Dixon, H. C. Ferguson, A. S. Fruchter, M. Giavalisco, R. L. Gilliland, I. Heyer, R. Katsanis, Z. Levay, R. A. Lucas, D. B. McElroy, L. Petro, M. Postman, H.-M. Adorf, and R. Hook. The Hubble Deep Field: Observations, Data Reduction, and Galaxy Photometry. *The Astronomical Journal*, 112: 1335, Oct. 1996. ISSN 0004-6256. doi:10.1086/118105. Publisher: IOP ADS Bibcode: 1996AJ....112.1335W.

D. J. Wilson, C. S. Froning, G. M. Duvvuri, K. France, A. Youngblood, P. C. Schneider, Z. Berta-Thompson, A. Brown, A. P. Buccino, S. Hawley, J. Irwin, L. Kaltenegger, A. Kowalski, J. Linsky, R. O. Parke Loyd, Y. Miguel, J. S. Pineda, S. Redfield, A. Roberge, S. Rugheimer, F. Tian, and M. Vieytes. The Mega-MUSCLES Spectral Energy Distribution of TRAPPIST-1. *The Astrophysical Journal*, 911(1):18, Apr. 2021. ISSN 0004-637X. doi:10.3847/1538-4357/abe771.

J. K. Wilson and N. M. Schneider. Io's sodium directional feature: Evidence for ionospheric escape. *Journal of Geophysical Research: Planets*, 104(E7):16567–16583, 1999. ISSN 2156-2202. doi:10.1029/1999JE900017.

J. K. Wilson, M. Mendillo, J. Baumgardner, N. M. Schneider, J. T. Trauger, and B. Flynn. The Dual Sources of Io's Sodium Clouds. *Icarus*, 157(2):476–489, June 2002. ISSN 00191035. doi:10.1006/icar.2002.6821.

R. J. Wilson, M. F. Vogt, G. Provan, A. Kamran, M. K. James, M. Brennan, and S. W. H. Cowley. Internal and External Jovian Magnetic Fields: Community Code to Serve the Magnetospheres of the Outer Planets Community. *Space Science Reviews*, 219(1):15, Feb. 2023. ISSN 1572-9672. doi:10.1007/s11214-023-00961-3.

S. Xinyi, Y. Jun, and W. Yong. A look-back to the 50-year exploration of Jupiter's atmosphere. *Reviews of Geophysics and Planetary Physics*, 56(1):67–82, Jan. 2025. ISSN 2097-1893. doi:10.19975/j.dqyxx.2024-011.

Y. Xu, Z. H. Yao, B. Zhang, P. A. Delamere, L. C. Ray, W. R. Dunn, S. V. Badman, E. H. Feng, Z. Q. Zheng, S. J. Bolton, D. Grodent, B. Bonfond, and Y. Wei. On the Relation Between Jupiter's Aurora and the Dawnside Current Sheet. *Geophysical Research Letters*, 50(13):e2023GL104123, July 2023. ISSN 0094-8276, 1944-8007. doi:10.1029/2023GL104123.

Z. H. Yao, D. Grodent, L. C. Ray, I. J. Rae, A. J. Coates, Z. Y. Pu, A. T. Lui, A. Radioti, J. H. Waite, G. H. Jones, R. L. Guo, and W. R. Dunn. Two fundamentally different drivers of dipolarizations at Saturn. *Journal of Geophysical Research: Space Physics*, 122(4):4348–4356, 2017. ISSN 2169-9402. doi:10.1002/2017JA024060.

Z. H. Yao, B. Bonfond, D. Grodent, E. Chané, W. R. Dunn, W. S. Kurth, J. E. P. Connerney, J. D. Nichols, B. Palmaerts, R. L. Guo, G. B. Hospodarsky, B. H. Mauk, T. Kimura, and S. J. Bolton. On the Relation Between Auroral Morphologies and Compression Conditions of Jupiter's Magnetopause: Observations From Juno and the Hubble Space Telescope. *Journal of Geophysical Research: Space Physics*, 127(10):e2021JA029894, 2022. ISSN 2169-9402. doi:10.1029/2021JA029894.

Z. H. Yao, Y. Xu, Z. L. Zeng, B. Zhang, D. Grodent, B. Bonfond, Y. N. Chen, W. R. Dunn, J. W. Sun, R. W. Ebert, J. E. P. Connerney, and F. Allegrini. Rotating Finger-Like Structures of Jovian Magnetodisc. *Geophysical Research Letters*, 52(15):e2025GL116277, 2025. ISSN 1944-8007. doi:10.1029/2025GL116277.

R. V. Yelle and S. Miller. Jupiter's Thermosphere and Ionosphere. In *Jupiter. The Planet, Satellites and Magnetosphere.* Cambridge University Press, Cambridge, 2004.

M. Yoneda, M. Kagitani, F. Tsuchiya, T. Sakanoi, and S. Okano. Brightening event seen in observations of Jupiter's extended sodium nebula. *Icarus*, 261:31–33, Nov. 2015. ISSN 0019-1035. doi:10.1016/j.icarus.2015.07.037.

I. Yoshikawa, F. Suzuki, R. Hikida, K. Yoshioka, G. Murakami, F. Tsuchiya, C. Tao, A. Yamazaki, T. Kimura, H. Kita, H. Nozawa, and M. Fujimoto. Volcanic activity on Io and its influence on the dynamics of the Jovian magnetosphere observed by EXCEED/Hisaki in 2015. *Earth, Planets and Space*, 69(1):110, Aug. 2017. ISSN 1880-5981. doi:10.1186/s40623-017-0700-9.

K. Yoshioka, F. Tsuchiya, M. Kagitani, T. Kimura, G. Murakami, D. Fukuyama, A. Yamazaki, I. Yoshikawa, and M. Fujimoto. The Influence of Io's 2015 Volcanic Activity on Jupiter's Magnetospheric Dynamics. *Geophysical Research Letters*, 45(19):10,193–10,199, 2018. ISSN 1944-8007. doi:10.1029/2018GL079264.

B. Zhang, P. A. Delamere, Z. Yao, B. Bonfond, D. Lin, K. A. Sorathia, O. J. Brambles, W. Lotko, J. S. Garretson, V. G. Merkin, D. Grodent, W. R. Dunn, and J. G. Lyon. How Jupiter's unusual magnetospheric topology structures its aurora. *Science Advances*, 7 (15):eabd1204, Apr. 2021. doi:10.1126/sciadv.abd1204.

Y. Zhang, L. J. Paxton, and A. T. Y. Lui. Polar rain aurora. *Geophysical Research Letters*, 34(20), 2007. ISSN 1944-8007. doi:10.1029/2007GL031602.

J. Zhao, R. Guo, Q. Shi, T. Tang, A. W. Degeling, Z. Yao, D. Grodent, S.-C. Bai, J.-S. Park, X. Ma, J. Chen, B. Zhang, H. Wang, A. Tian, and Q. Zong. Dayside Magnetodisk Reconnection in Jovian System: Galileo and Voyager Observation. *Journal of Geophysical Research: Planets*, 129(7):e2023JE008240, 2024. ISSN 2169-9100. doi:10.1029/2023JE008240.